NASA-CR-196450



JPL Publication 93-1



# An Atlas of Monthly Mean Distributions of SSMI Surface Wind Speed, ARGOS Buoy Drift, AVHRR/2 Sea Surface Temperature, and ECMWF Surface Wind Components During 1990

D. Halpern
W. Knauss
Jet Propulsion Laboratory
Pasadena, California

O. Brown
University of Miami
Miami, Florida

F. Wentz
Remote Sensing Systems
Santa Rosa, California



January 1993

National Aeronautics and Space Administration

Jet Propulsion Laboratory
California Institute of Technology
Pasadena, California

TECHNICAL REPORT STANDARD TITLE PAGE

| 1. Report No. JPL Pub. 93-1 | 2. Government Accession No. | 3. Recipient's Catalog No. |
|---|---|---|
| 4. Title and Subtitle An Atlas of Monthly Mean Distributions of SSMI Surface Wind Speed, ARGOS Buoy Drift, AVHRR/2 Sea Surface Temperature, and ECMWF Surface Wind Components During 1990 | | 5. Report Date January 1993<br>6. Performing Organization Code |
| 7. Author(s) D. Halpern, W. Knauss, O. Brown, and F. Wentz | | 8. Performing Organization Report No. |
| 9. Performing Organization Name and Address<br>JET PROPULSION LABORATORY<br>California Institute of Technology<br>4800 Oak Grove Drive<br>Pasadena, California 91109 | | 10. Work Unit No.<br>11. Contract or Grant No. NAS7-918<br>13. Type of Report and Period Covered JPL Publication |
| 12. Sponsoring Agency Name and Address<br>NATIONAL AERONAUTICS AND SPACE ADMINISTRATION<br>Washington, D.C. 20546 | | 14. Sponsoring Agency Code RE4 BP-578-22-29-40-00 |

15. Supplementary Notes

16. Abstract

The following monthly mean global distributions for 1990 are proposed with a common color scale and geographical map: 10-m height wind speed estimated from the Special Sensor Microwave Imager (SSMI) on a United States (U.S.) AirForce Defense Meteorological Satellite Program (DMSP) spacecraft; sea surface temperature estimated from the advanced very high resolution radiometer (AVHRR/2) on a U.S. National Oceanic and Atmospheric Administration (NOAA) spacecraft; Cartesian components of free-drifting buoys which are tracked by the ARGOS navigation system on NOAA satellites; and Cartesian components on the 10-m height wind vector computed by the European Center for Medium-Range Weather Forecasting (ECMWF). Charts of monthly mean value, sampling distribution, and standard deviation value are displayed. Annual mean distributions are displayed.

| 17. Key Words (Selected by Author(s)) | 18. Distribution Statement |
|---|---|
| Geosciences and Oceanography (General)<br>Meteorology and Climatology<br>Physical Oceanography | Unclassified - Unlimited |

| 19. Security Classif. (of this report) | 20. Security Classif. (of this page) | 21. No. of Pages | 22. Price |
|---|---|---|---|
| Unclassified | Unclassified | 111 | |

The research described in this publication was carried out, in part, by the Jet Propulsion Laboratory, California Institute of Technology, under a contract with the National Aeronautics and Space Administration.

## ACKNOWLEDGMENTS

Many people contributed to the preparation of the data sets displayed in the atlas, and we thank them for their tremendous support. James Brown (RSMAS) and Joan Splain (RSMAS) participated in processing the MCSST data set. Charles Walton (NESDIS) kindly sent validation results of the MCSST data product. We are extremely grateful to NASA (NAGW-273 (OB), RTOP-578-22-29 (DH, WK), NAS8-38075 (FW)) and ONR (N00014-89-J-1144 (OB)) for their continued support of our research.

CONTENTS

## ABSTRACT

The following monthly mean global distributions for 1990 are presented with a common color scale and geographical map: 10-m height wind speed estimated from the Special Sensor Microwave Imager (SSMI) on a United States (U.S.) Air Force Defense Meteorological Satellite Program (DMSP) spacecraft; sea surface temperature estimated from the advanced very high resolution radiometer (AVHRR/2) on a U.S. National Oceanic and Atmospheric Administration (NOAA) spacecraft; Cartesian components of free-drifting buoys which are tracked by the ARGOS navigation system on NOAA satellites; and Cartesian components of the 10-m height wind vector computed by the European Center for Medium-Range Weather Forecasting (ECMWF). Charts of monthly mean value, sampling distribution, and standard deviation value are displayed. Annual mean distributions are displayed.

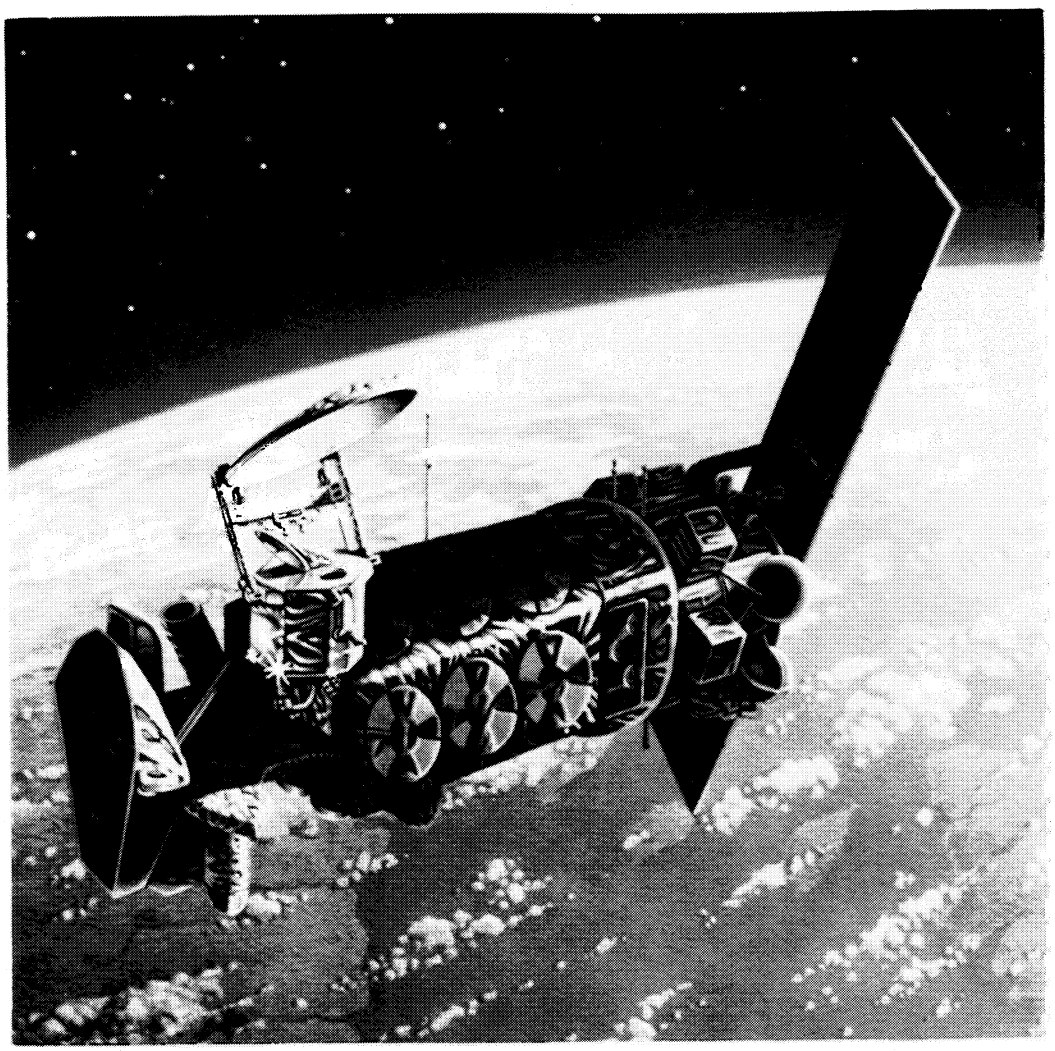

Plate 1. Defense Meteorological Satellite Program (DMSP) satellite with Special Sensor Microwave Imager (SSMI) located at the upper left. (Courtesy of Elena Lobl, Hughes Aircraft Company, Los Angeles.)

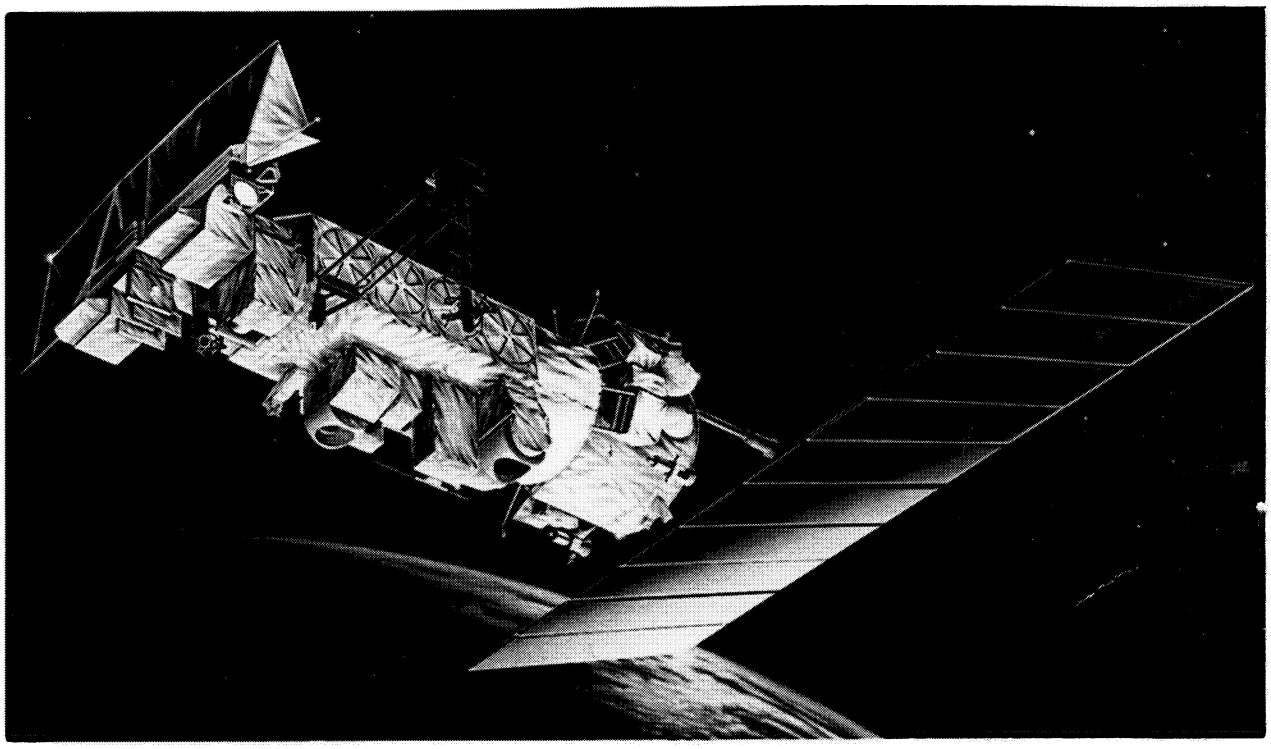

Plate 2. NOAA-11 spacecraft. (Courtesy of Michael Cummings, GE Aerospace, Princeton.)

# 1 INTRODUCTION

This is the fourth volume of a series of annual summaries (Halpern *et al.*, 1991, 1992a, 1992b) of monthly mean global distributions of surface oceanographic variables.

Progress in climate research depends on the availability of a variety of geophysical data sets to describe the boundary conditions and forcing functions of the climate system. The importance of long-period global data sets is highlighted in the United States (U.S.) National Aeronautics and Space Administration (NASA) Earth Observing System (EOS) and the U.S. Committee on Earth and Environmental Sciences (CEES) Global Change Research Program. The unique perspective from space provides the opportunity for observations well suited for the global ocean, which is an essential component of the climatic system and which remains severely undersampled.

Stommel and Fieux (1978), in their guide to oceanographic atlases, stated that "the oceanographic atlas is one of the main tools of the oceanographer." Because of the scarcity of oceanographic data, very few atlases cover the world ocean, and none provide monthly mean distributions for a particular year. Several years of monthly mean data are necessary to analyze the seasonal cycle and interannual variations.

Since about 10 years ago, substantial advances in remote and *in situ* techniques to record temperature, sea level, horizontal current, and surface wind have helped define annual cycles and interannual variations. Innovative ideas of how the ocean and atmosphere are coupled together occurred in parallel with new instrumentation. Analyses of monthly mean global distributions of surface oceanographic variables are becoming *de rigueur*.

Although both satellite- and ground-based recording systems provide essential information for global climate studies, satellite-borne instrumentation yields unprecedented spatial and temporal coverage of the global ocean. This report contains monthly mean distributions for 1990 of satellite measurements of surface wind speed, sea surface temperature, and drifting-buoy positions. Very little averaging or interpolation of the data was made in order to retain the sampling characteristics of each data set. The report also displays surface wind vector components, which were computed by a numerical forecast-analysis system.

Data presented in Appendices A2, A5, and A7 are available on magnetic tape from the Physical Oceanography Distributed Active Archive Center, M/S 300-323, Jet Propulsion Laboratory, 4800 Oak Grove Drive, Pasadena, CA 91109.

# 2 DATA PROCESSING

## 2.1 SSMI Wind Speed

The Special Sensor Microwave Imager (SSMI) is a 7-channel, 4-frequency, linearly polarized, passive microwave radiometer flown on the U.S. Air Force's Defense Meteorological Satellite Program (DMSP) F8 spacecraft in a circular sun-synchronous near-polar orbit at an altitude of approximately 860 km and an orbit period of 102.0 min. The orbit has an ascending (south-to-north) equatorial crossing at 0613 local time. The SSMI was launched on 7 July 1987 and is the first of a series of about ten; the second SSMI was launched on a DMSP satellite in December 1990. Data from only the first SSMI are used. The nearly 1400-km swath of SSMI produces complete coverage between 87°36'S to 87°36'N every 3 days. Each of the 7 separate passive radiometers measures naturally occurring microwave emissions from land, water and ice surfaces and from the intervening atmosphere. The SSMI receives both vertical and horizontal linearly polarized radiation at 19.3, 37.0 and 85.5 GHz and vertical only at 22.2 GHz.

### 2.1.1 Microwave Radiometer Measurement

The emitted microwave radiation at the ocean surface is affected by roughness of the sea surface, which is correlated with the near-surface wind speed. Wentz (1989) prepared the SSMI surface wind speed data product used in this report. Attenuation of 37-GHz radiation propagating

from the sea surface to the satellite is very small, except when an appreciable amount of rain in the atmosphere scatters the 37-GHz radiation. The Wentz (1989) algorithm relates wind speed at 19.5-m height (w, m $s^{-1}$) to the 37-GHz brightness temperatures, which are computed from the SSMI 37-GHz horizontal and vertical polarized radiance measurements, and to the radiative transfer and absorption between the sea surface and SSMI. The horizontal and vertical polarized (denoted by superscript "h" and "v" for horizontal and vertical, respectively) 37-GHz brightness temperatures ($T_B^h$, $T_B^v$) are defined by (Wentz, 1983):

$$T_B^h = T_{Bu} + \tau(E^h T_s + (1-E^h)(1+\omega^h w)(T_{Bd} + \tau T_{B\text{-}cold})) \quad (1a)$$

$$T_B^v = T_{Bu} + \tau(E^v T_s + (1-E^v)(1+\omega^v w)(T_{Bd} + \tau T_{B\text{-}cold})), \quad (1b)$$

where $T_{Bu}$ is the upwelling brightness temperature (K) caused by atmospheric emission and absorption, $T_{Bd}$ is the downwelling brightness temperature (K) produced by atmospheric emission and absorption, ($E^h$, $E^v$) are the emissivities of the sea surface for 37-GHz electromagnetic radiation, ($\omega^h$, $\omega^v$) are coefficients (Table 1) describing the intensities of electromagnetic radiation scattering at the sea surface, $\tau$ is atmospheric transmittance along the viewing path between the sea surface and SSMI, $T_{B\text{-}cold}$ is the 37-GHz cold brightness temperature of cosmic background radiation and equals 2.8 K, and $T_s$ is the sea surface temperature (K).

The upward and downward atmospheric brightness temperatures for a non-scattering atmosphere are (Wentz, 1992)

$$T_{Bu} = (1 - \tau)(T_a - 14.6)$$
$$T_{Bd} = (1 - \tau)(T_a - 13.0),$$

where $T_a$ is the surface air temperature (K). Let the air temperature at the sea surface equal the sea surface temperature, *i. e.*, $T_a = T_s$, and let $T_s$ be specified by Reynolds' (1982) climatological-mean monthly, 1°-latitude x 1°-longitude sea surface temperature analysis.

Sea surface emissivities ($E^h$, $E^v$) are given by

$$(E^h, E^v) = (E_o^h, E_o^h) + (\Delta E_o^h, \Delta E_o^h) + (b^h, b^v)[w(\theta - 49)],$$

where ($E_o^h$, $E_o^v$) are emissivities for a specular or perfectly flat sea surface, ($\Delta E_o^h$, $\Delta E_o^v$) account for changes in emissivities because of occurrences of surface roughness and foam, ($b^h$, $b^v$)[w ($\theta$ - 49)] account for changes in incidence angle $\theta$ of the SSMI radiometer, and ($b^h$, $b^v$) are wind-induced emissivity coefficients. Table 1 contains values of ($b^h$, $b^v$). Microwave radiation at frequencies above 10 GHz is only weakly sensitive to salinity changes (Maul, 1985), and the specular emissivity for an ocean surface of constant salinity of 35 PSU is (Wentz, 1992)

$$E_o^h = (s_o^h + s_1^h t + s_2^h t^2 + s_3^h t^3 + s_4^h u + s_5^h tu + s_6^h u^2 + s_7^h t^2 u)/T_s$$

Table 1

Parameters used by Wentz (1989) to calculate SSMI wind speed from 37-GHz horizontal and vertical polarized radiance measurements.

| Symbol | Parameter | Unit | V-polarization | H-polarization |
|---|---|---|---|---|
| b | Wind-induced emissivity coefficient | s $m^{-1}$ $degree^{-1}$ | $-1.193\times10^{-4}$ | $1.052\times10^{-4}$ |
| $m_1$ | Wind-induced emissivity coefficient | s $m^{-1}$ | $0.70\times10^{-3}$ | $4.10\times10^{-3}$ |
| $m_2$ | Wind-induced emissivity coefficient | s $m^{-1}$ | $2.50\times10^{-3}$ | $7.30\times10^{-3}$ |
| $\omega$ | Surface scattering coefficient | s $m^{-1}$ | $3.52\times10^{-3}$ | $8.55\times10^{-3}$ |
| $s_1$ | Specular emissivity coefficient | none | $-5.637\times10^{-1}$ | $-6.171\times10^{-1}$ |
| $s_2$ | Specular emissivity coefficient | $K^{-1}$ | $1.481\times10^{-2}$ | $1.437\times10^{-2}$ |
| $s_3$ | Specular emissivity coefficient | $K^{-2}$ | $-2.96\times10^{-5}$ | $-7.07\times10^{-5}$ |
| $s_4$ | Specular emissivity coefficient | K $degree^{-1}$ | 2.123 | -1.701 |
| $s_5$ | Specular emissivity coefficient | $degree^{-1}$ | $1.17\times10^{-2}$ | $0.55\times10^{-2}$ |
| $s_6$ | Specular emissivity coefficient | K $degree^{-2}$ | $4.1\times10^{-2}$ | $-1.9\times10^{-2}$ |
| $s_7$ | Specular emissivity coefficient | $K^{-1}$ $degree^{-1}$ | $-0.71\times10^{-4}$ | $-1.27\times10^{-4}$ |

$$E_o^v = (s_o^v + s_1^v t + s_2^v t^2 + s_3^v t^3 + s_4^v u + s_5^v tu + s_6^v u^2 + s_7^v t^2 u)/T_s$$

and

$$t = T_s - 273.16$$
$$u = \theta - 51.$$

Table 1 contains values of ($s_i^h$, $s_i^v$), where i = 0 to 7. The incidence angle is computed from the geometry of the DMSP/SSMI orbit. Wind-forced variations of emissivities are given by (Wentz *et al.*, 1986)

$$(\Delta E_o^h, \Delta E_o^v) = (m_1^h, m_1^v)\, w, \qquad \text{for } w \le 7 \text{ m s}^{-1},$$
$$(\Delta E_o^h, \Delta E_o^v) = (m_1^h, m_1^v)\, w + c^{-1}\, [(m_2^h, m_2^v) - (m_1^h, m_1^v)]\, (w - 7)^2, \qquad \text{for } 7 < w < 17 \text{ m s}^{-1},$$
$$(\Delta E_o^h, \Delta E_o^v) = (m_2^h, m_2^v)\, w - d\, [(m_2^h, m_2^v) - (m_1^h, m_1^v)], \qquad \text{for } w \ge 17 \text{ m s}^{-1}.$$

The constants c (= 20 m s$^{-1}$) and d (= 12 m s$^{-1}$) provide continuity between the segments of ($\Delta E_o^h$, $\Delta E_o^v$). The coefficients ($m_1^h$, $m_1^v$) and ($m_2^h$, $m_2^v$) are listed in Table 1.

The two unknowns, w and $\tau$, in equations (1a) and (1b) are determined by Newton's iteration method. "First-guess" values for w and $\tau$ are 8 m s$^{-1}$ and 0.8, respectively, which represent typical values over the ocean. Convergence is defined when the difference between successive iterations of w becomes less than 0.05 m s$^{-1}$. Convergence is usually found after 3 to 5 iterations. If convergence is not reached after 10 iterations, then the measured brightness temperatures ($T_B^h$, $T_B^v$) are considered erroneous or caused by heavy rain.

SSMI wind speeds referenced to 10-m height, which are equal to 94.3% of w (Wentz, 1989), are used in the report.

### 2.1.2 Environmental Corrections

Environmental conditions reduce the amount of emitted radiation measured at the satellite. At 37 GHz, microwave emission from the ocean surface is masked by the emission and attenuation characteristics of rain. If the integrated liquid water content throughout the atmosphere is greater than 0.25 kg m$^{-2}$, then the Wentz (1989) algorithm is considered invalid because there would be too much radiative scattering from water droplets. Brightness temperatures measured within about 100 km of land, which is defined with a geographical data base, are not used to estimate surface wind speed because the emissivity of land is very different from that of water. For the same reason, surface wind speed within 200 km of the climatological-mean monthly position of the ice edge was not used in the report.

### 2.1.3 1/3° x 1/3° Gridded Monthly Data Set

The Wentz (1989) data set contains wind speed values in nonoverlapping areas of 25 km x 25 km, which are arrayed across the 1394-km SSMI swath width. Geographical coordinates are provided at the center of each 25-km x 25-km region. SSMI wind speeds within nonoverlapping 1/3° x 1/3° squares were arithmetically averaged to form the basic data set for the report. The origin of the global 1/3° x 1/3° grid is 90°N and 0° longitude.

Most of the 1/3° x 1/3° areas contained at least 50 wind speed values per month, or about 1 - 2 values per day. For each month, the standard deviation of daily-averaged SSMI surface wind speeds was computed for 1/3° x 1/3° areas containing 10 or more daily values per month.

The total number of 1/3° x 1/3° monthly-averaged SSMI wind speeds displayed an annual cycle (Figure 1A). A maximum occurred each year during Southern Hemisphere summer when the ice cover around Antarctica was at a minimum. Each 1/3° x 1/3° SSMI wind speed represented the arithmetic mean of several values. The total number of individual SSMI values was low in July 1987 and January 1988 (Figure 1B) because the instrument was not operated the whole of both months. The December 1987 data set ended on 4 December because of a 40-day off-period to avoid possible damage to the SSMI by increased solar heating of the bearing and power transfer assembly (Hollinger *et al.*, 1990). During subsequent winters, the DMSP spacecraft solar arrays were repositioned and the SSMI was not turned off.

(A) Number of Data Grid-Points per Monthly Global Distribution of SSMI 10-m Height Wind Speed

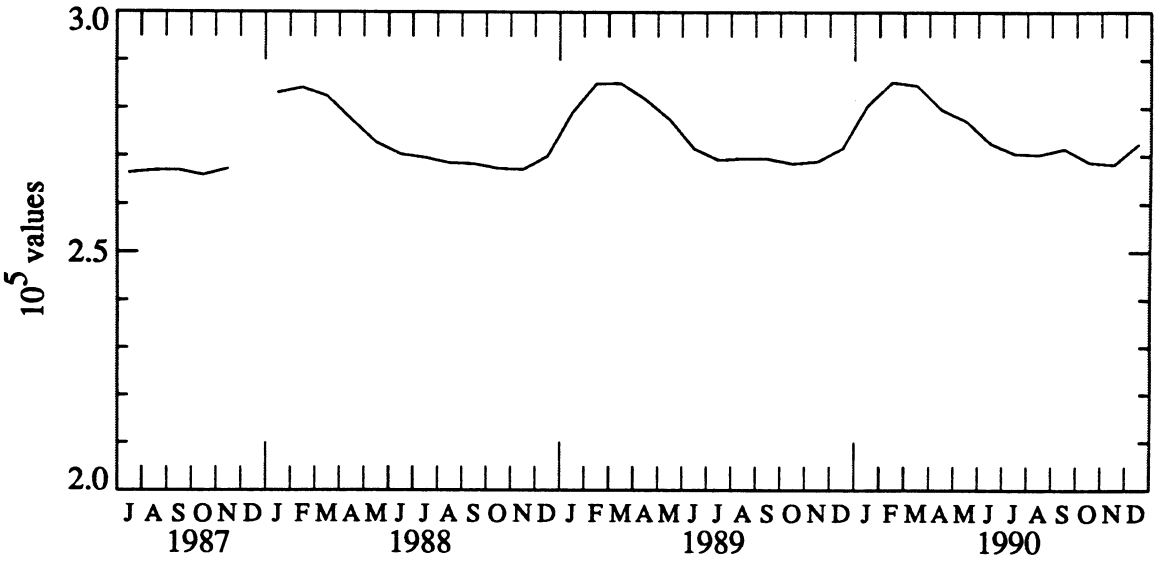


(B) Total Number of 25 km x 25 km Data Values per Monthly Global Distribution of SSMI 10-m Height Wind Speed

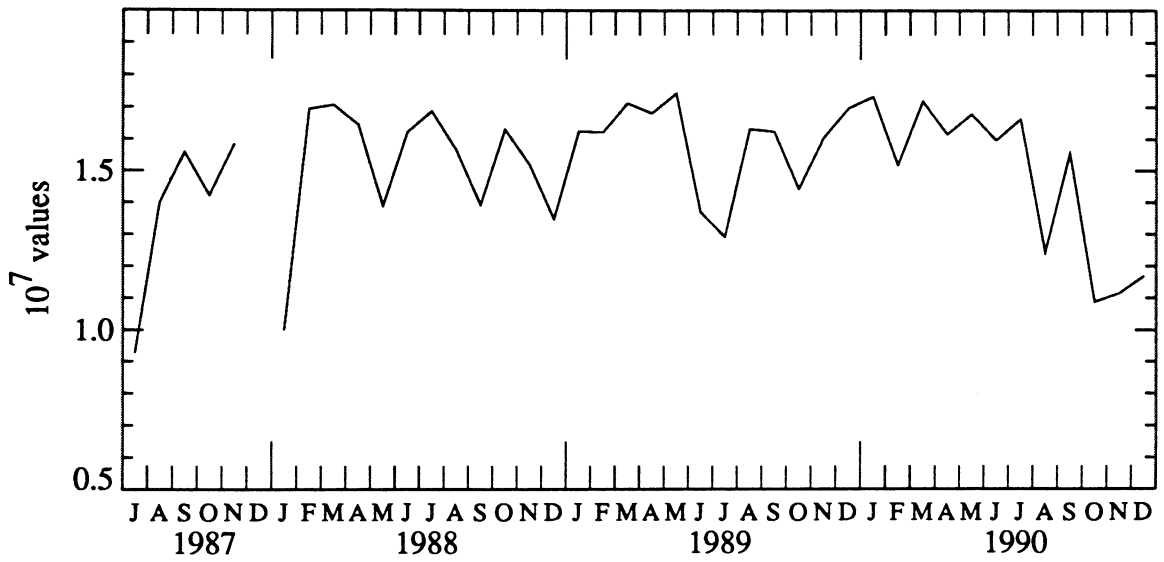


Figure 1. Time series of monthly totals of (A) number of pixels or picture elements and (B) number of 10-m height wind speeds.

### 2.1.4 Wind Speed Accuracy

The SSMI accuracy specification for wind speed retrievals under rain-free conditions is ± 2 m $s^{-1}$ rms over the range 3 - 25 m $s^{-1}$. Wentz (1992) compared SSMI wind speeds with a National Oceanic and Atmospheric Administration (NOAA) National Data Buoy Center moored buoy wind data set prepared by Goodberlet *et al.* (1990), and found differences of zero bias and 1.6 m $s^{-1}$ rms. Model functions different than Wentz' (1989) physically-based algorithm exist. The Environmental Research and Technology (ERT) algorithm for SSMI surface wind speed did not meet the accuracy specification (Goodberlet *et al.*, 1990). Bates' (1991) statistical algorithm with brightness temperatures from five SSMI channels had a 1.1 m $s^{-1}$ bias and a 1.8 m $s^{-1}$ rms difference with moored buoy wind measurements at four sites from 5°S to 5°N along 165°E.

## 2.2 ARGOS Buoy Drift

Since the late 1970s free-drifting buoys have been tracked throughout the world ocean by ARGOS, which is the French navigation system on NOAA polar orbiting satellites. The number of ARGOS-tracked drifting buoys has increased substantially during the past few years because of numerous scientific investigations regarding the role of ocean currents in climate variability (Paduan and Niiler, 1991) and because international weather services continue to require barometric pressure measurements in large areas of the global ocean where few ships travel. ARGOS buoy drift data first appeared in the 1989 atlas (Halpern *et al.*, 1992b) because the number of drifting buoys was considered sufficient for a global perspective.

Canada's Marine Environmental Data Service (MEDS), which is a Responsible National Oceanographic Data Center (RNODC) for Drifting Buoy Data, continuously acquires ARGOS-tracked drifting-buoy positions transmitted in real time via the Global Telecommunications System (GTS) and receives time-delay data. Throughout 1990 MEDS received real-time position data from approximately 50% of the nearly 560 drifting buoys (MEDS, 1991). MEDS continuously updates their archive because investigators submit additional drifting buoy data months and even years after the recorded time of the buoy's position. No time-delay buoy drift data for 1990 had been added to the MEDS archive by July 1991 when the 1990 drifting-buoy data set was acquired from MEDS.

### 2.2.1 Buoy Drift Measurements

ARGOS positions are determined with an accuracy of about 0.5 km. Approximately 5 ARGOS positions of drifting buoys were determined during a transmission day. ARGOS transmission days were not continuous. In the tropical Pacific Ocean a transmission day usually occurred at 3-day intervals and in the Southern Ocean the transmission was approximately daily.

The following quality-control procedure was used. First, drifting buoy data were separated from other data on the MEDS magnetic tapes, which contain Intergovernmental Oceanographic Commission (IOC) - World Meteorological Organization (WMO) coded data for drifting buoys, moored buoys, sailing boats, whales, and other objects not classified as drifting buoys. Only drifting buoy data indicated by MEDS to be of high quality were used. Data were eliminated when the position did not change throughout the month. When the beginning of a buoy's data set indicated a speed between successive positions greater than 2.5 m $s^{-1}$, the positions were deleted because the buoy was assumed to be operational while on a moving ship. Calculation of monthly mean Cartesian components of buoy drift required at least 20 days of position data per month. If the buoy positions at the beginning or end of a month were located poleward of 65°, the buoy was likely to be influenced by ice and was eliminated from the composite data set. If the average of all successive speeds within a month was less than 0.01 m $s^{-1}$ or if the monthly averaged zonal and meridional distances moved by a buoy were less than 8 km, the buoy was eliminated from the composite data set. The average monthly number of drifting buoys in the usable data set was 194. The number of usable drifting buoys per month is listed in Figure 2.

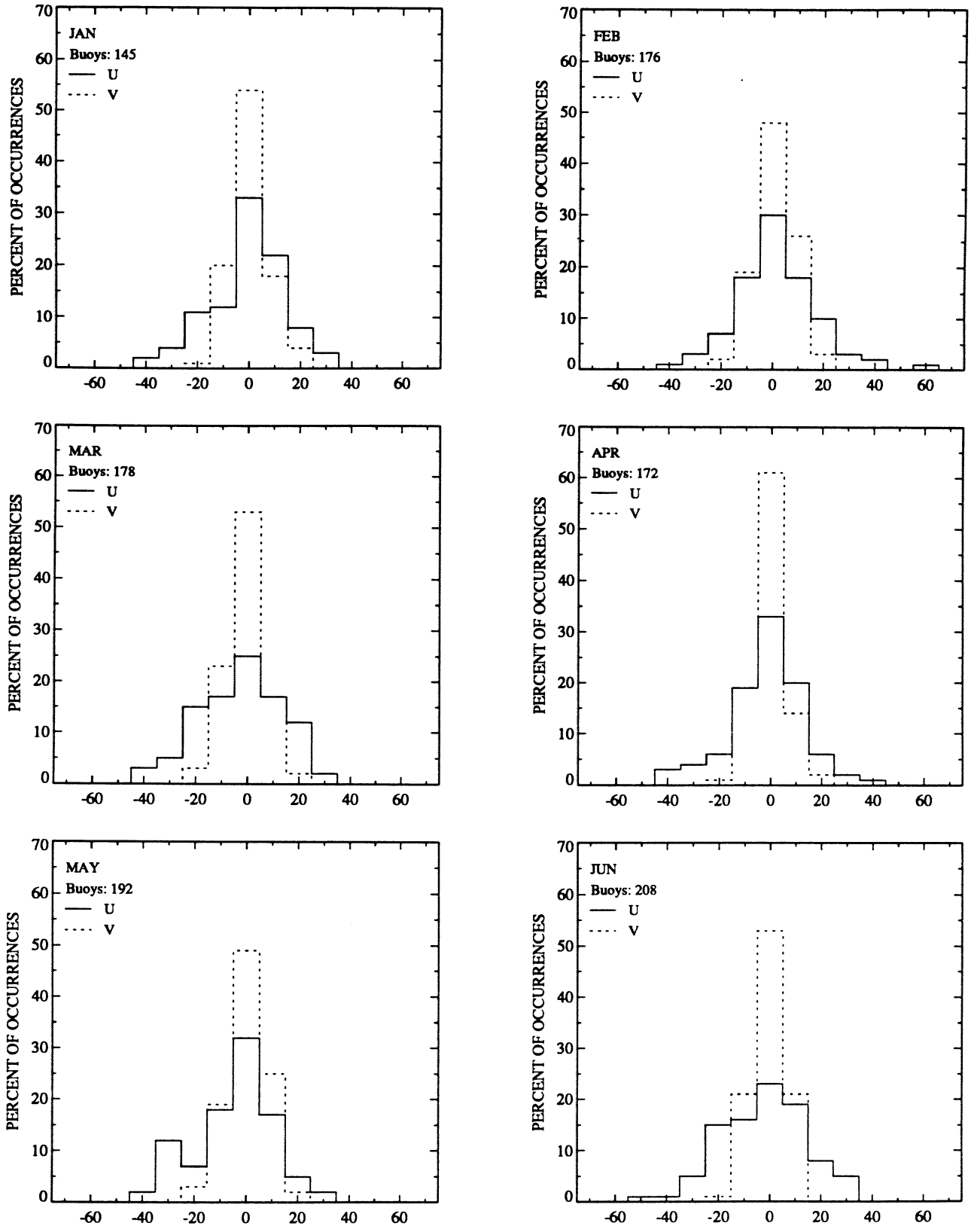


Figure 2. Monthly mean histograms of east-west (U, positive eastward; solid line) and north-south (V, positive northward; dash line) components of ARGOS buoy drift. Number of buoys per month is shown in each panel.

# 1990 ARGOS Monthly Mean Buoy Drift, cm $s^{-1}$

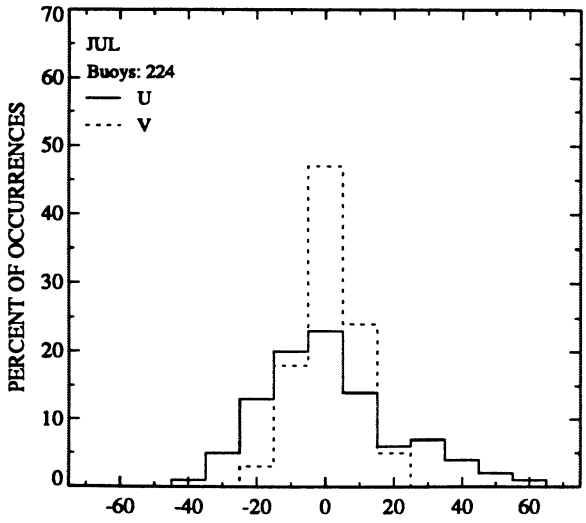


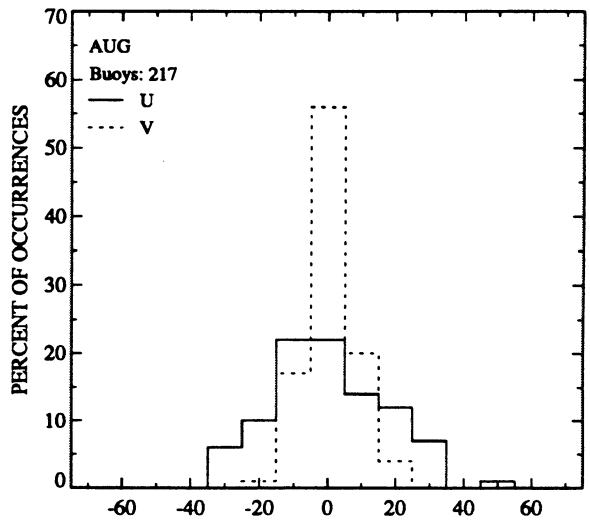


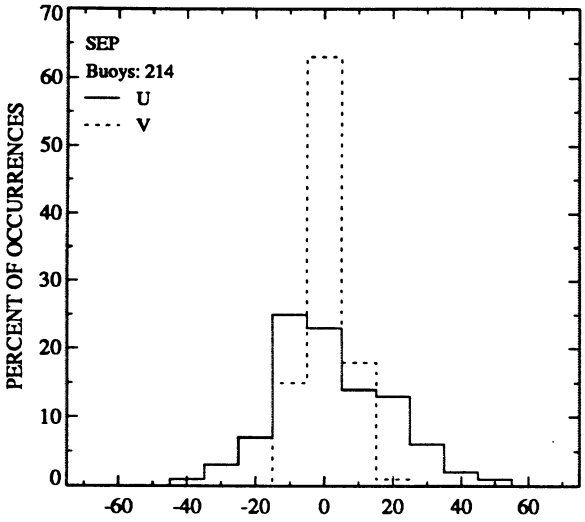


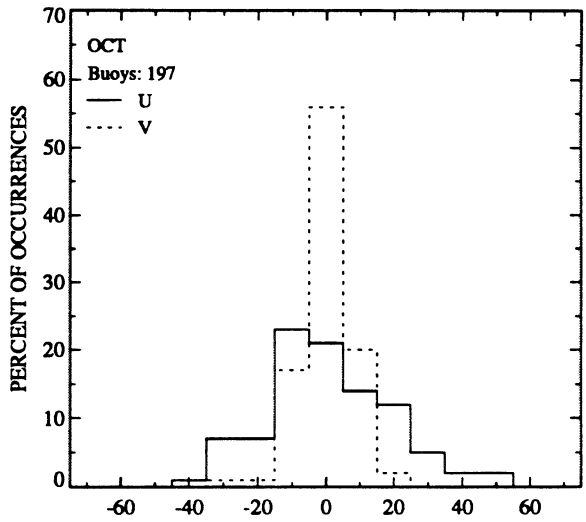


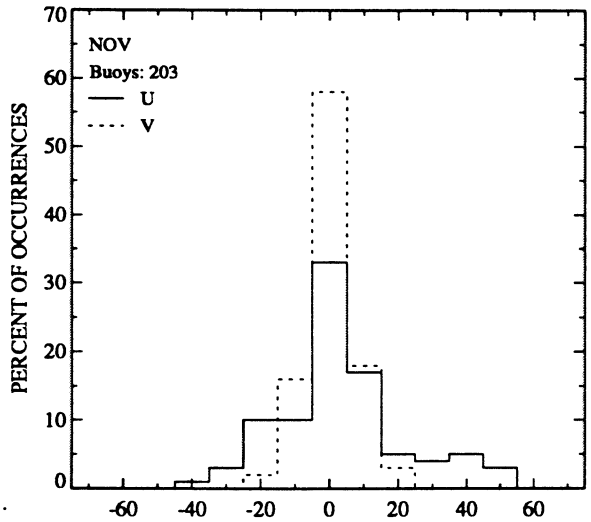


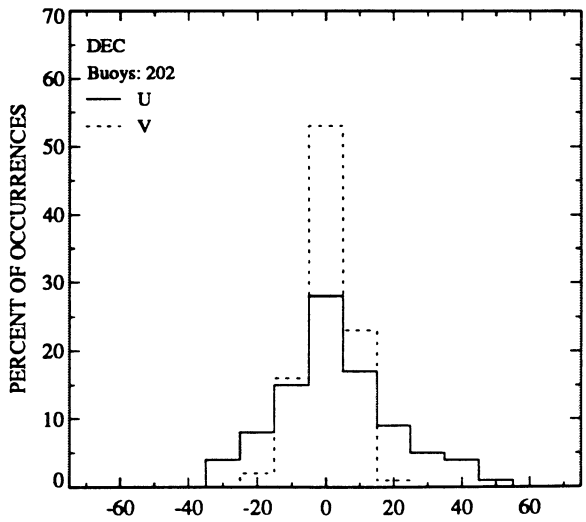

For each buoy in the usable data set, the monthly mean displacement vector was computed from the first and last recorded positions. Accordingly, the monthly mean buoy drift vector was equal to the dispacement vector divided by the time interval between the first and last positions. Monthly mean east-west (positive eastward) and north-south (positive northward) components of buoy drift are displayed in this report.

### 2.2.2 Buoy Drift Presentation

A line of arbitrary thickness, which is color coded to represent the speed of the buoy drift, is drawn between the first and last positions of the month. The range of drift speeds was very large compared to the already-defined color code with a limited number of contour intervals. Unlike the color codes used to present SSMI wind speed and AVHRR/2 MCSST (§ 2.3), which displayed virtually all data values, the buoy drift color code does not represent drift speeds greater than 0.4 m $s^{-1}$ in the east-west direction and 0.2 m $s^{-1}$ in the north-south direction. During several months the maximum zonal and meridional components of buoy drift speeds were greater than the limits specified by the color code (Figure 2); fortunately, when this occurred the large drift speeds were confined to small geographical regions, such as the Gulf Stream.

### 2.2.3 Interpretation of Buoy Drift

Large uncertainties are associated with interpretation of successive positions of a freely drifting buoy as a current vector at a specified depth. A variety of drifting buoys existed in the ocean during 1990 and there are fundamental differences between the behavior of each buoy in similar environmental conditions. The configuration of a drifter system greatly influences its drift (Niiler *et al.*, 1987; Geyer, 1989; Brügge and Dengg, 1991). The depth of the drogue, which is typically less than 25 m and as deep as 120 m (Thomson *et al.*, 1990), influences the buoy drift (Bitterman and Hansen, 1989). The MEDS drifting buoy data set for 1990 indicated no drogues were attached to any buoys. However, some buoys, particularly in the tropical Pacific Ocean, contained a drogue at 15-m depth but information about the drogue depth was not transmitted on the GTS (D. Hansen, personal communication, 1992). Many drift buoys in the Southern Ocean had no drogue or contained a 100-m nylon line.

Caution must be exercised in the interpretation of the buoy drift as near-surface current because of the unknown status and quality of the buoy and drogue. A minimum interpretation of the buoy drift diagrams displayed in Appendix A4 is the geographical distribution of ARGOS-tracked drift buoys.

## 2.3 AVHRR/2 Sea Surface Temperature

The NOAA satellite platforms (called NOAA-j where j is an integer) are in sun-synchronous orbits at altitudes of 833 or 870 km with ascending equatorial crossings at 0730 or 1400 local time. Since the 1981 launch of NOAA-7, odd-numbered NOAA satellites have a five-channel advanced very high resolution radiometer called AVHRR/2. Even-numbered satellites have a four-channel advanced very high resolution radiometer called AVHRR. NOAA-11 was operational in 1990.

The AVHRR/2 scan rate is 360 swaths per min with a total field of view of ± 55.4° from nadir and with an effective ground resolution of 1.1 km at nadir in five co-registered bands. Two spectral channels are in the visible range (0.58 - 0.68 and 0.725 - 1.1 μm) and three in the infrared range (3.55 - 3.93 (*i. e.*, 3.7) μm, 10.3 - 11.3 (*i. e.*, 11) μm, 11.5 - 12.5 (*i. e.*, 12) μm). The AVHRR/2 Channel 3 data at 3.7 μm on most NOAA-j spacecraft have been very noisy (NOAA-11 being the exception) and may be unusable, especially when the satellite is in daylight. The design goal for the noise equivalent differential temperature for each channel was 0.12 K at 300 K (Kidwell, 1991).

### 2.3.1 Infrared Radiometer Measurement

Infrared radiation received by a satellite radiometer is determined primarily by the sea surface emissivity and temperature and by atmospheric transmittance. Infrared radiation emitted from the ocean surface at wavelengths of about 3.5 - 4.0 μm propagates through a dry atmosphere with little attenuation, while under similar conditions the radiation in the 10 - 12 μm window can have approximately 10 - 15% attenuation (Maul, 1985). Only about 30% of the emitted radiation at 10 - 12 μm is transmitted through a wet atmosphere with 5.5-cm precipitable water. The oceanic emissivity in both spectral bands is approximately constant and close to unity for small zenith angles or nadir viewing. Emissivity changes with zenith angle, but the change from near-unity is small for zenith angles less than 40° (Bramson, 1968). The NOAA AVHRR/2 algorithms assume unit emissivity for all bands and angles. Thus the amount of radiation emitted at the surface can be assumed to be proportional to the sea surface temperature.

Atmospheric absorption of emitted radiation at the AVHRR/2 infrared wavelengths is primarily by water vapor, which occurs in the lower levels of the atmosphere so that the atmosphere is perceived to be optically thin. The transmission of emitted radiation through the atmosphere differs for each AVHRR/2 wavelength so that the difference of satellite-measured radiances at two or more wavelengths is independent of atmospheric absorber concentration. For small cumulative amounts of water vapor in the atmosphere, a linear combination of AVHRR/2 infrared radiation measurements recorded at the satellite yields an estimate of sea surface temperature, which is known as multi-channel sea surface temperature (MCSST) (Maul, 1985; McClain *et al.*, 1985).

This report contains daytime MCSST data produced operationally by NOAA's National Environmental Satellite and Data Information Service (NESDIS). The procedure to compute the MCSST was described by McClain *et al.* (1985) and Kidwell (1991). Three MCSST algorithms were used in 1990. From 1 January - 1 March the daytime MCSST algorithm is (Kidwell, 1991)

$$\begin{aligned} \text{MCSST (C)} = {} & 1.01345T_{11} \\ & + 2.659762(T_{11}-T_{12}) \\ & + 0.526548(T_{11}-T_{12})(\text{SEC sza} - 1) \\ & - 277.742, \end{aligned}$$

where MCSST (C) is the sea surface temperature in °C, $T_{11}$ and $T_{12}$ are the brightness temperatures in K computed from radiance measurements at 11 μm (AVHRR/2 Channel 4) and 12 μm (AVHRR/2 Channel 5), respectively, and sza is the satellite zenith angle. From 2 March - 17 April the daytime MCSST algorithm was (Kidwell, 1991)

$$\begin{aligned} \text{MCSST (K)} = {} & (0.19410T_{12} - 48.15)/(0.20524T_{12} - 0.17334T_{11} - 6.25) \\ & \times (T_{11} - T_{12} + 1.32) + 0.94575T_{12} + 0.60(T_{11}-T_{12}) \\ & \times (\text{SEC sza} - 1) + 12.16, \end{aligned}$$

where MCSST (K) is the sea surface temperature in K. From 18 April - 31 December the daytime MCSST algorithm was (Kidwell, 1991)

$$\begin{aligned} \text{MCSST (C)} = {} & 1.0155T_{11} + 2.50(T_{11}-T_{12}) + 0.73(T_{11}-T_{12})(\text{SEC sza} - 1) \\ & - 277.99. \end{aligned}$$

### 2.3.2 Environmental Corrections

Major sources of error are water vapor absorption in the lower atmosphere and aerosol extinction. Radiance measurements from only cloud-free areas are processed by NOAA into MCSSTs. Very conservative cloud tests, which involve various combinations of the visible and infrared AVHRR/2 data, detect clouds so that cloud-free MCSSTs are computed (McClain *et al.*, 1985); on a typical day, less than 2% of the maximum possible number of MCSSTs are retained.

### 2.3.3 1/3° x 1/3° Gridded 28-Day Data Set

The 1.1-km AVHRR/2 observations are available only within areas containing a downlink ground station to receive high-resolution data transmission or from limited onboard local area

coverage (LAC) recordings (≈ 12 minutes per orbit). Global AVHRR/2 measurements have an effective ground resolution of 4 km. A processor on board the NOAA spacecraft generates an average radiance for each channel from four 1.1-km elements within each nonoverlapping group of five consecutive 1.1-km measurements along a scan. Each daytime MCSST archived on the NESDIS global area coverage (GAC) data tapes represents the average sea surface temperature within an 8-km x 8-km area, which occurs in a cloud-free environment at a variable spacing ranging from 8 km in the U.S. coastal waters to 25 km in the open ocean. The 8-km x 8-km MCSSTs are mapped at the University of Miami's Rosenstiel School of Marine and Atmospheric Sciences (RSMAS) onto a cylindrical equi-rectangular grid of 2048 (longitude) x 1024 (latitude) space-elements (Olson *et al.*, 1988). At the equator the dimensions of each space-element are approximately 18 km x 18 km, and geographical coordinates are assigned to the center of the element. The origin of the grid is 90°N, 180°W. RSMAS produces MCSSTs averaged over 7 days. For this report, four consecutive 7-day values (except during January when there were only three 7-day values) are arithmetically averaged to form 28-day mean MCSST values. A 1024 x 512 grid was created by computing the arithmetic mean of four 18-km x 18-km MCSSTs adjacent to each other in a 2-dimensional array. The average MCSSTs of 4-element groups, which were independent of each other, represent an approximate 1/3° x 1/3° gridded MCSST data set.

The total number of 1/3° x 1/3° monthly averaged MCSST values was smallest during June, July, and August, which coincided with intense cloud cover over huge oceanic areas of the middle latitudes of the Southern Hemisphere, and was highest during December, January, and February (Figure 3A). The range between maxima and minima was more than 25% of the annual mean.

The RSMAS MCSST data set contains the number of 8-km x 8-km values averaged to yield the 2048 x 1024 grid. The total number of 8-km x 8-km MCSST values per month (Figure 3B) was low throughout 1987 and most of 1988 compared to subsequent years.

### 2.3.4 Sea Surface Temperature Accuracy

The coefficients used in the NOAA MCSST algorithm change only as the operational satellite is replaced and on rare occasions when the continuous validation procedure indicates a need for a change. NOAA continuously monitors the performance of the MCSST data product with satellite-tracked drifting buoy sea surface temperature measurements, which are recorded within 25 km and 4 h of the location of the MCSST. During 1990, the MCSST was 0.04°C higher than the *in situ* data and the rms difference was 0.64°C for an average of 444 matchups per month throughout the global ocean (Table 2).

## 2.4 ECMWF Surface Wind Components

Month-to-month variations of upper ocean circulation are primarily caused by spatial and temporal changes in the surface wind vector: both east-west ($u$; positive eastward) and north-south ($v$; positive northward) wind components are important. To augment the SSMI scalar surface wind speed data (§2.1), this report contains the Cartesian components of the surface wind field computed by the European Center for Medium-Range Weather Forecasting (ECMWF). The ECMWF data were acquired from ECMWF in September 1991. The ECMWF forecast-analysis system, like all operational atmospheric general circulation models, is complex and continually being improved.

ECMWF analyses, instead of other model-generated results, are used because Trenberth and Olson (1988) considered them to be the best operational global analyses available for general use. Kalnay *et al.* (1990) showed that ECMWF northern hemisphere daily 1000- and 500-hPa rms height errors of the 1-, 3-, and 5-day forecasts during August 1989 were smaller than National Meteorological Center (NMC) results.

The area of each element of the ECMWF 144 x 73 grid was approximately 2.5° x 2.5°. ECMWF forecast-analyses of surface wind components at 10-m height were issued twice a day, at 0000 and 1200 GMT. Wind speed, $s$, was computed at 12-h intervals: $s = (u^2 + v^2)^{1/2}$.

(A) Number of Data Grid-Points per Monthly Global Distribution of AVHRR/2 Sea Surface Temperature

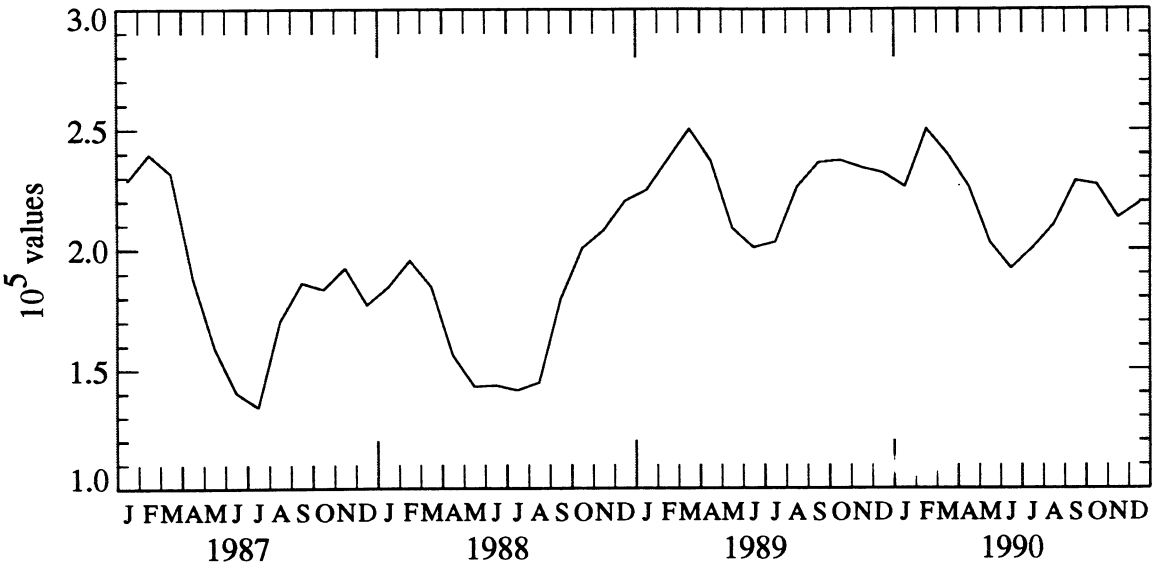


(B) Total Number of Data Values per Monthly Global Distribution of AVHRR/2 Sea Surface Temperature

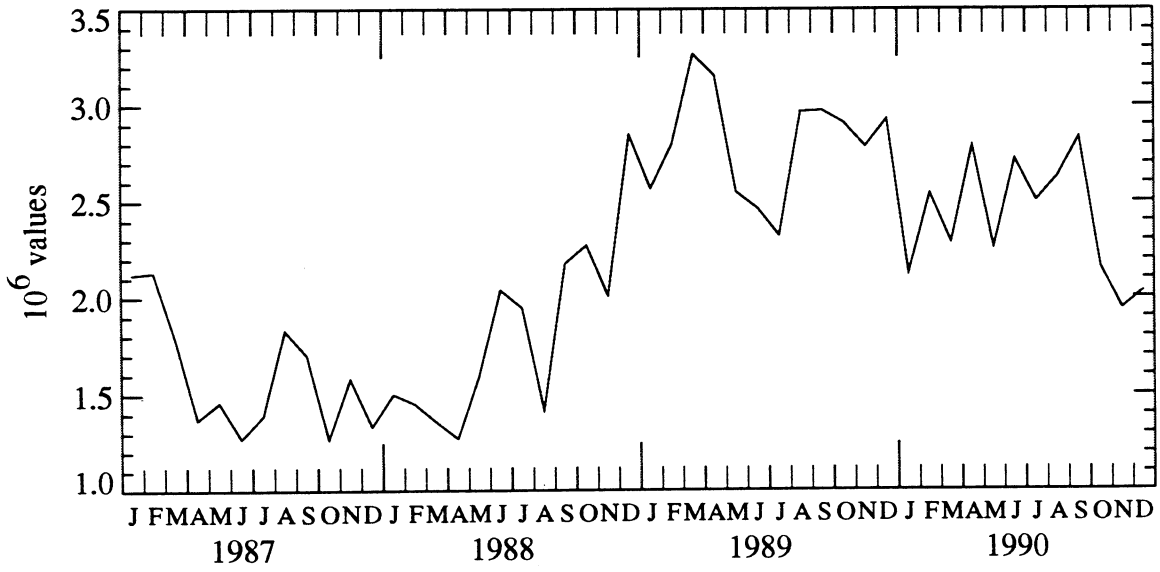


Figure 3. Time series of monthly totals of (A) number of pixels or picture elements and (B) number of sea surface temperatures.

Table 2

Monthly mean bias and root-mean-square (rms) difference between daytime MCSST and drifting buoy sea surface temperature (DRIBU SST) global matchups during 1989.
Bias = DRIBU SST - MCSST.
(Courtesy of E.P. McClain, NOAA NESDIS)

| Month | Number of Matchups | Bias °C | RMS Difference °C |
|---|---|---|---|
| Jan | 405 | -0.13 | 0.64 |
| Feb | 354 | -0.14 | 0.68 |
| Mar | 395 | -0.15 | 0.56 |
| Apr | 399 | -0.08 | 0.62 |
| May | 360 | -0.10 | 0.60 |
| Jun | 347 | -0.15 | 0.65 |
| Jul | 383 | -0.06 | 0.65 |
| Aug | 457 | -0.11 | 0.73 |
| Sep | 548 | 0.04 | 0.70 |
| Oct | 552 | 0.05 | 0.58 |
| Nov | 542 | 0.18 | 0.64 |
| Dec | 588 | 0.14 | 0.63 |

## 3 DATA PRESENTATION

All data are presented in the form of color-coded maps. To ease interpretation of features among different parameters, a common color code is used: blues represent low values, reds are high values, yellow and green are in the middle range, white means no data, and black represents land. Data are linearly scaled for color and an incremental color scale represents a contour interval. A single geographical scale is used for all maps. The land mask, which was prepared by O. Brown from the U.S. Central Intelligence Agency (CIA) World Data Base II, is the same throughout this report.

The color maps were generated on a Sun™-4 computer using IDL®, which prepared the PostScript® files, and printed on a Tektronix™ Phaser CP Color Printer. All data values are retained in the PostScript® image files. The SSMI images contain 1080 x 540 pixels (picture elements) and the AVHRR images contain 1024 x 512 pixels. All images are plotted on a 5.75-in. x 2.875-in. map. The PostScript® interpreter linearly transforms the size of each pixel within the user image file into a source-image coordinate system, which is compatible with the 300 dot-per-in. resolution of the Tektronix™, to achieve the maximum rendition of the image within the specified dimensions (Adobe Systems, 1985).

Data presented in Appendices A2, A5, and A7 are available on magnetic tape from the Physical Oceanography Distributed Active Archive Center, M/S 300-323, Jet Propulsion Laboratory, 4800 Oak Grove Drive, Pasadena, CA 91109.

## 4 REFERENCES


Adobe Systems, Inc. (1985) *PostScript® Language Reference Manual.* Addison-Wesley, 321 pp.

Bates, J.J. (1991) High frequency variability of SSMI-derived wind speed and moisture during an intraseasonal oscillation. *Journal of Geophysical Research, 96,* 3411-3424.

Bitterman, D.S., and D.V. Hansen (1989) Direct measurements of current shear in the tropical Pacific Ocean and its effect on drift buoy performance. *Journal of Atmospheric and Oceanic Technology, 6,* 274-279.

Bramson, M.A. (1968) *Infrared Radiation: A Handbook for Applications*. Plenum Press, New York, 623 pp.

Brügge, B., and J. Dengg (1991) Differences in drift behavior between drogued and undrogued satellite-tracked drifting buoys. *Journal of Geophysical Research, 96*, 7249-7263.

Geyer, W.R. (1989) Field calibration of mixed-layer drifters. *Journal of Atmospheric and Oceanic Technology, 6*, 333-342.

Goodberlet, M.A., C.T. Swift and J.C. Wilkerson (1990) Ocean surface wind speed measurements of the special sensor microwave imager (SSMI). *IEEE Transactions on Geoscience and Remote Sensing, 28*, 823-828.

Halpern, D., V. Zlotnicki, J. Newman, O. Brown and F. Wentz (1991) An atlas of monthly mean distributions of GEOSAT sea surface height, SSMI surface wind speed, AVHRR/2 sea surface temperature, and ECMWF surface wind components during 1988. JPL Publication 91-8, Jet Propulsion Laboratory, Pasadena, 110 pp.

Halpern, D., V. Zlotnicki, J. Newman, D. Dixon, O. Brown and F. Wentz (1992a) An atlas of monthly mean distributions of GEOSAT sea surface height, SSMI surface wind speed, AVHRR/2 sea surface temperature, and ECMWF surface wind components during 1987. JPL Publication 92-3, Jet Propulsion Laboratory, Pasadena, 111 pp.

Halpern, D., W. Knauss, O. Brown and F. Wentz (1992b) An atlas of monthly mean distributions of SSMI surface wind speed, ARGOS buoy drift, AVHRR/2 sea surface temperature, and ECMWF surface wind components during 1989. JPL Publication 92-17, Jet Propulsion Laboratory, Pasadena, 112 pp.

Hollinger, J.P., J.L. Pierce and G.A. Poe (1990) SSMI instrument evaluation. *IEEE Transactions on Geoscience and Remote Sensing, 28*, 781-790.

Kalnay, E., M. Kanamitsu and W.E. Baker (1990) Global numerical weather prediction at the National Meteorological Center. *Bulletin of the American Meteorological Society, 71*, 1410-1428.

Kidwell, K.B. (1991) NOAA polar orbiter data users guide. National Environmental Satellite, Data, and Information Service, National Oceanic and Atmospheric Administration, Washington, DC 20233.

Maul, G.A. (1985) *Introduction to Satellite Oceanography*. Matinus Nijhoff, Dordrecht, 606 pp.

McClain, E.P., W.G. Pichel and C.C. Walton (1985) Comparative performance of AVHRR-based multichannel sea surface temperatures. *Journal of Geophysical Research, 90*, 11587-11601.

MEDS (1991) RNODC for drifting buoys 1990 annual report. Marine Environmental Data Service, Department of Fisheries and Oceans, Ottawa, Ontario, 60 pp.

Niiler, P.P., R.E. Davis and H.J. White (1987) Water-following characteristics of a mixed layer drifter. *Deep-Sea Research, 34*, 1867-1881.

Olson, D.B., G.P. Podesta, R.H. Evans and O.B. Brown (1988) Temporal variations in the separation of Brazil and Malvinas Currents. *Deep-Sea Research, 35*, 1971-1990.

Paduan, J.D., and P.P. Niiler (1991) The WOCE/TOGA surface velocity program. ARGOS Newsletter, No. 42, 1-5. (Available from Service ARGOS Inc., Landover, MD 20785)

Reynolds, R.W. (1982) A monthly averaged climatology of sea surface temperature. NOAA Technical Report NWS 31, National Oceanic and Atmospheric Administration, Silver Springs, Maryland, 35 pp.

Stommel, H., and M. Fieux (1978) *Oceanographic Atlases*. Woods Hole Press, Woods Hole, Massachusetts, 6 pp + 97 charts.

Thomson, R.E., P.H. LeBlond, and W.J. Emery (1990) Analysis of deep-drogued satellite-tracked drifter measurements in the northeast Pacific. *Atmosphere-Ocean, 28*, 409-443.

Trenberth, K.E., and J.G. Olson (1988) ECMWF global analysis 1979-1986: Circulation statistics and data evaluation. NCAR Technical Note NCAR/TN-300+STR, National Center for Atmospheric Research, Boulder, 94 pp.

Wentz, F. (1983) A model function for ocean microwave brightness temperatures. *Journal of Geophysical Research, 88*, 1892-1908.

Wentz, F.J. (1989) User's manual: SSMI geophysical tapes. RSS Technical Report 060989, Remote Sensing Systems, Santa Rosa, California, 16 pp.

Wentz, F. (1992) Measurement of oceanic wind vector using satellite microwave radiometers. *IEEE Transactions on Geoscience and Remote Sensing, 30*, 960-972.

Wentz, F.J., L.A. Mattox and S. Peteherych (1986) New algorithms for microwave measurements of ocean winds: Applications to SEASAT and the special sensor microwave imager. *Journal of Geophysical Research, 91*, 2289-2307.

# APPENDIX

## Atlas of Monthly Mean Distributions

A1

Annual Mean and Sampling Distribution of SSMI Surface Wind Speed

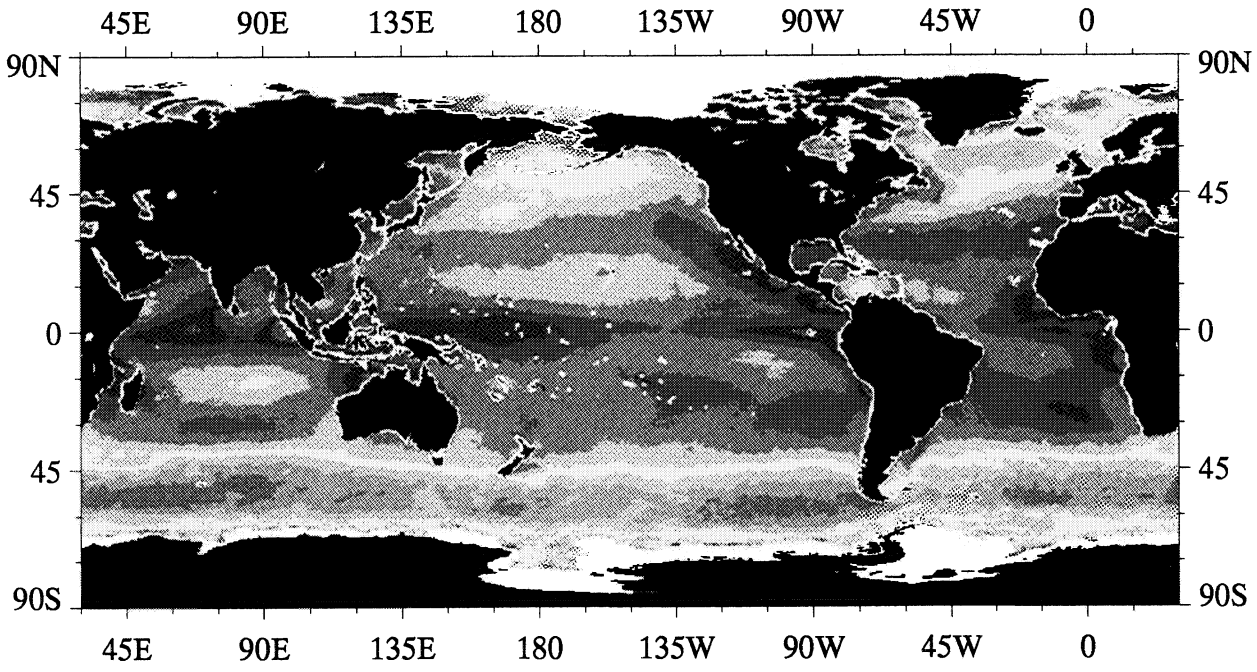


Annual Mean 1990

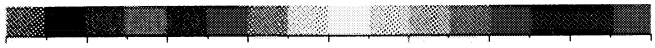


SSMI Wind Speed Referenced to 10 m, m $s^{-1}$

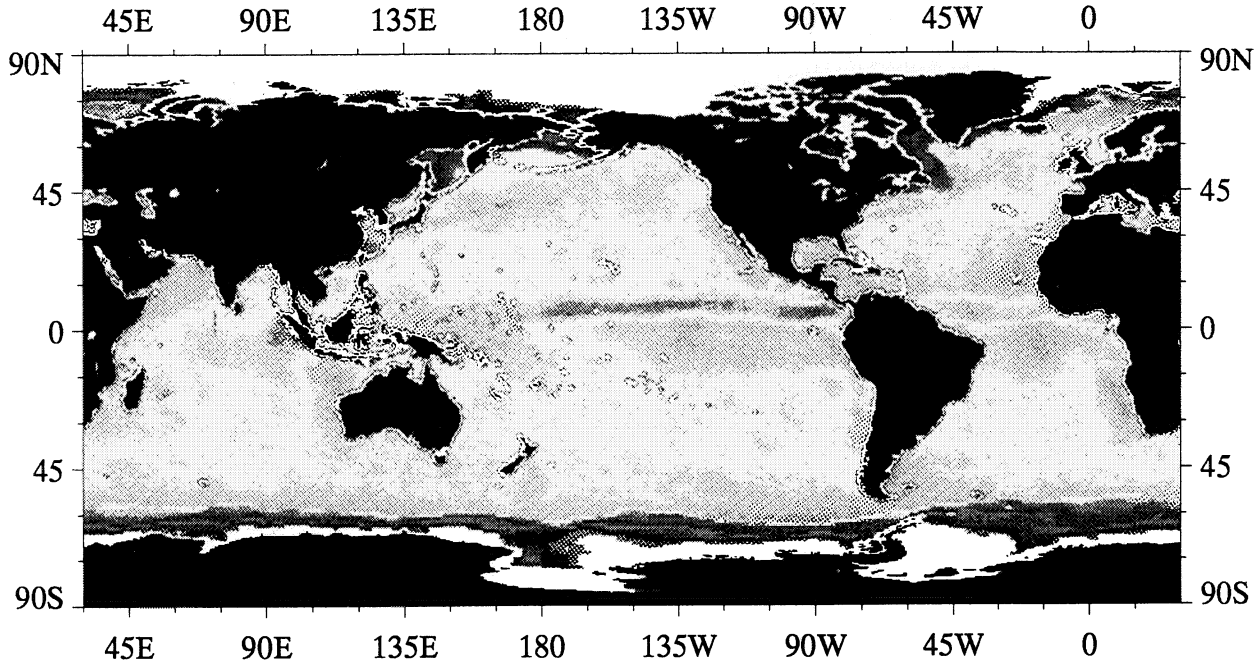


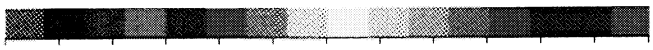


Number x 100 of SSMI Wind Speed Values per Pixel During 1990, max = 1194

A2

Monthly Mean SSMI Surface Wind Speed

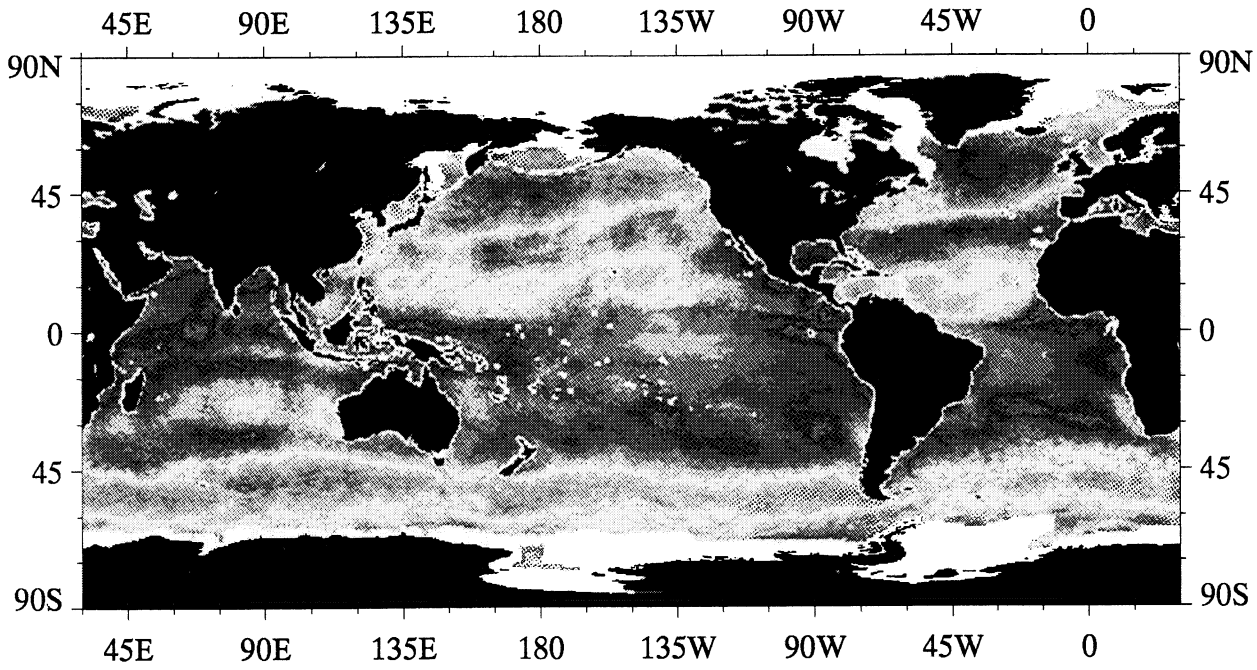


January 1990

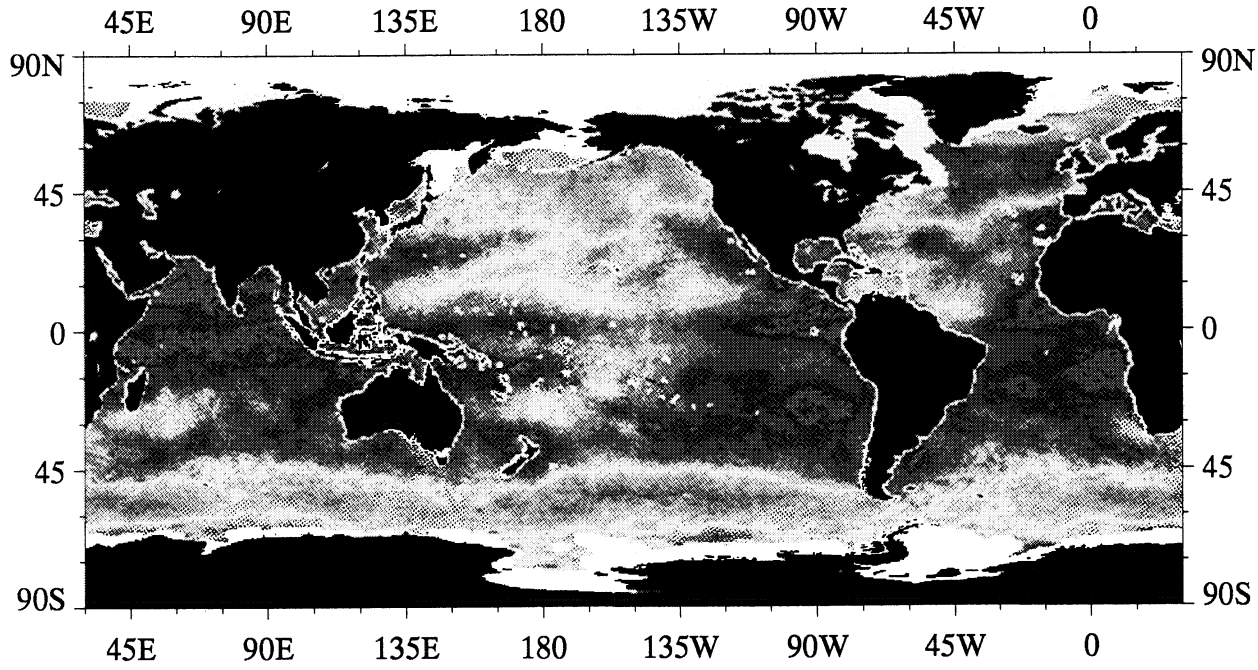


February 1990

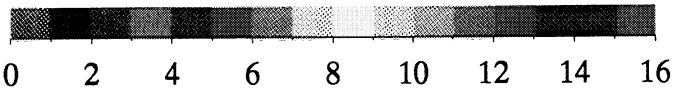


SSMI Wind Speed Referenced to 10 m, m $s^{-1}$

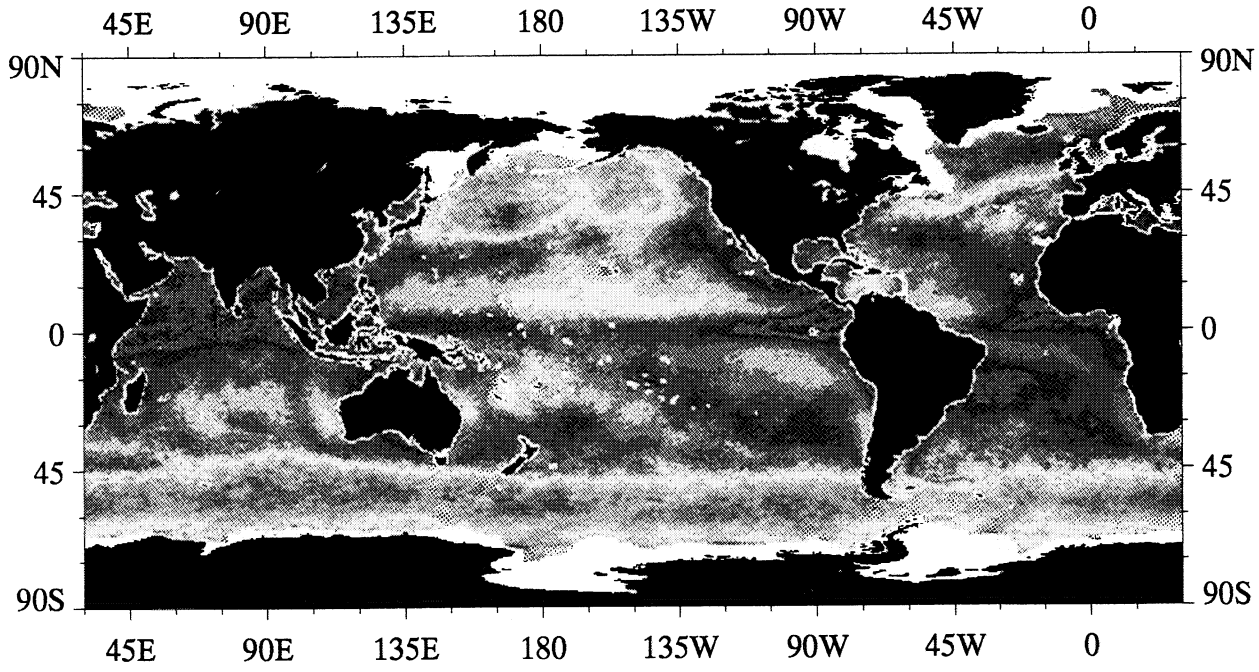


March 1990

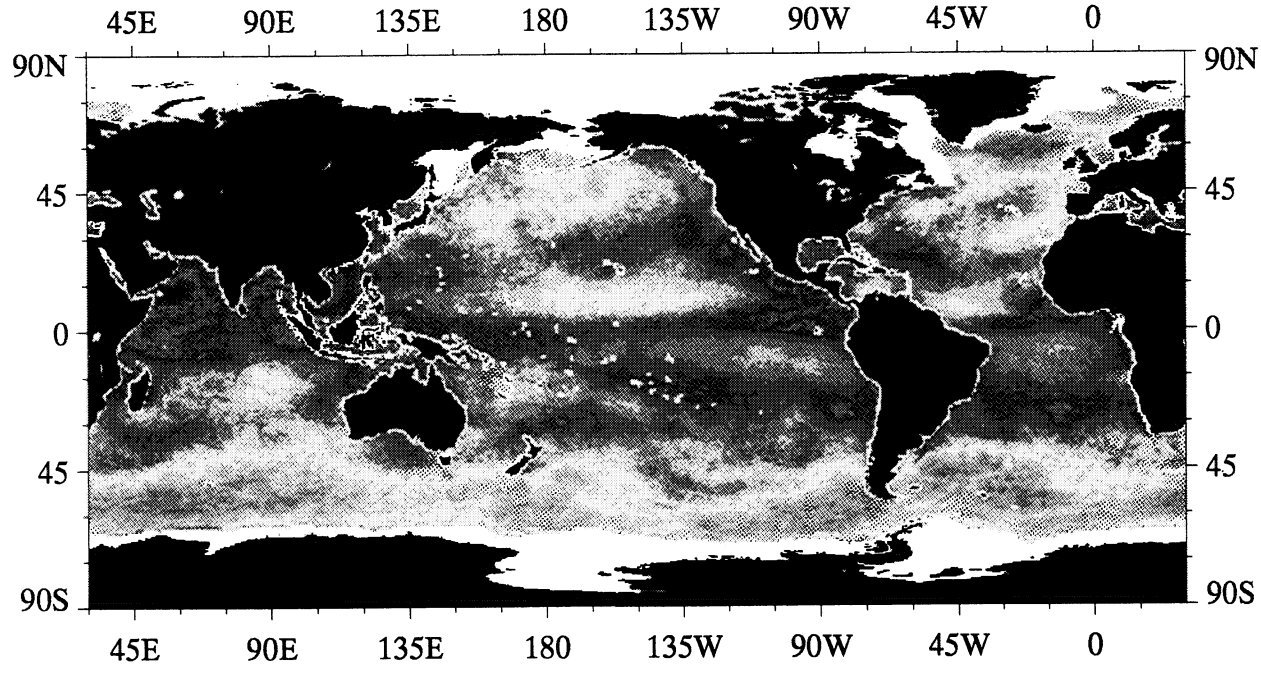


April 1990

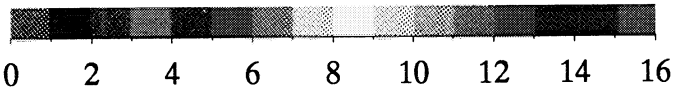


SSMI Wind Speed Referenced to 10 m, m $s^{-1}$

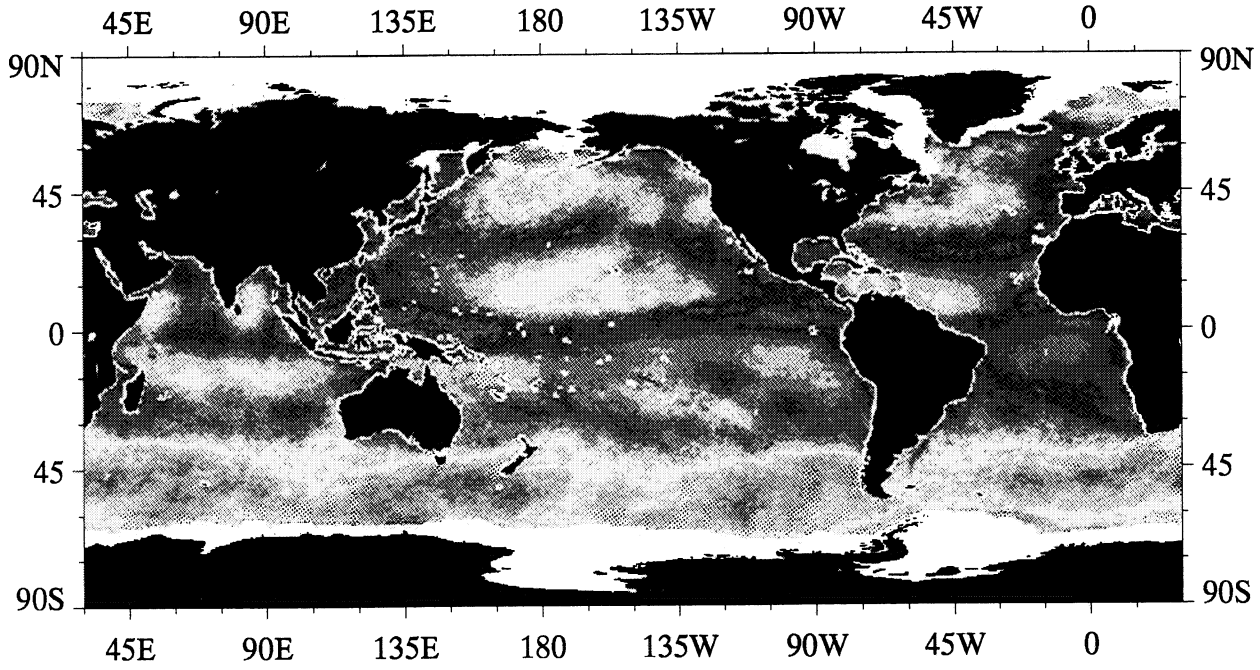


May 1990

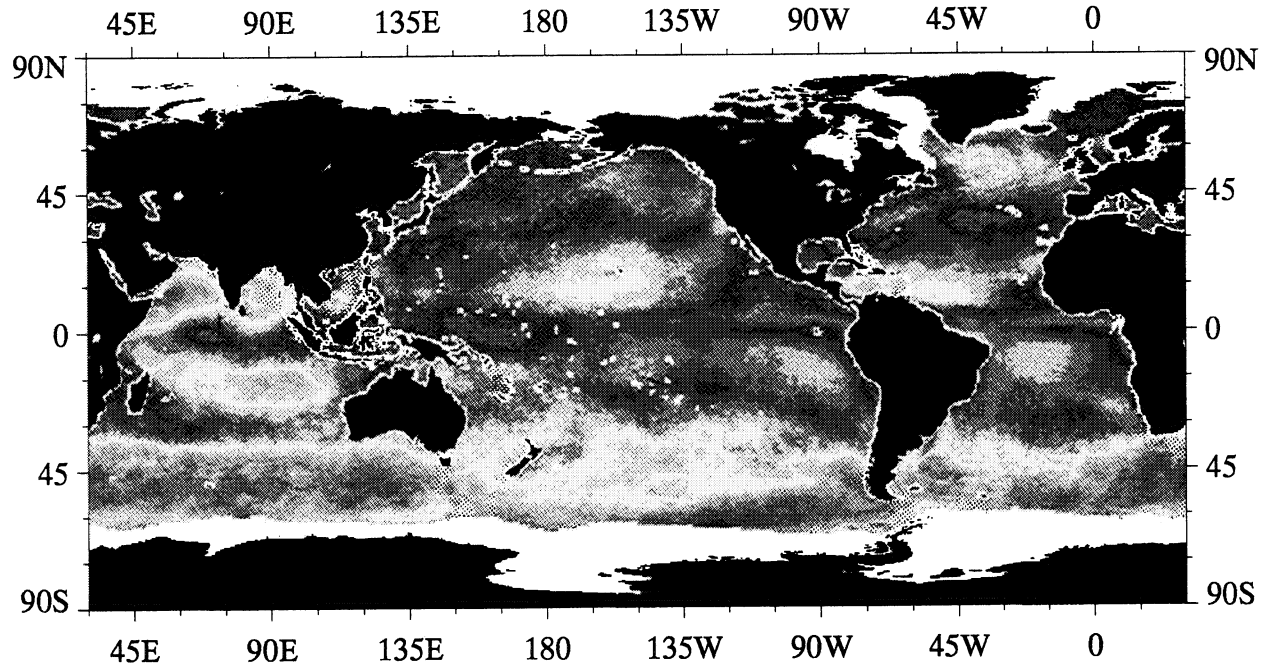


June 1990

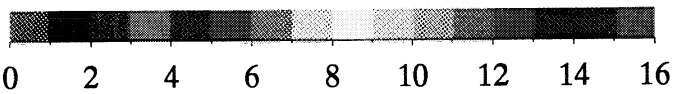


SSMI Wind Speed Referenced to 10 m, m $s^{-1}$

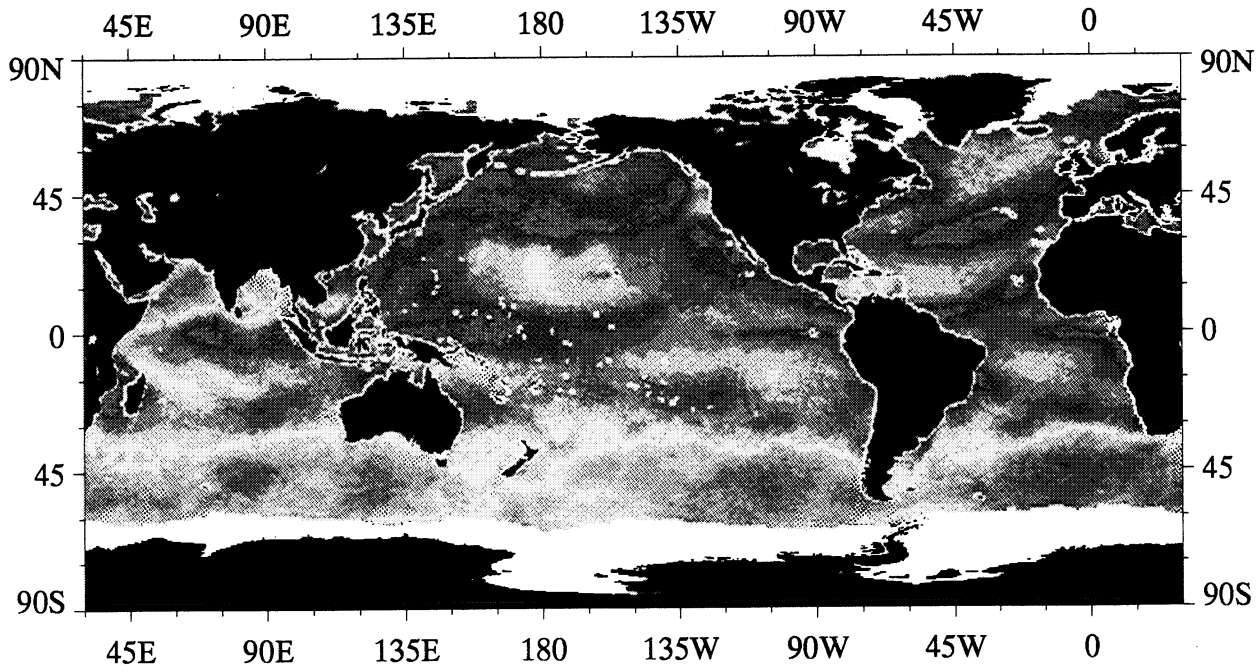


July 1990

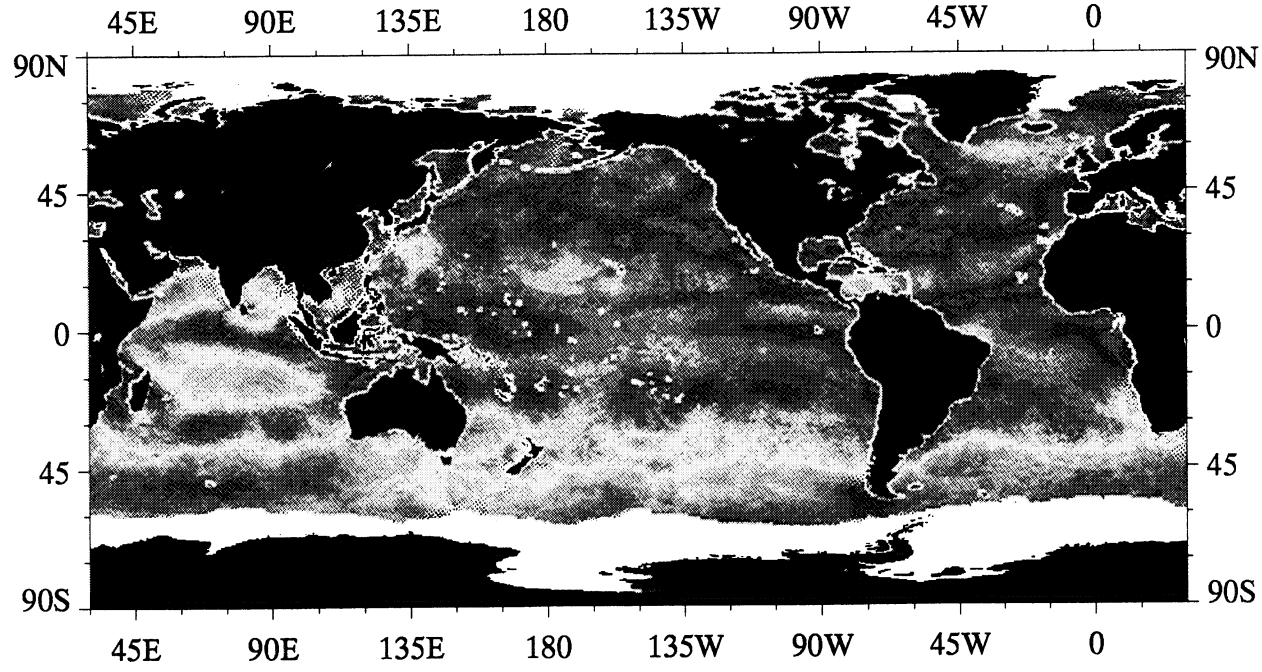


August 1990

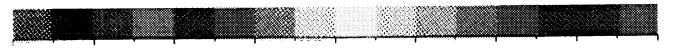


SSMI Wind Speed Referenced to 10 m, m $s^{-1}$

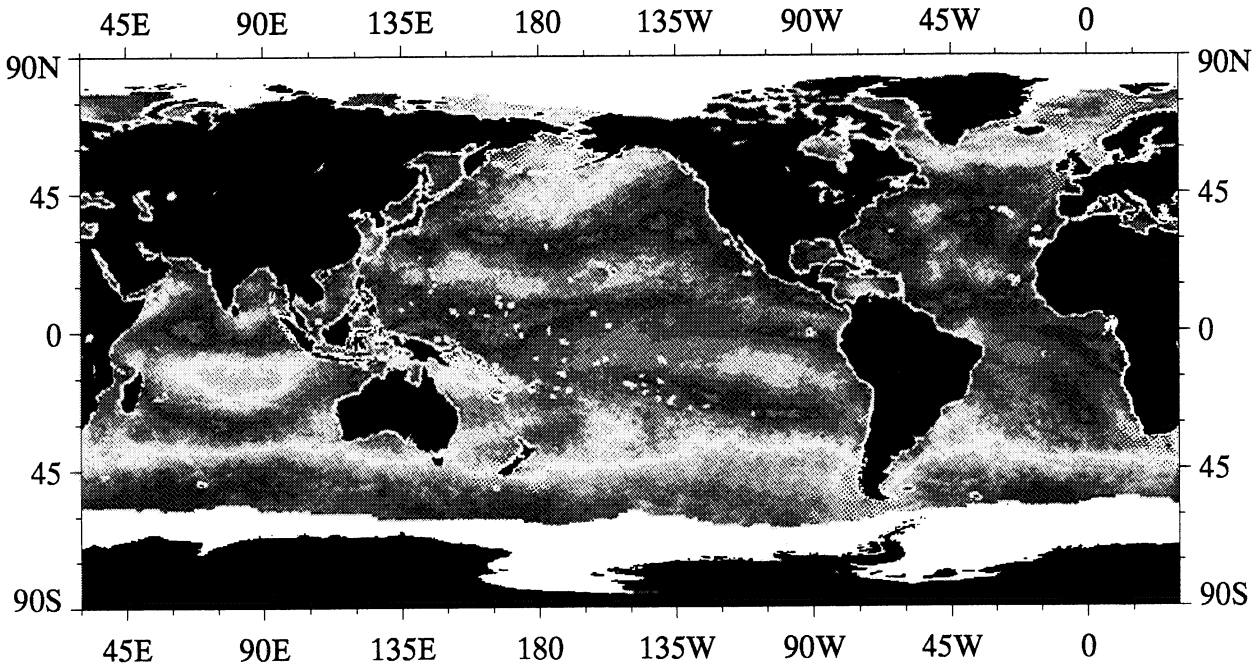


September 1990

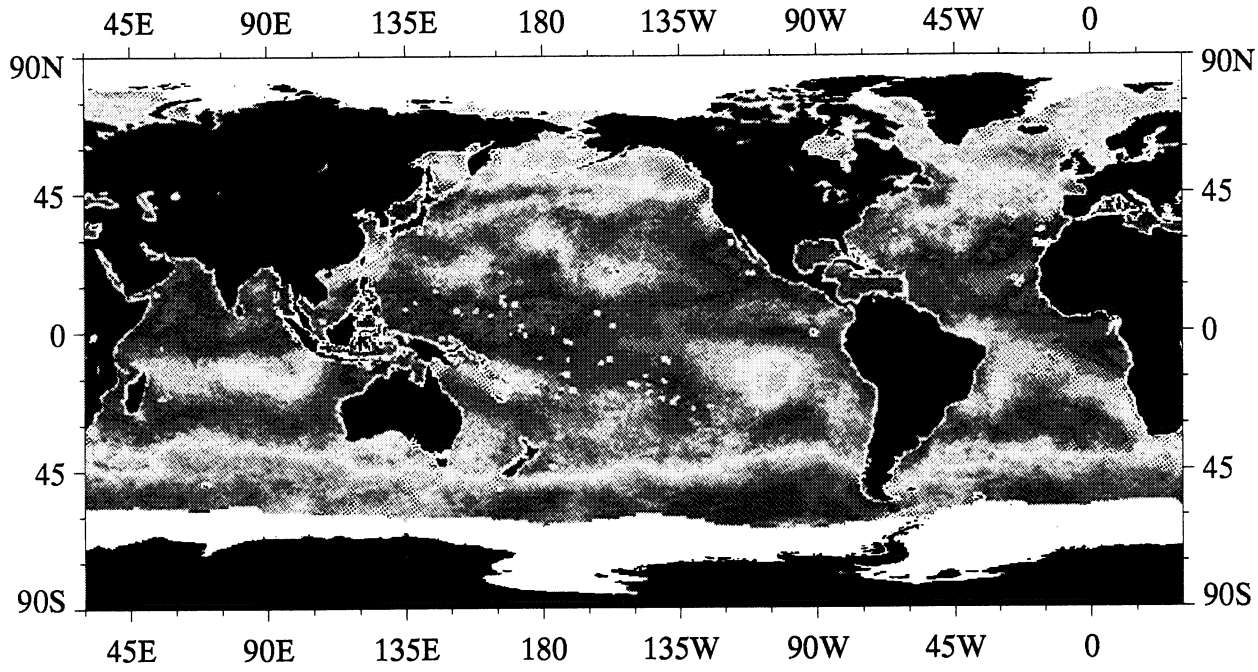


October 1990

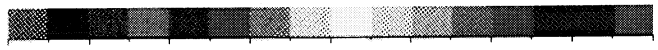


SSMI Wind Speed Referenced to 10 m, m $s^{-1}$

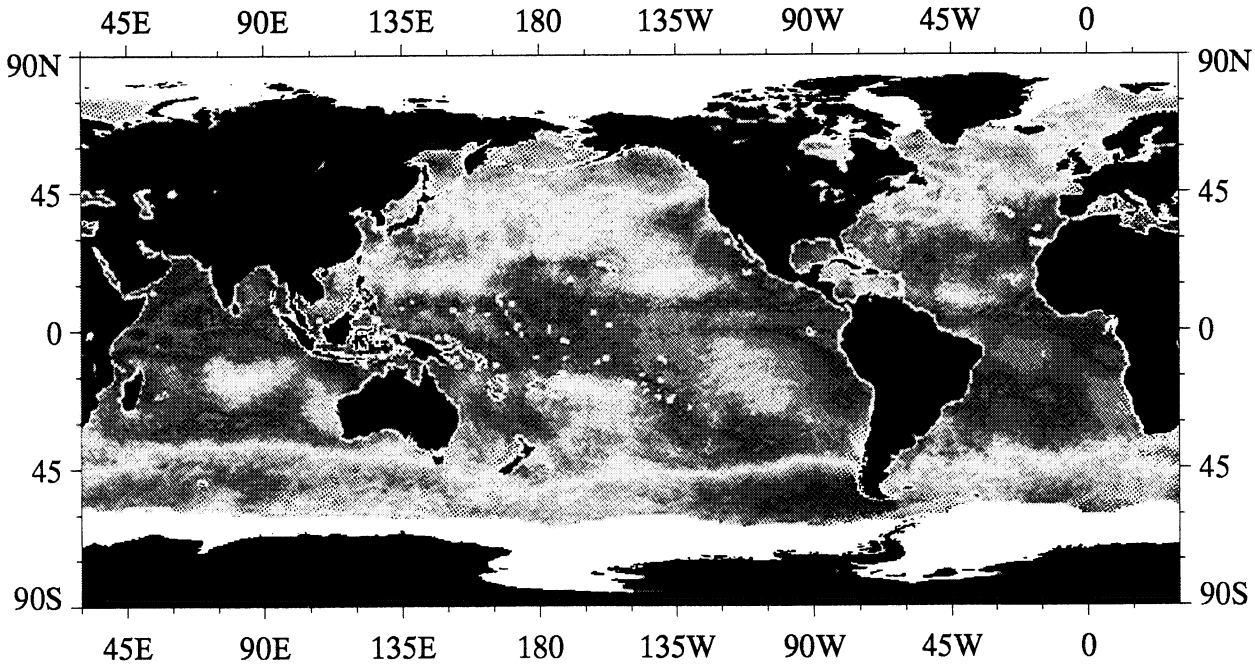


November 1990

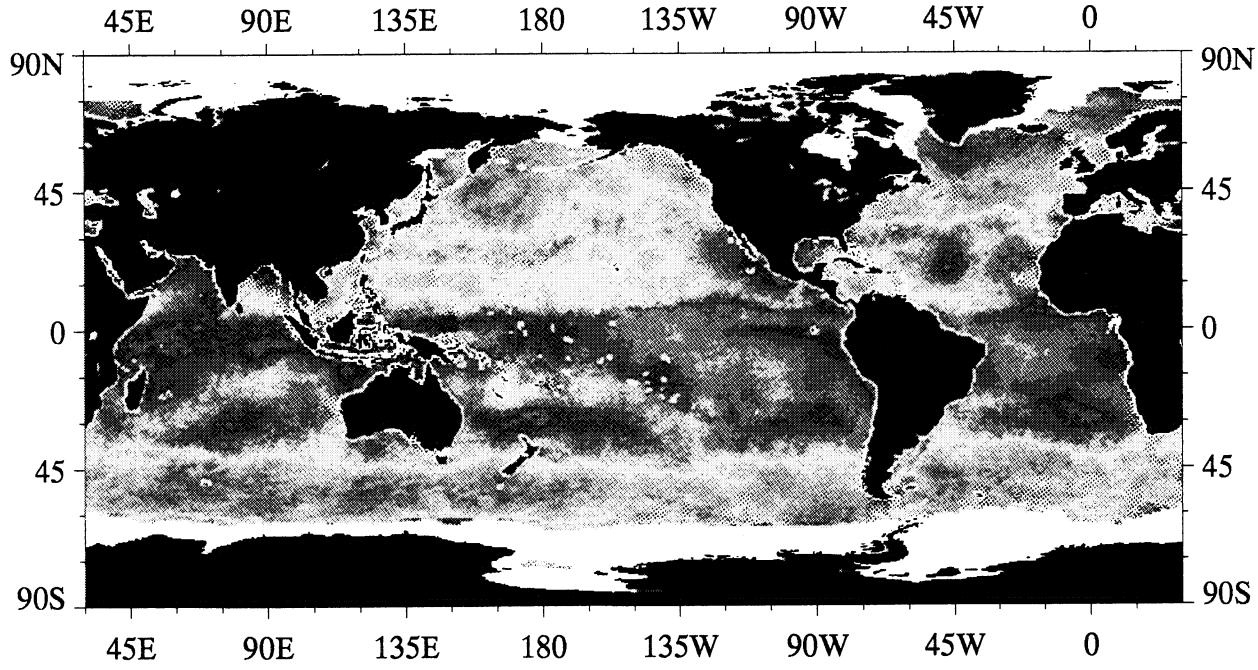


December 1990


SSMI Wind Speed Referenced to 10 m, m $s^{-1}$

A3

Monthly SSMI Sampling Distribution

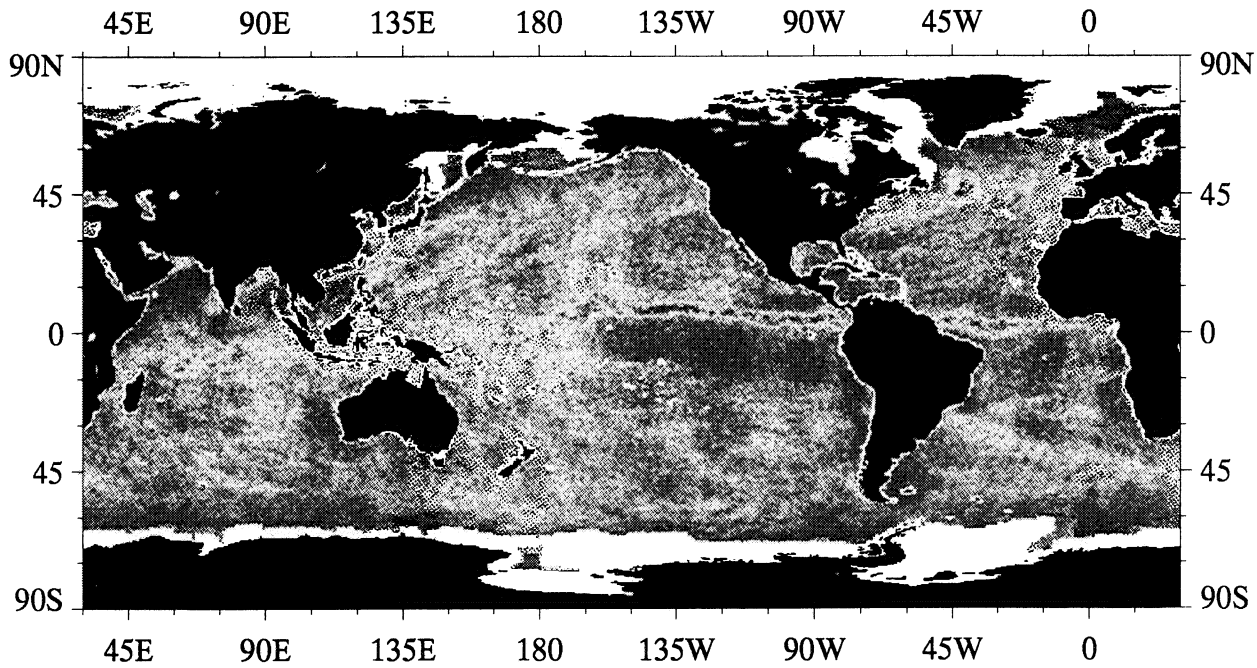


January 1990, max = 135

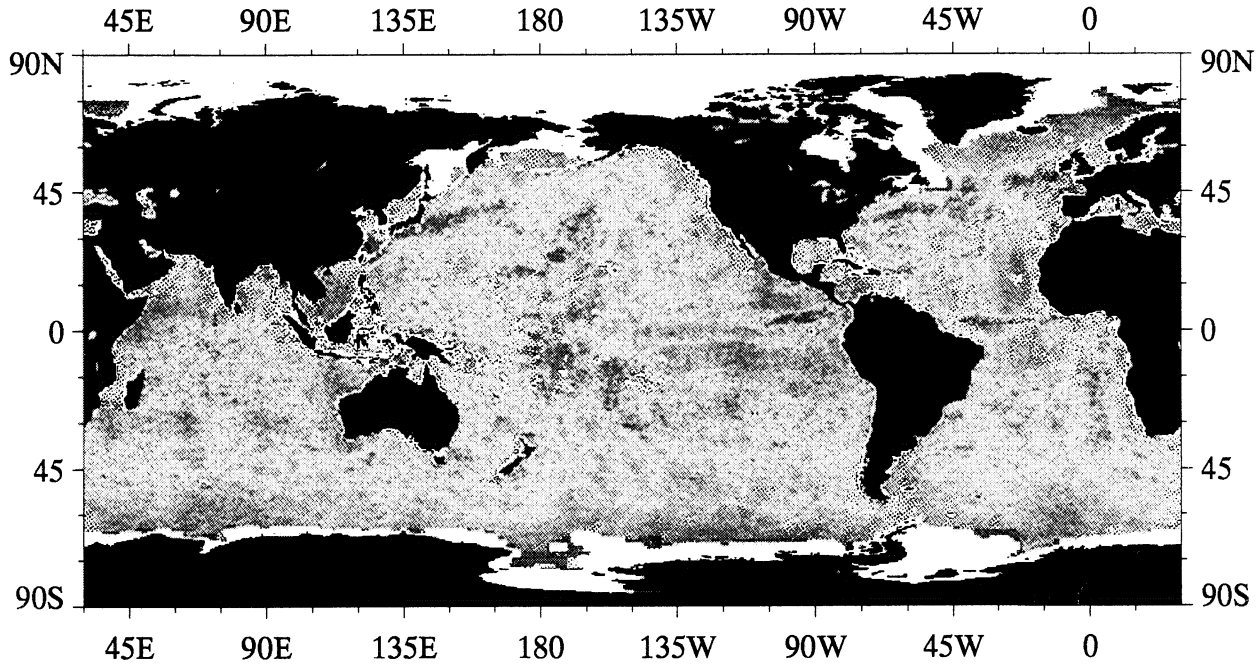


February 1990, max = 125

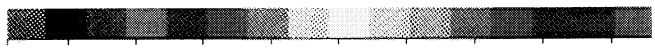


Number of SSMI Wind Speed Values per Pixel

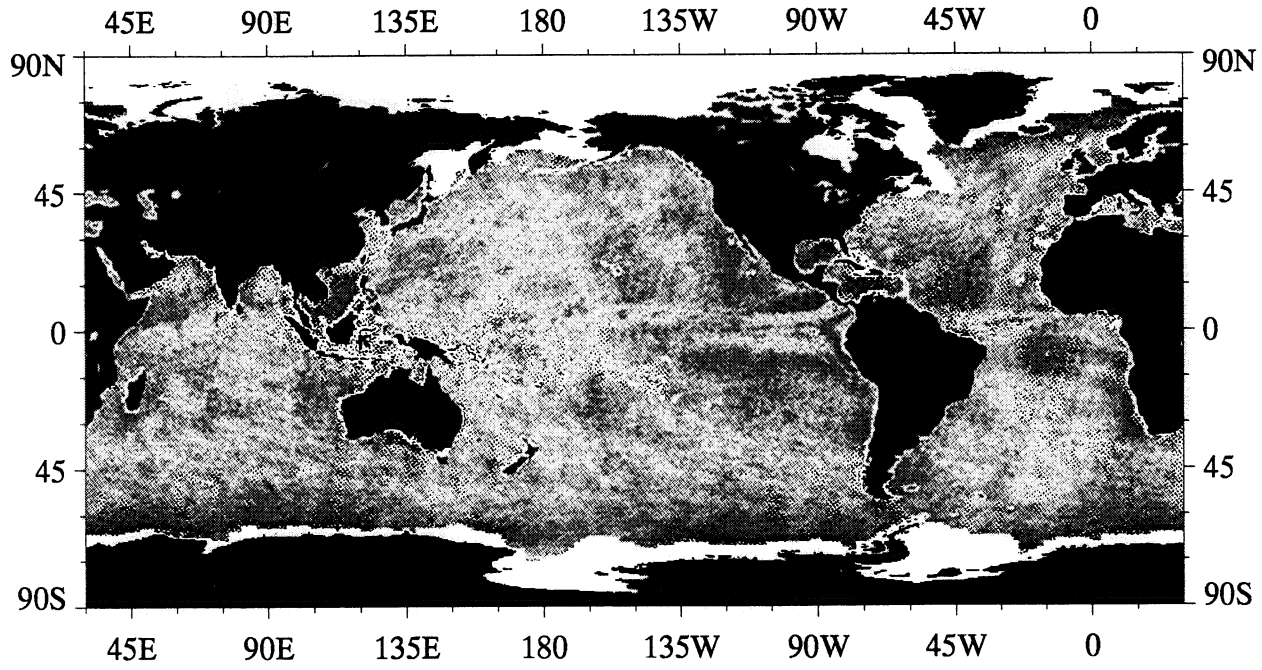


March 1990, max = 146

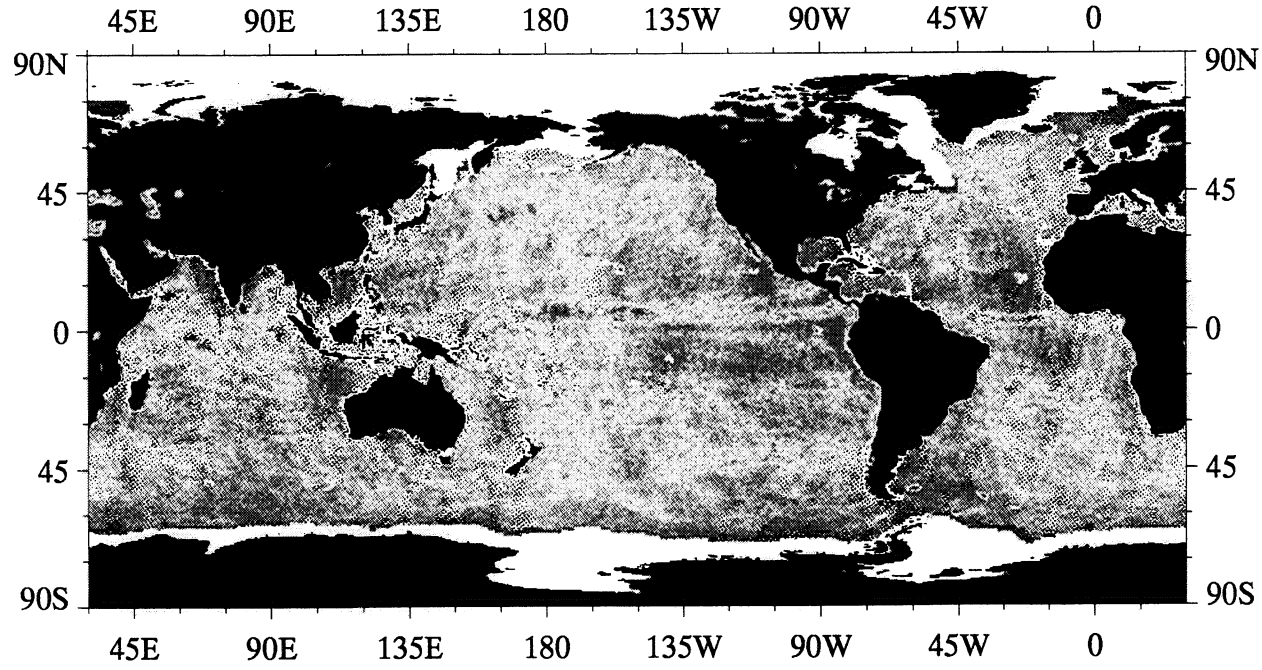


April 1990, max = 138


Number of SSMI Wind Speed Values per Pixel

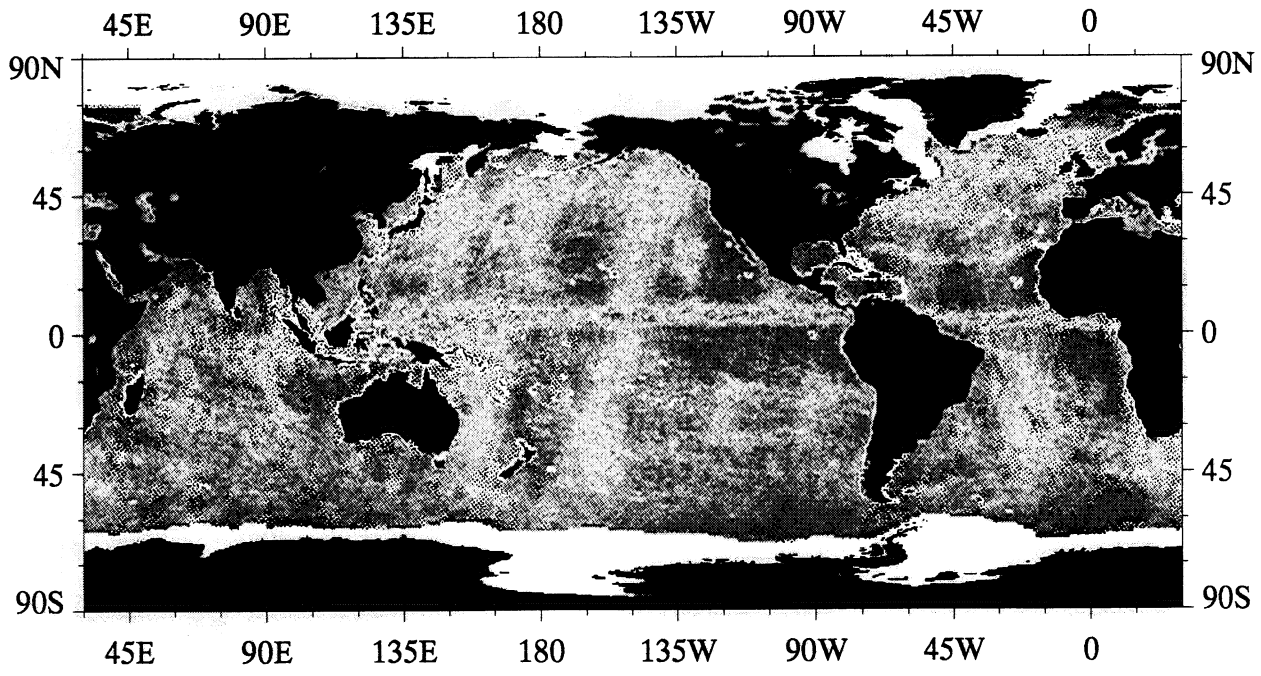


May 1990, max = 141

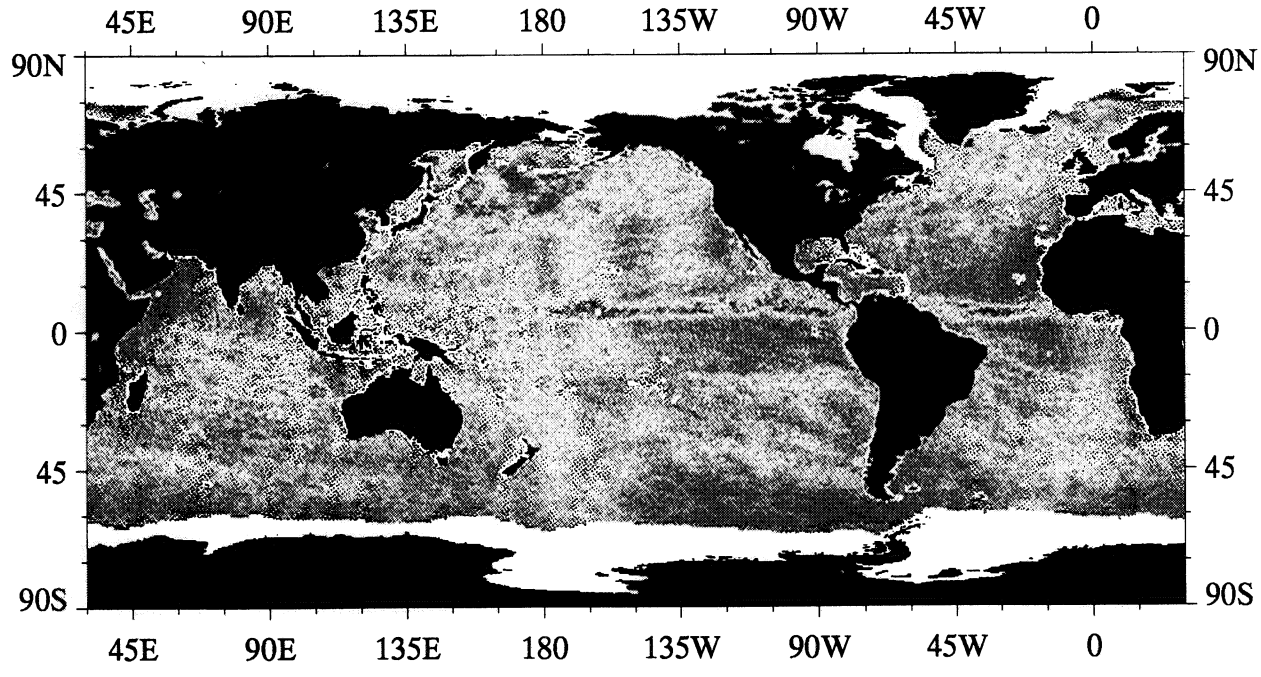


June 1990, max = 97

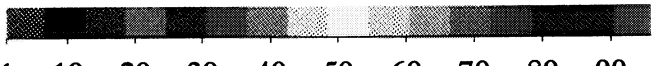


Number of SSMI Wind Speed Values per Pixel

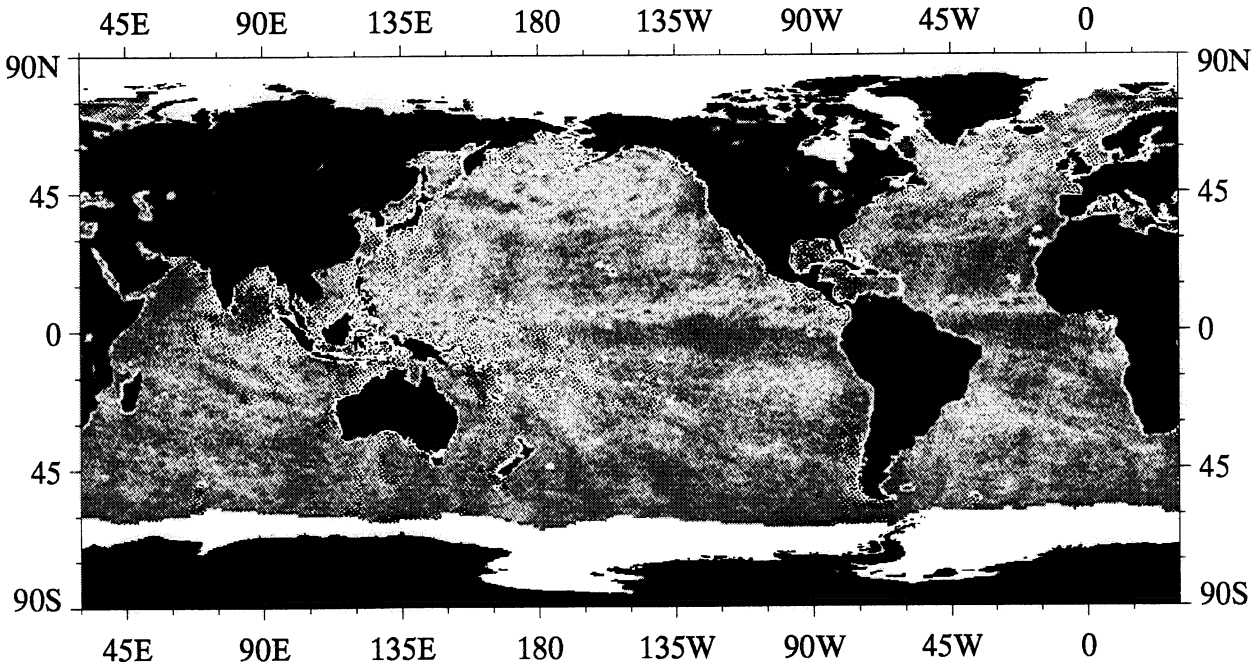


July 1990, max = 116

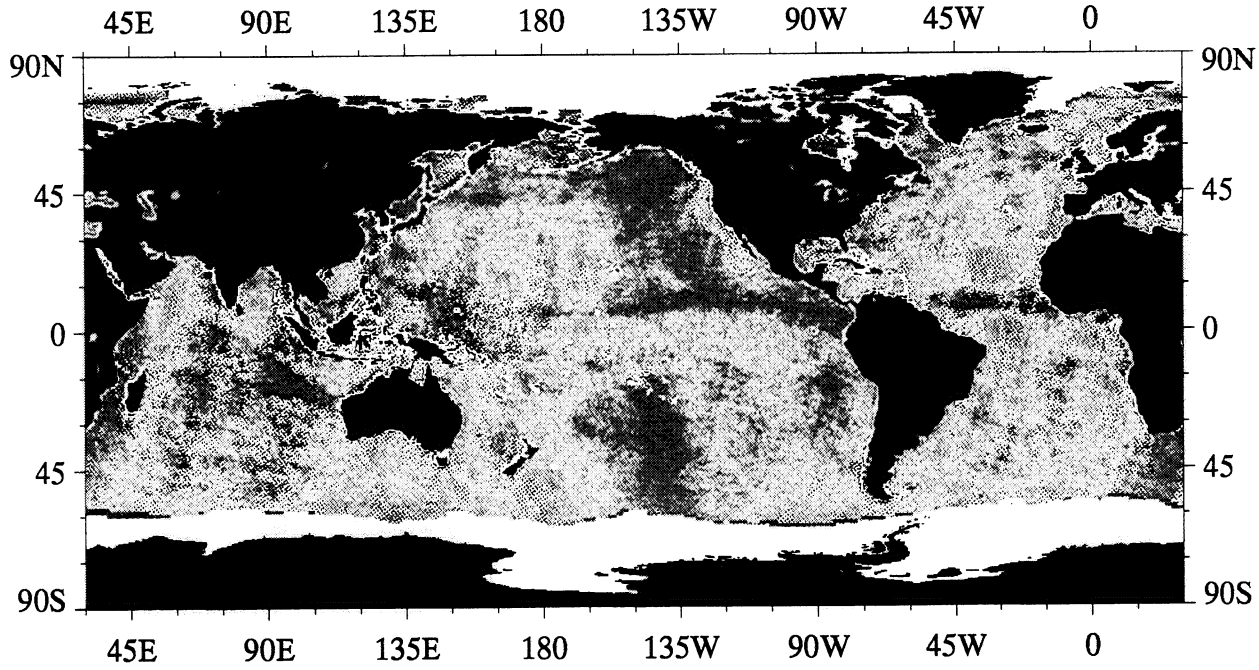


August 1990, max = 109

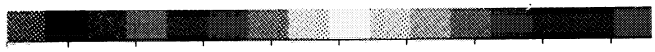


Number of SSMI Wind Speed Values per Pixel

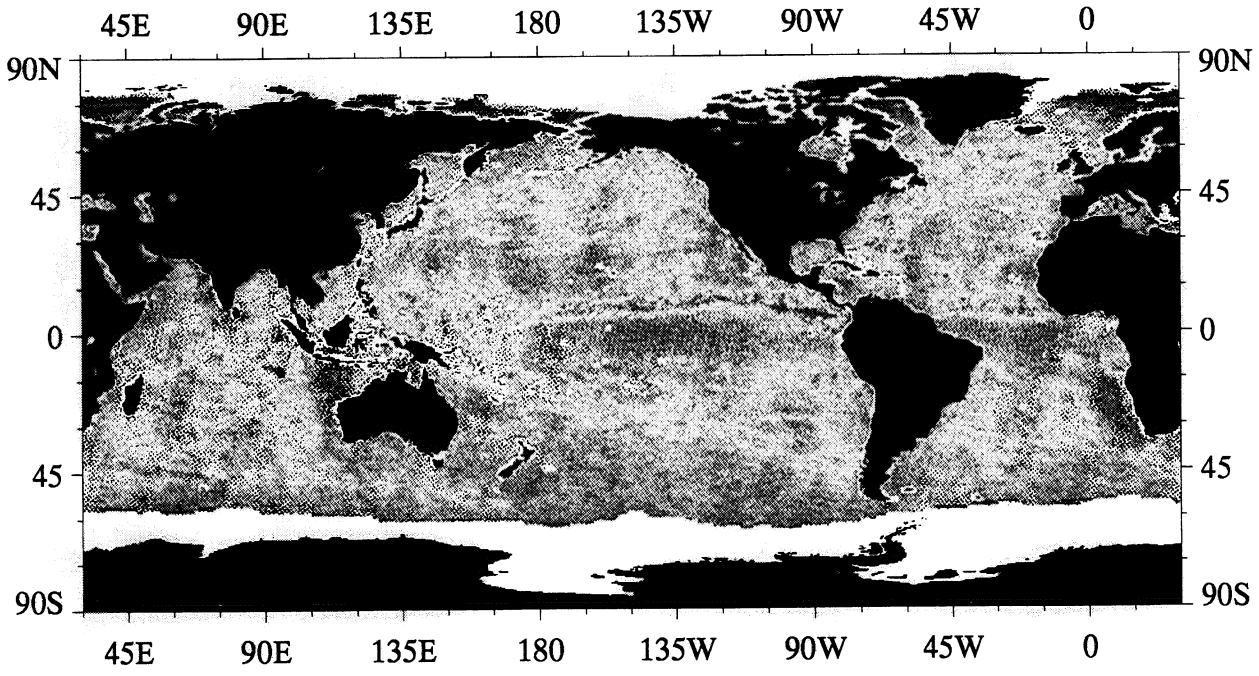


September 1990, max = 123

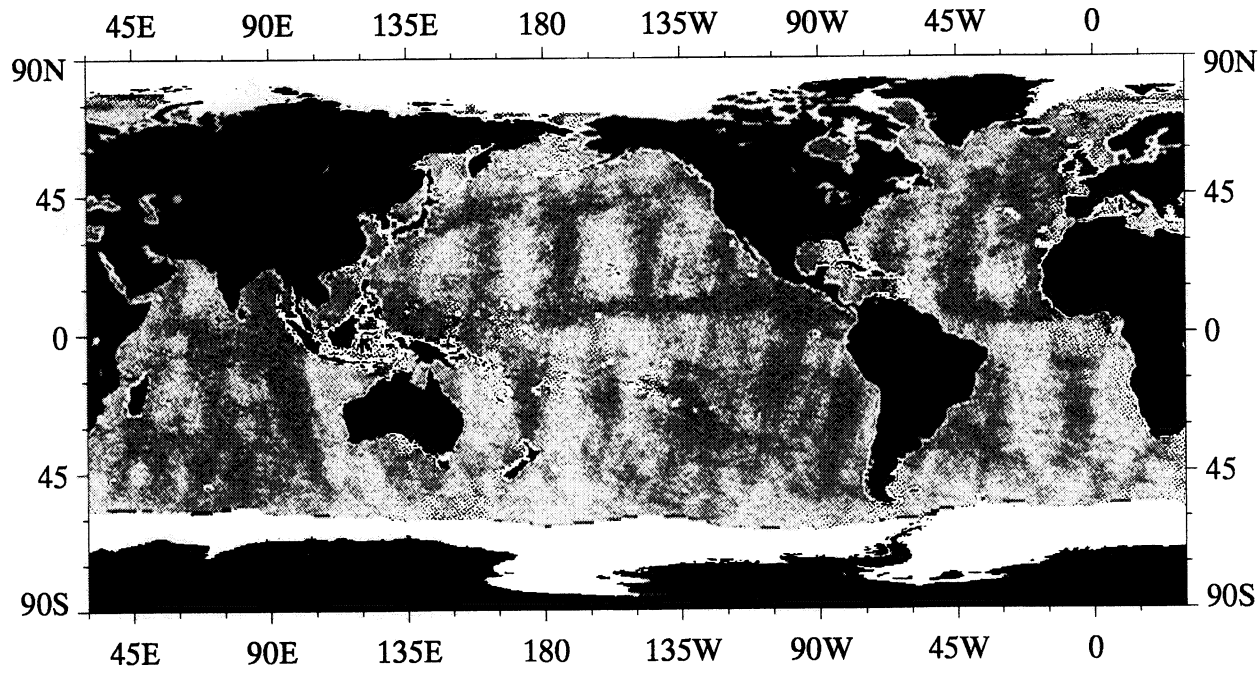


October 1990, max = 96

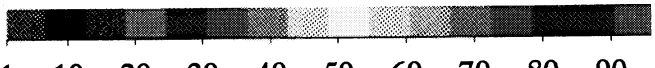


Number of SSMI Wind Speed Values per Pixel

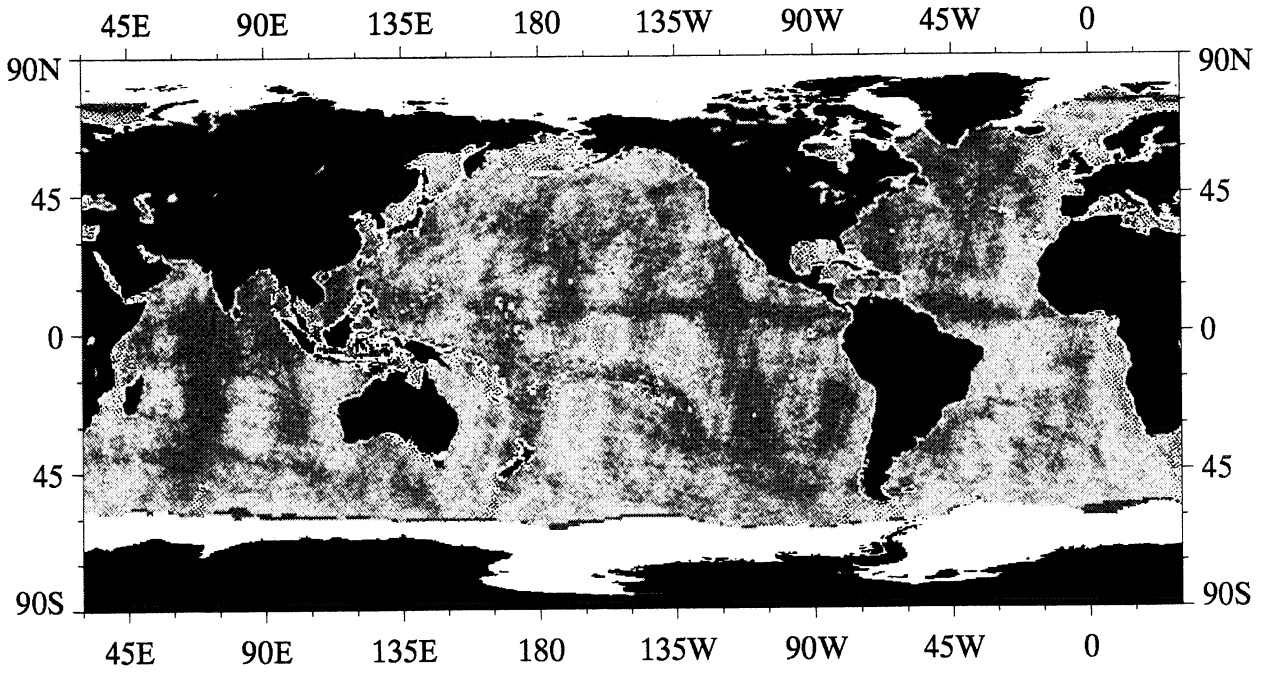


November 1990, max = 112

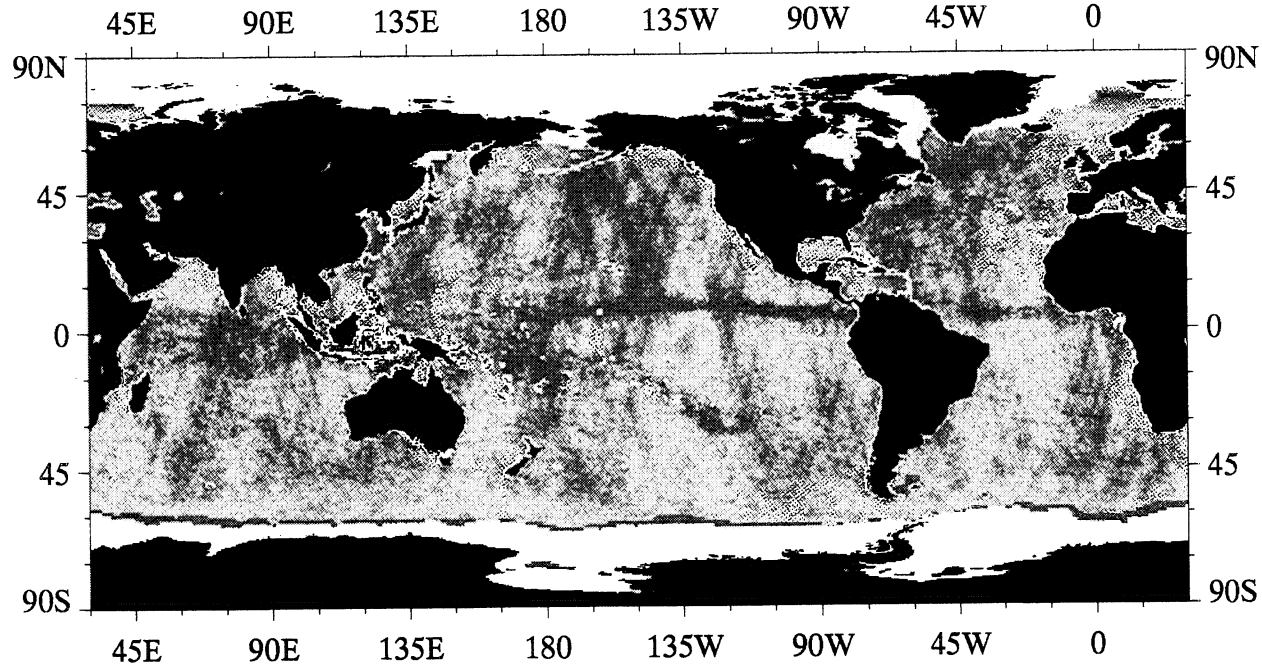


December 1990, max = 106

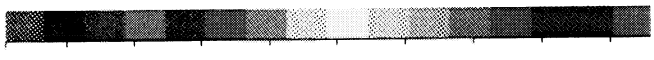


Number of SSMI Wind Speed Values per Pixel

A4

Monthly Standard Deviation of SSMI Surface Wind Speed

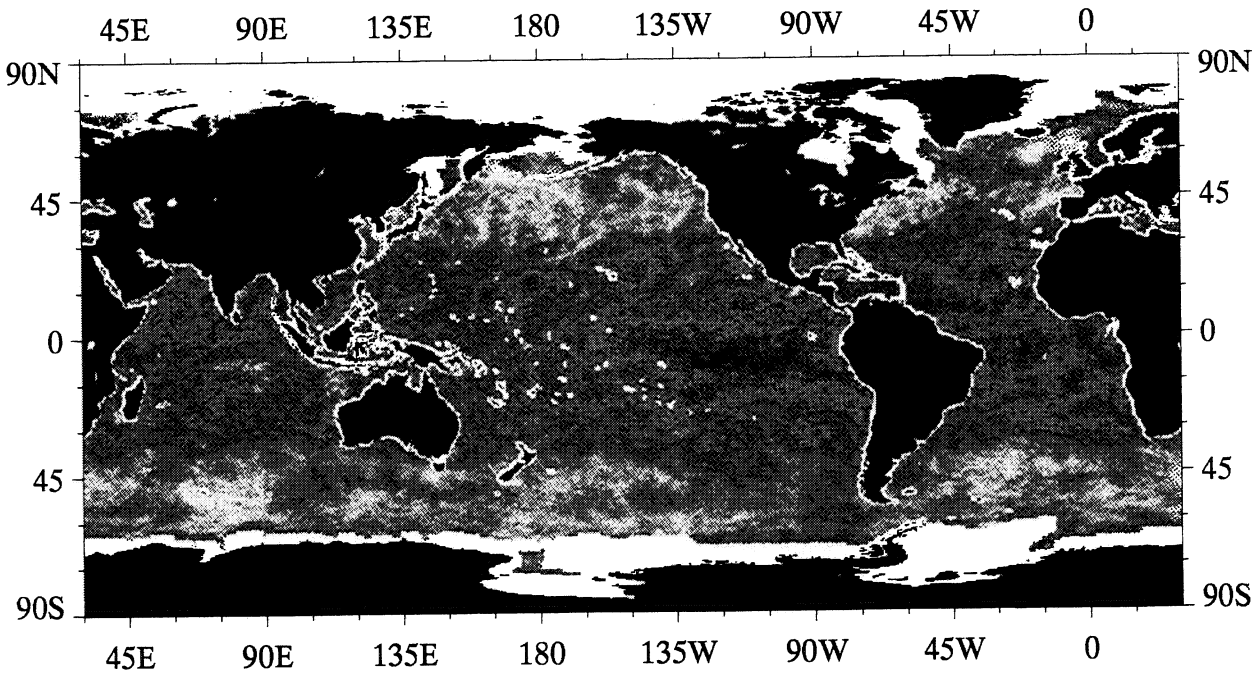


January 1990

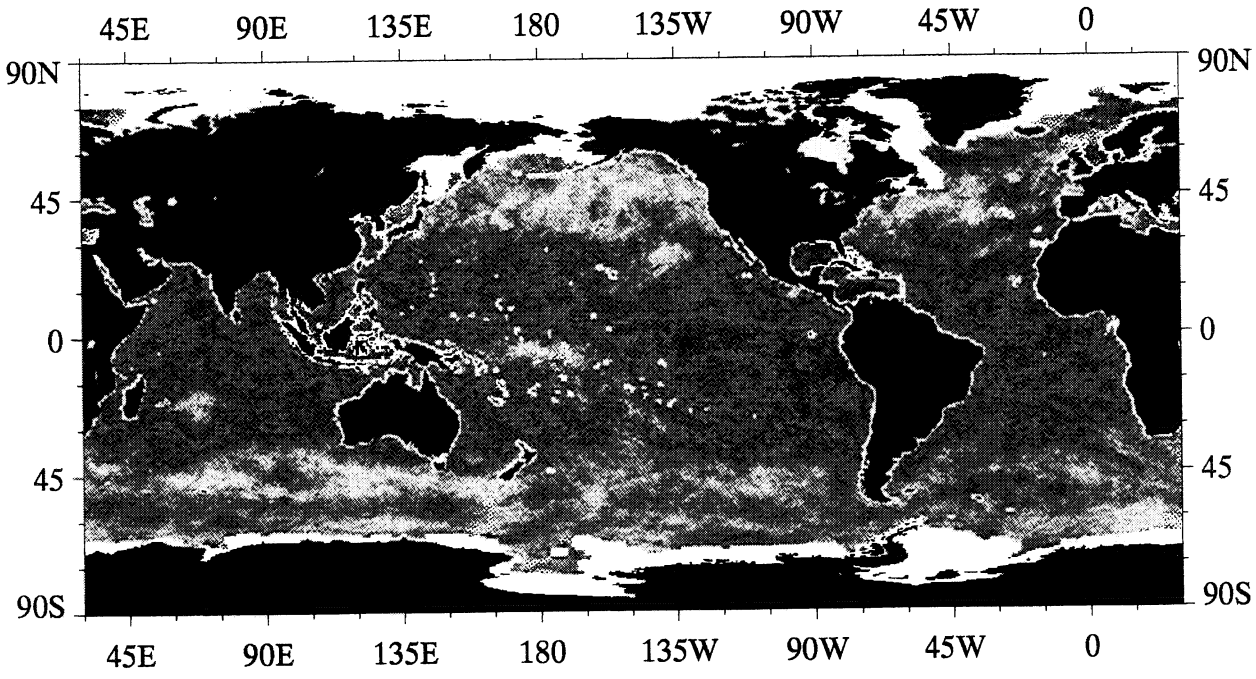


February 1990

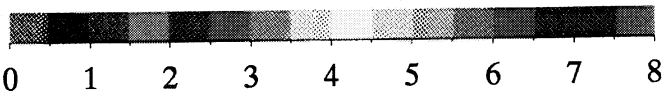


Standard Deviation of SSMI 10 m Wind Speed, m $s^{-1}$

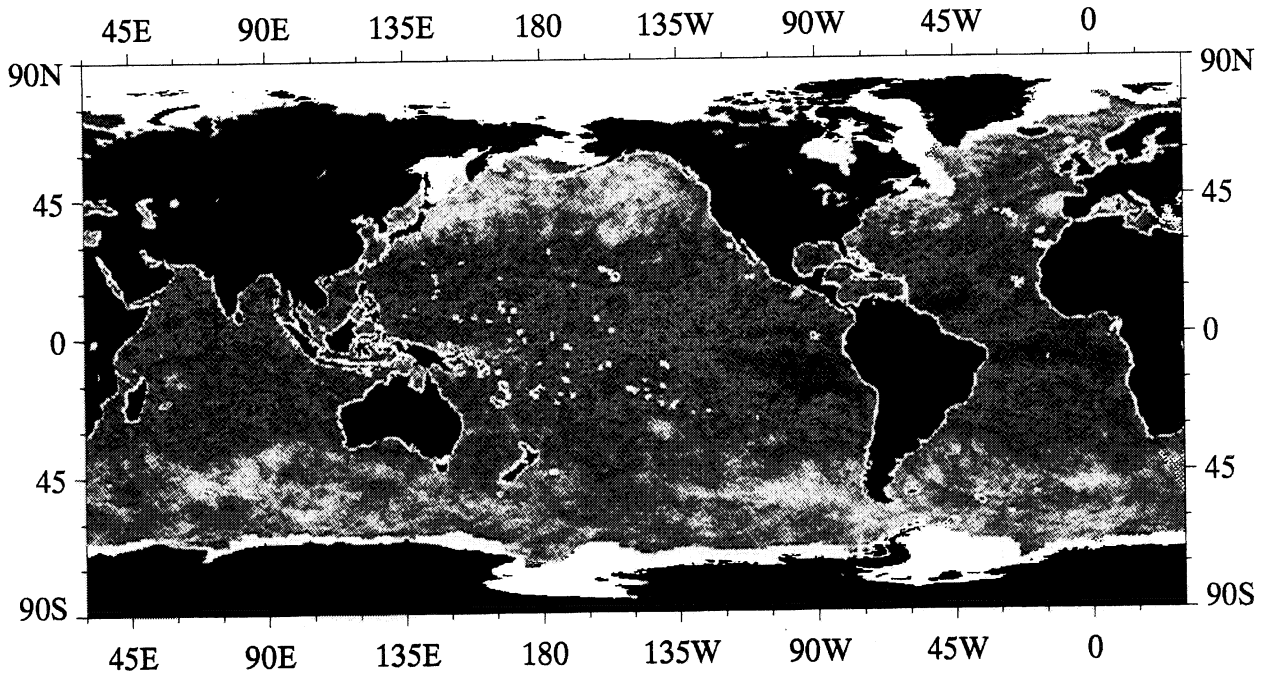


March 1990

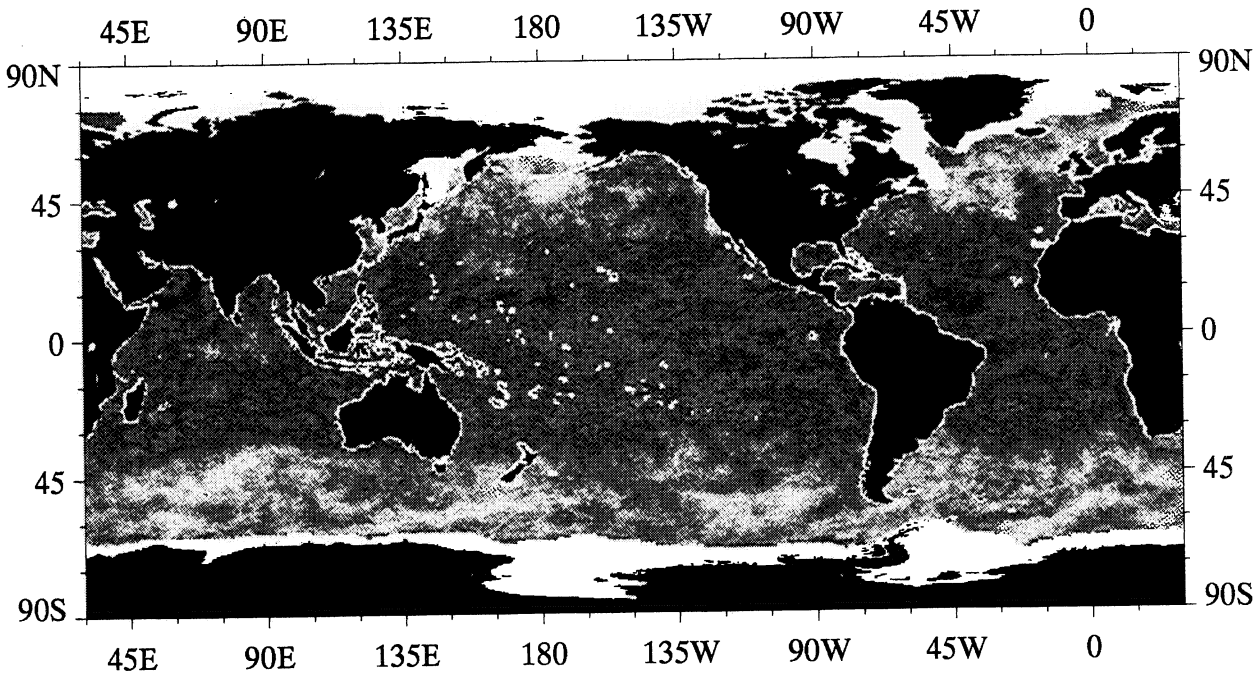


April 1990

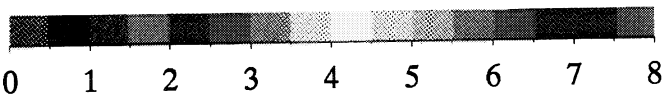


Standard Deviation of SSMI 10 m Wind Speed, m $s^{-1}$

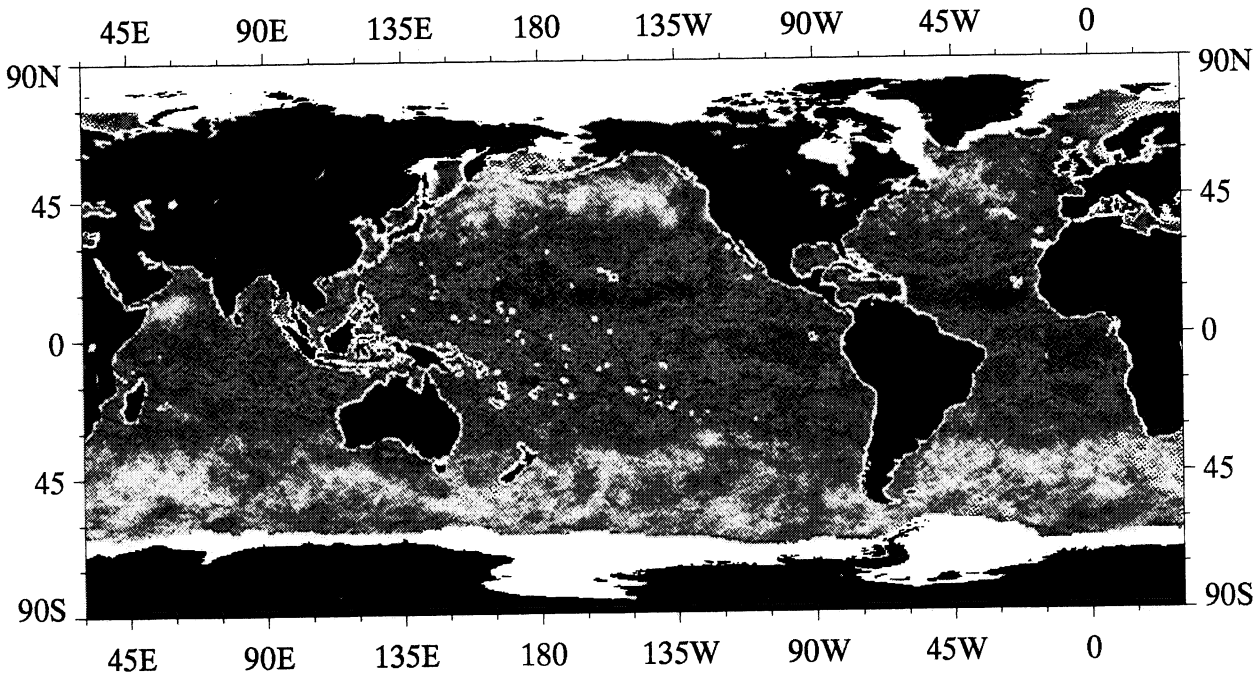


May 1990

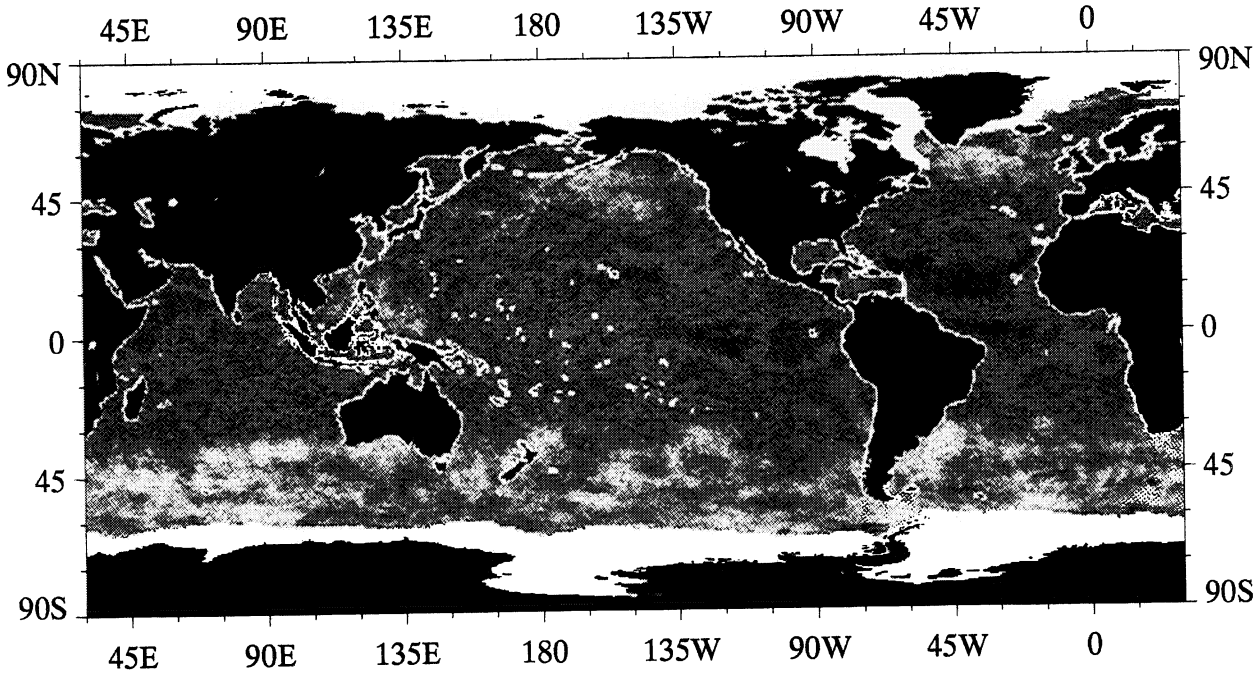


June 1990

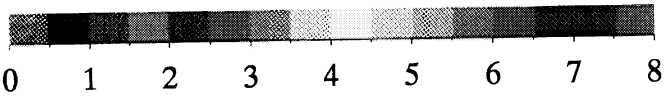


Standard Deviation of SSMI 10 m Wind Speed, m $s^{-1}$

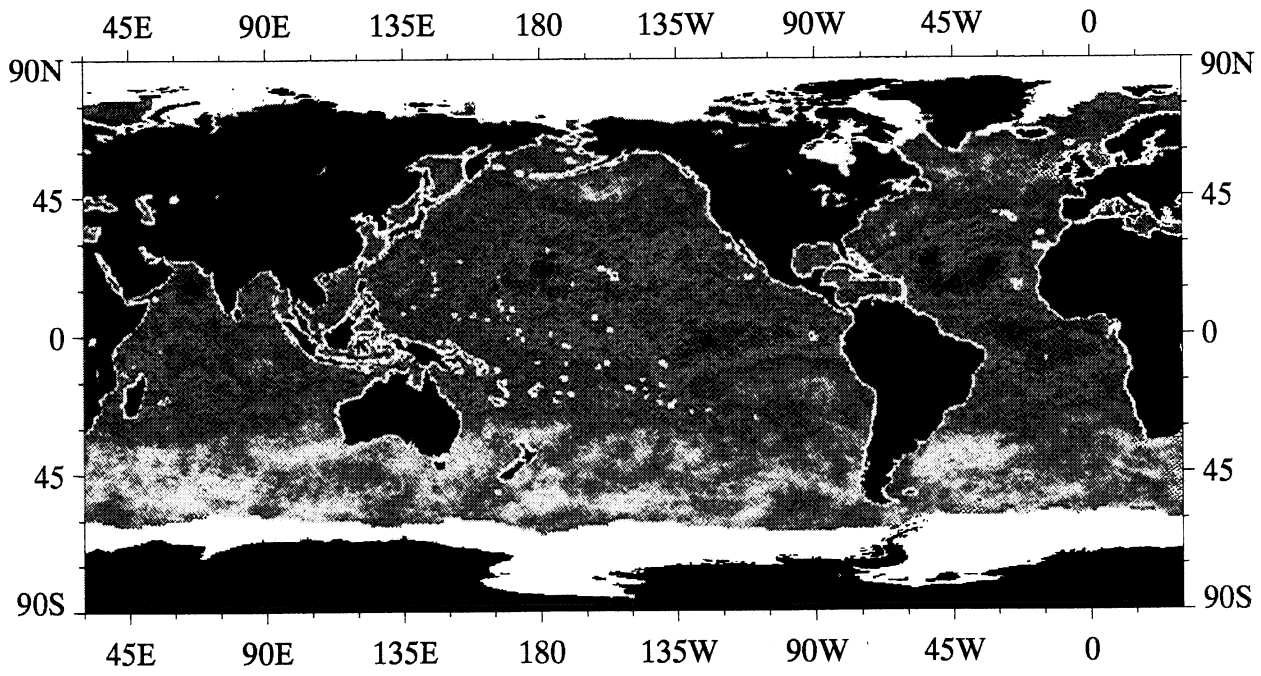


July 1990

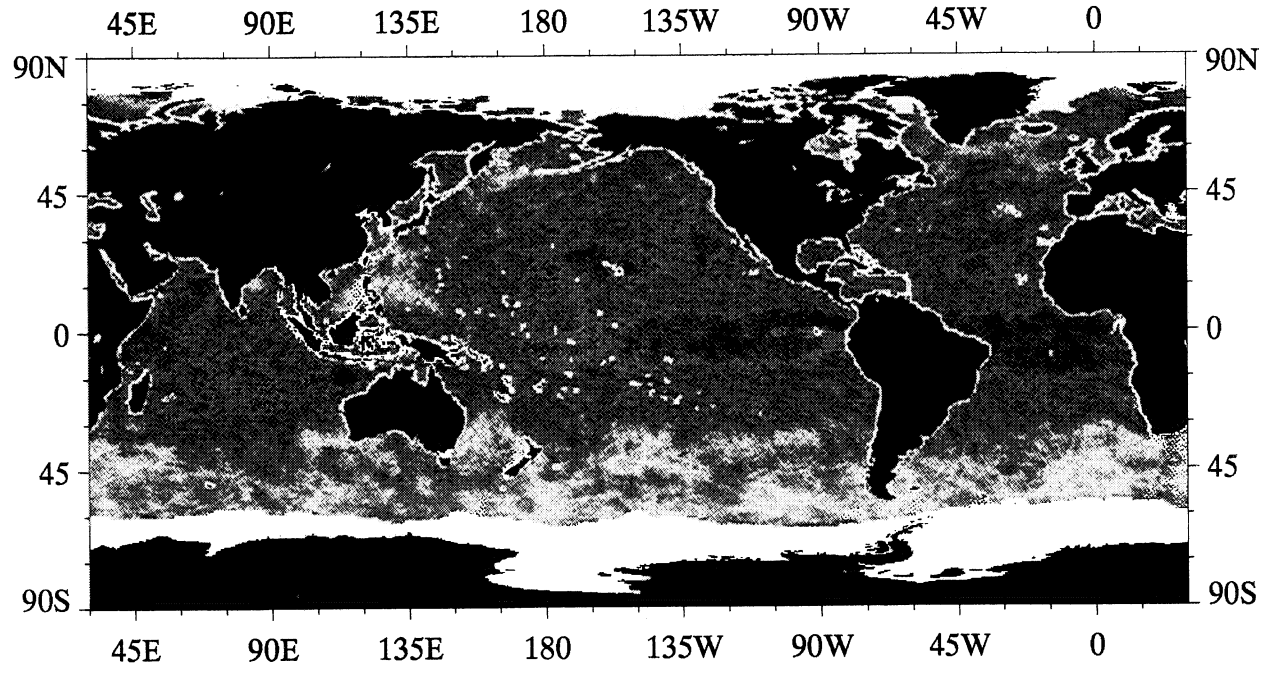


August 1990

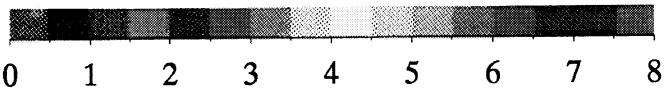


Standard Deviation of SSMI 10 m Wind Speed, m $s^{-1}$

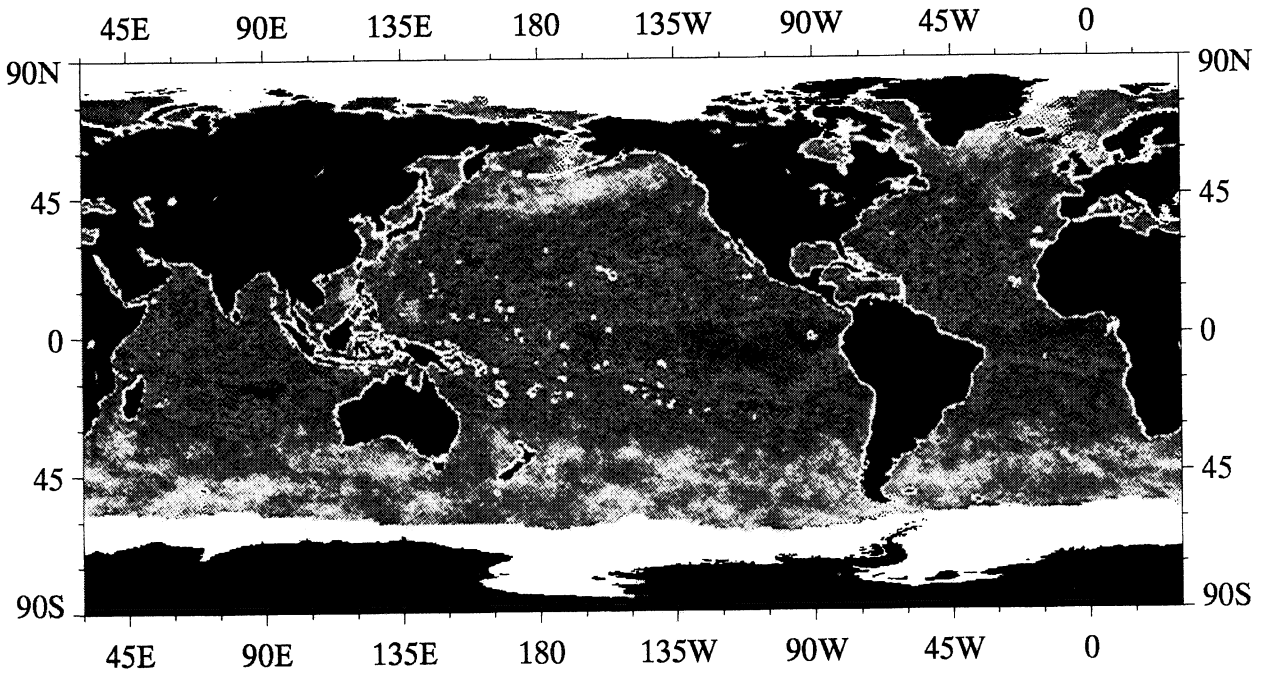


September 1990

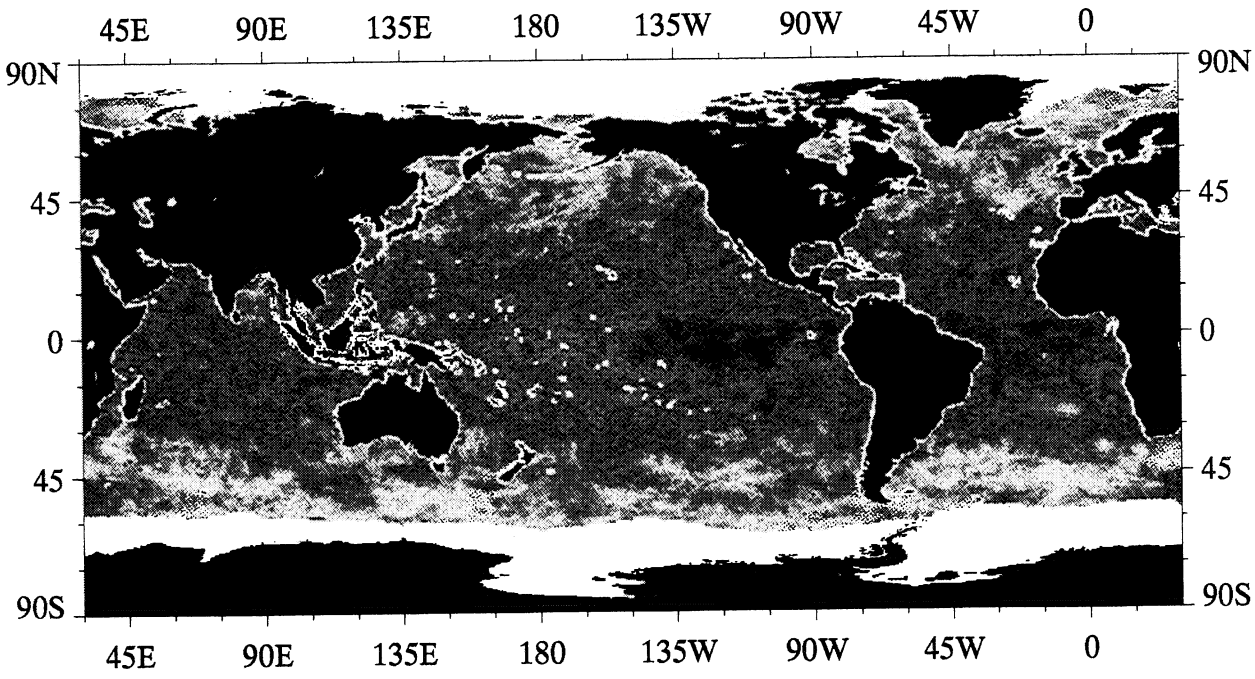


October 1990

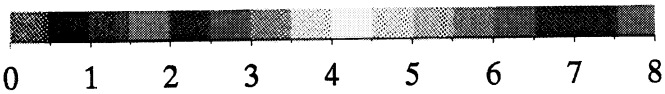


Standard Deviation of SSMI 10 m Wind Speed, m $s^{-1}$

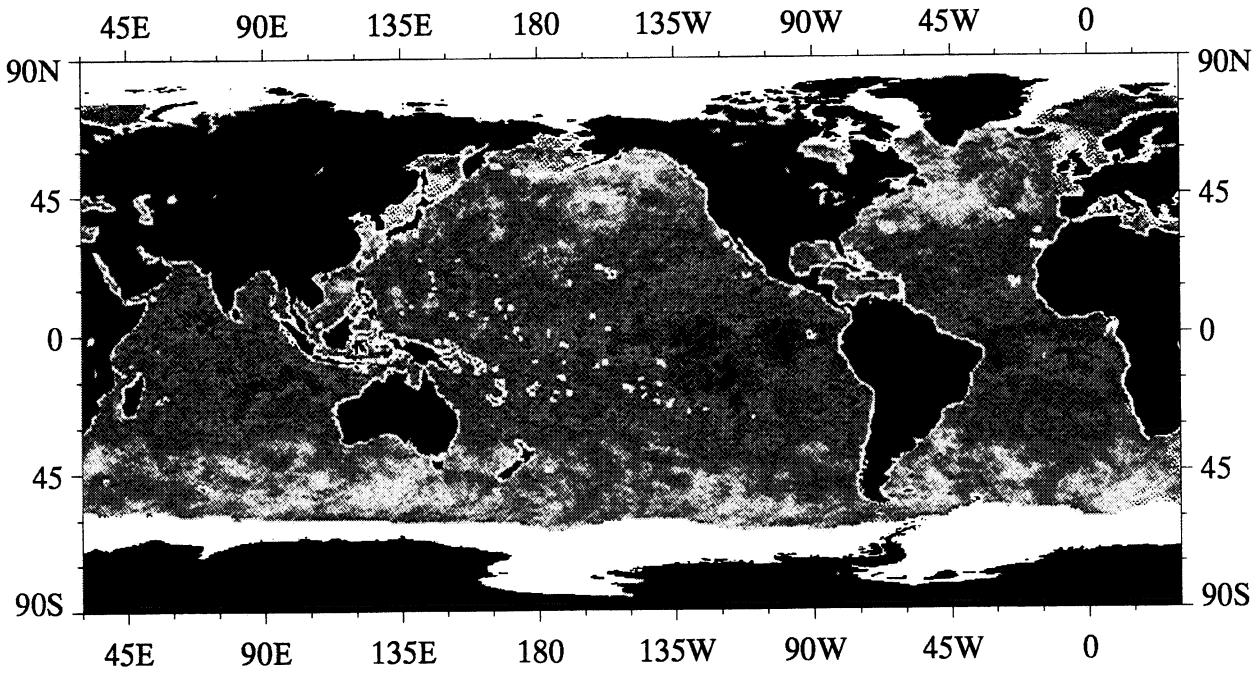


November 1990

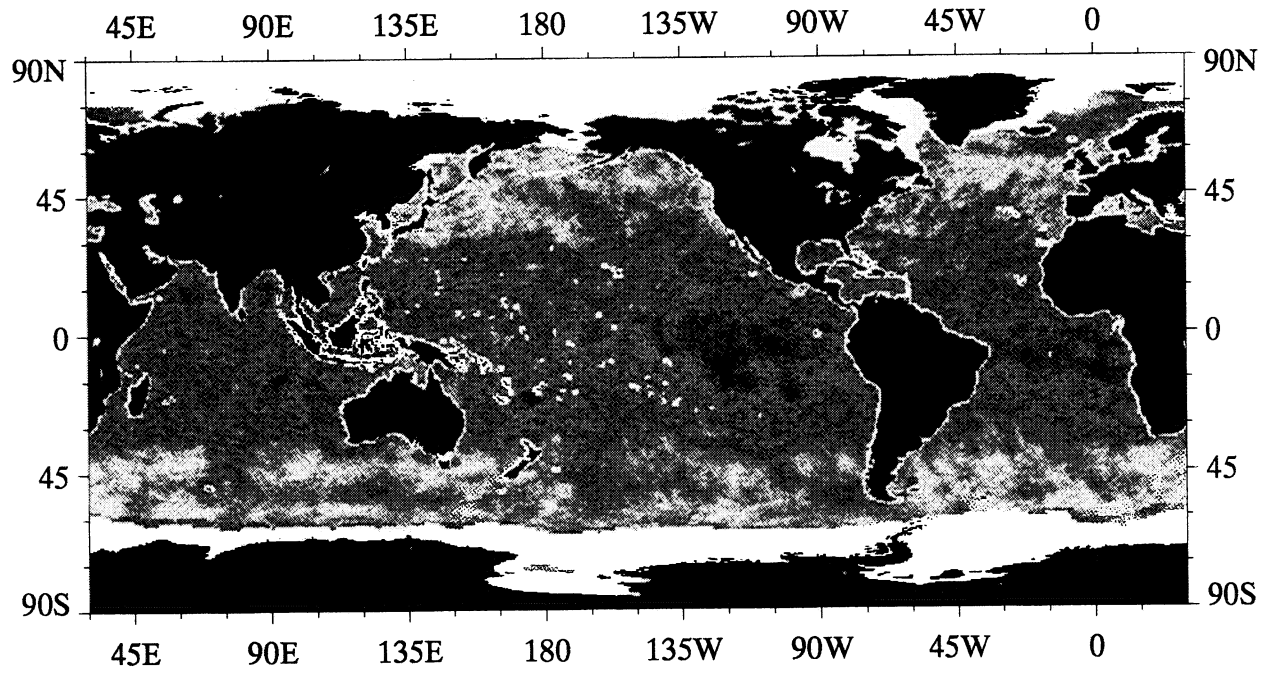


December 1990

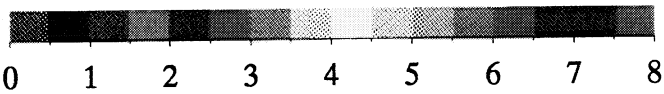


Standard Deviation of SSMI 10 m Wind Speed, m $s^{-1}$

A5

Monthly Mean ARGOS Buoy Drift

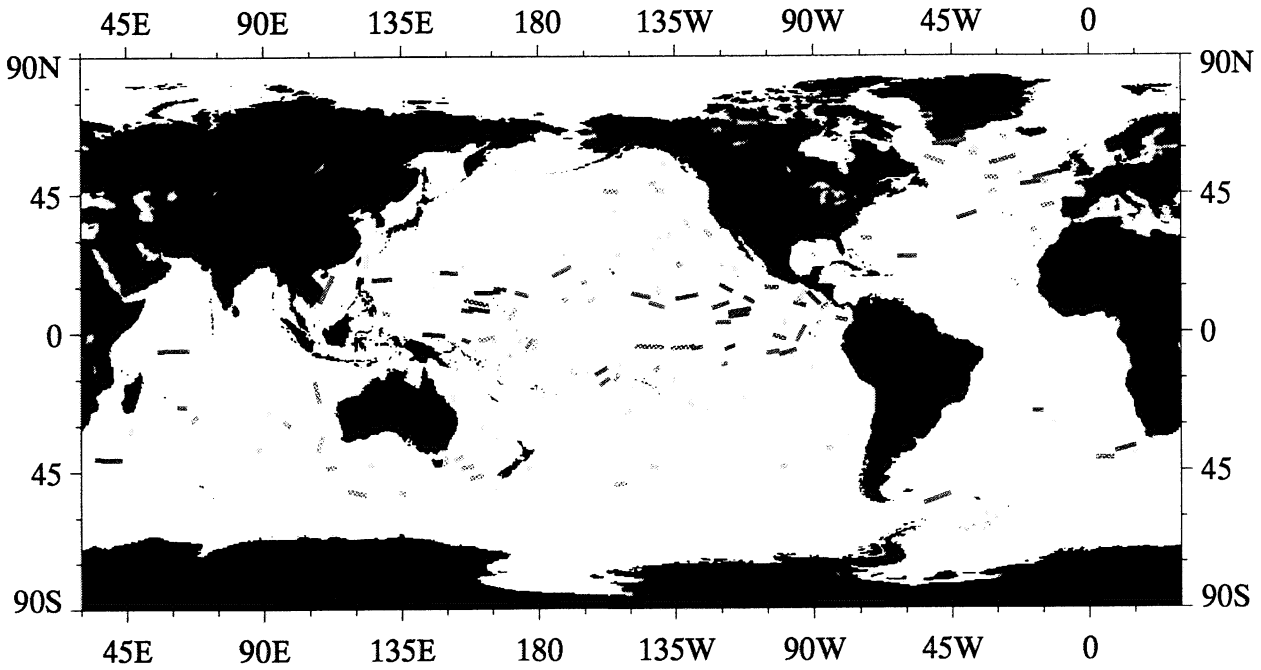


Zonal Speed, January 1990

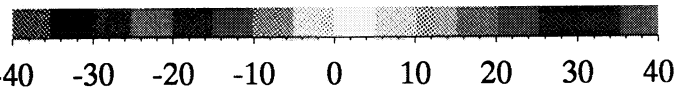


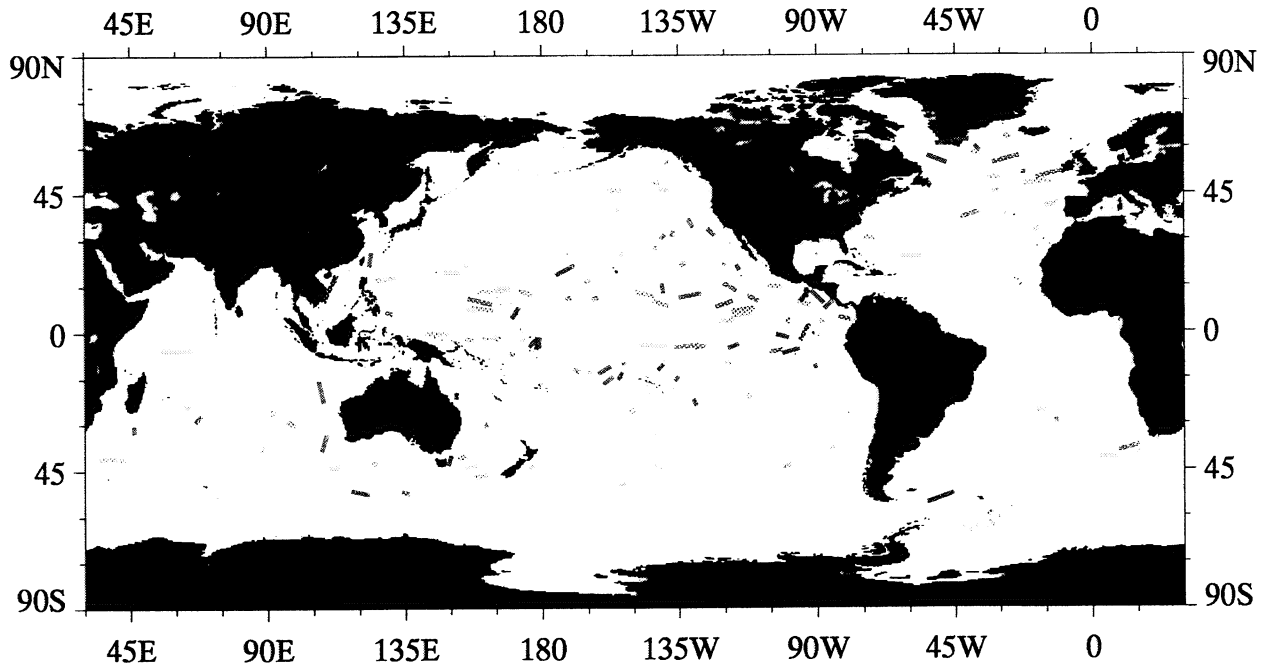


Meridional Speed, January 1990

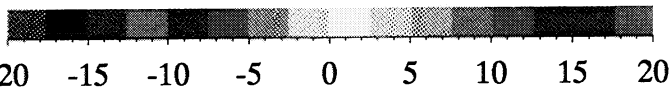


ARGOS Buoy Drift, cm $s^{-1}$

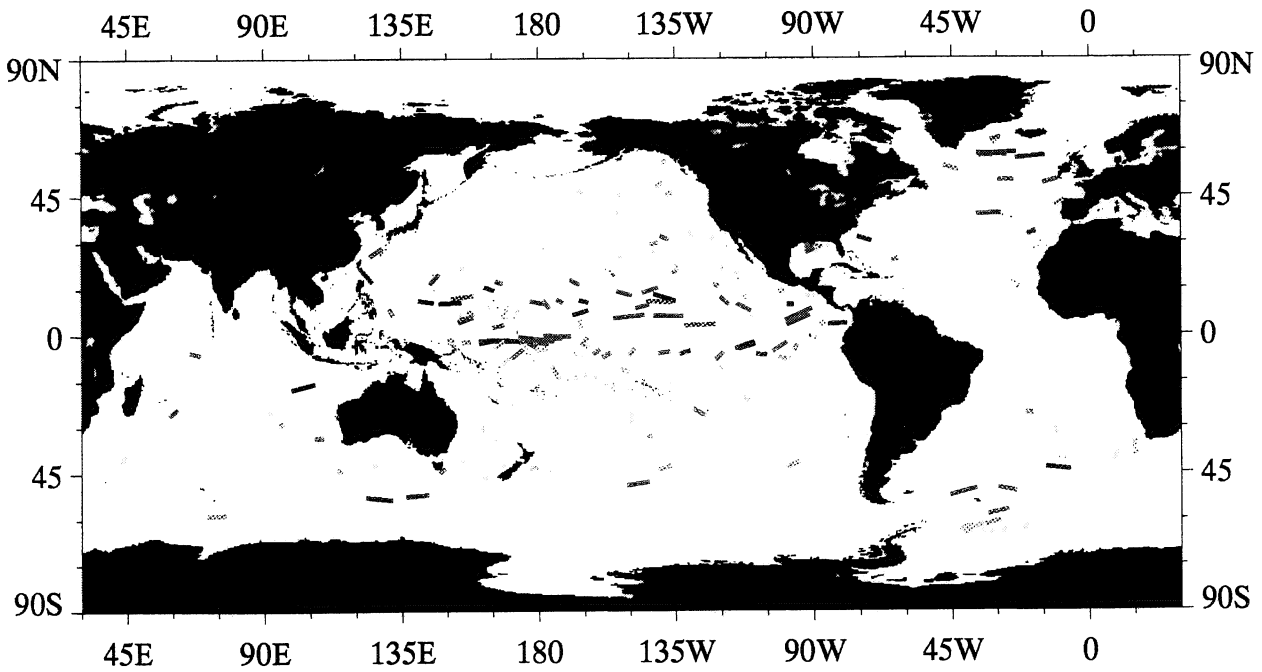


Zonal Speed, February 1990


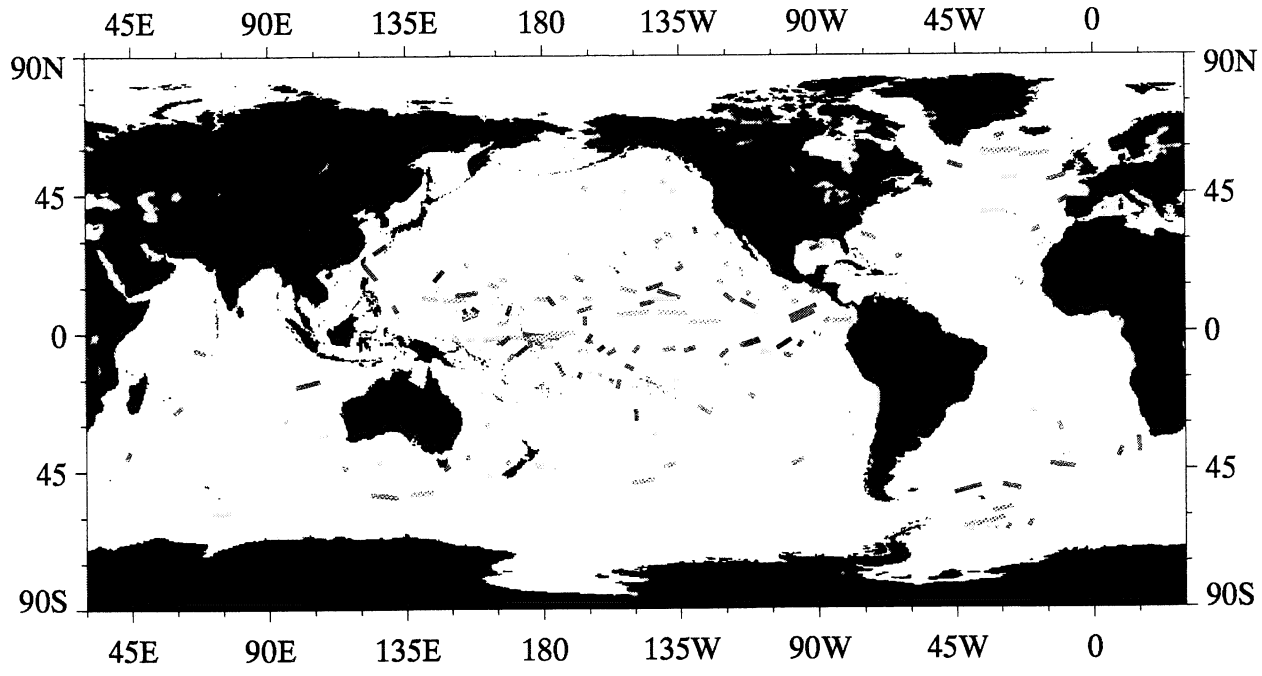


Meridional Speed, February 1990


ARGOS Buoy Drift, cm $s^{-1}$

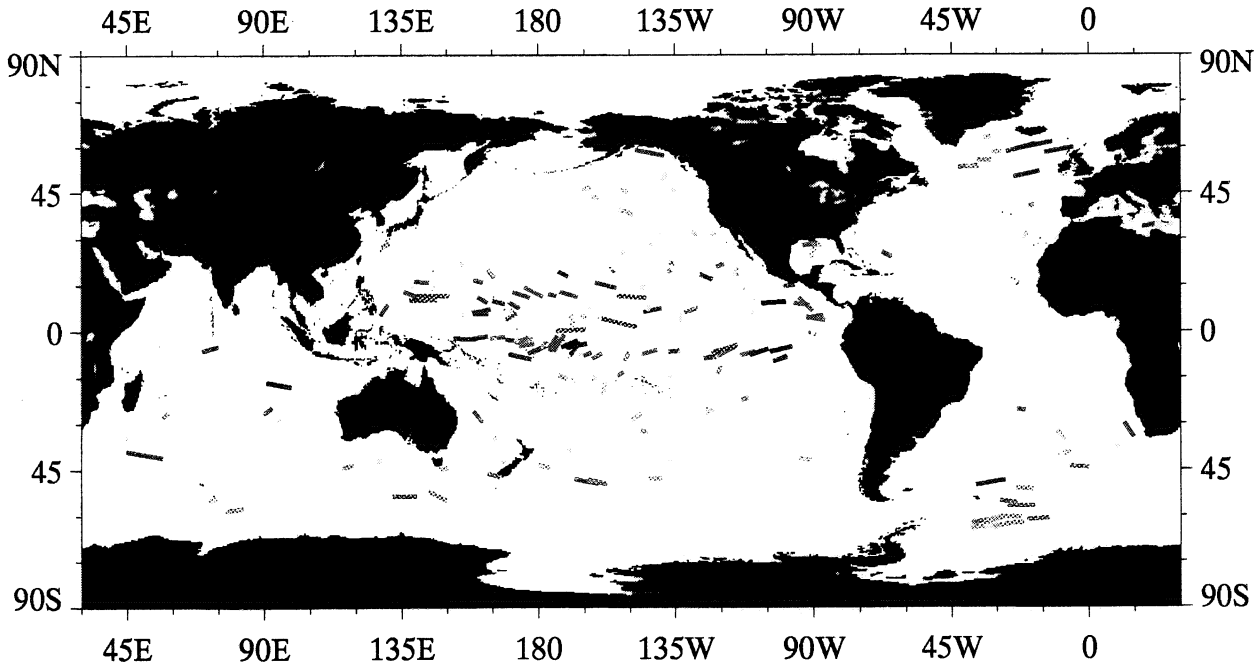


Zonal Speed, March 1990

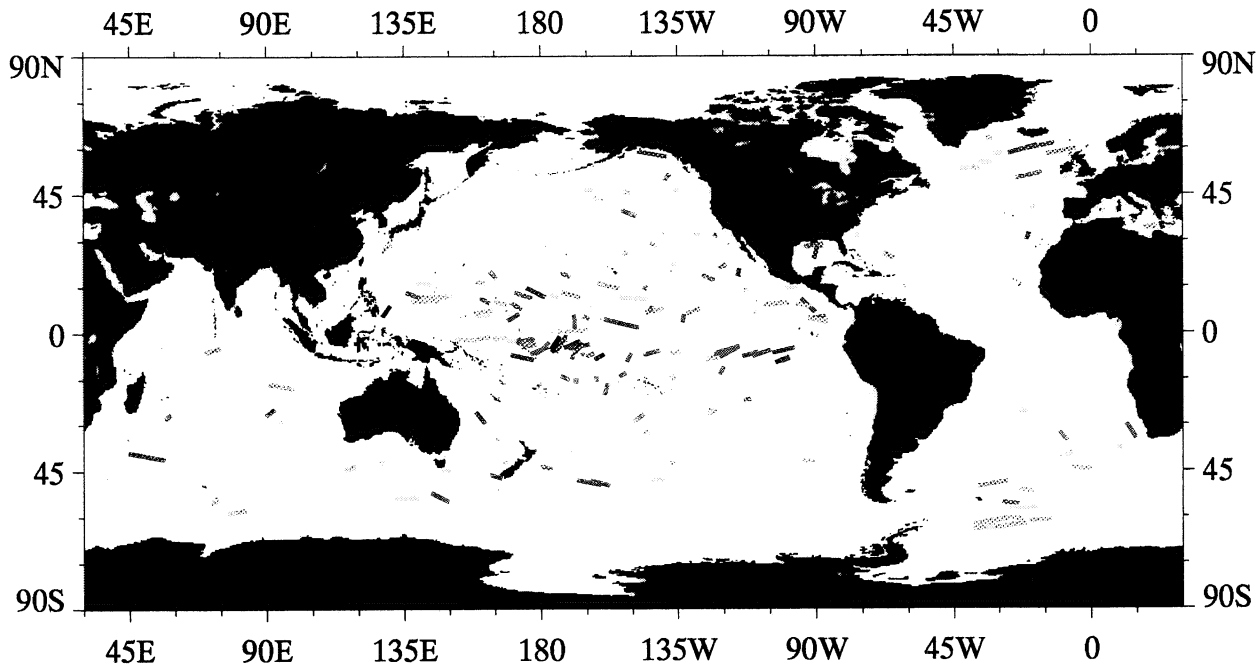


Meridional Speed, March 1990

ARGOS Buoy Drift, cm $s^{-1}$

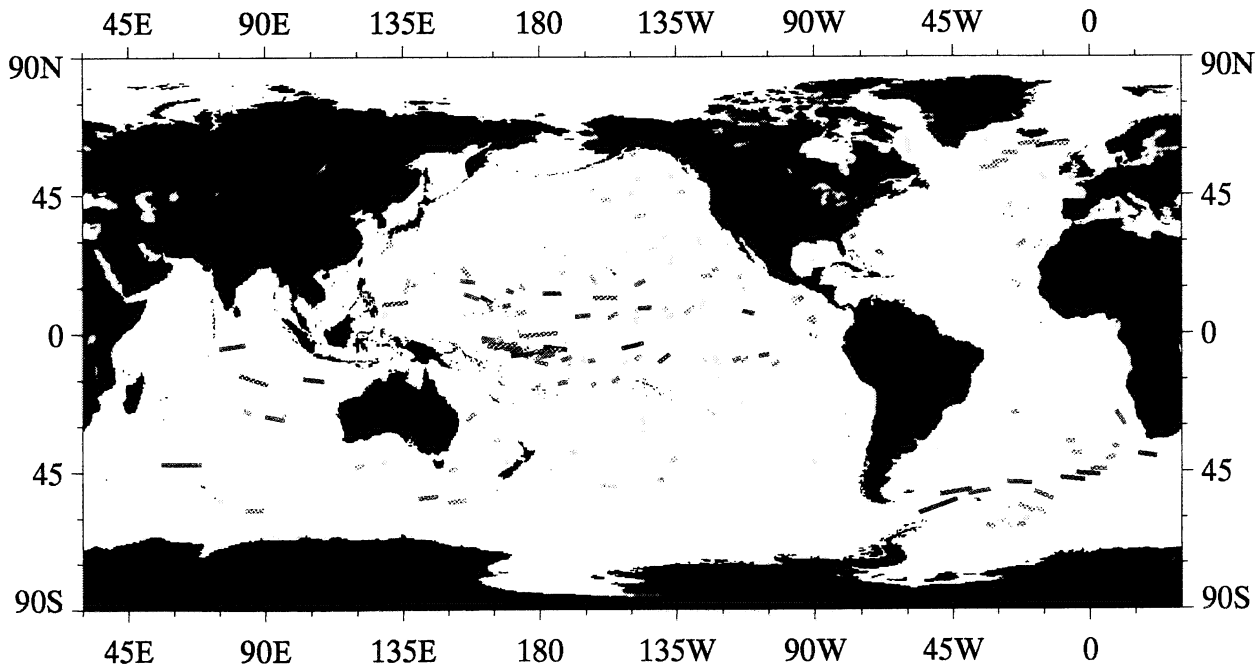


Zonal Speed, April 1990


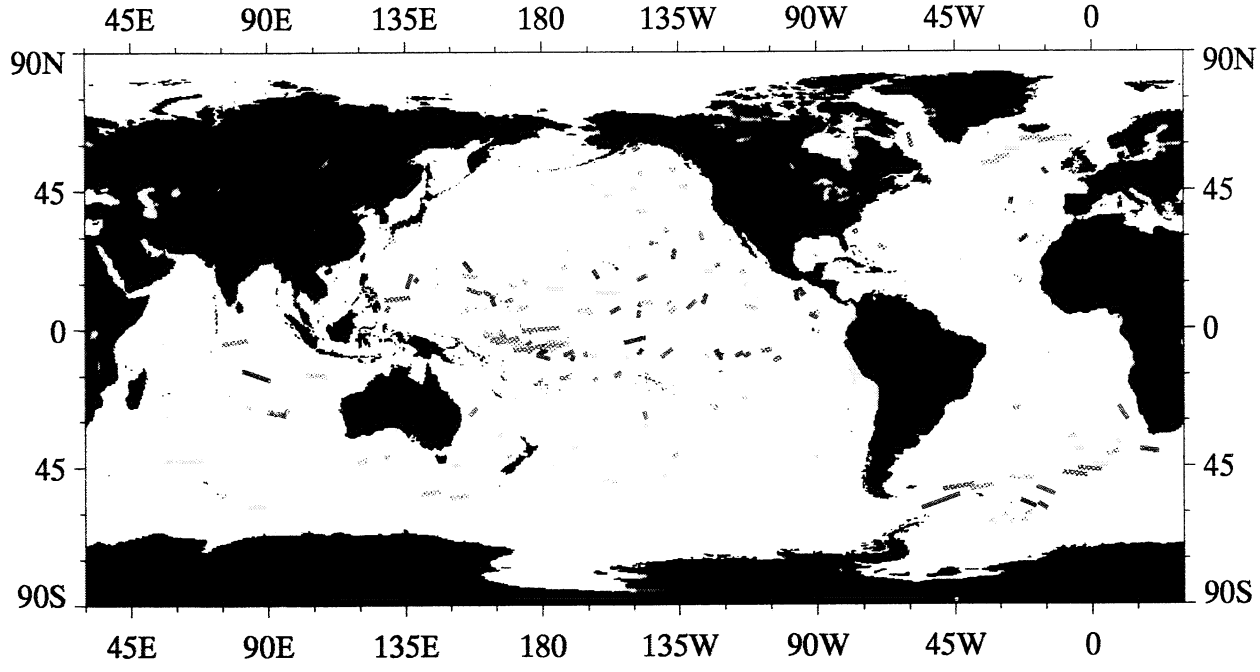


Meridional Speed, April 1990

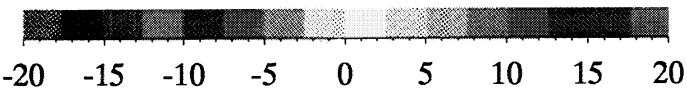


ARGOS Buoy Drift, cm $s^{-1}$

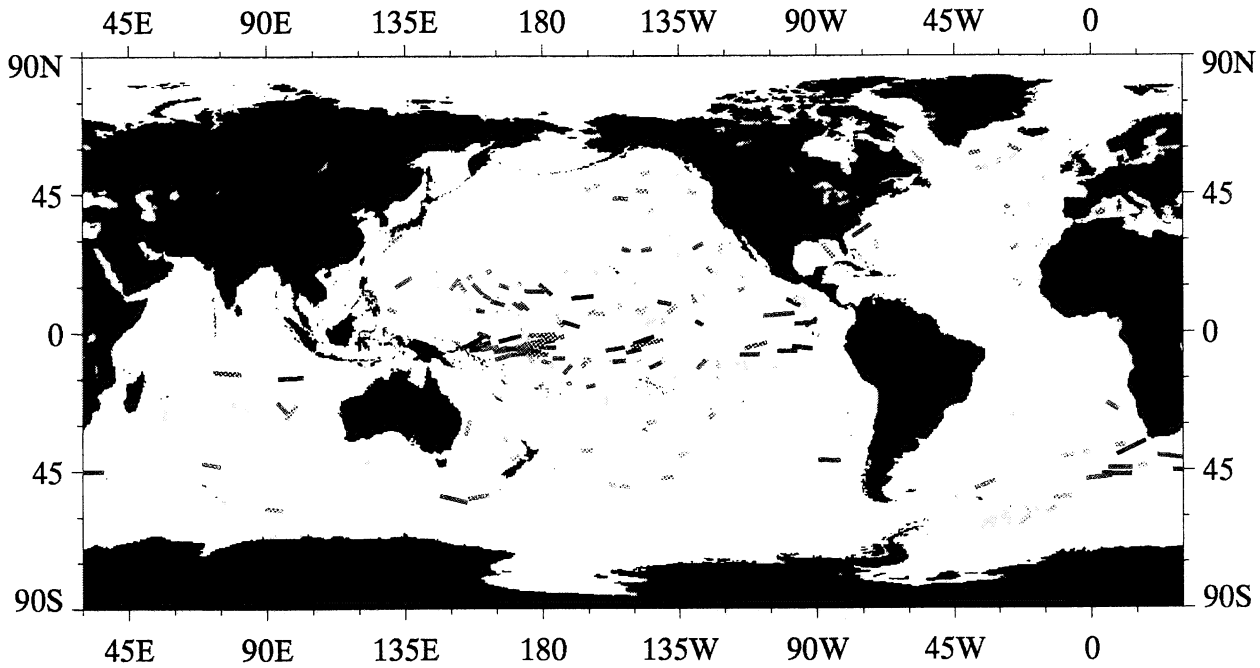


Zonal Speed, May 1990

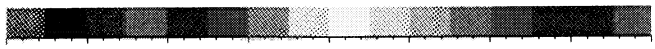


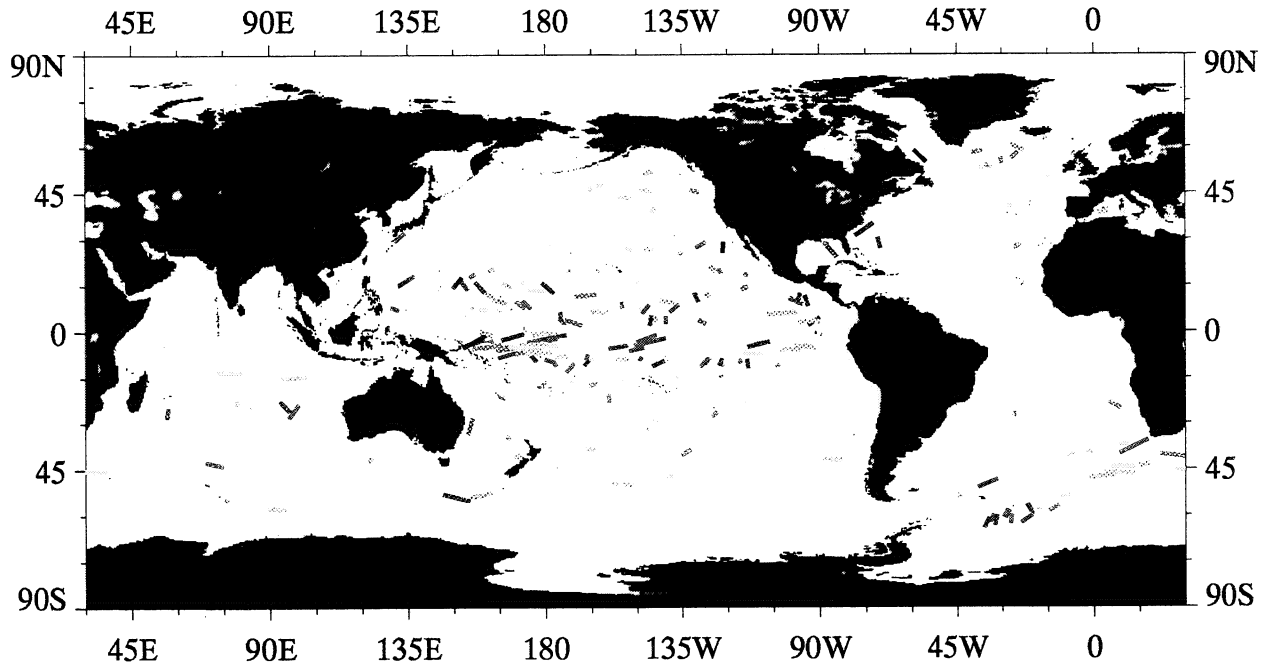


Meridional Speed, May 1990


ARGOS Buoy Drift, cm $s^{-1}$

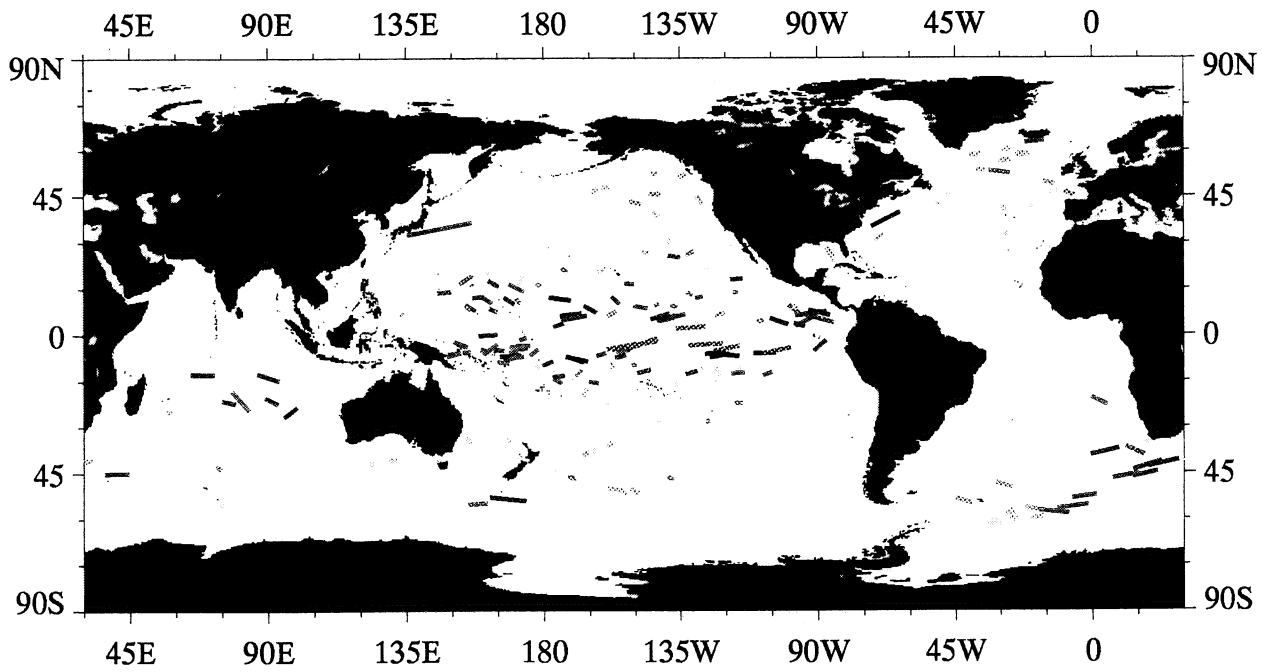


Zonal Speed, June 1990

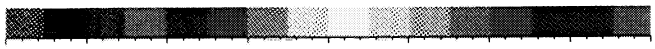


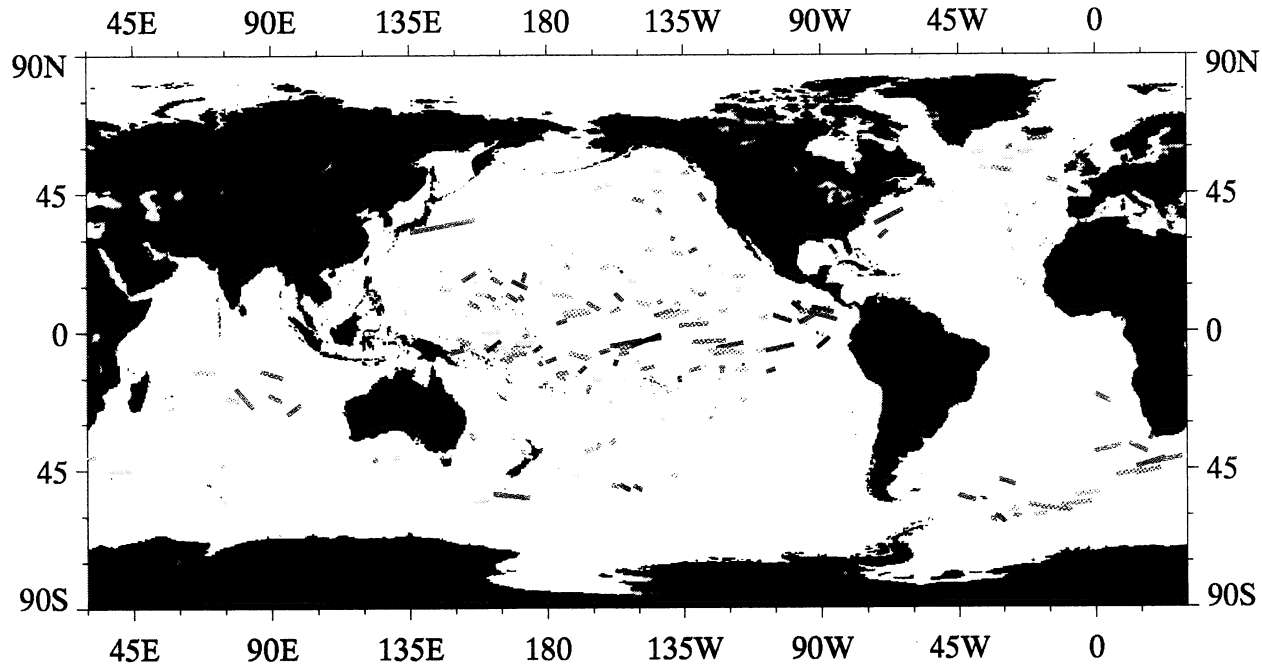


Meridional Speed, June 1990

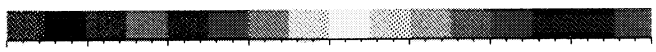


ARGOS Buoy Drift, cm $s^{-1}$

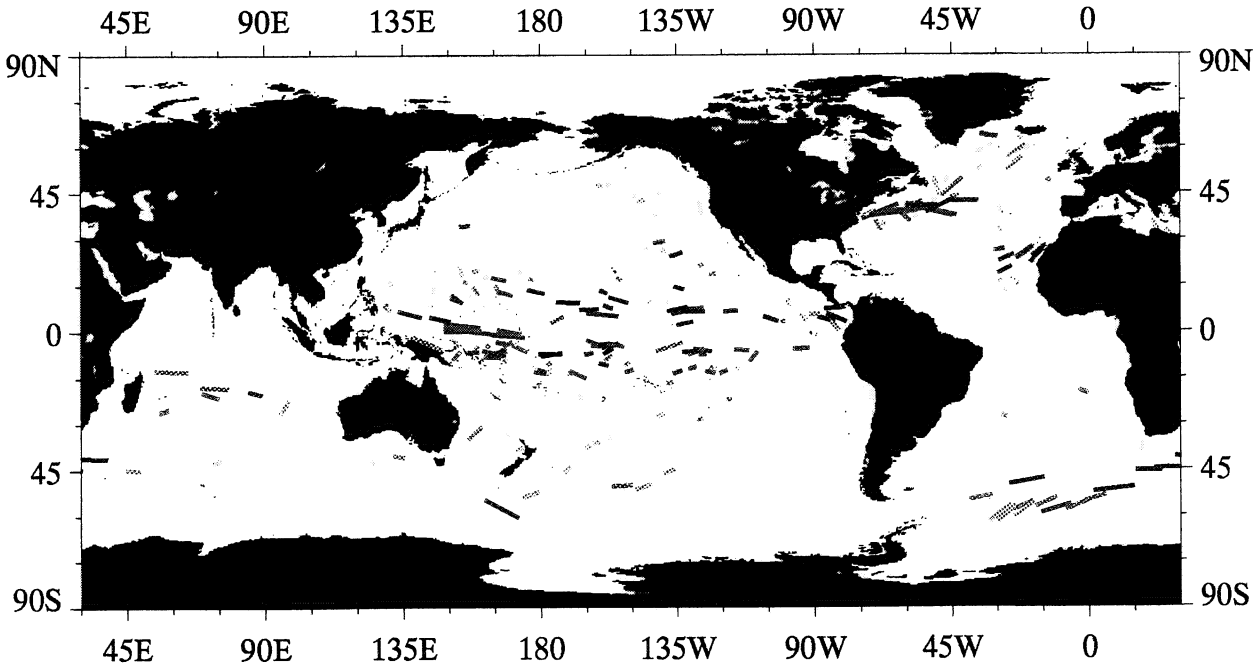


Zonal Speed, July 1990

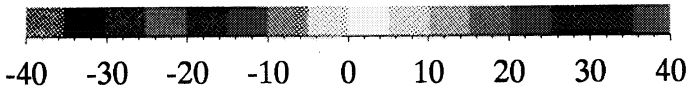


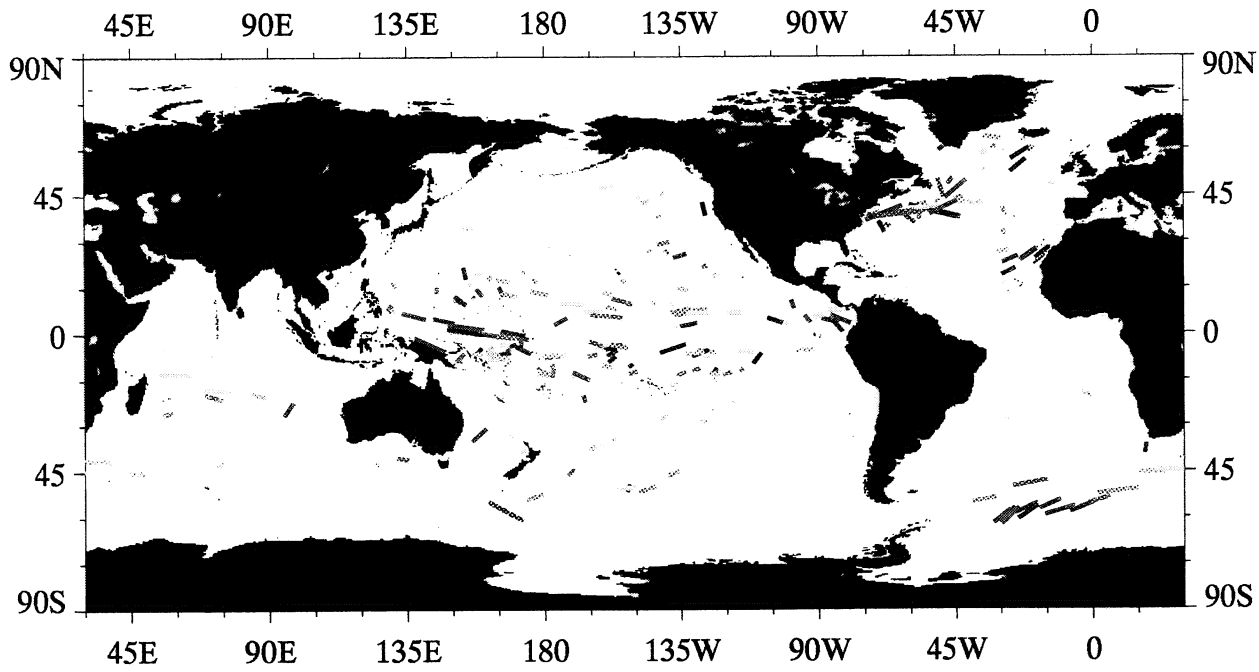


Meridional Speed, July 1990

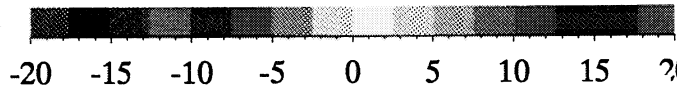


ARGOS Buoy Drift, cm $s^{-1}$

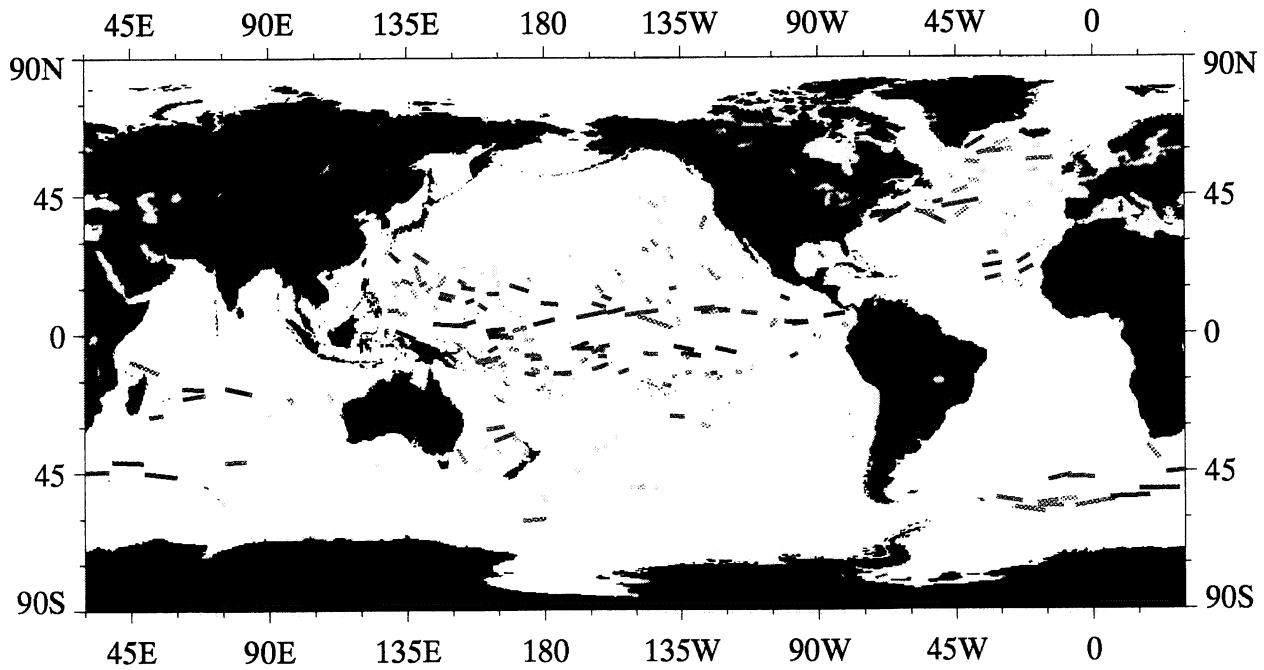


Zonal Speed, August 1990

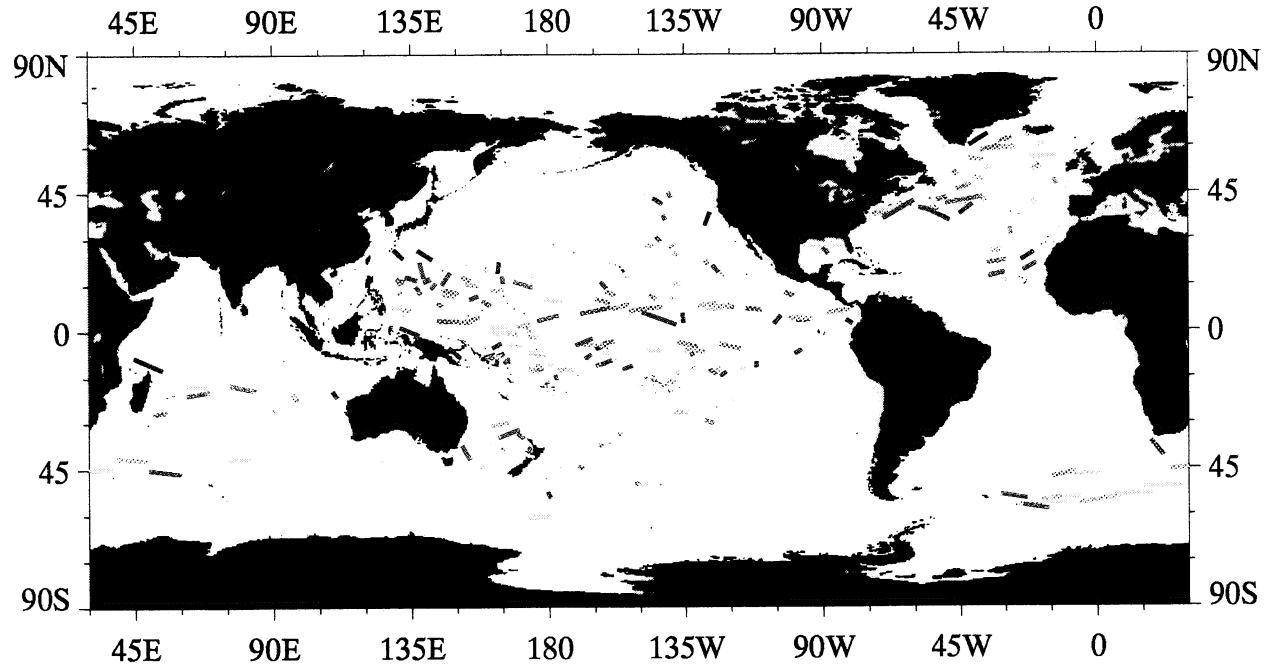


Meridional Speed, August 1990

ARGOS Buoy Drift, cm $s^{-1}$

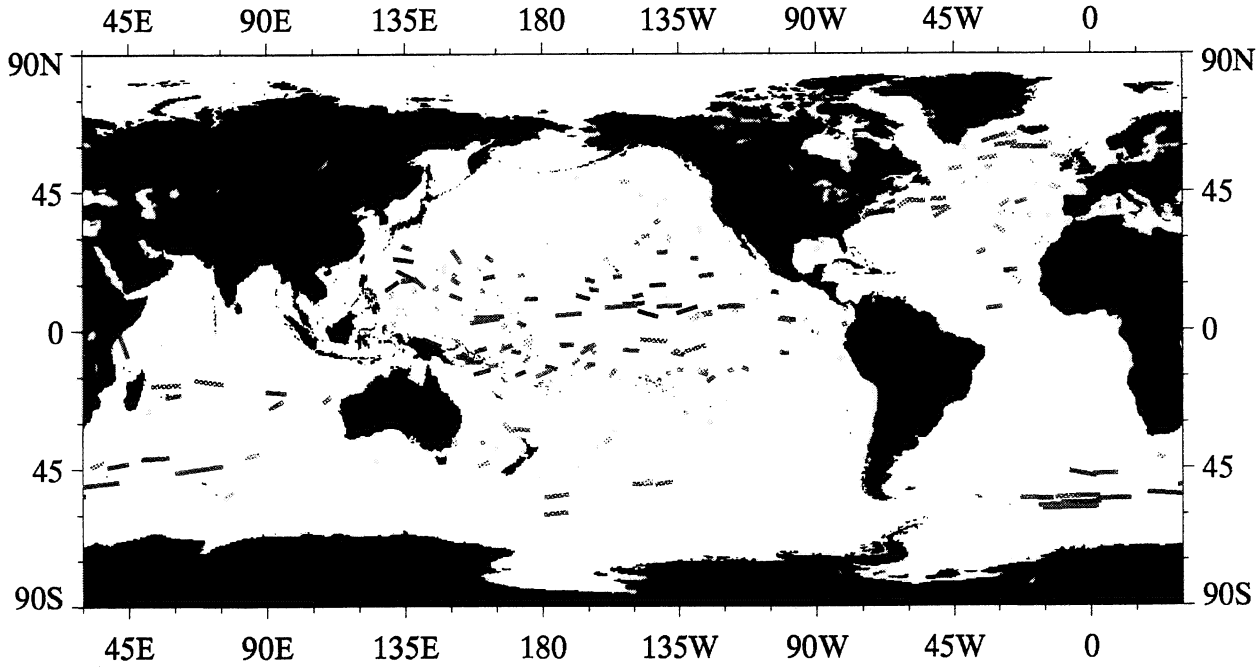


Zonal Speed, September 1990

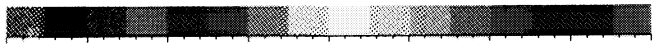


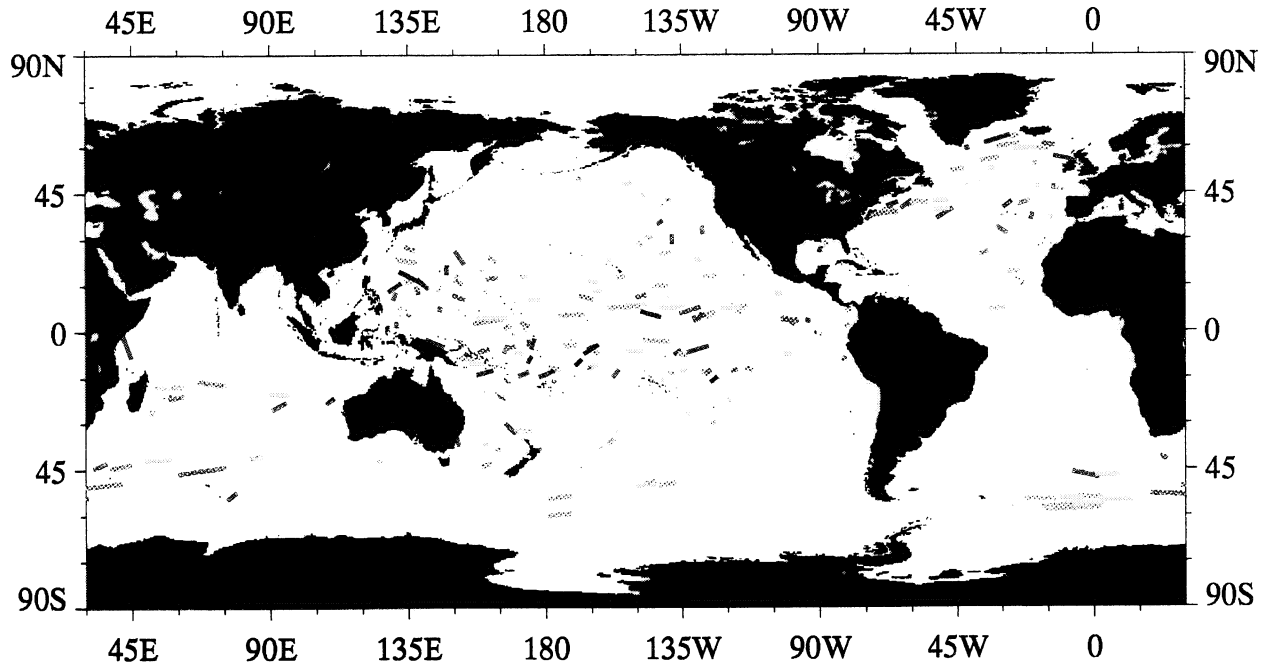


Meridional Speed, September 1990

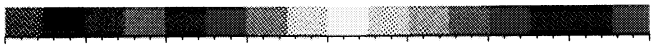


ARGOS Buoy Drift, cm $s^{-1}$

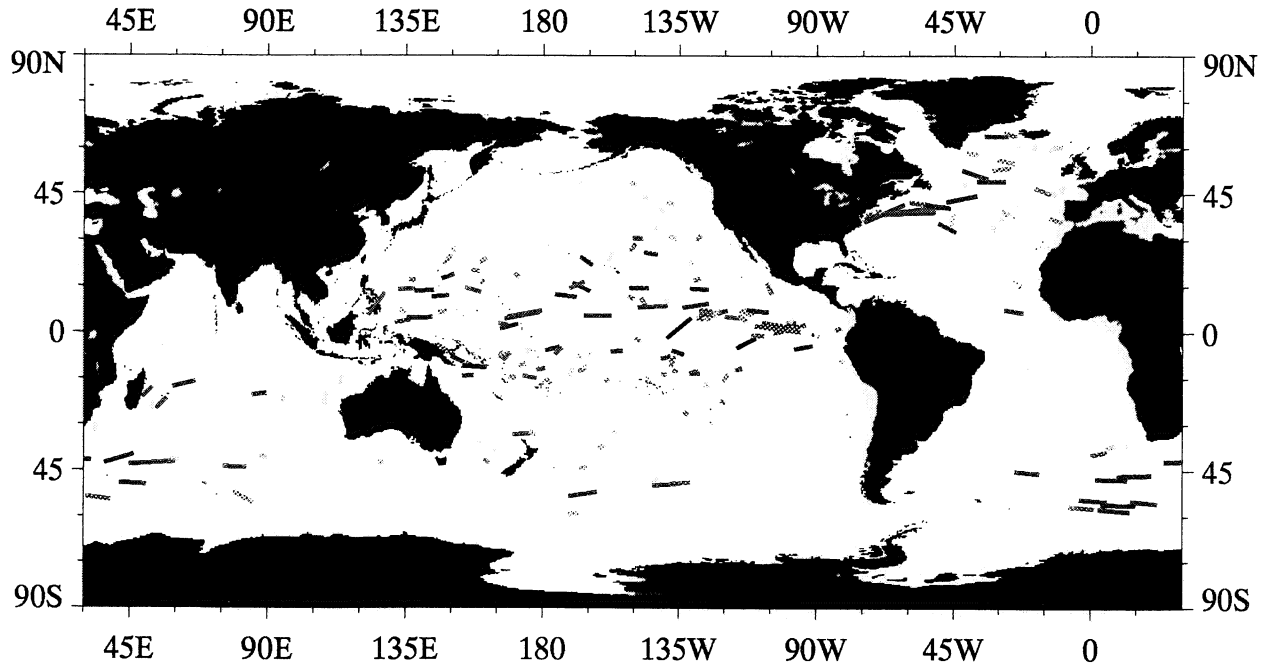
45E 90E 135E 180 135W 90W 45W 0
90N
45
0
45
90S
Zonal Speed, October 1990
-40 -30 -20 -10 0 10 20 30 40

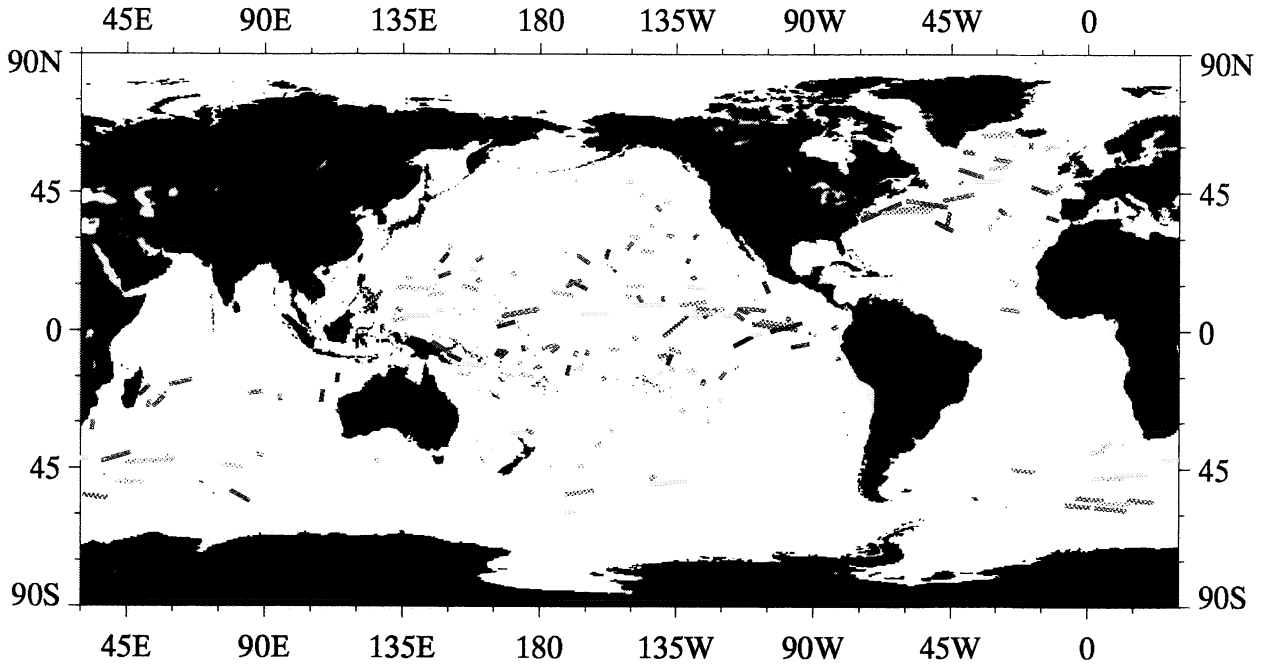
45E 90E 135E 180 135W 90W 45W 0
90N
45
0
45
90S
Meridional Speed, October 1990
-20 -15 -10 -5 0 5 10 15 20
ARGOS Buoy Drift, cm s-1

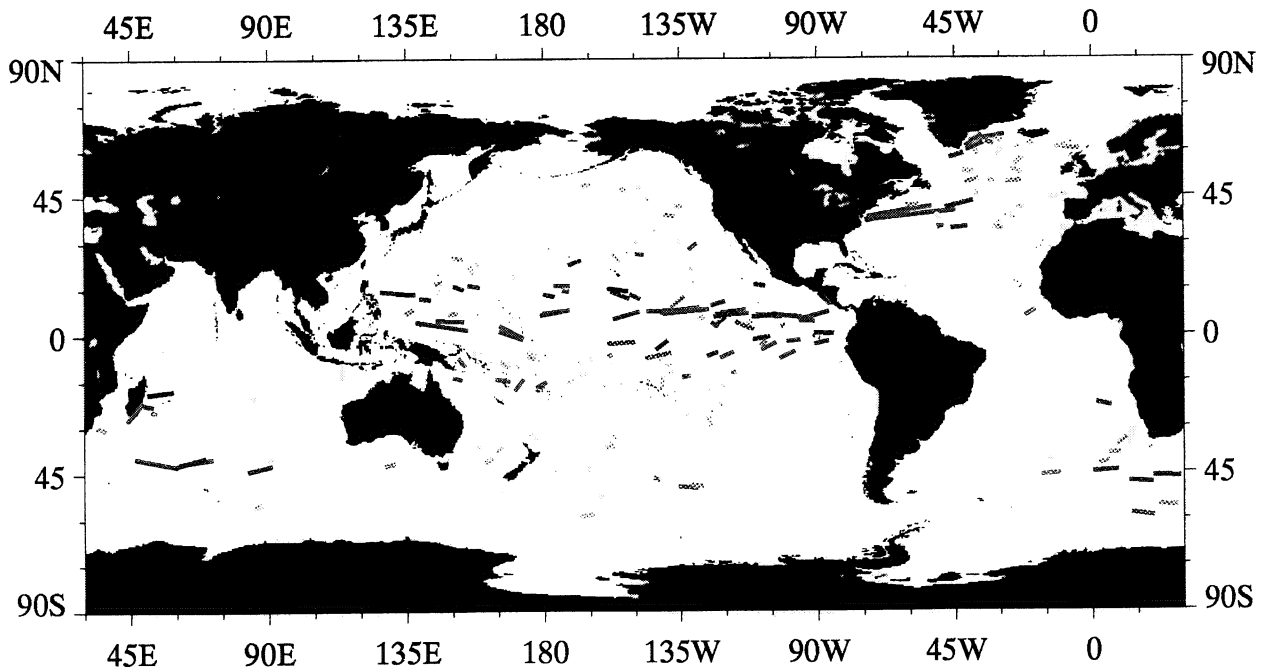


Zonal Speed, November 1990

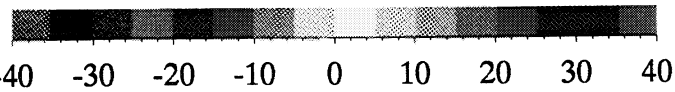


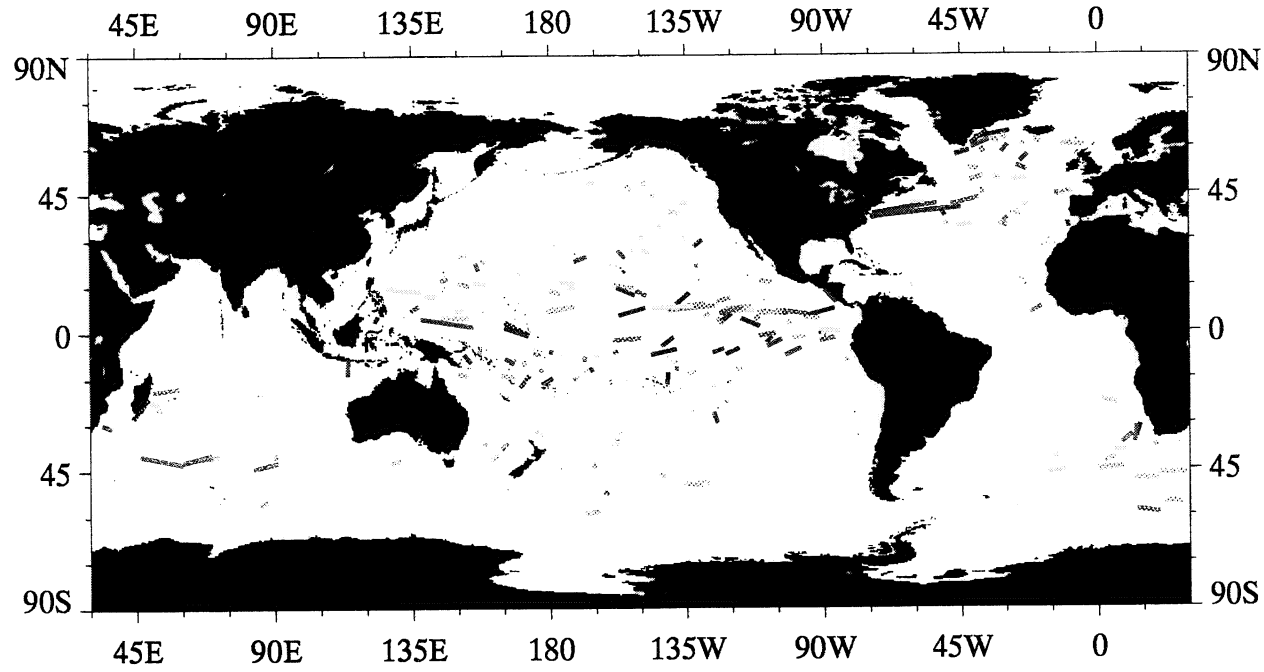


Meridional Speed, November 1990

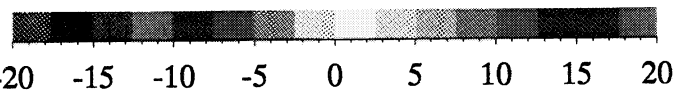


ARGOS Buoy Drift, cm $s^{-1}$

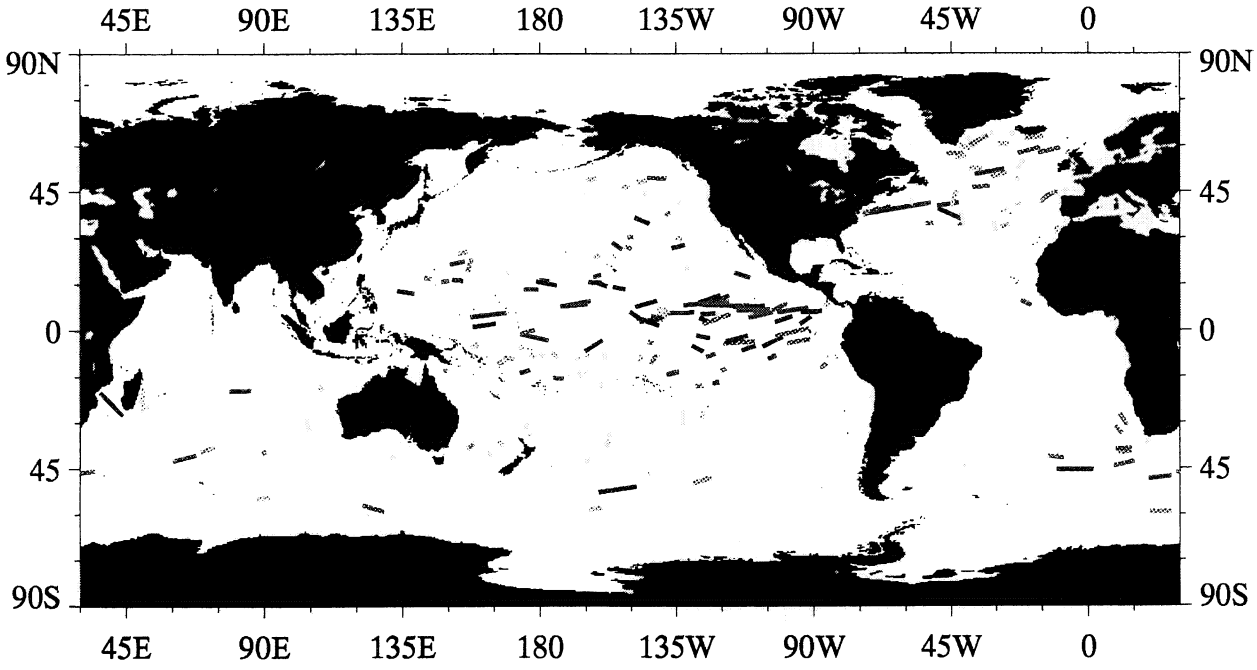
45E 90E 135E 180 135W 90W 45W 0
90N
45
0
45
90S
Zonal Speed, December 1990
-40 -30 -20 -10 0 10 20 30 40

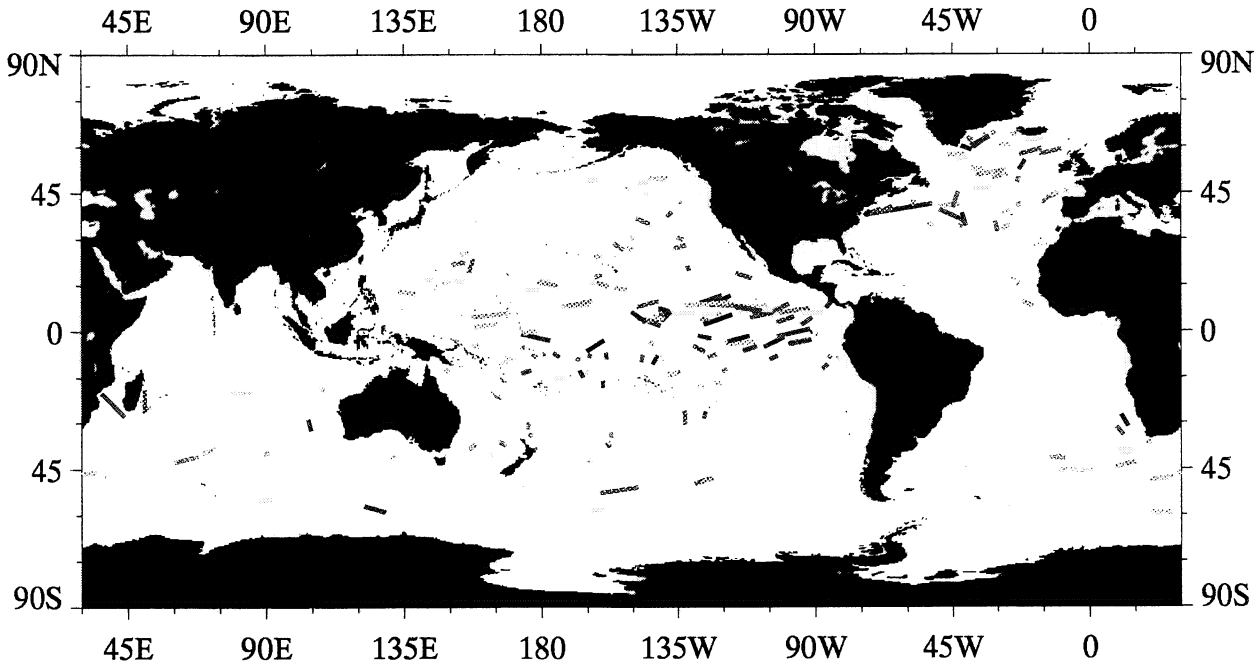
45E 90E 135E 180 135W 90W 45W 0
90N
45
0
45
90S
Meridional Speed, December 1990
-20 -15 -10 -5 0 5 10 15 20
ARGOS Buoy Drift, cm s-1

A6.

Annual Mean and Sampling Distribution of AVHRR/2 Sea Surface Temperature

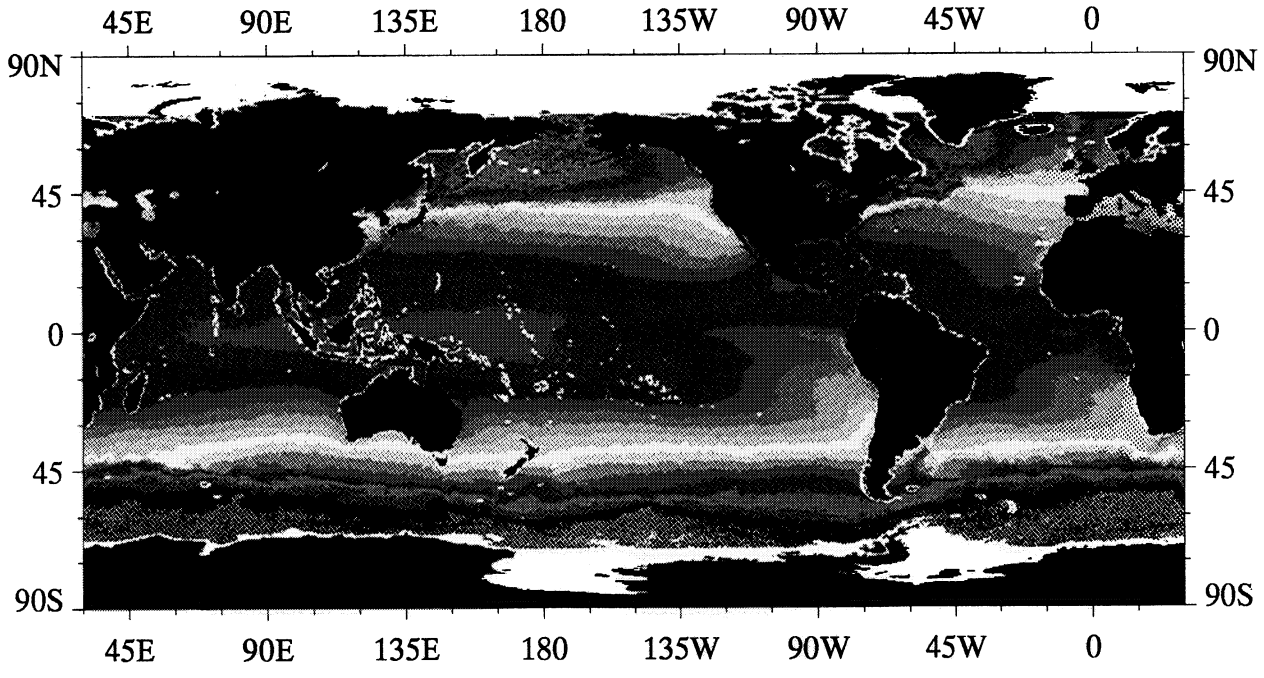


Annual Mean 1990

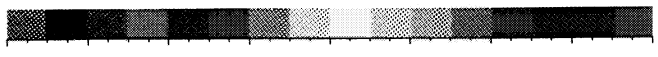


AVHRR Sea Surface Temperature, °C

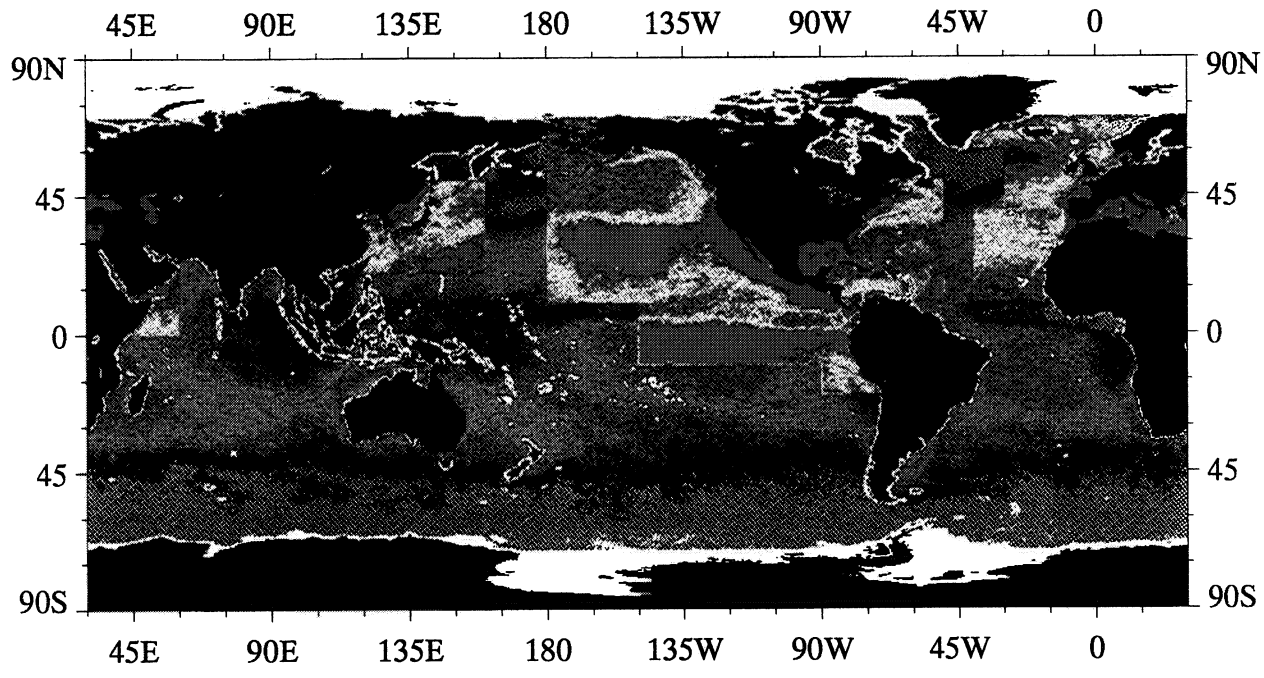


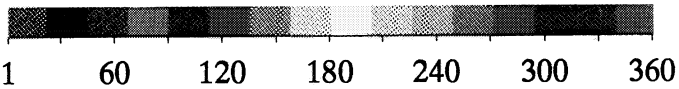


Number of Sea Surface Temperature Values per Pixel During 1990, max = 2059

A7

28-Day Mean AVHRR/2 Sea Surface Temperature

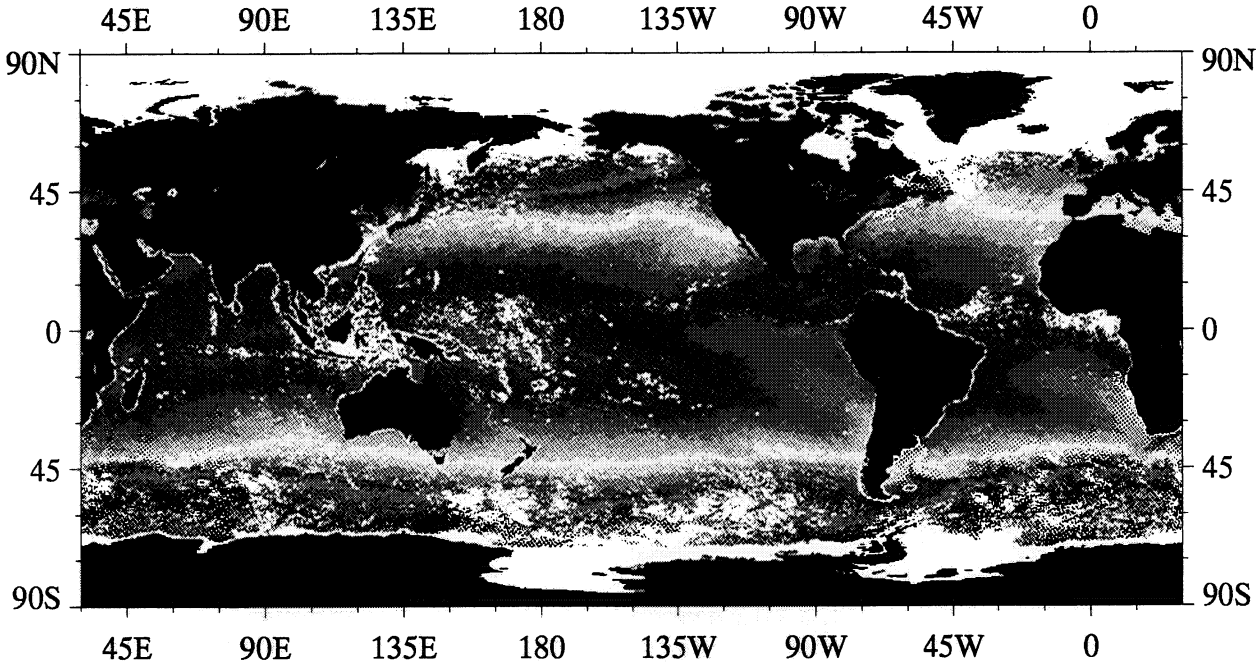


4 January to 31 January 1990

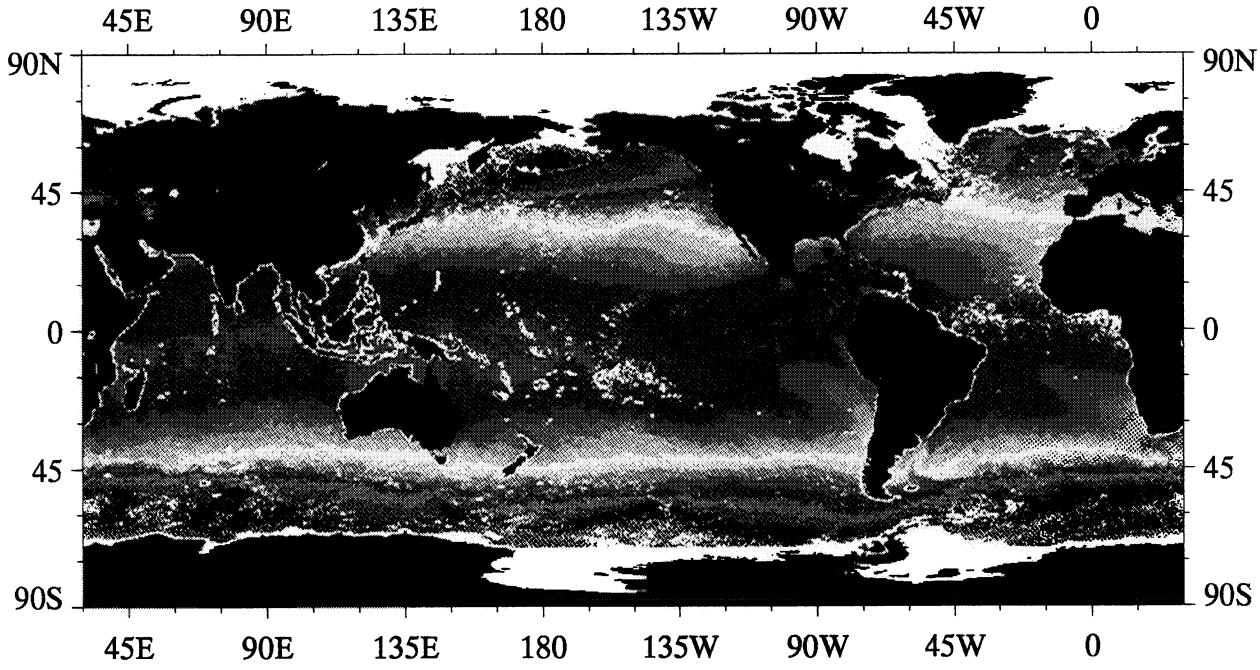


31 January to 28 February 1990

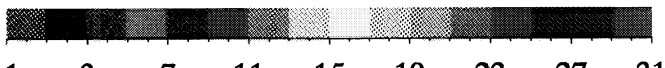


AVHRR Sea Surface Temperature, °C

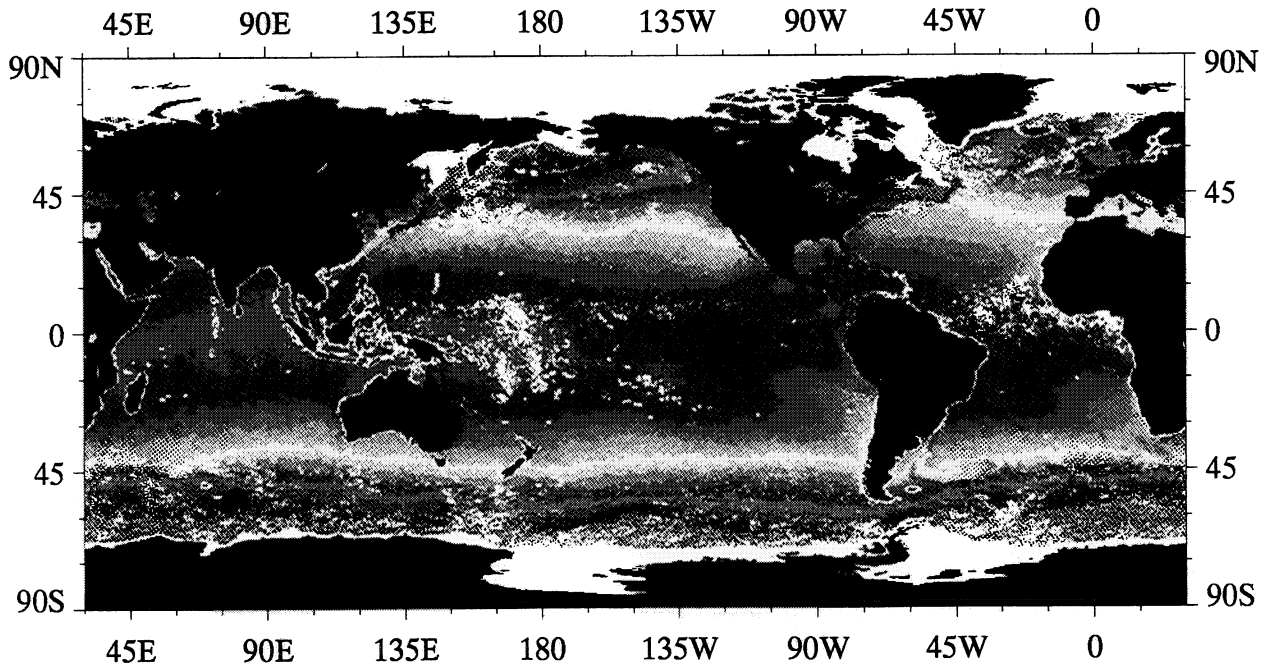


1 March to 28 March 1990

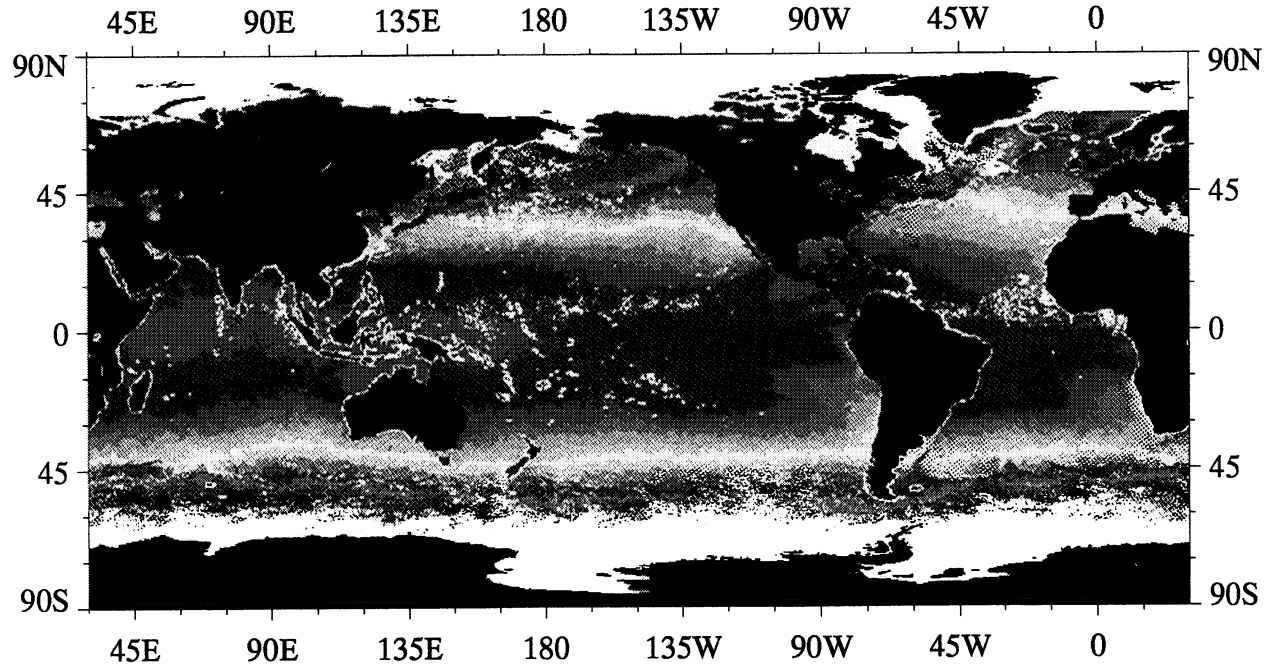


29 March to 24 April 1990

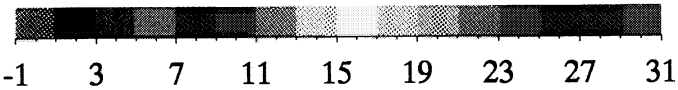


AVHRR Sea Surface Temperature, °C

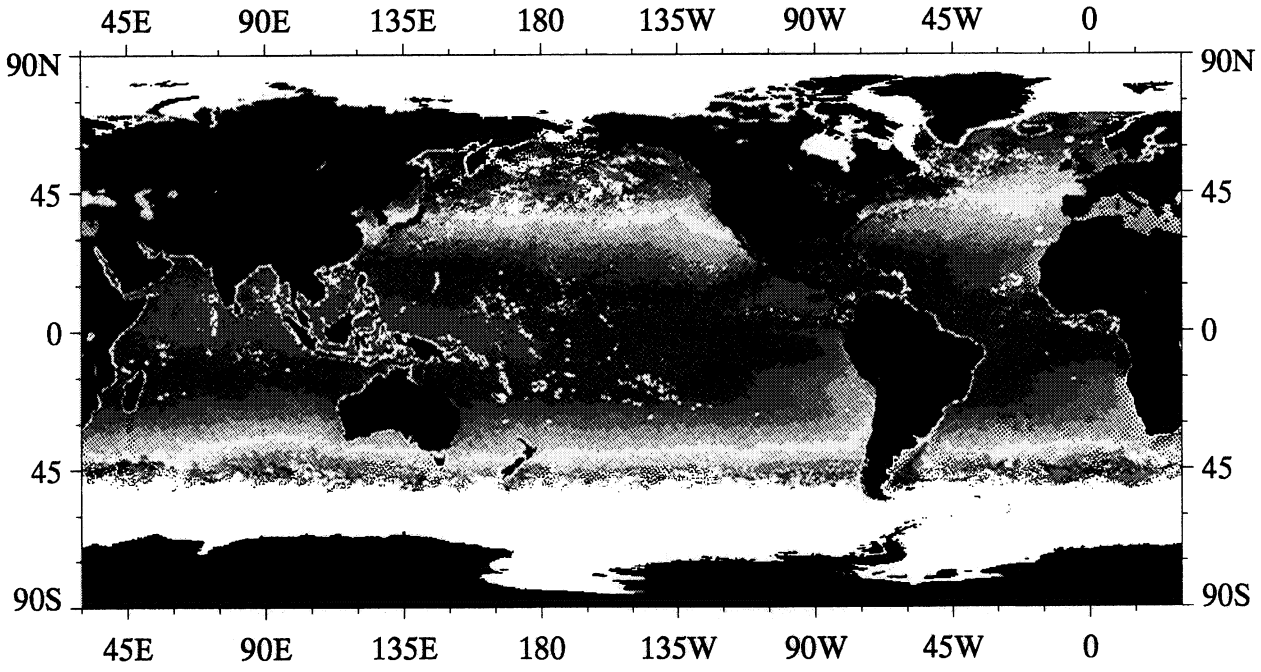


3 May to 30 May 1990

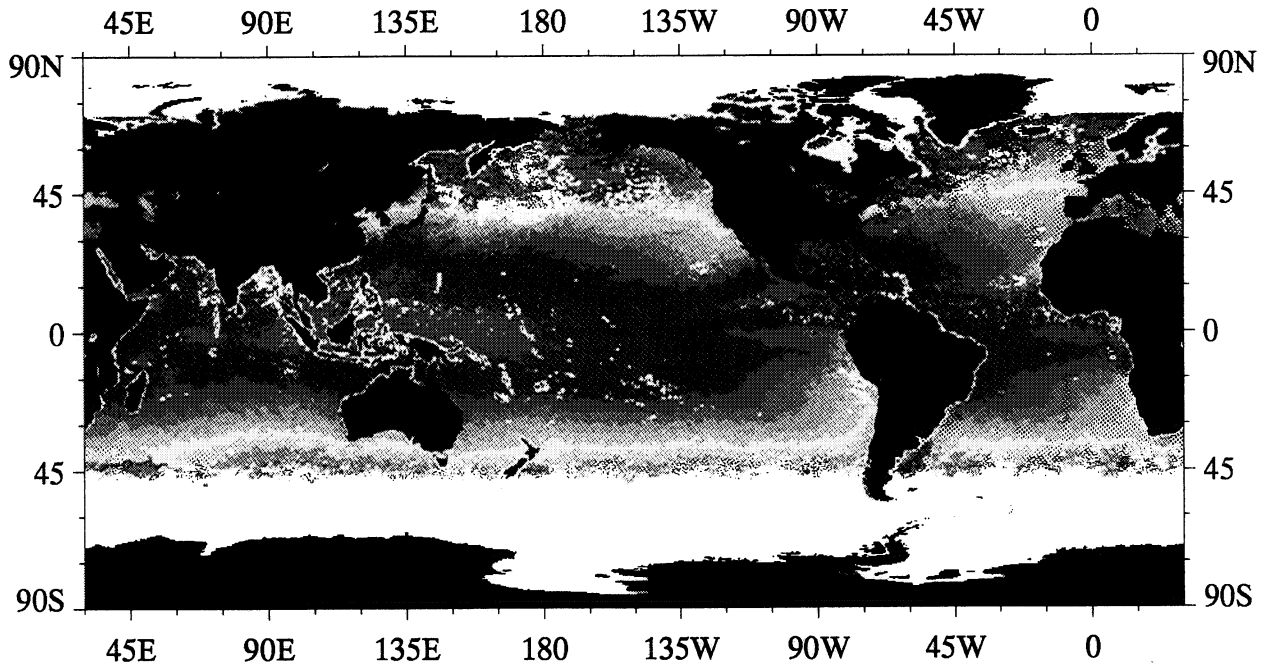


31 May to 27 June 1990


AVHRR Sea Surface Temperature, °C

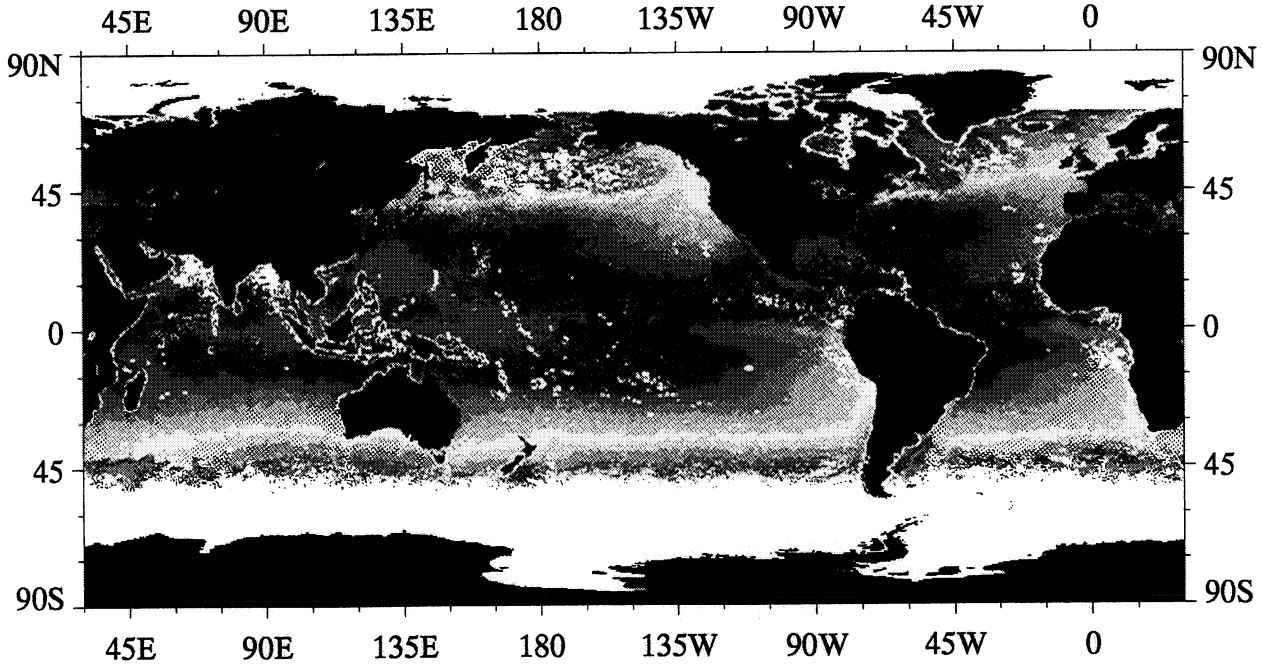


4 July to 1 August 1990

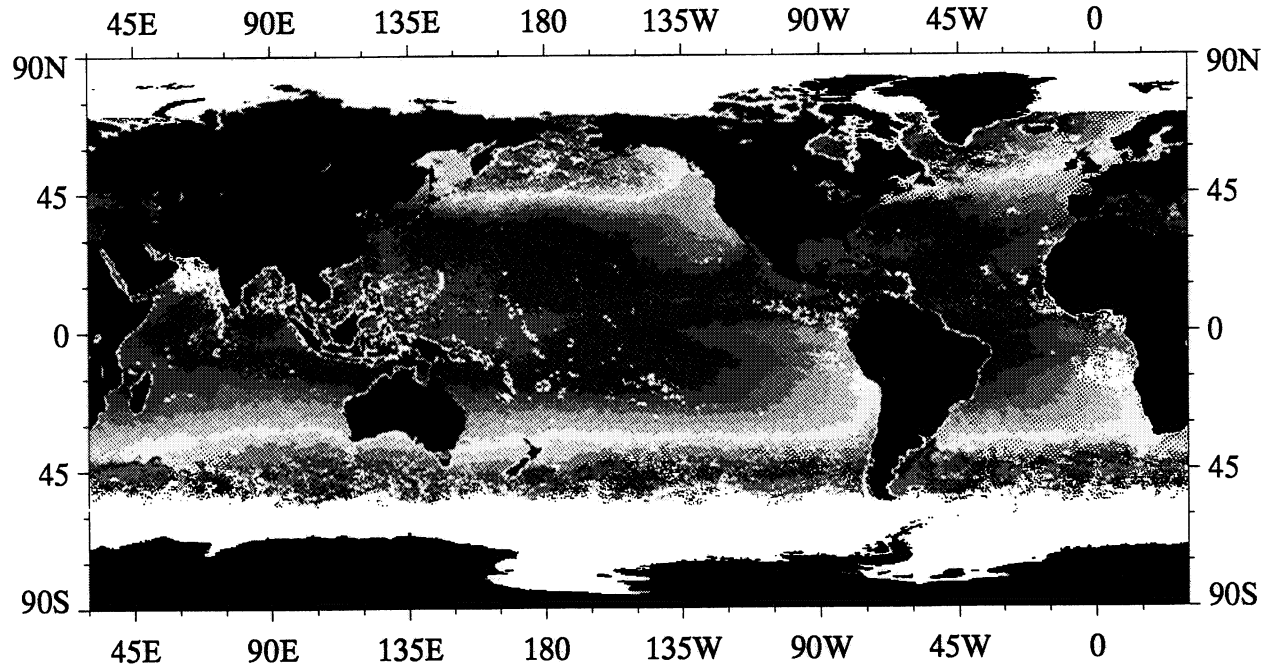


1 August to 29 August 1990

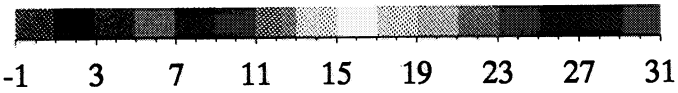


AVHRR Sea Surface Temperature, °C

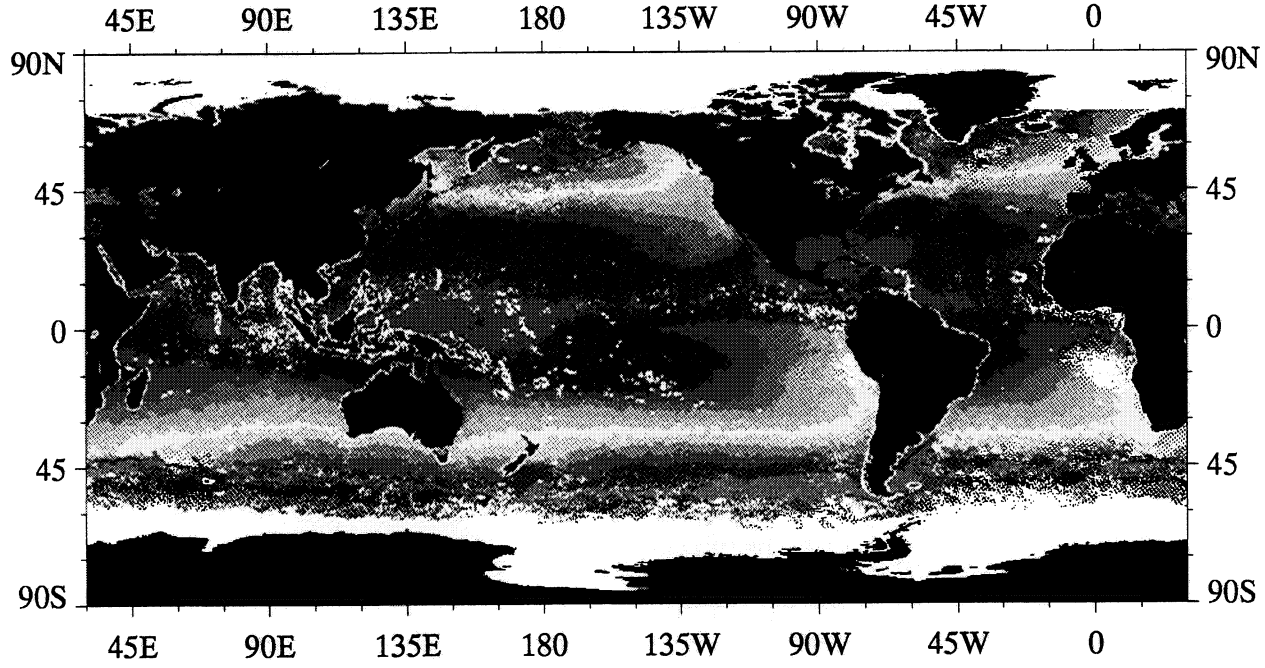


30 August to 26 September 1990

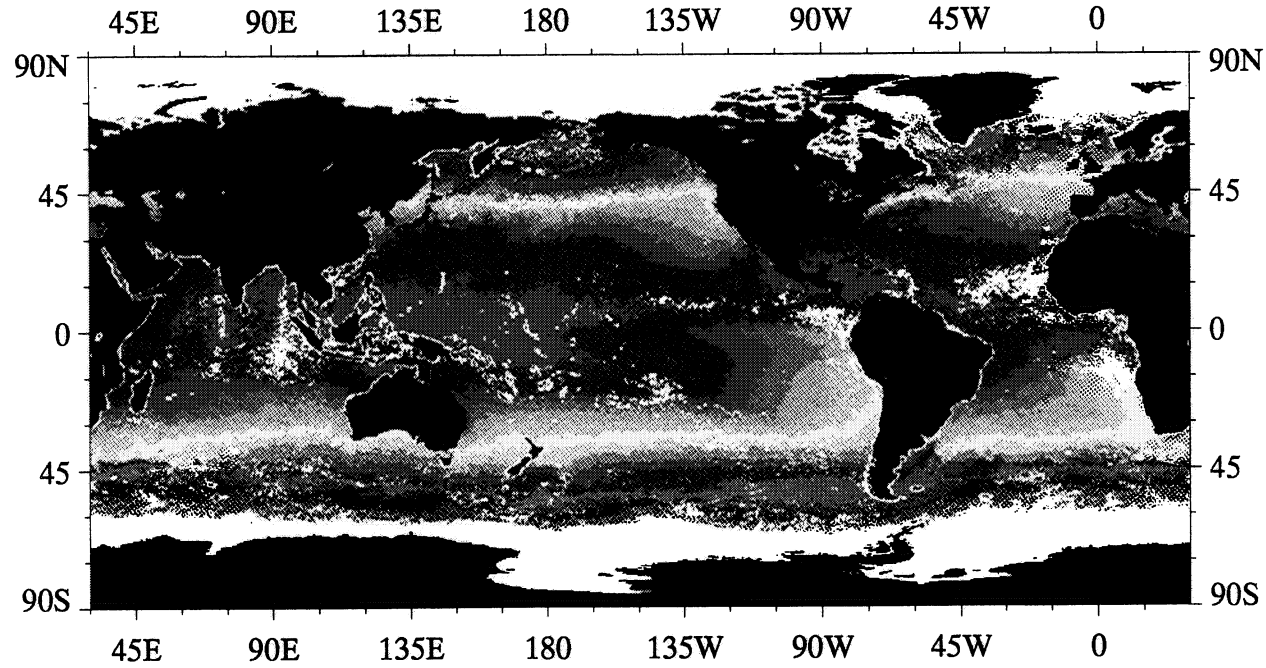


4 October to 31 October 1990

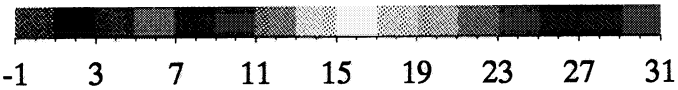


AVHRR Sea Surface Temperature, °C

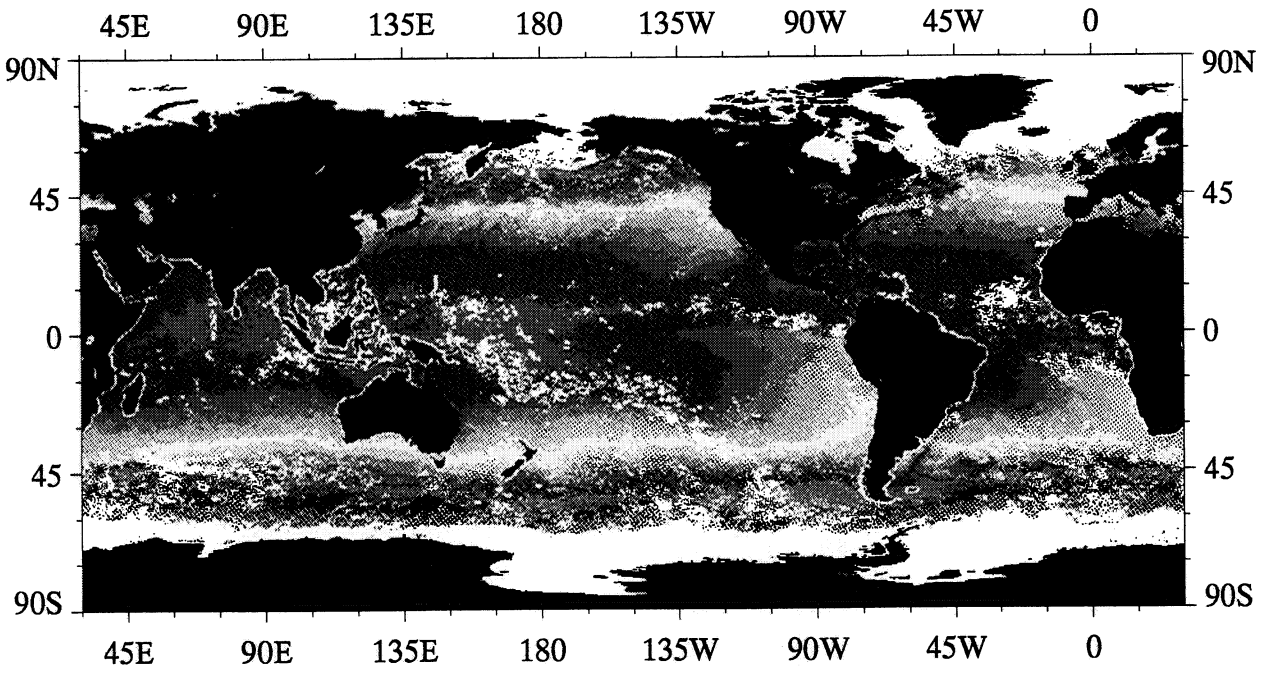


31 October to 28 November 1990

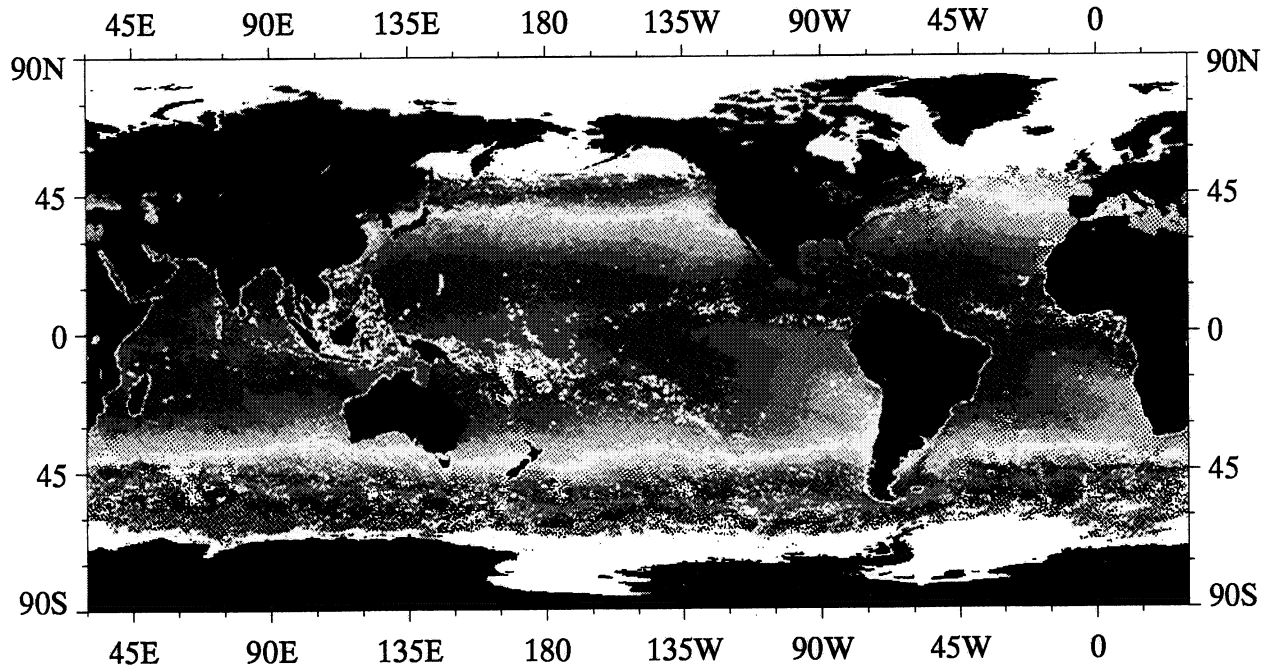


28 November to 26 December 1990

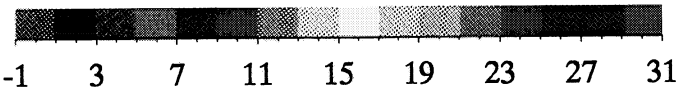


AVHRR Sea Surface Temperature, °C

A8

28-Day AVHRR/2 Sampling Distribution

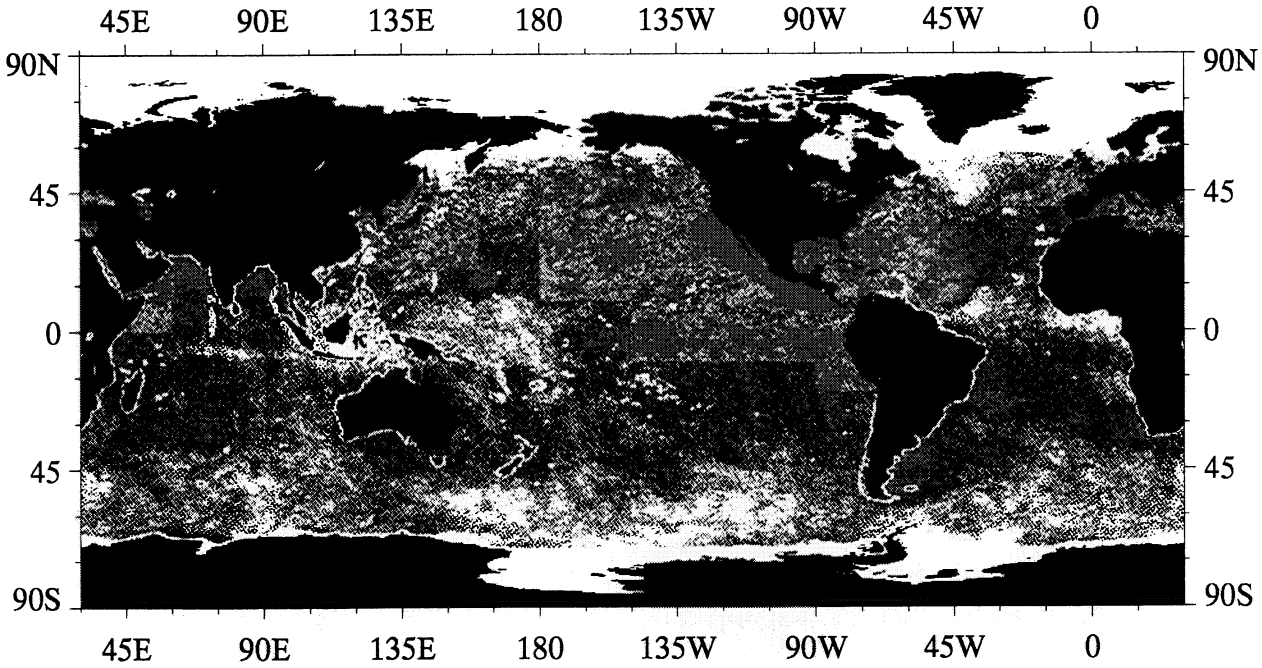


4 January to 31 January 1990, max = 172

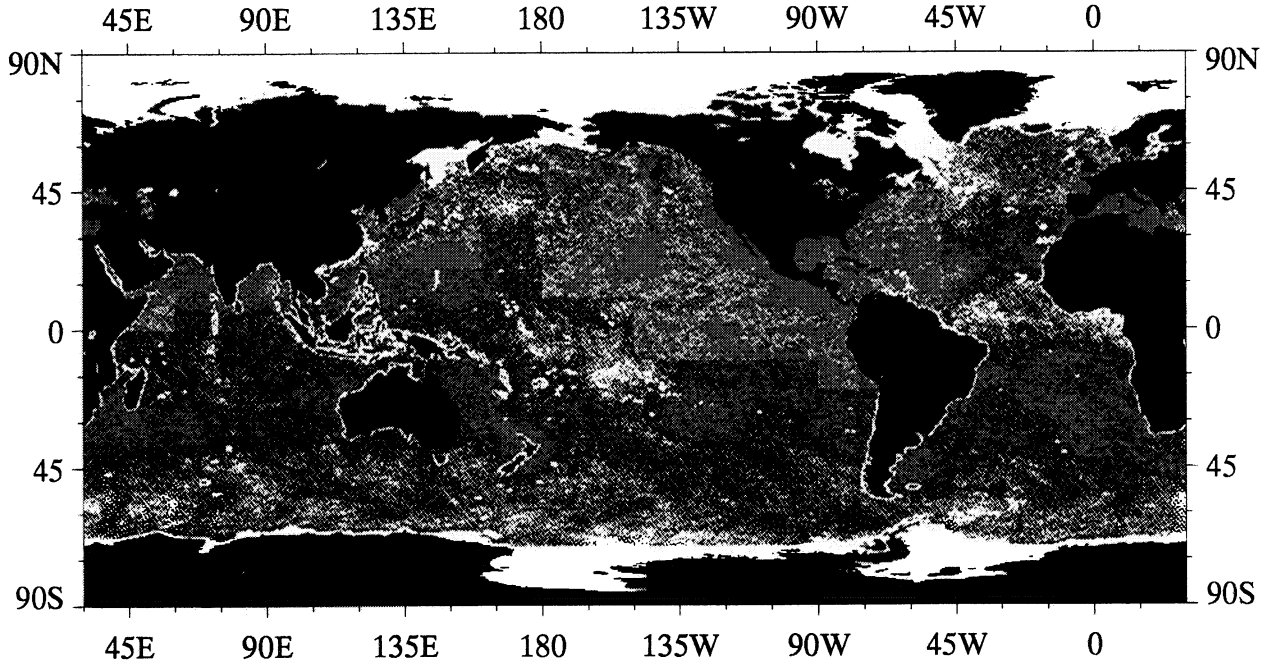


31 January to 28 February 1990, max = 201

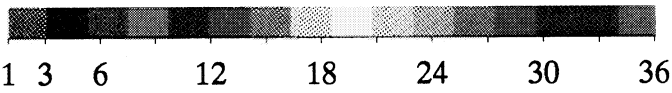


Number of AVHRR Sea Surface Temperature Values per Pixel

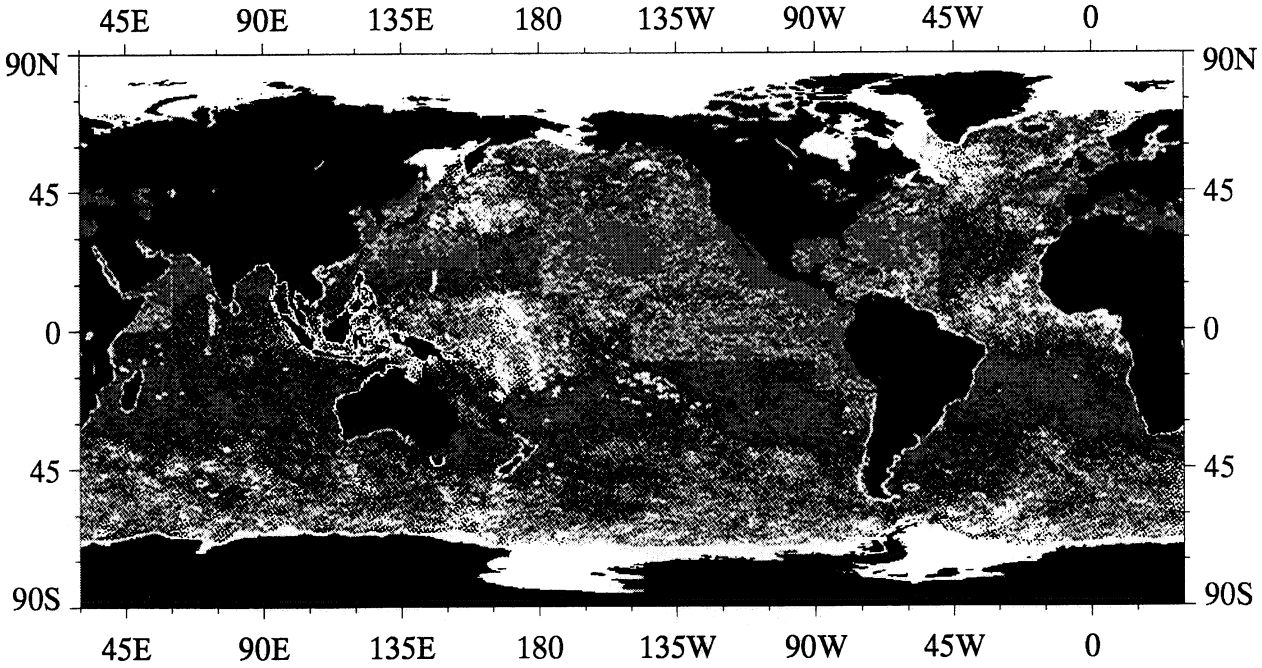


1 March to 28 March 1990, max = 154

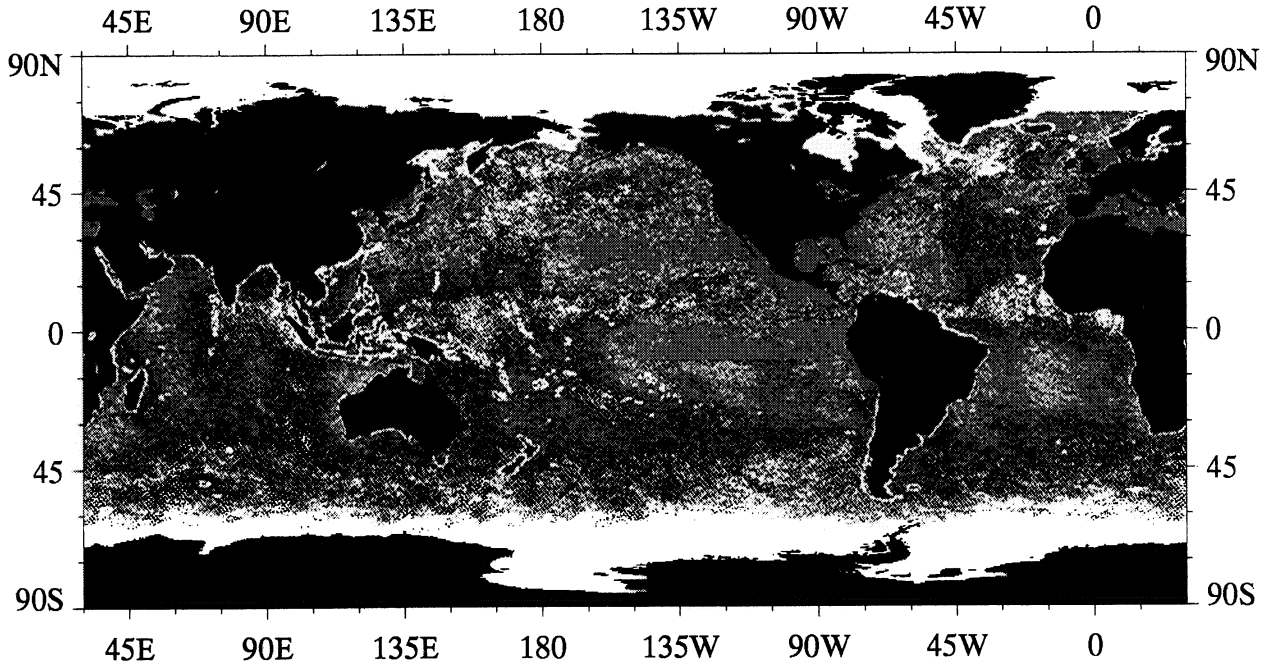


29 March to 24 April 1990, max = 217

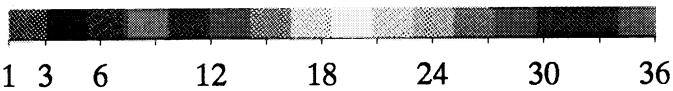


Number of AVHRR Sea Surface Temperature Values per Pixel

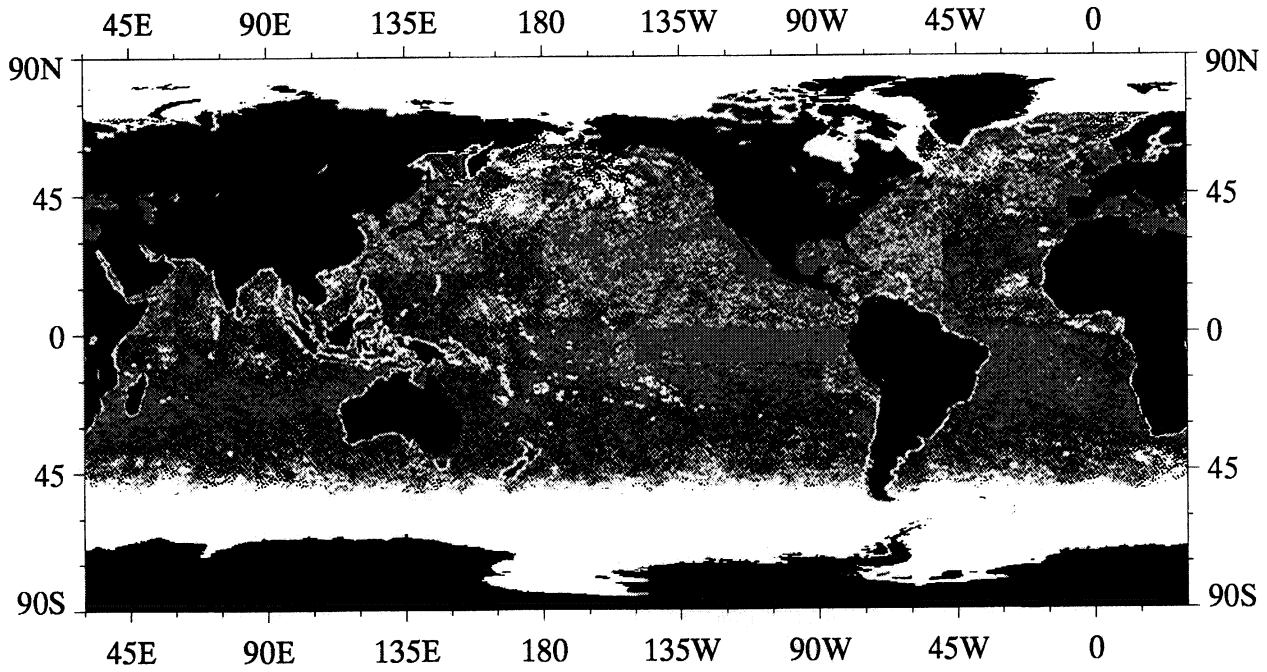


3 May to 30 May 1990, max = 184

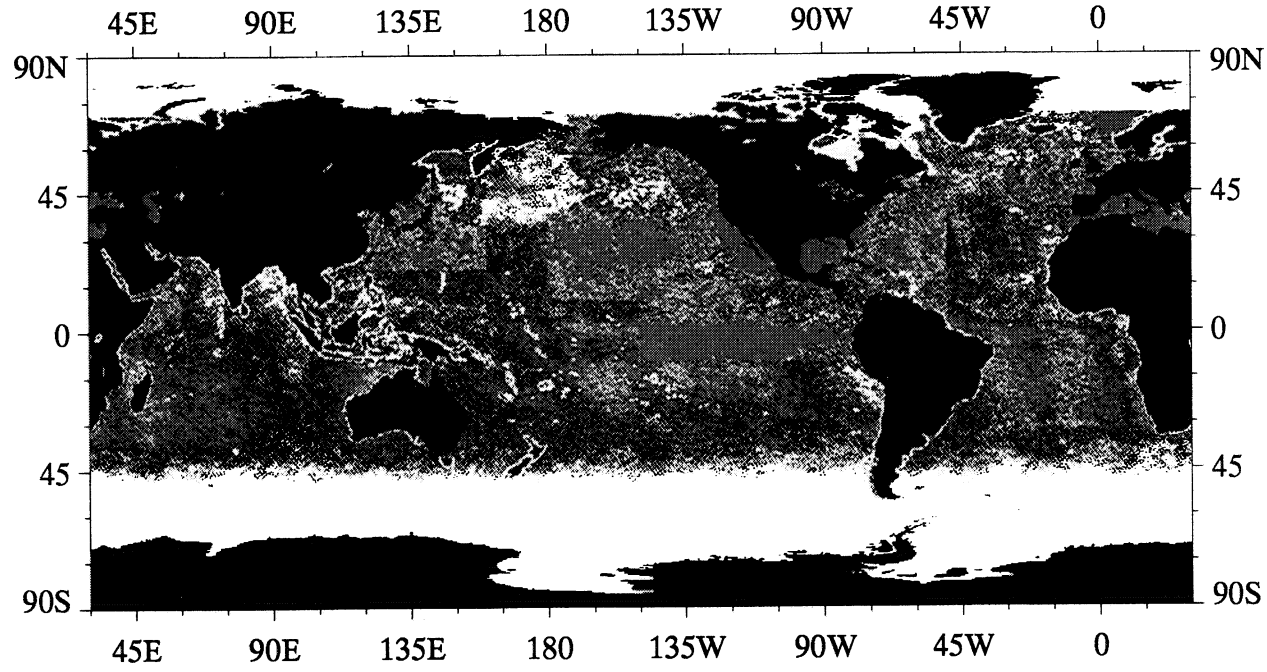


31 May to 27 June 1990, max = 246

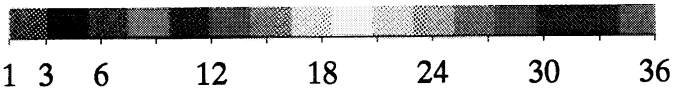


Number of AVHRR Sea Surface Temperature Values per Pixel

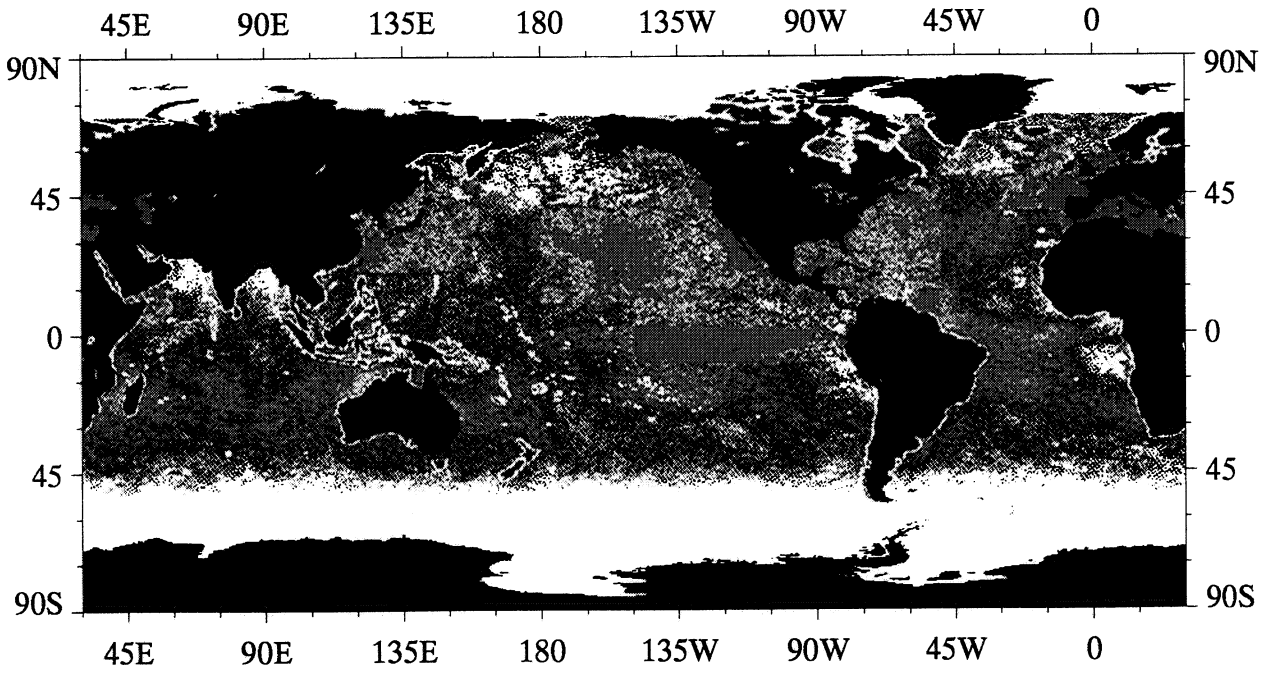


4 July to 1 August 1990, max = 208

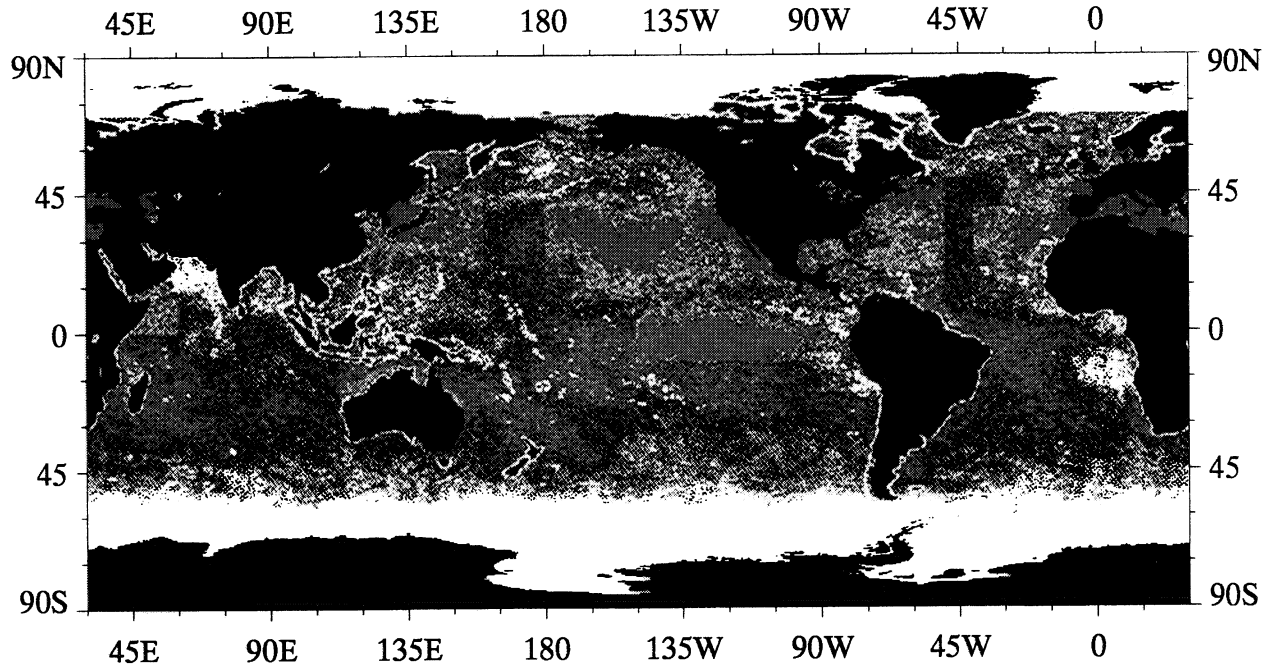


1 August to 29 August 1990, max = 199

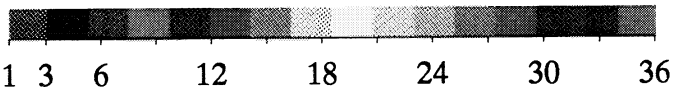


Number of AVHRR Sea Surface Temperature Values per Pixel

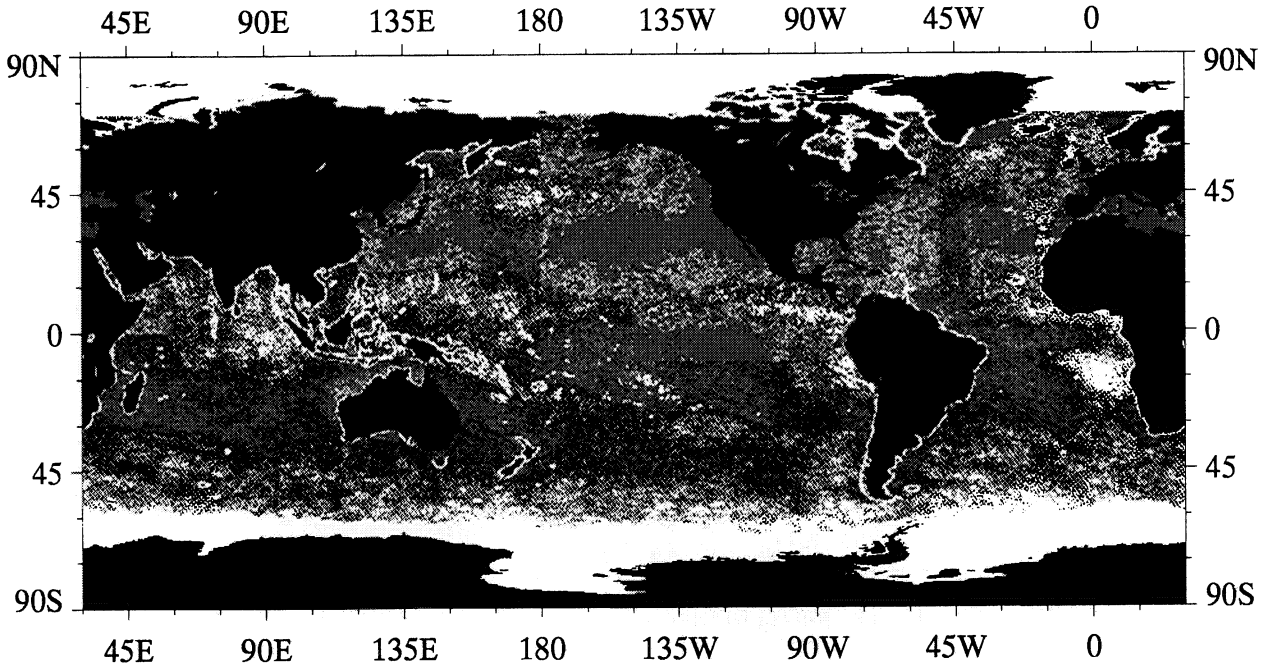


30 August to 26 September 1990, max = 195

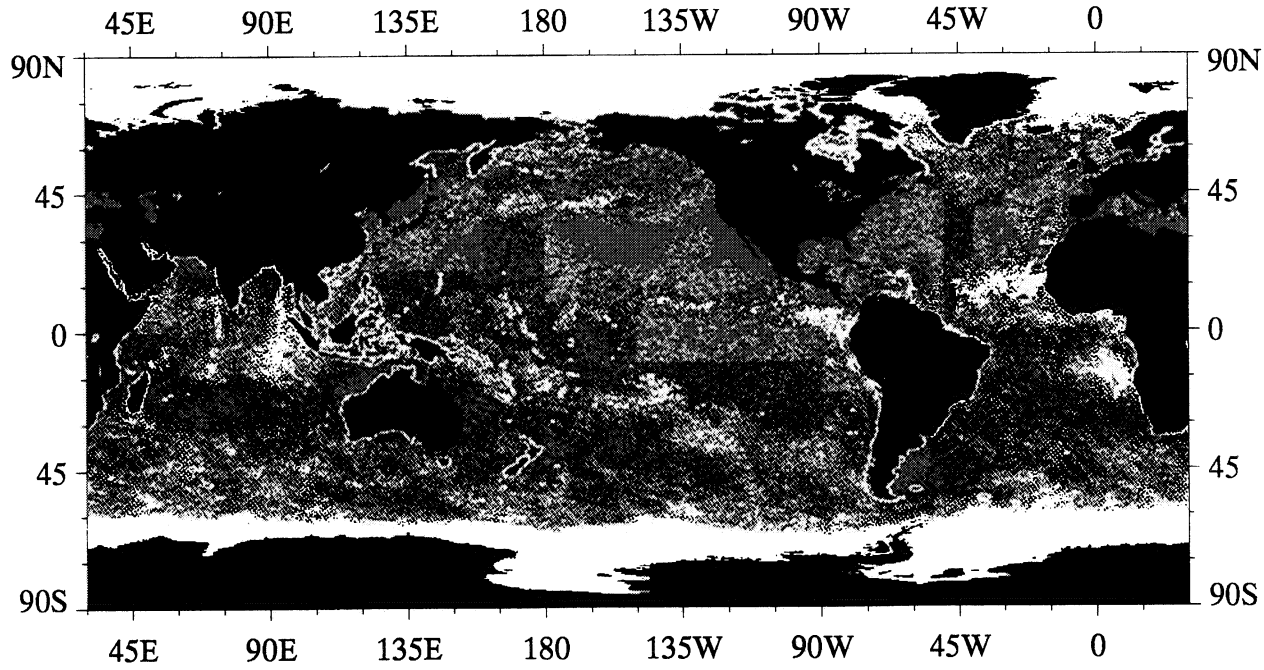


4 October to 31 October 1990, max = 267

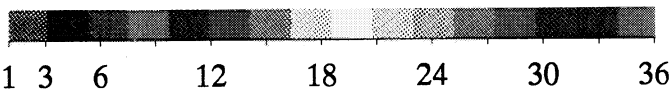


Number of AVHRR Sea Surface Temperature Values per Pixel

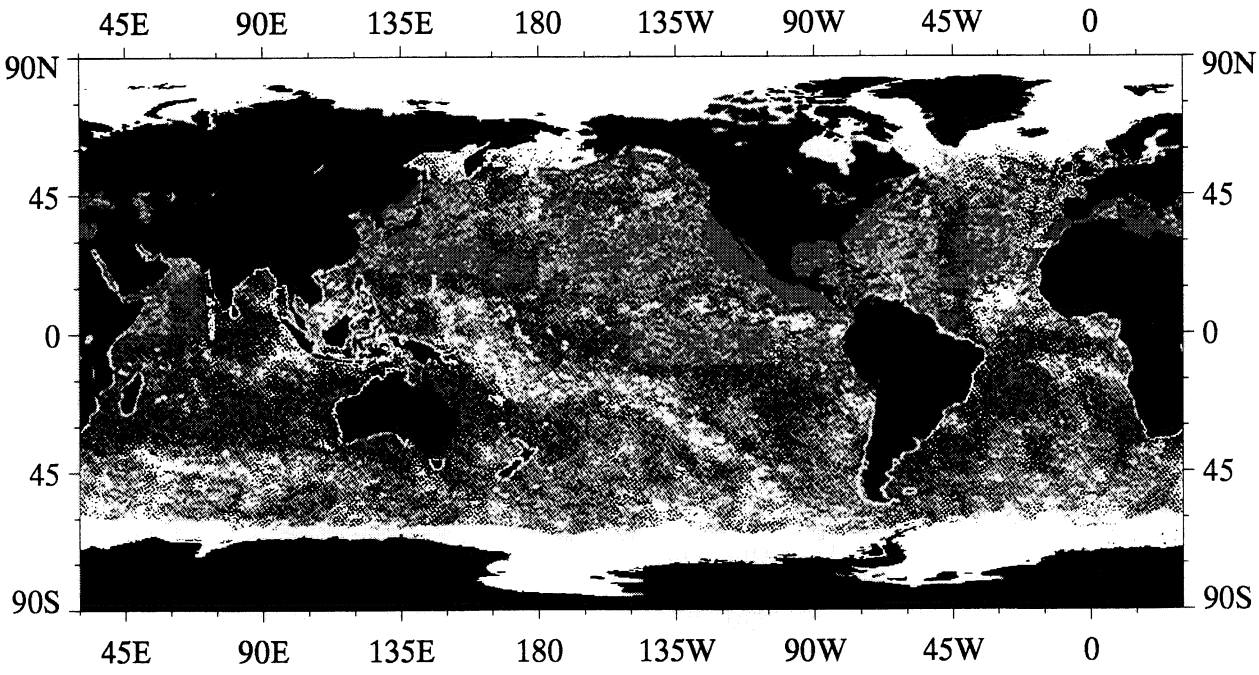


31 October to 28 November 1990, max = 179

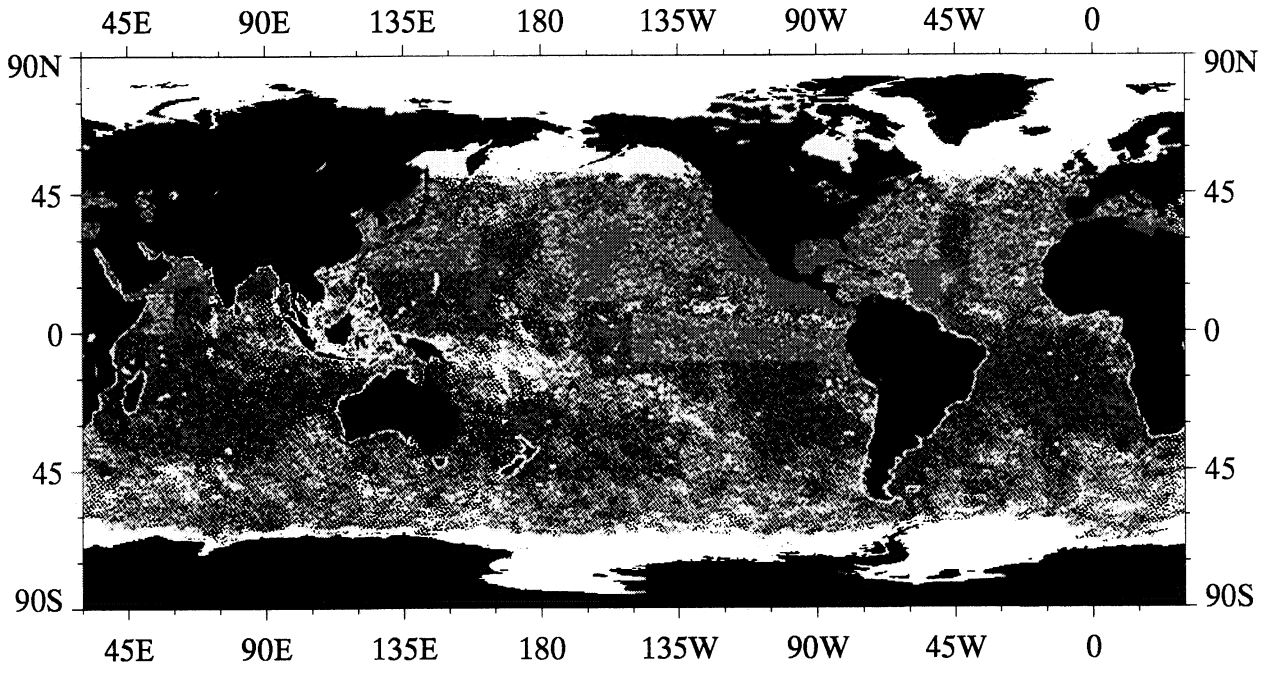


28 November to 26 December 1990, max = 186

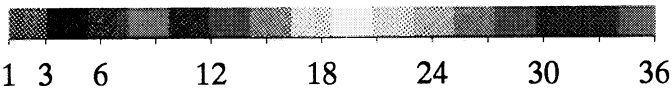


Number of AVHRR Sea Surface Temperature Values per Pixel

A9

Annual Mean ECMWF Surface Wind Components

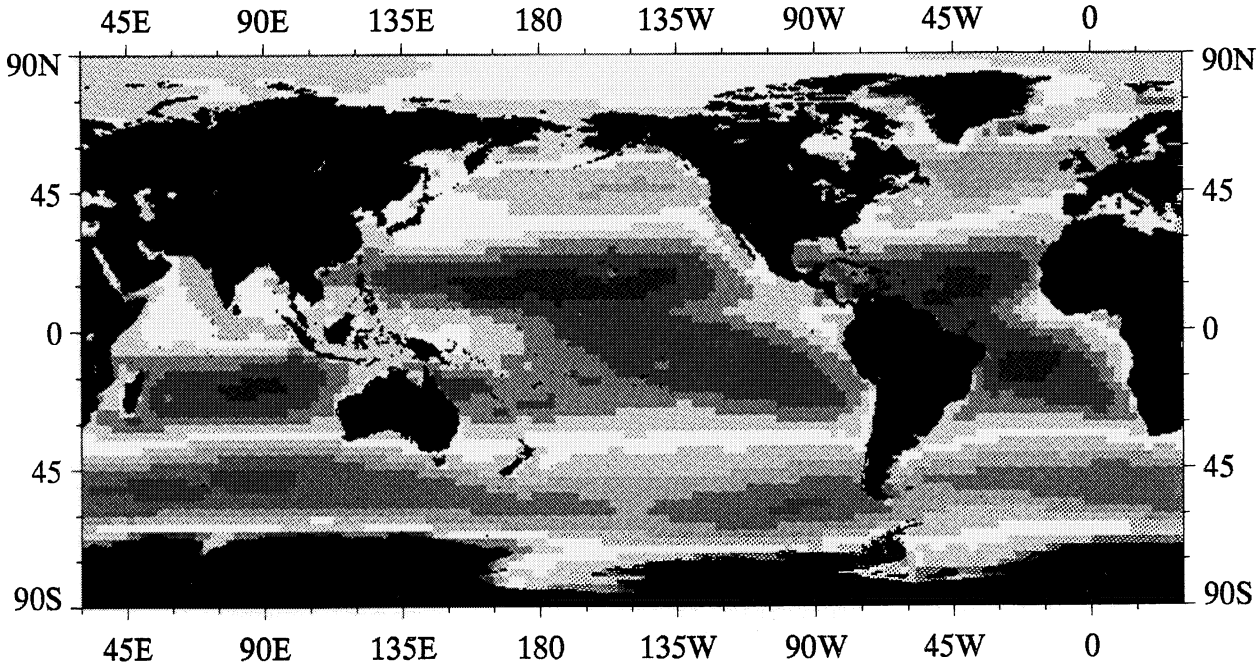


Zonal Wind Speed, Annual Mean 1990

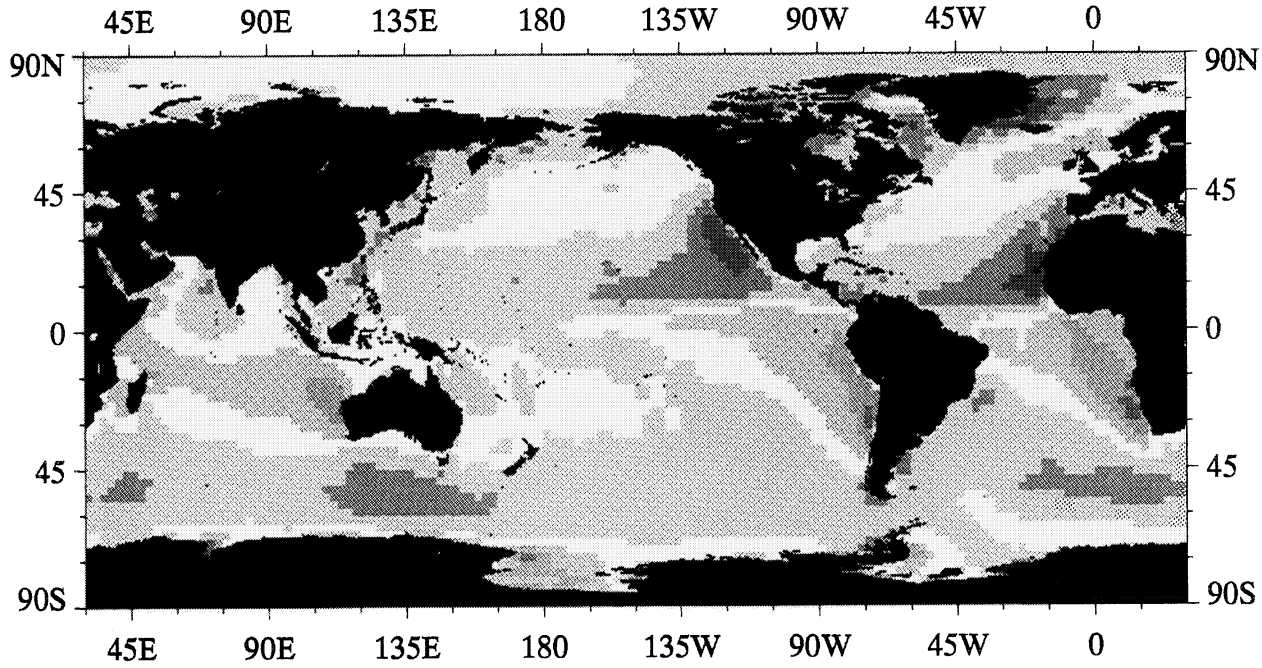


Meridional Wind Speed, Annual Mean 1990

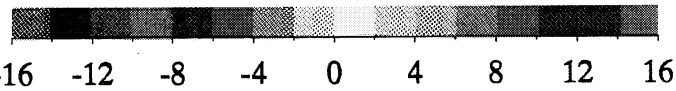


ECMWF 10 m Wind Speed, m $s^{-1}$

A10

Monthly Mean ECMWF Surface Wind Components

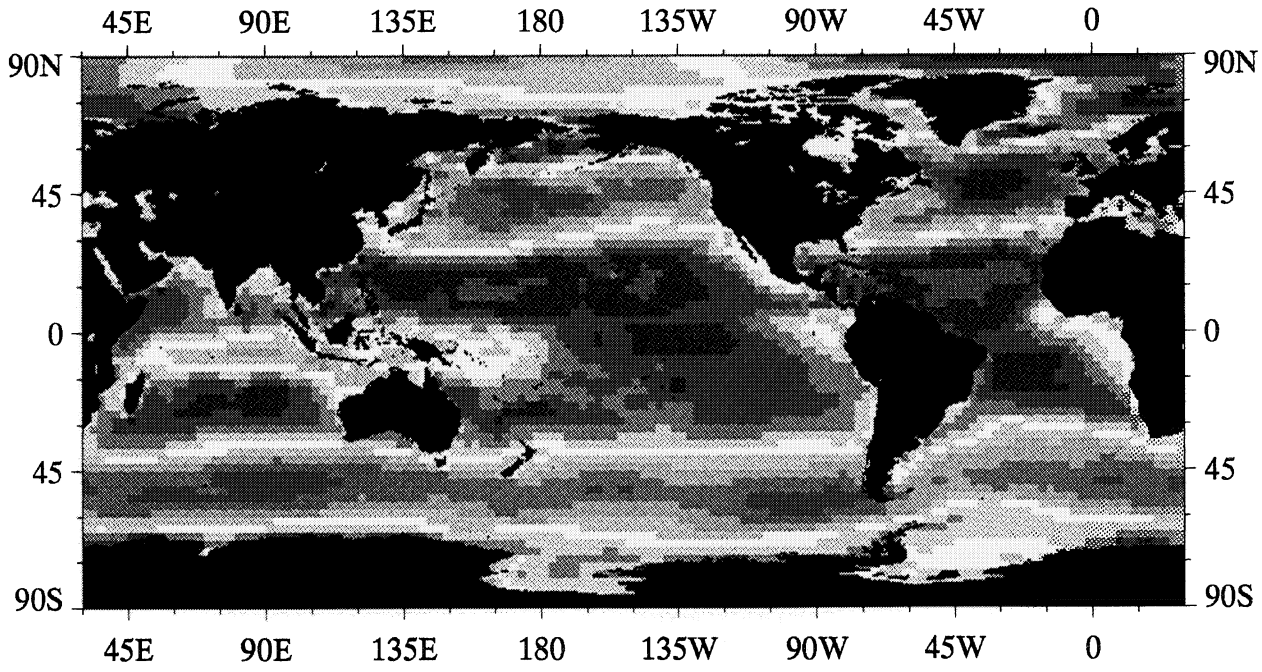


Zonal Wind Speed, January 1990

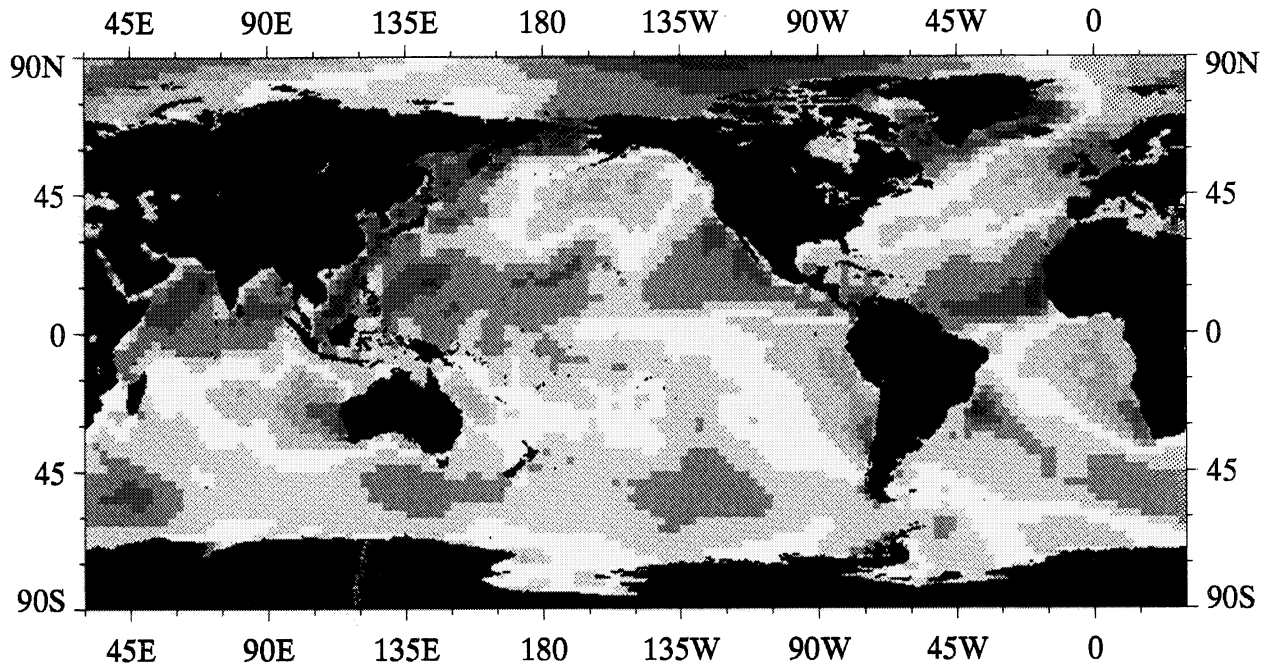


Meridional Wind Speed, January 1990

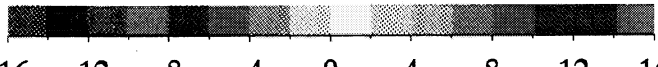


ECMWF 10 m Wind Speed, m $s^{-1}$

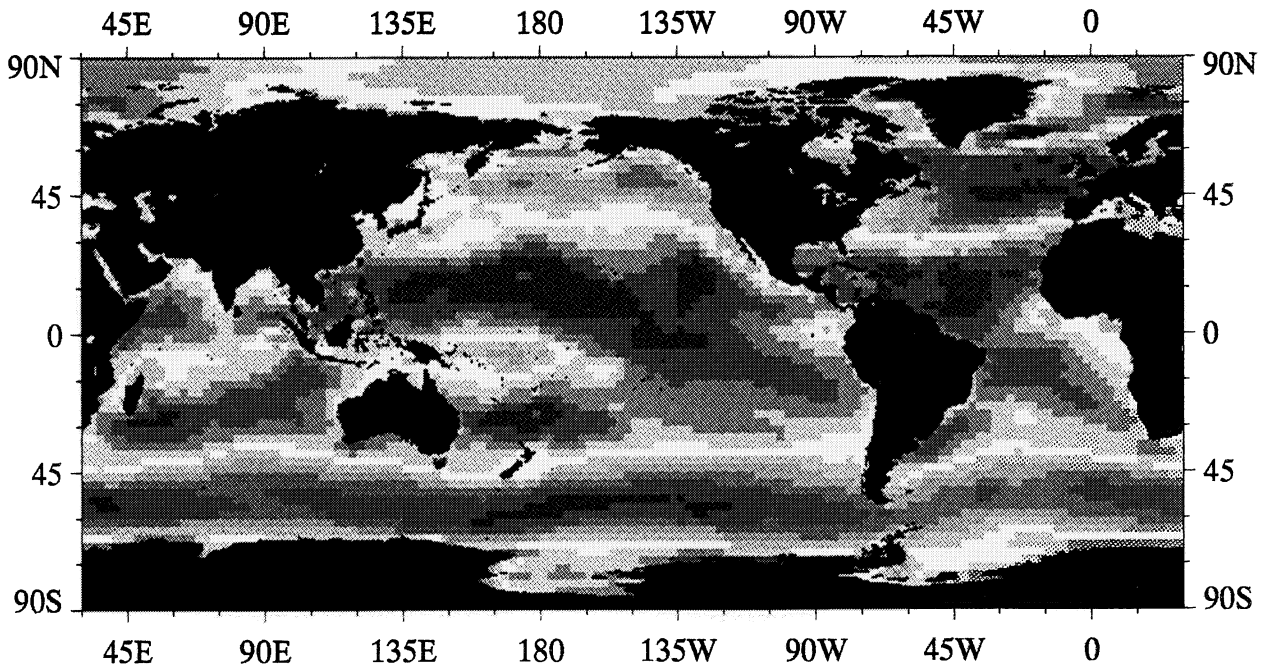


Zonal Wind Speed, February 1990

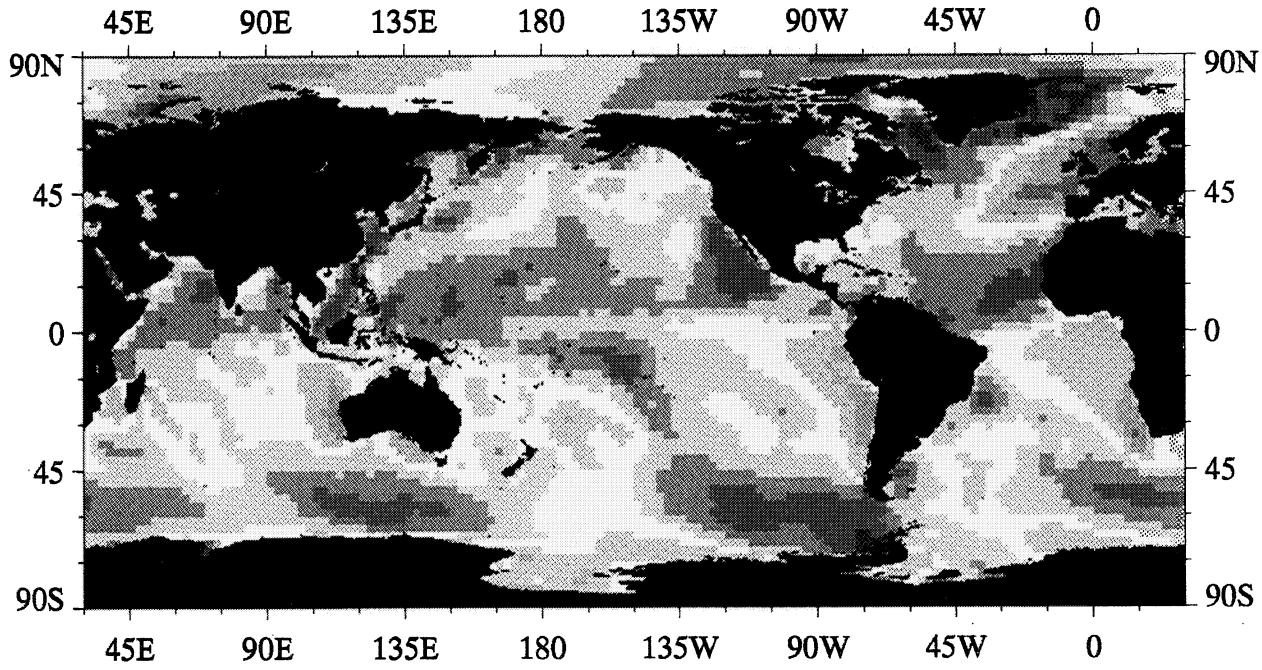


Meridional Wind Speed, February 1990

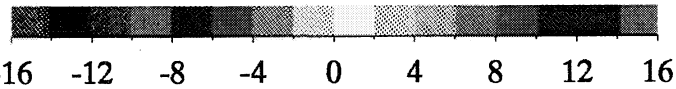


ECMWF 10 m Wind Speed, m $s^{-1}$

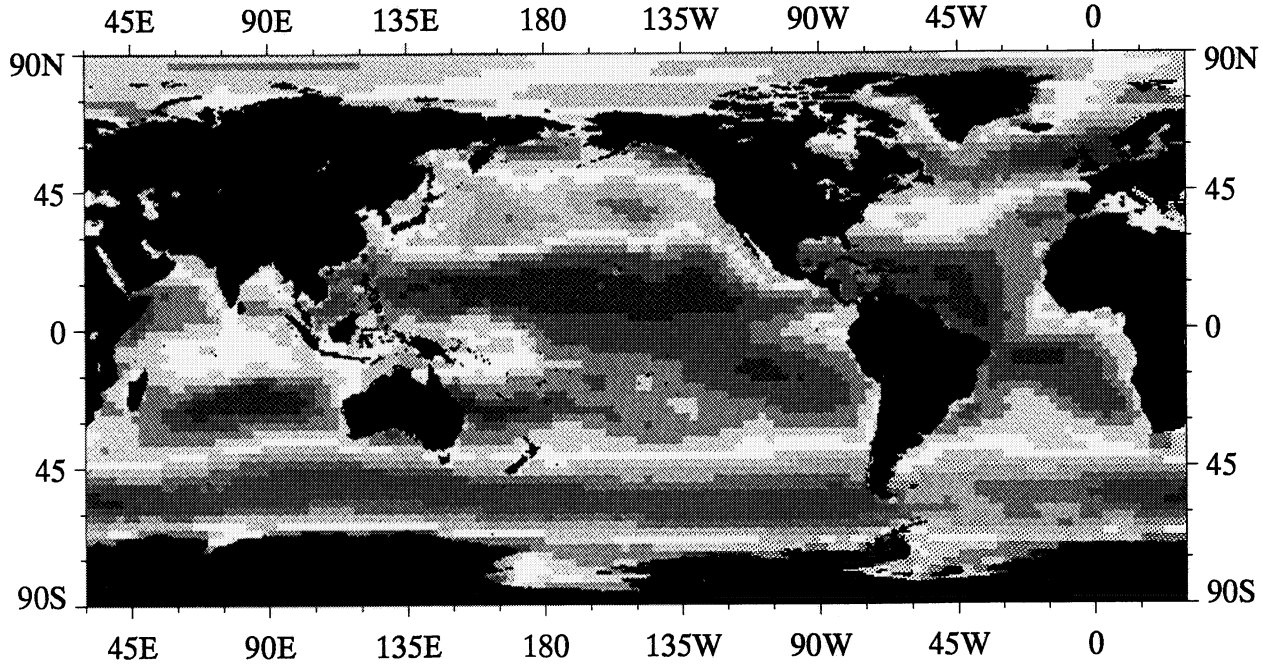


Zonal Wind Speed, March 1990

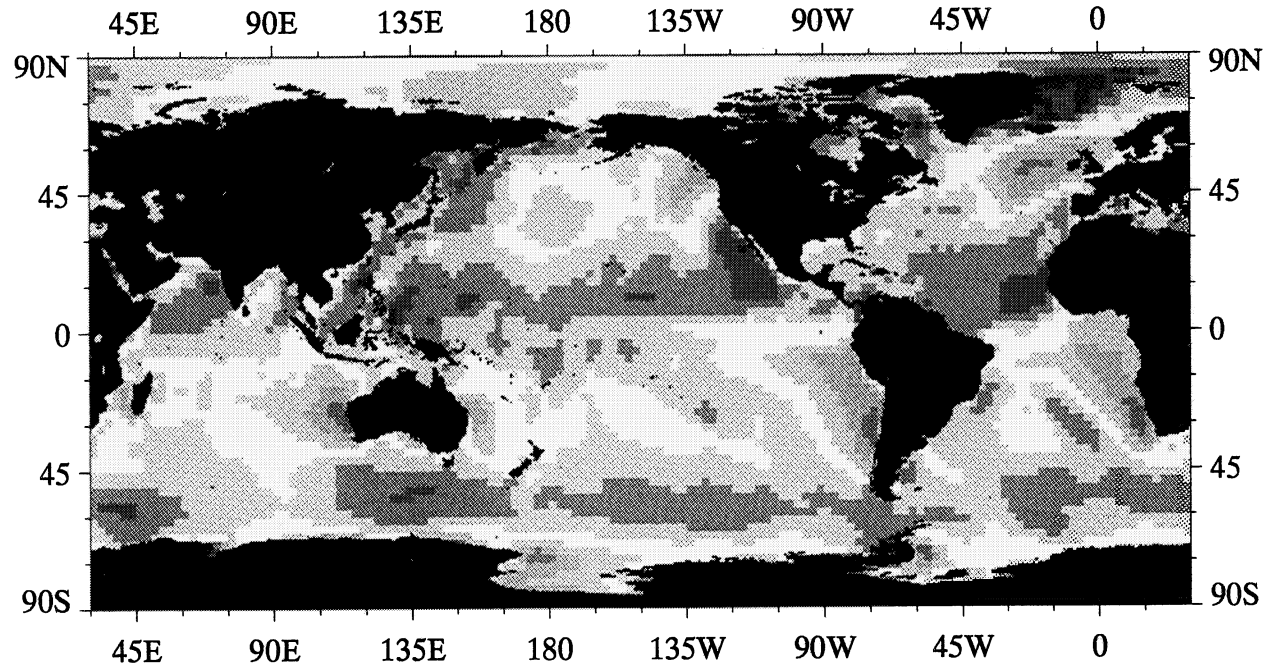


Meridional Wind Speed, March 1990

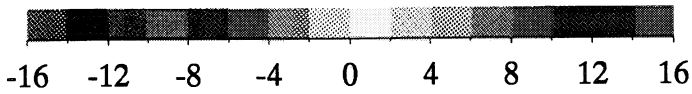


ECMWF 10 m Wind Speed, m $s^{-1}$

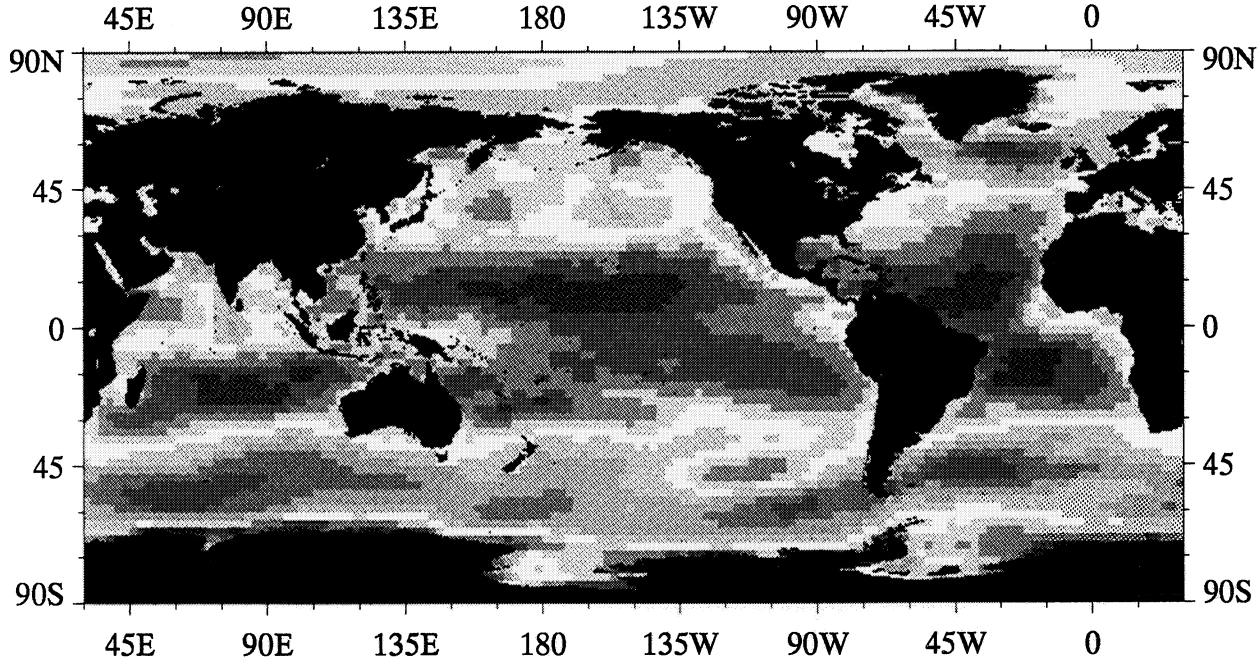


Zonal Wind Speed, April 1990

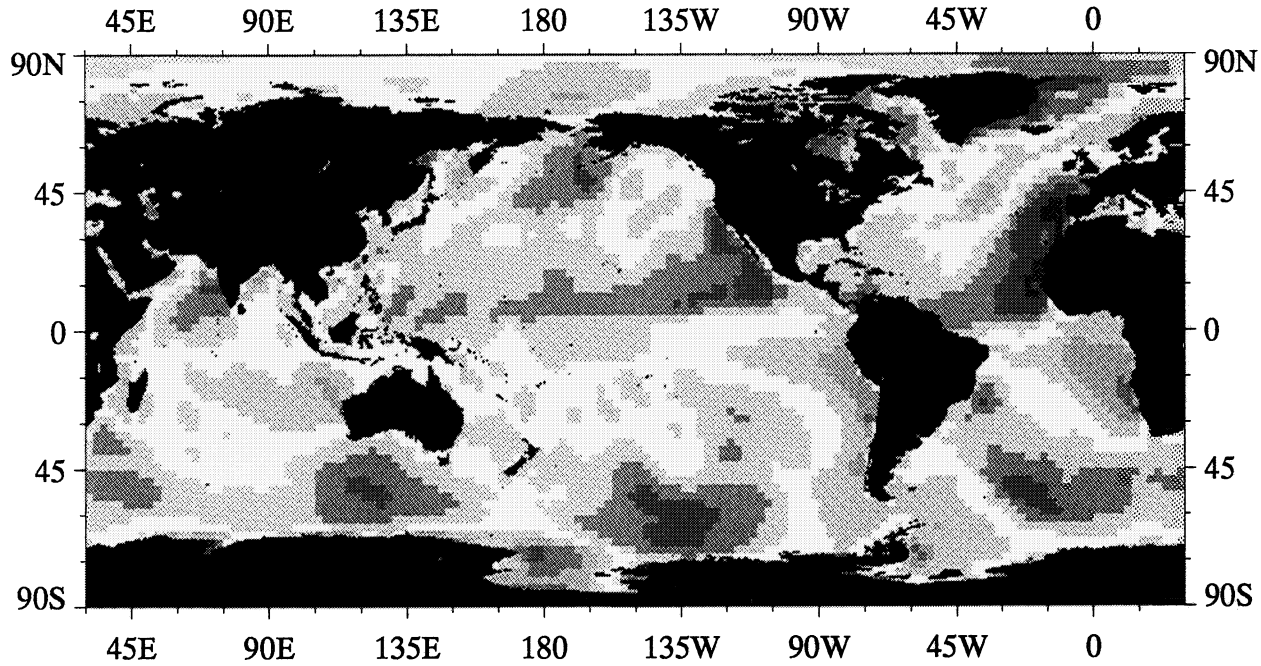


Meridional Wind Speed, April 1990


ECMWF 10 m Wind Speed, m $s^{-1}$

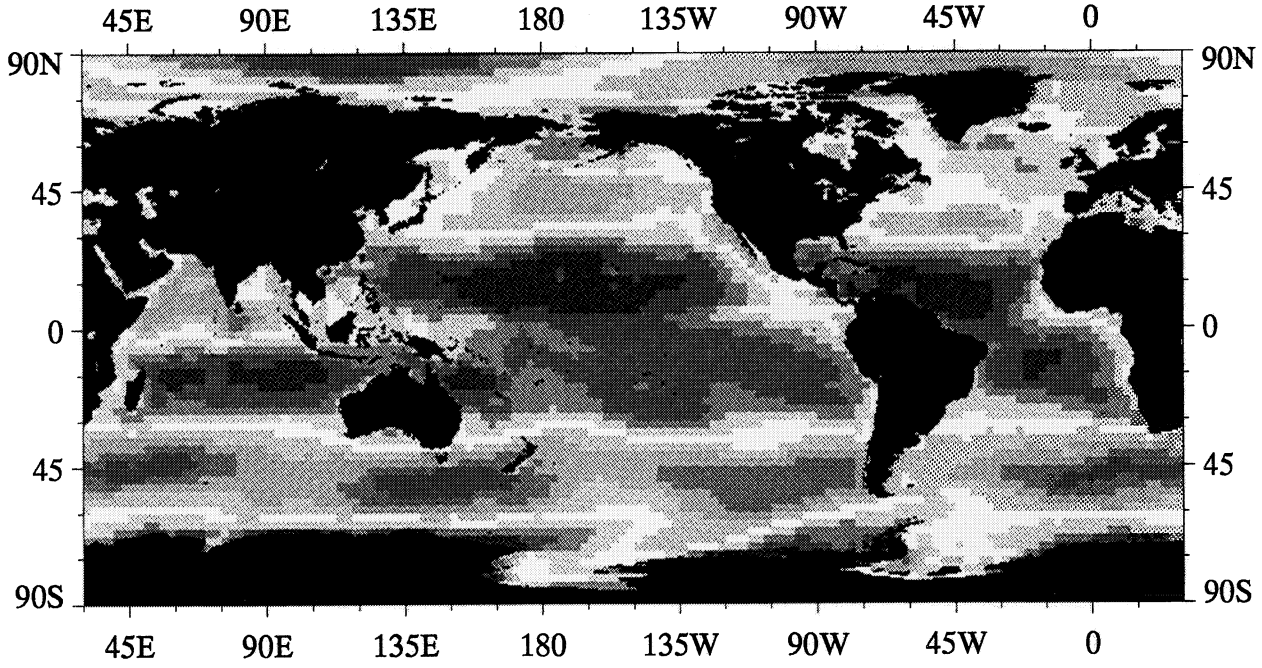


Zonal Wind Speed, May 1990

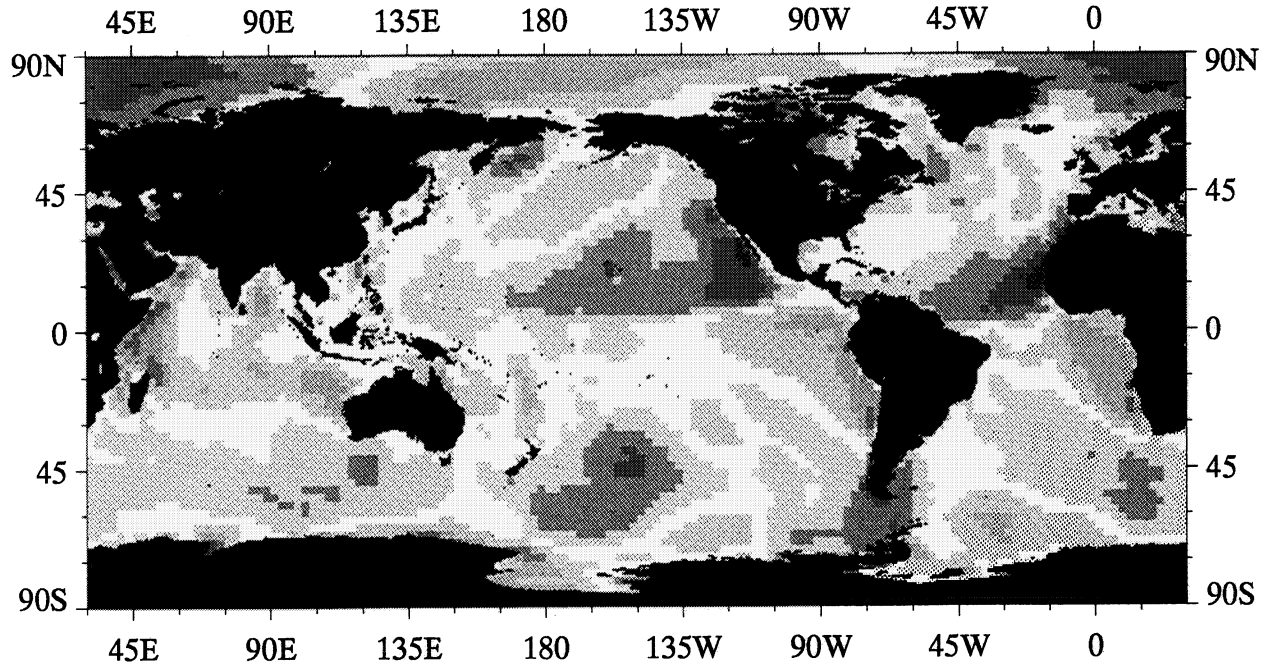


Meridional Wind Speed, May 1990


ECMWF 10 m Wind Speed, m $s^{-1}$

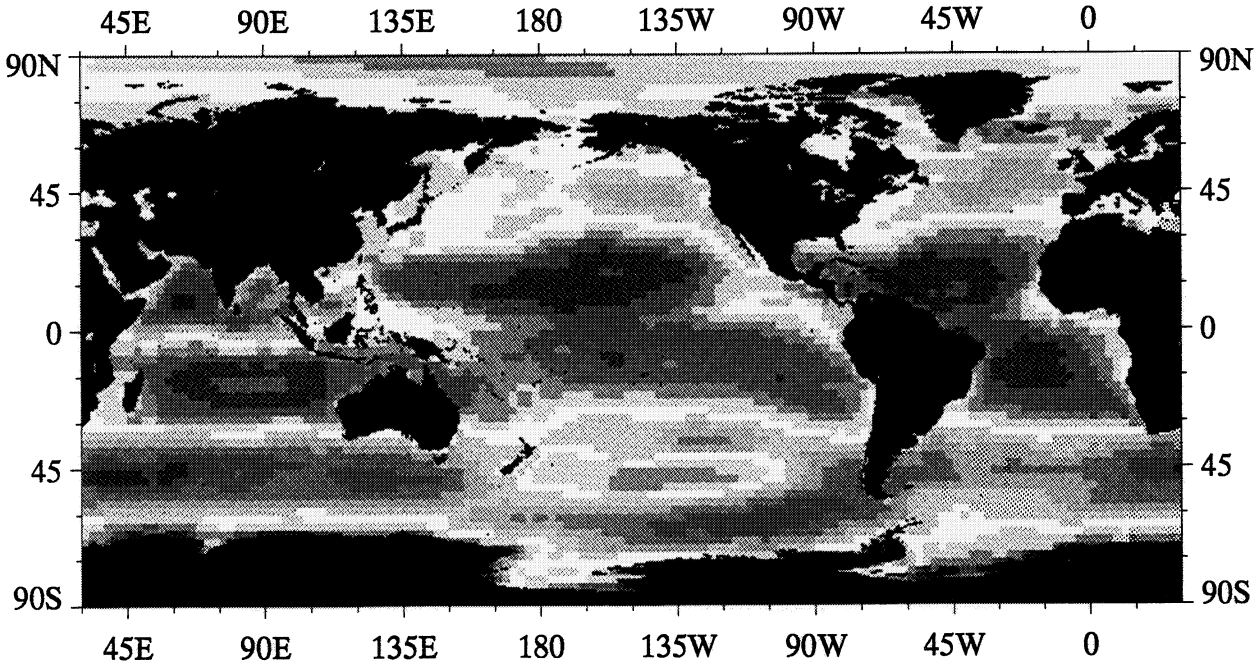


Zonal Wind Speed, June 1990

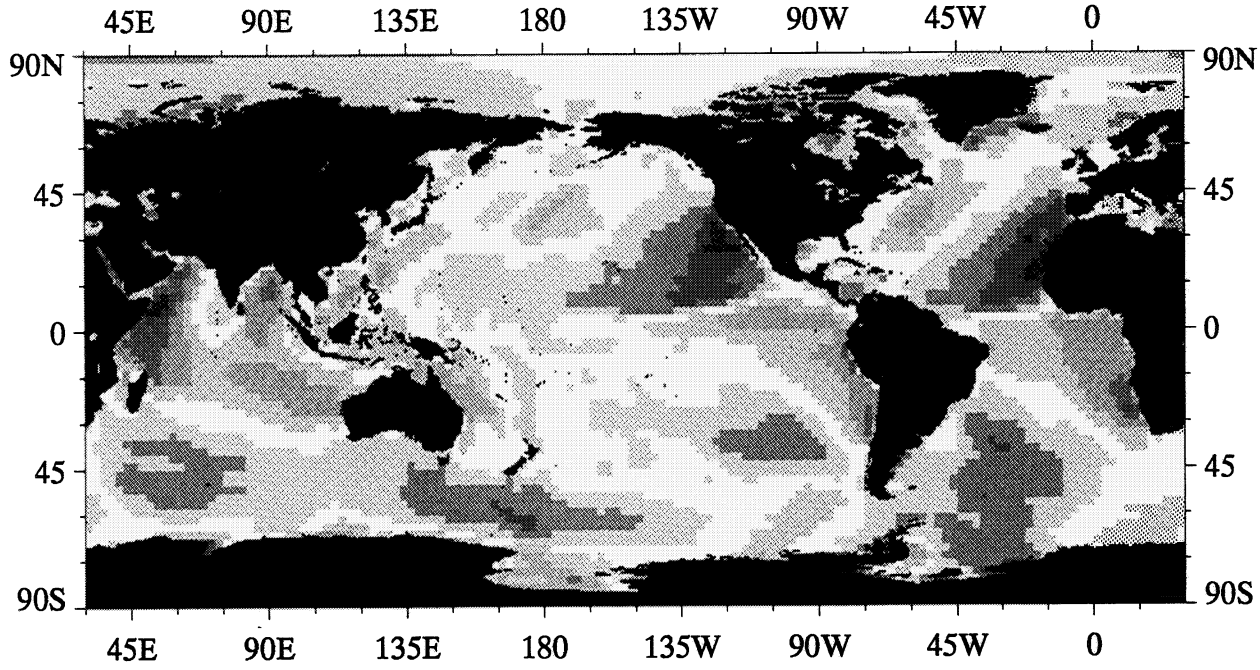


Meridional Wind Speed, June 1990


ECMWF 10 m Wind Speed, $m\ s^{-1}$

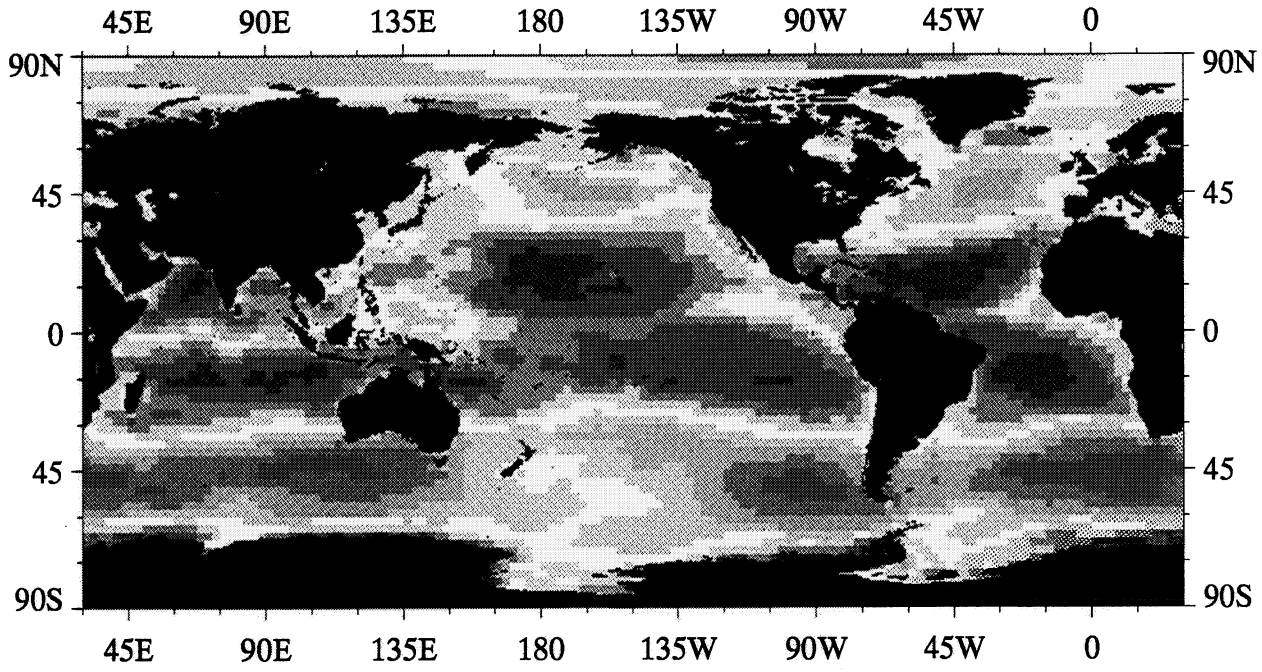


Zonal Wind Speed, July 1990

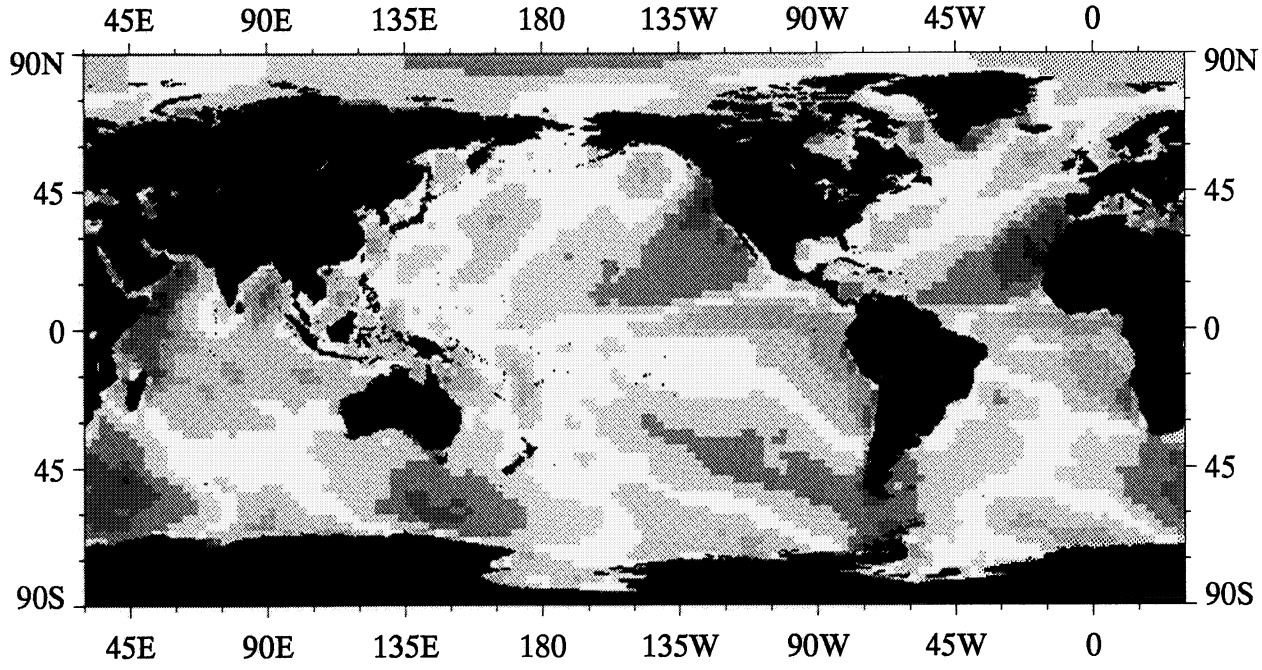


Meridional Wind Speed, July 1990

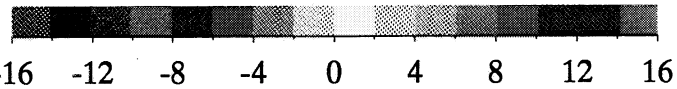


ECMWF 10 m Wind Speed, m $s^{-1}$

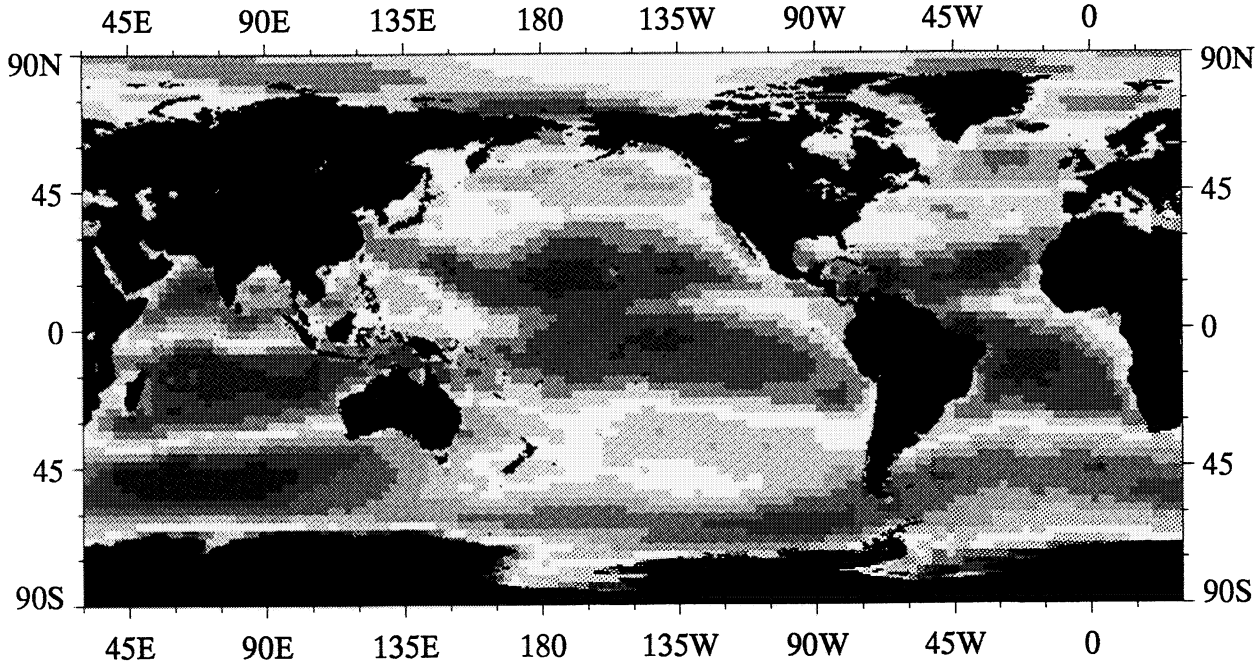


Zonal Wind Speed, August 1990

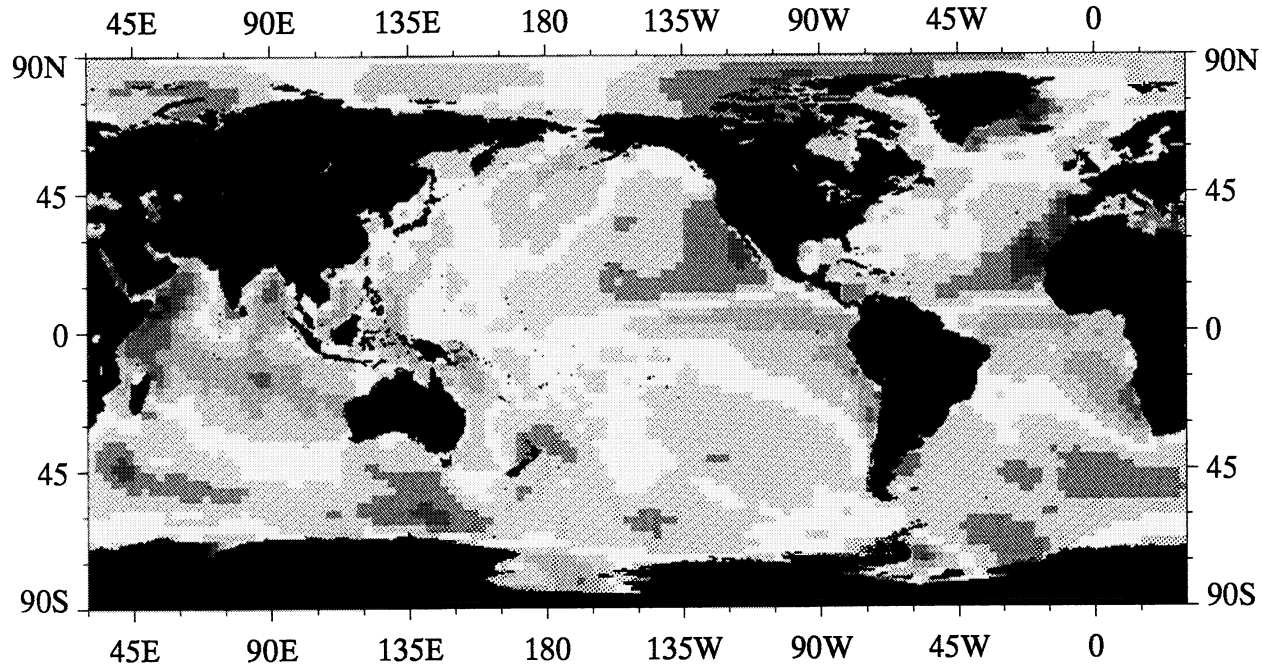


Meridional Wind Speed, August 1990


ECMWF 10 m Wind Speed, m $s^{-1}$

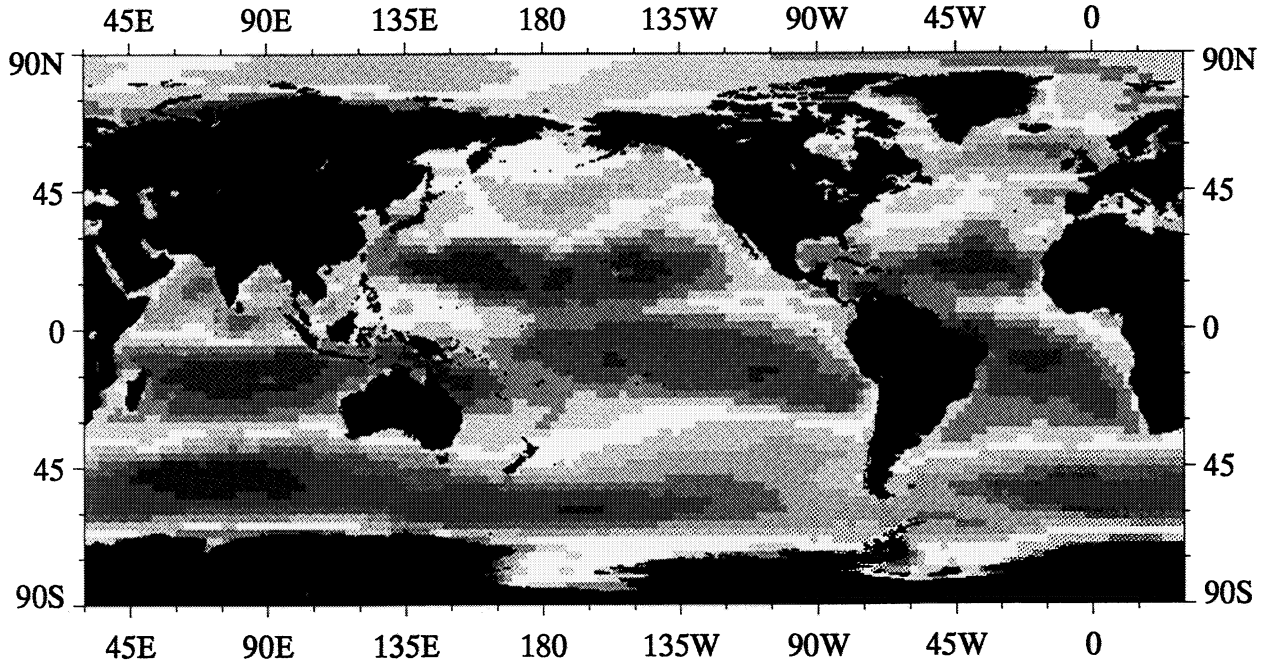


Zonal Wind Speed, September 1990

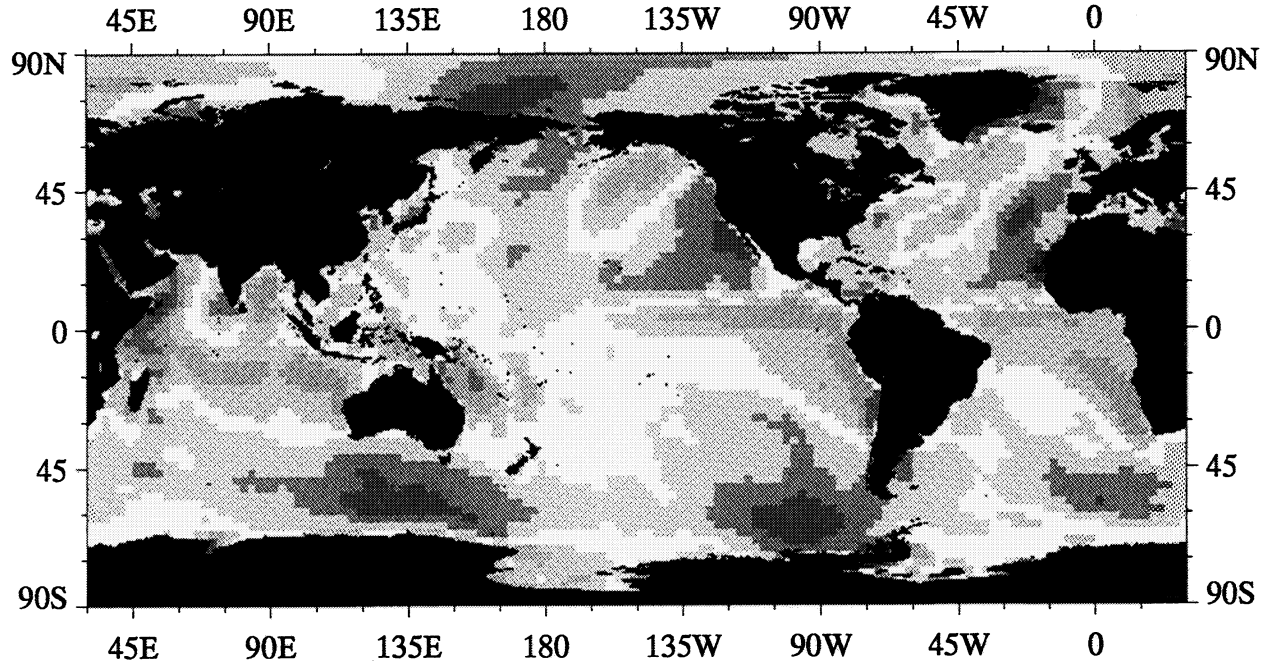


Meridional Wind Speed, September 1990

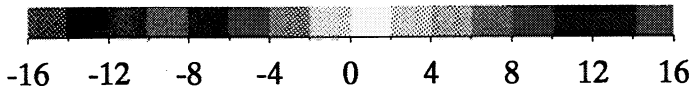


ECMWF 10 m Wind Speed, m $s^{-1}$

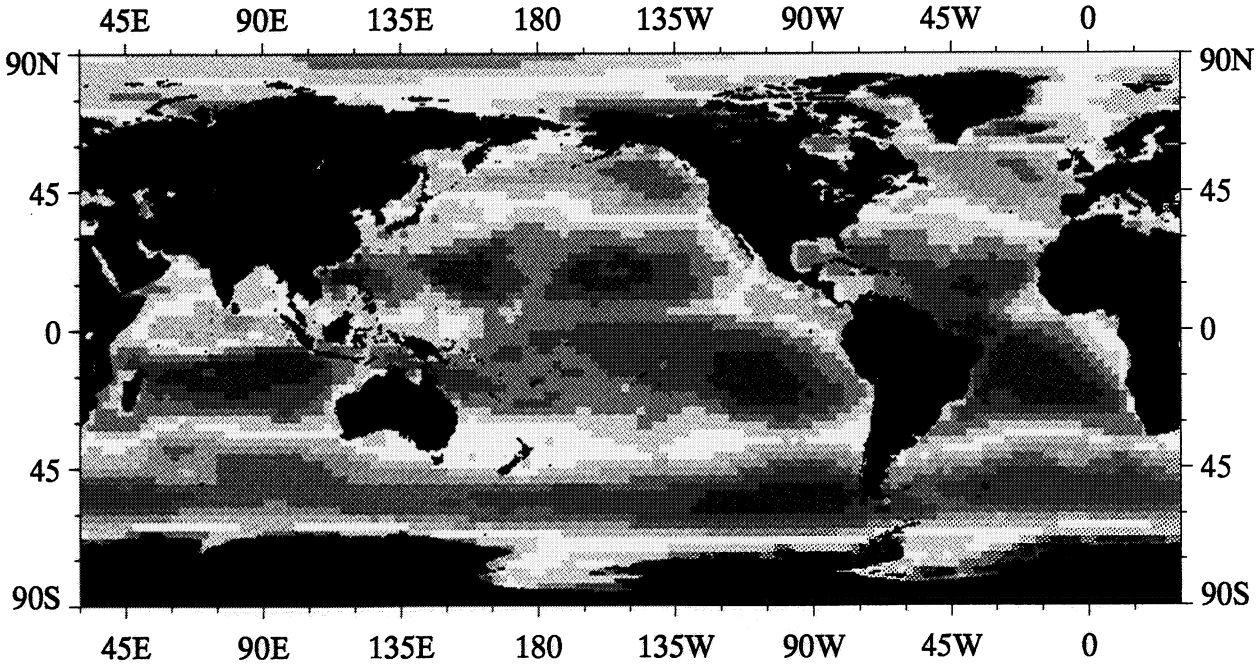


Zonal Wind Speed, October 1990

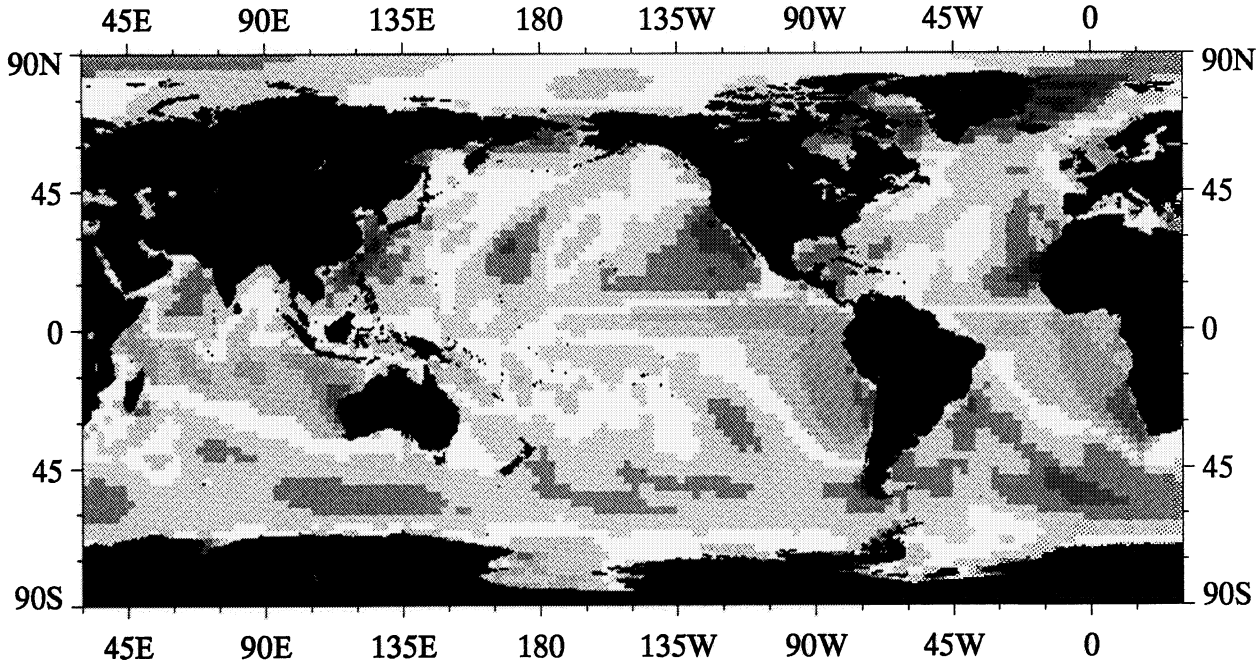


Meridional Wind Speed, October 1990


ECMWF 10 m Wind Speed, m $s^{-1}$

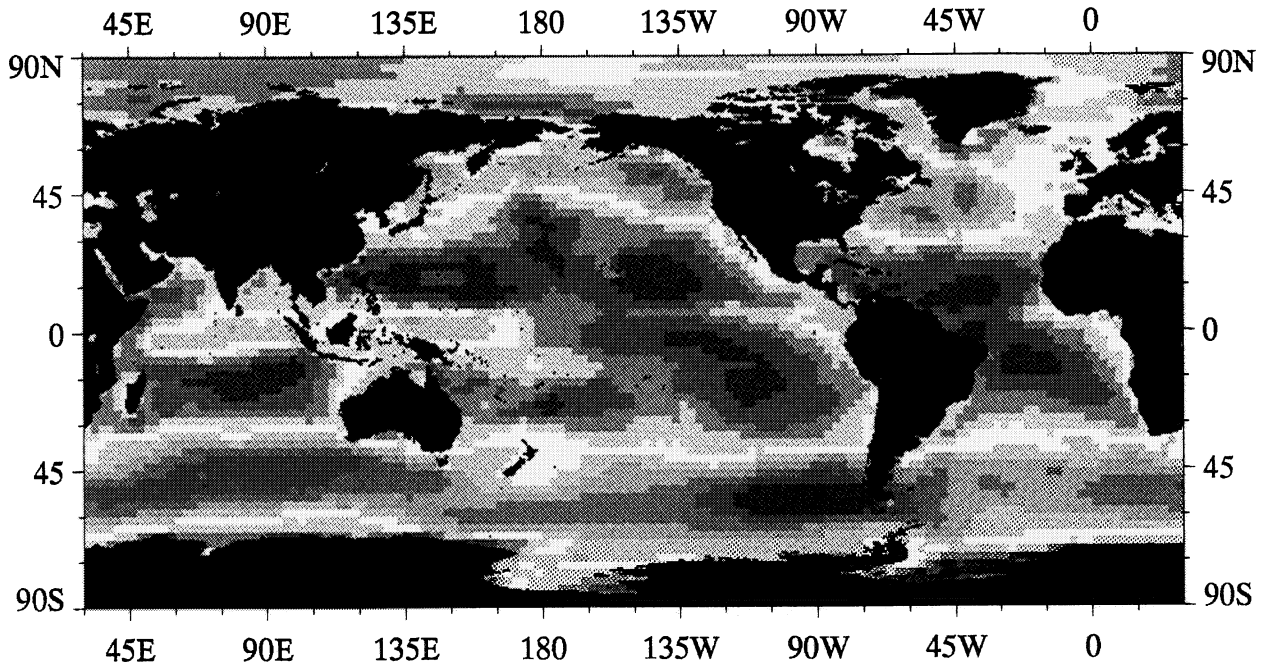


Zonal Wind Speed, November 1990

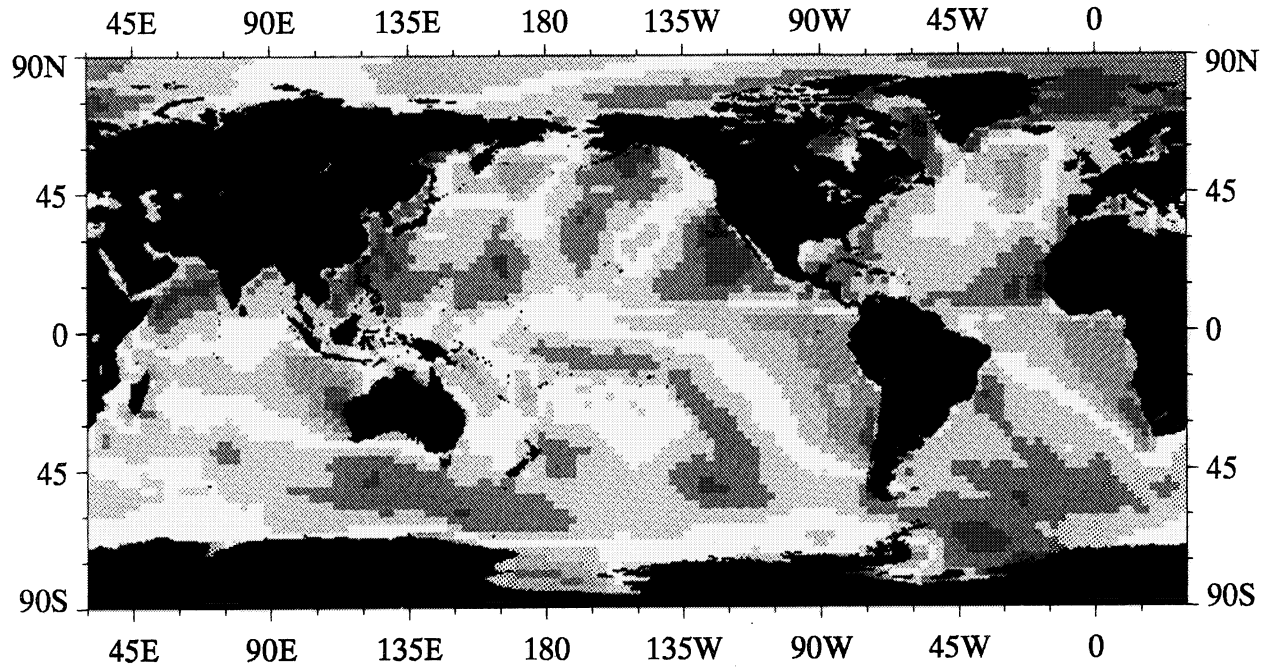


Meridional Wind Speed, November 1990

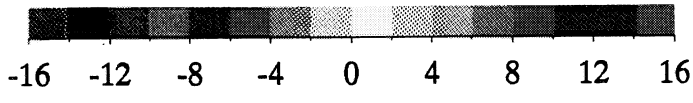


ECMWF 10 m Wind Speed, m $s^{-1}$

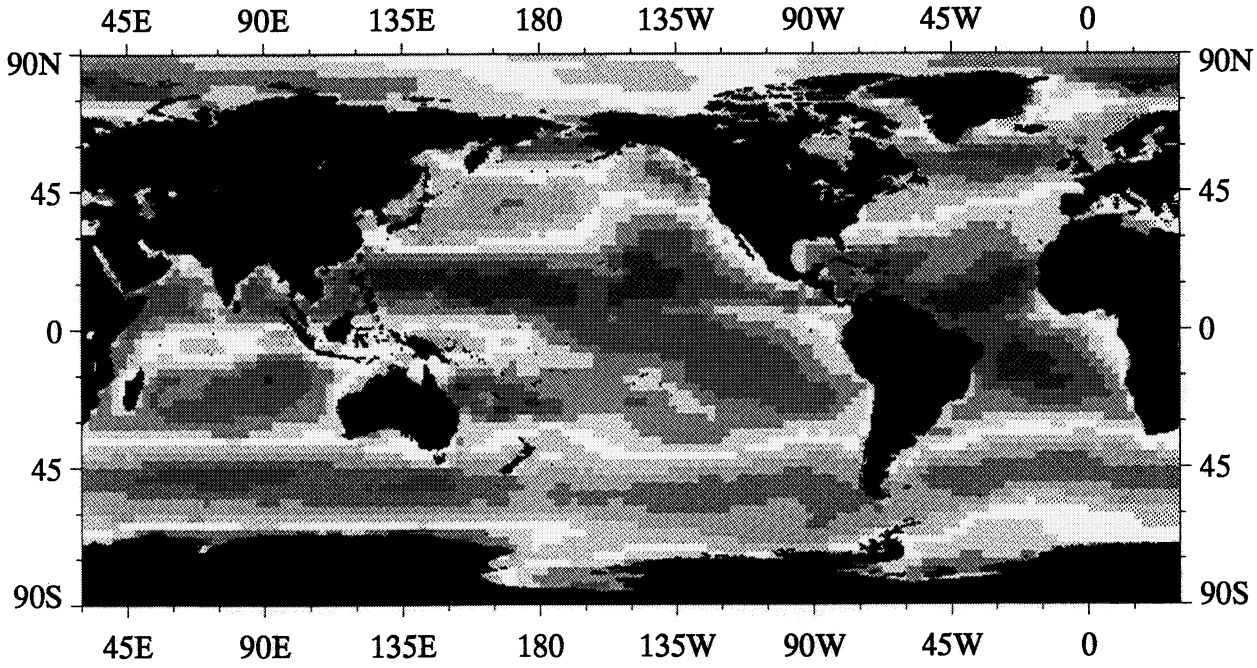


Zonal Wind Speed, December 1990

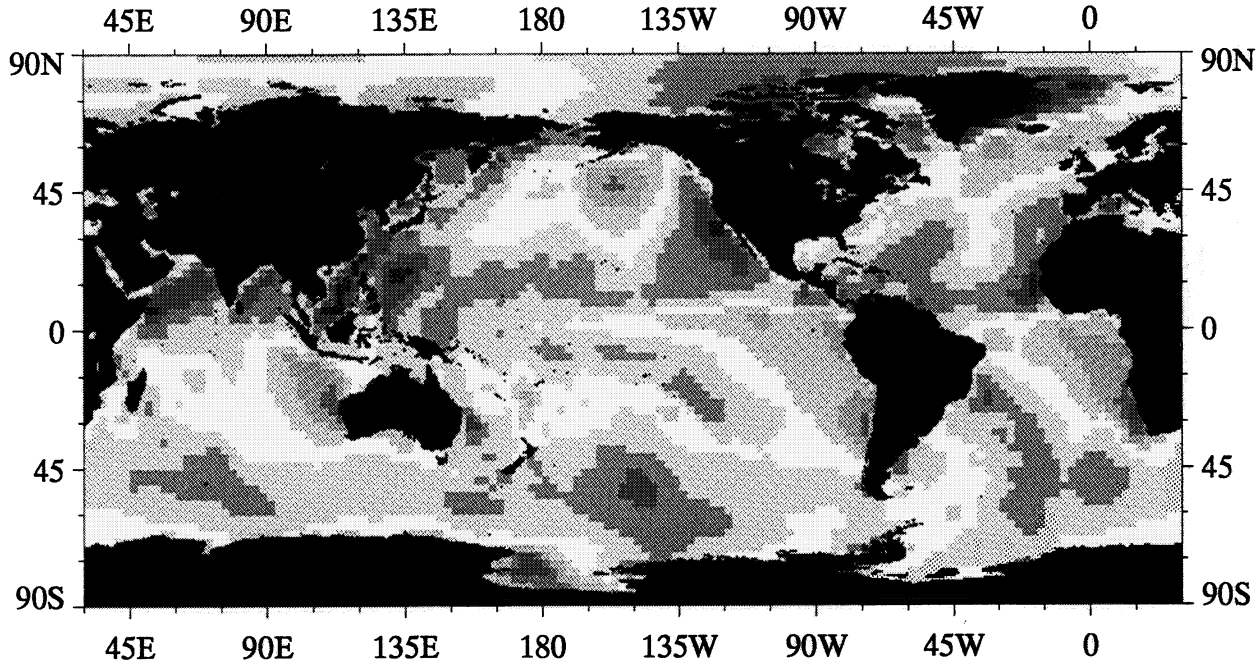


Meridional Wind Speed, December 1990

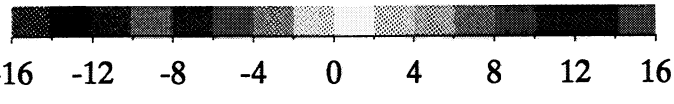


ECMWF 10 m Wind Speed, m $s^{-1}$

A11

Monthly Standard Deviation of ECMWF Surface Wind Components

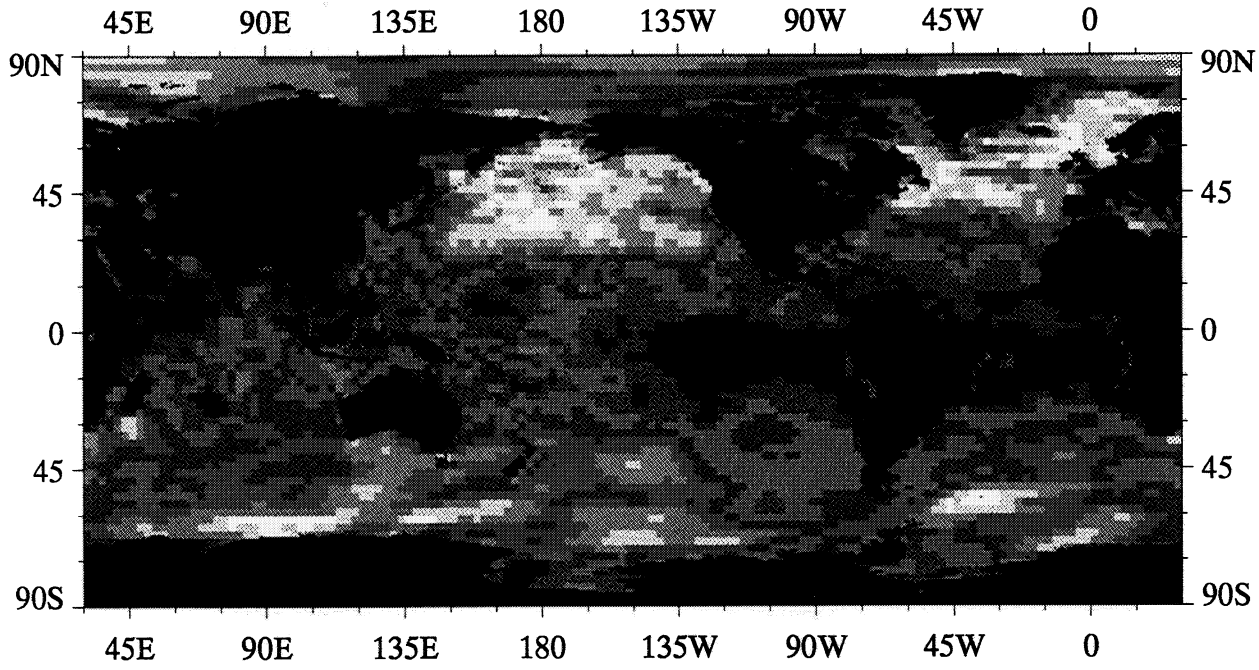


Zonal Wind Speed, January 1990

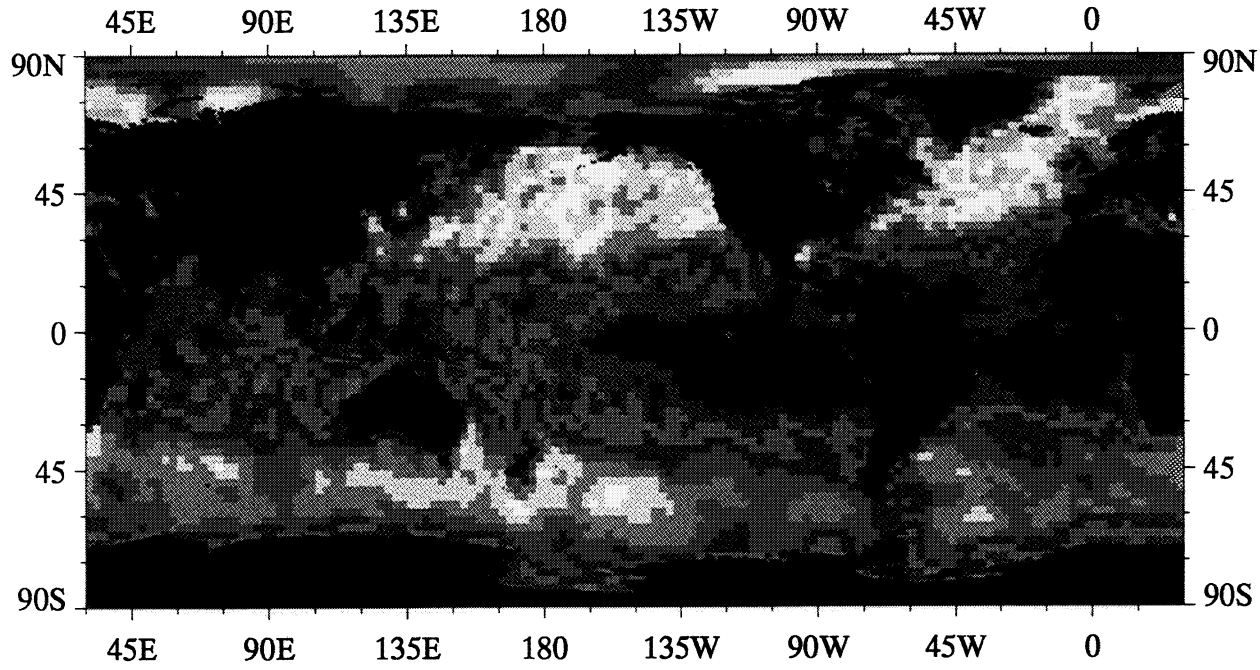


Meridional Wind Speed, January 1990

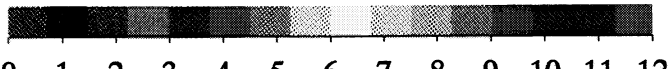


Standard Deviation of ECMWF 10 m Wind Speed, m $s^{-1}$

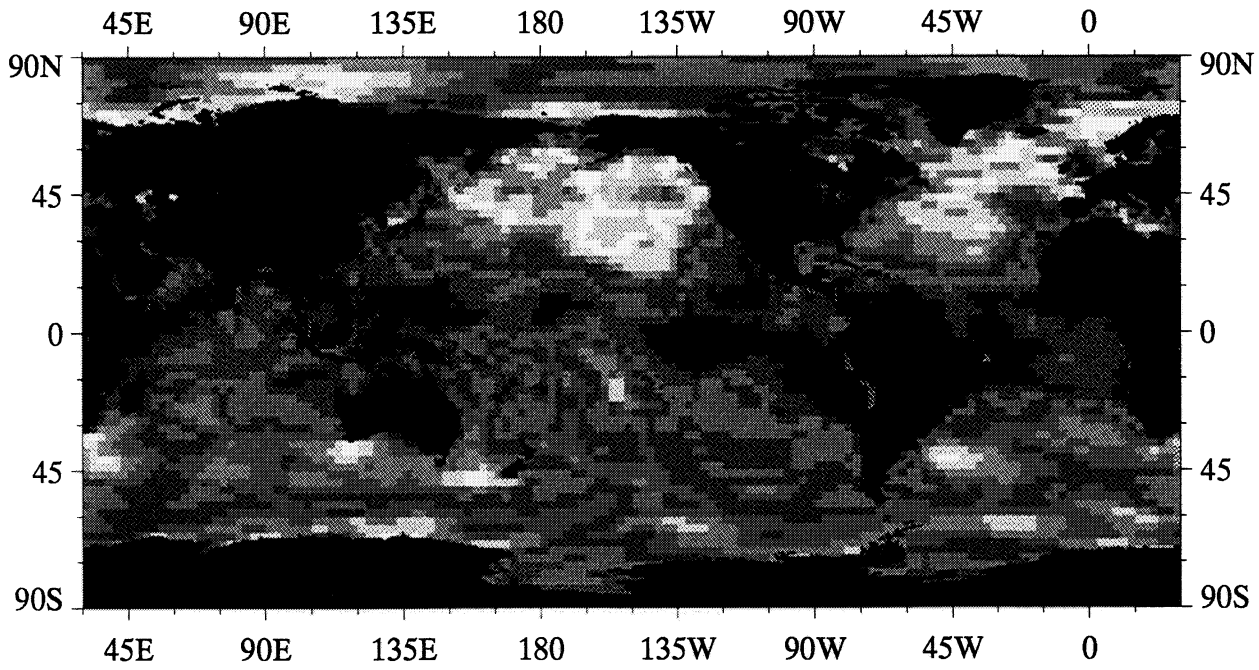


Zonal Wind Speed, February 1990

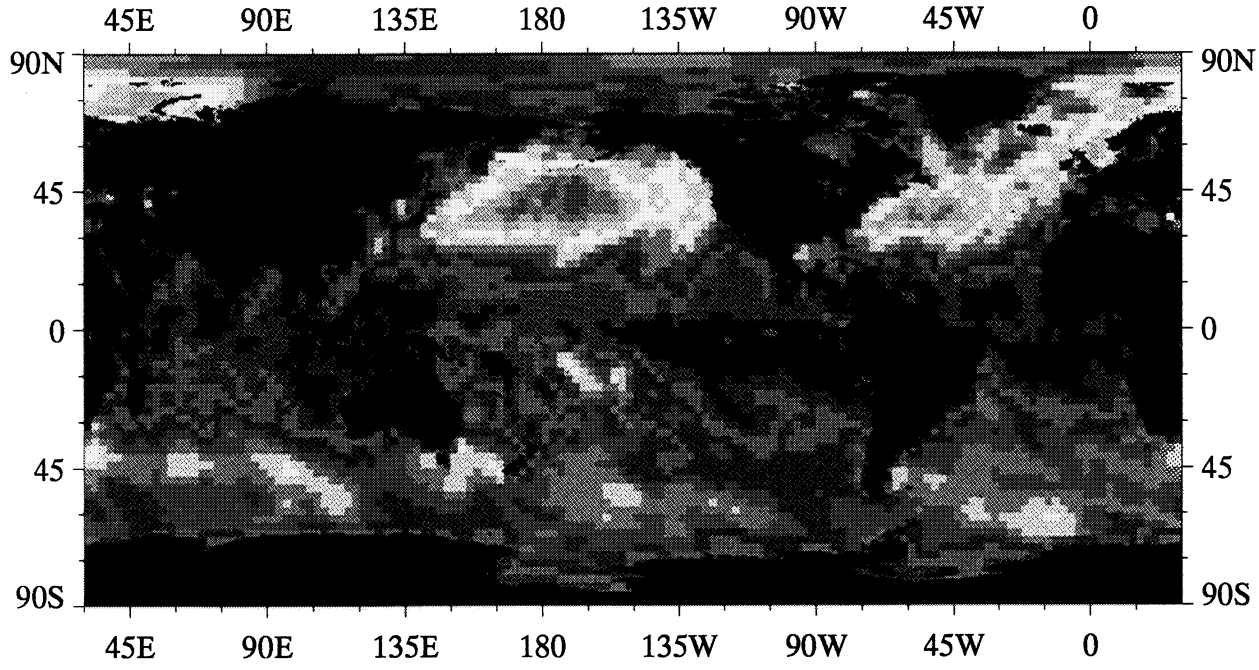


Meridional Wind Speed, February 1990


Standard Deviation of ECMWF 10 m Wind Speed, m $s^{-1}$

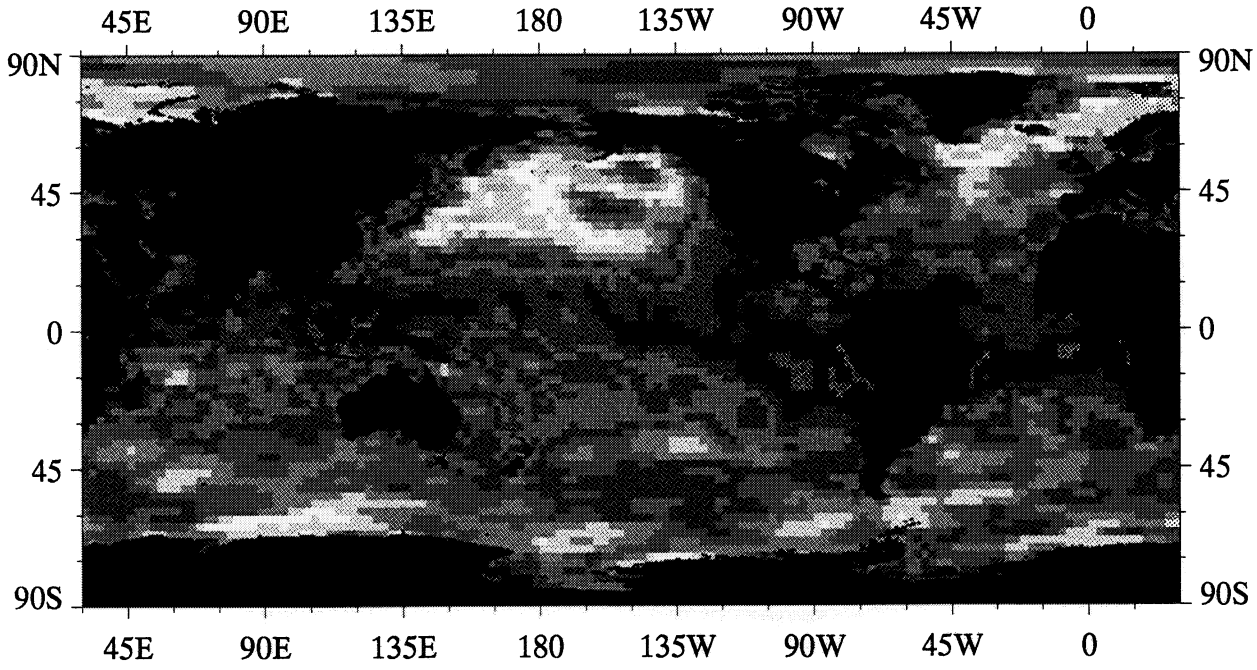


Zonal Wind Speed, March 1990

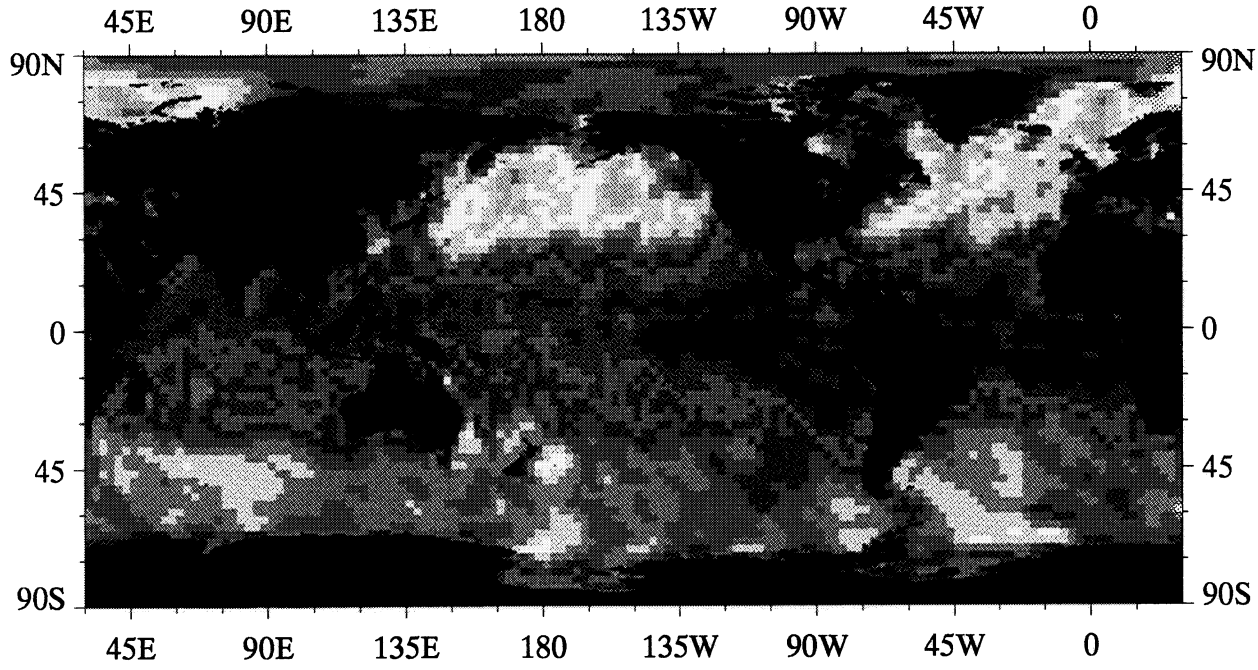


Meridional Wind Speed, March 1990

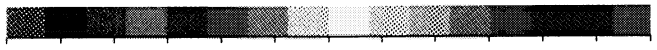


Standard Deviation of ECMWF 10 m Wind Speed, m $s^{-1}$

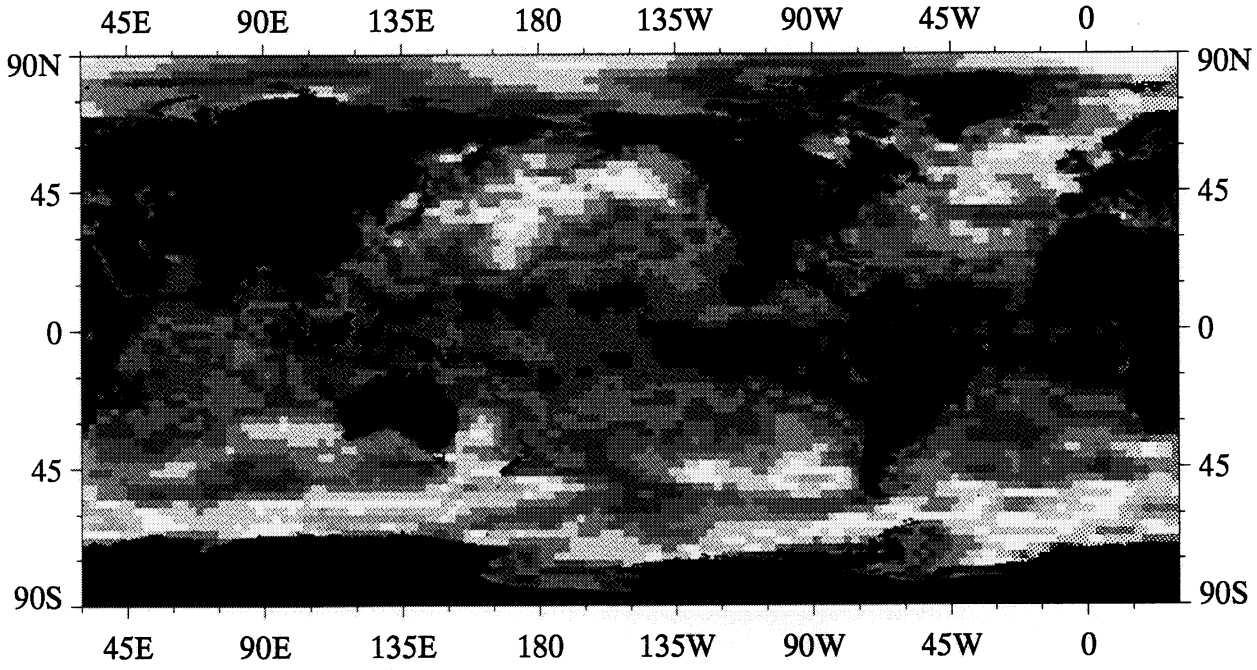


Zonal Wind Speed, April 1990

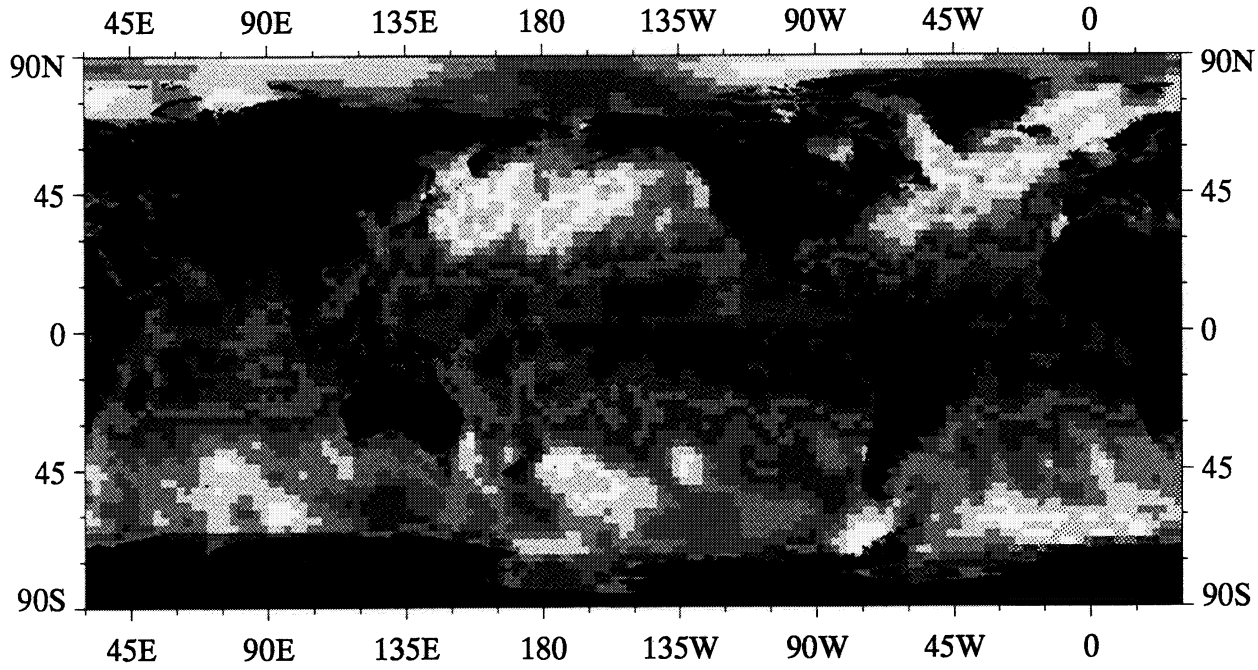


Meridional Wind Speed, April 1990


Standard Deviation of ECMWF 10 m Wind Speed, m $s^{-1}$

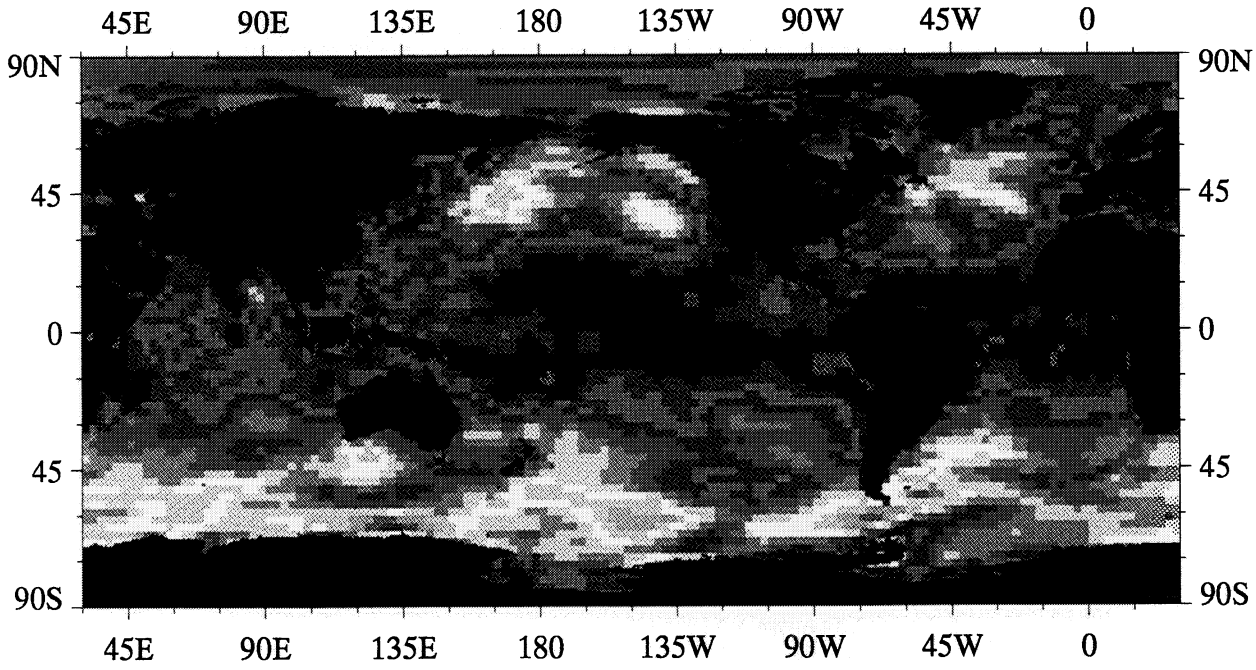


Zonal Wind Speed, May 1990

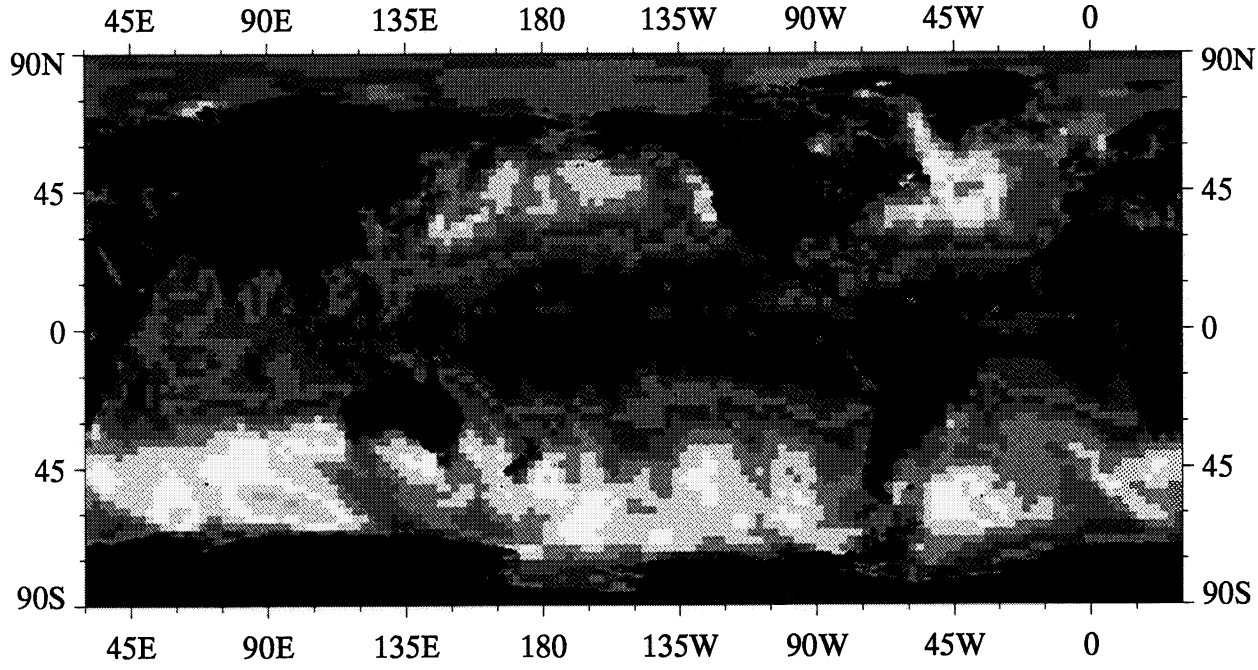


Meridional Wind Speed, May 1990


Standard Deviation of ECMWF 10 m Wind Speed, m $s^{-1}$

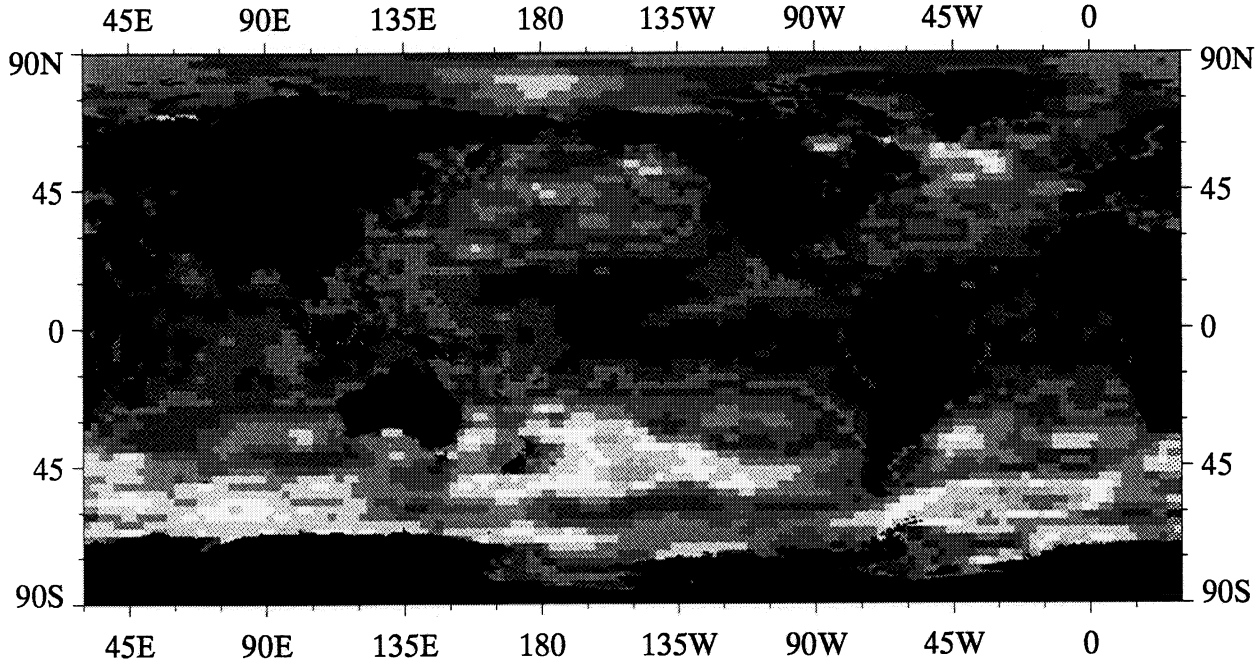


Zonal Wind Speed, June 1990

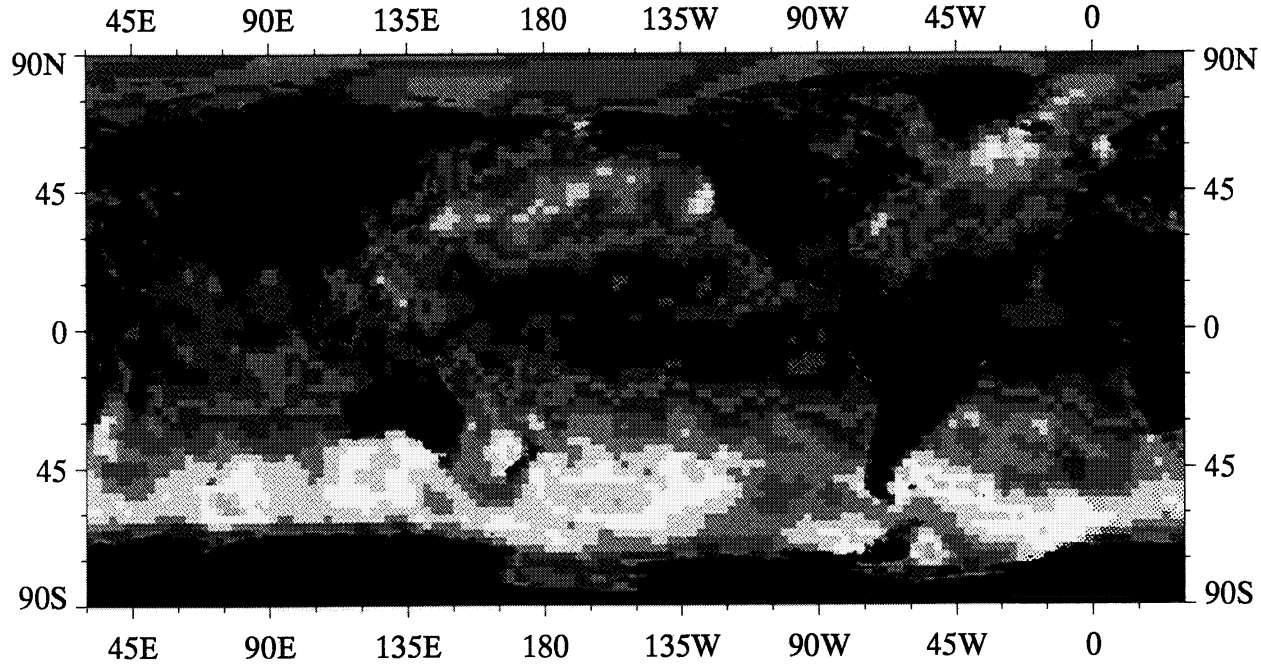


Meridional Wind Speed, June 1990


Standard Deviation of ECMWF 10 m Wind Speed, m $s^{-1}$



C-2

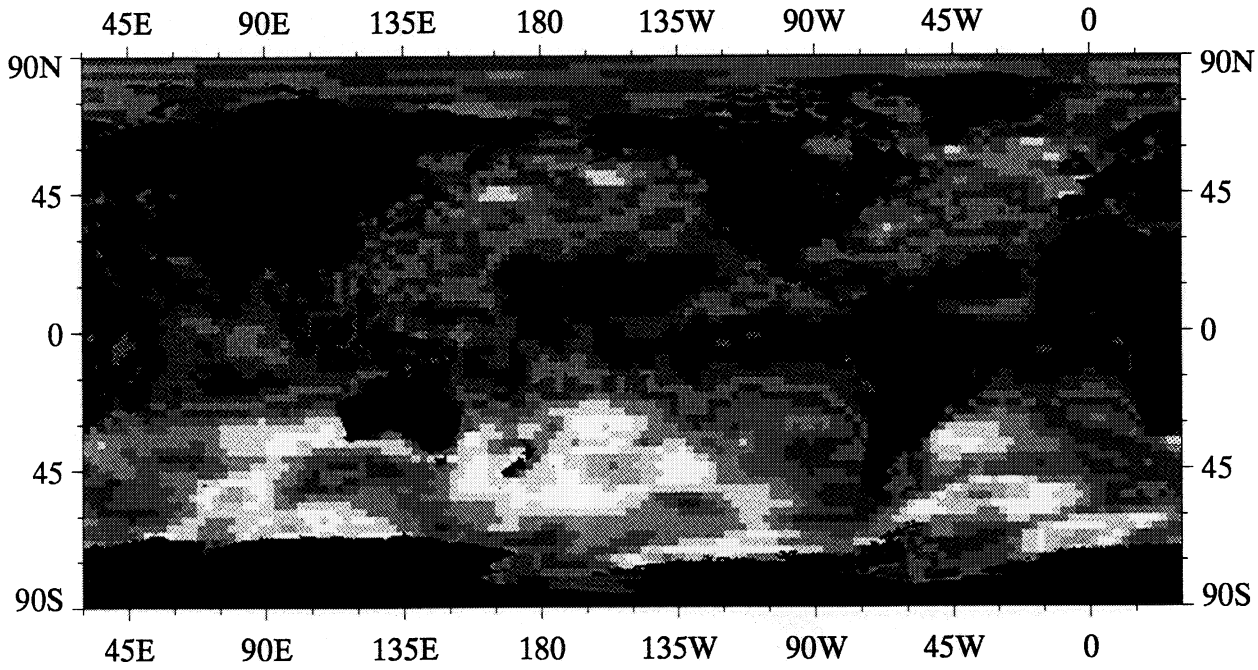


Zonal Wind Speed, July 1990

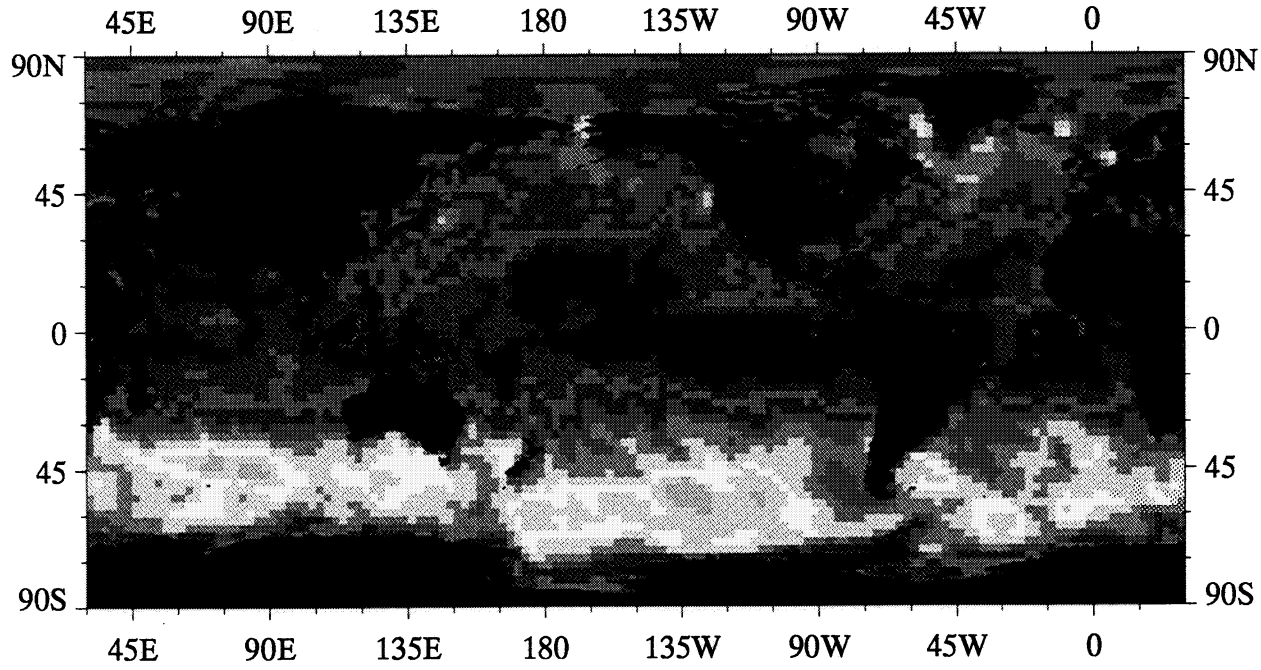


Meridional Wind Speed, July 1990

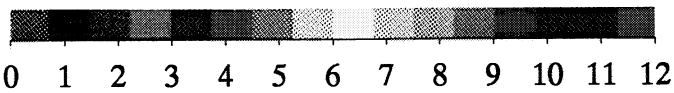


Standard Deviation of ECMWF 10 m Wind Speed, $m\ s^{-1}$

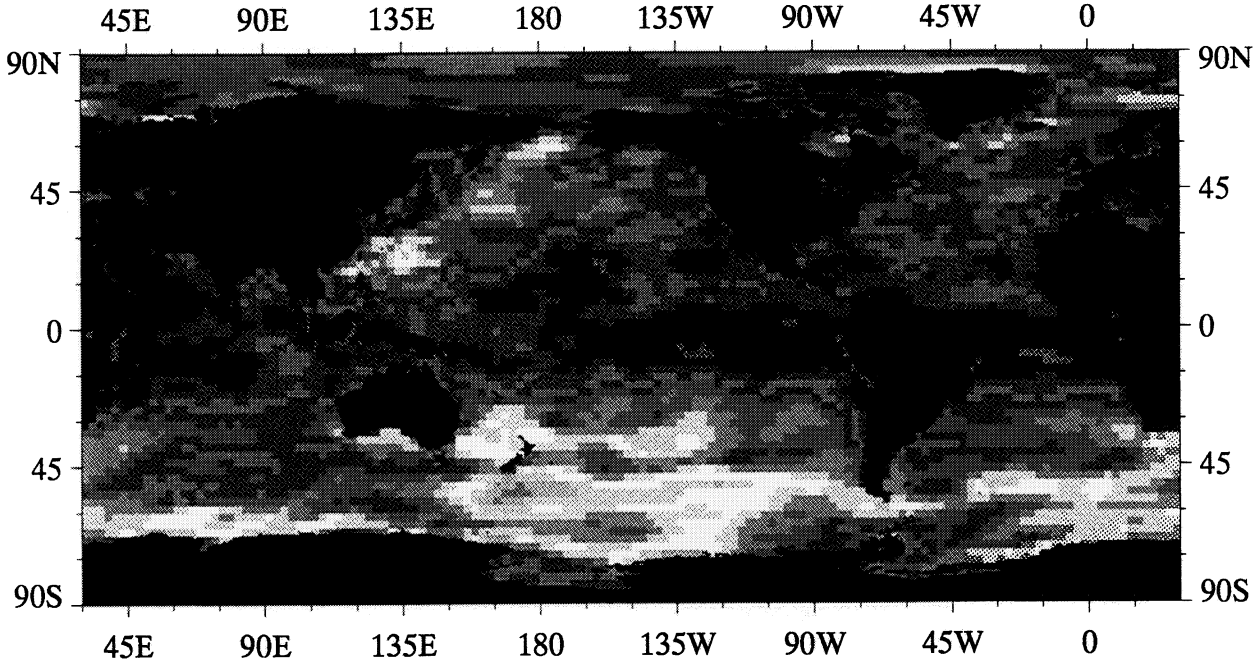


Zonal Wind Speed, August 1990

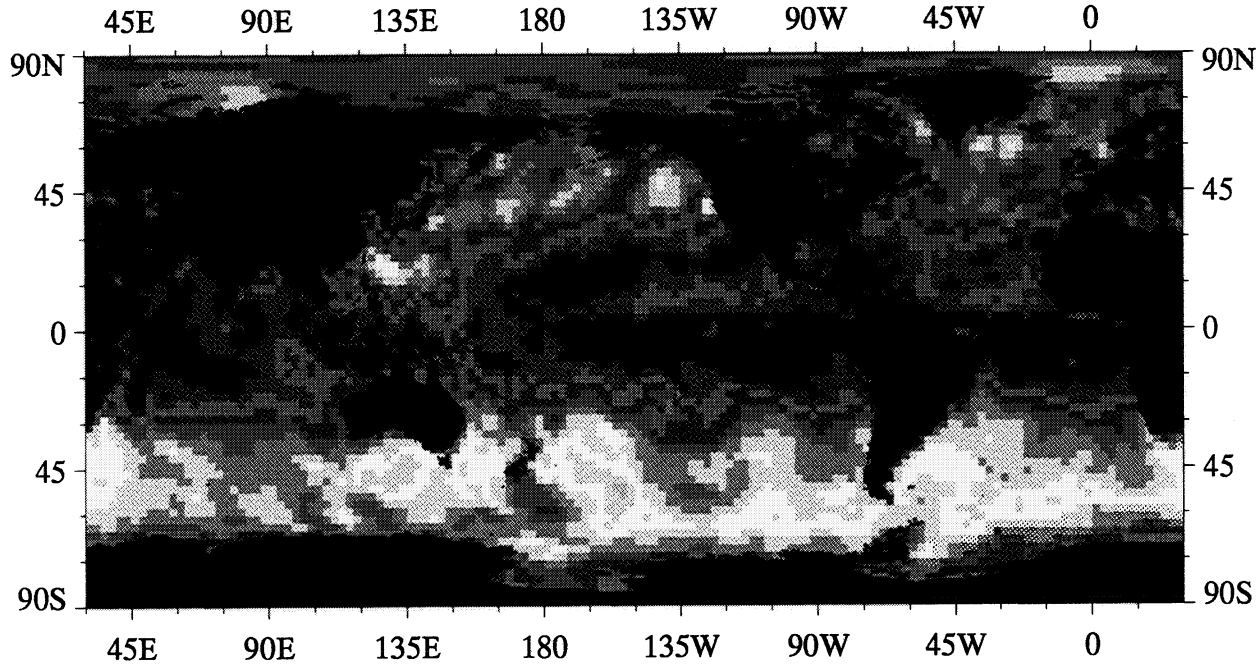


Meridional Wind Speed, August 1990


Standard Deviation of ECMWF 10 m Wind Speed, m $s^{-1}$

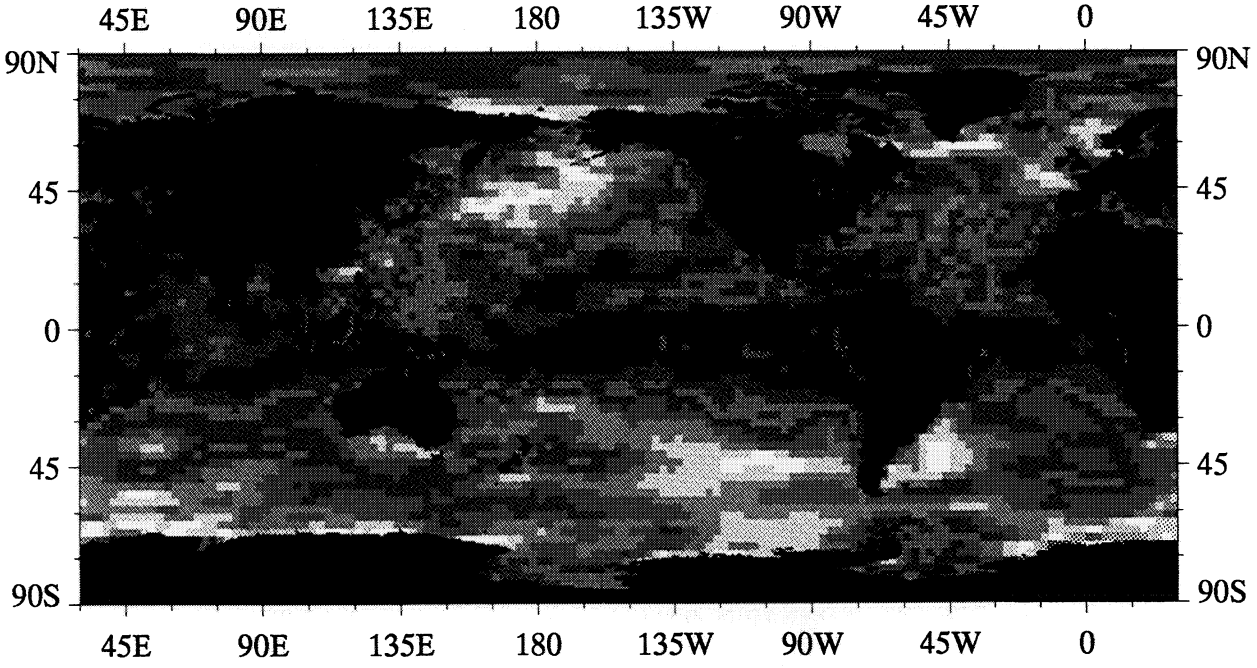


Zonal Wind Speed, September 1990

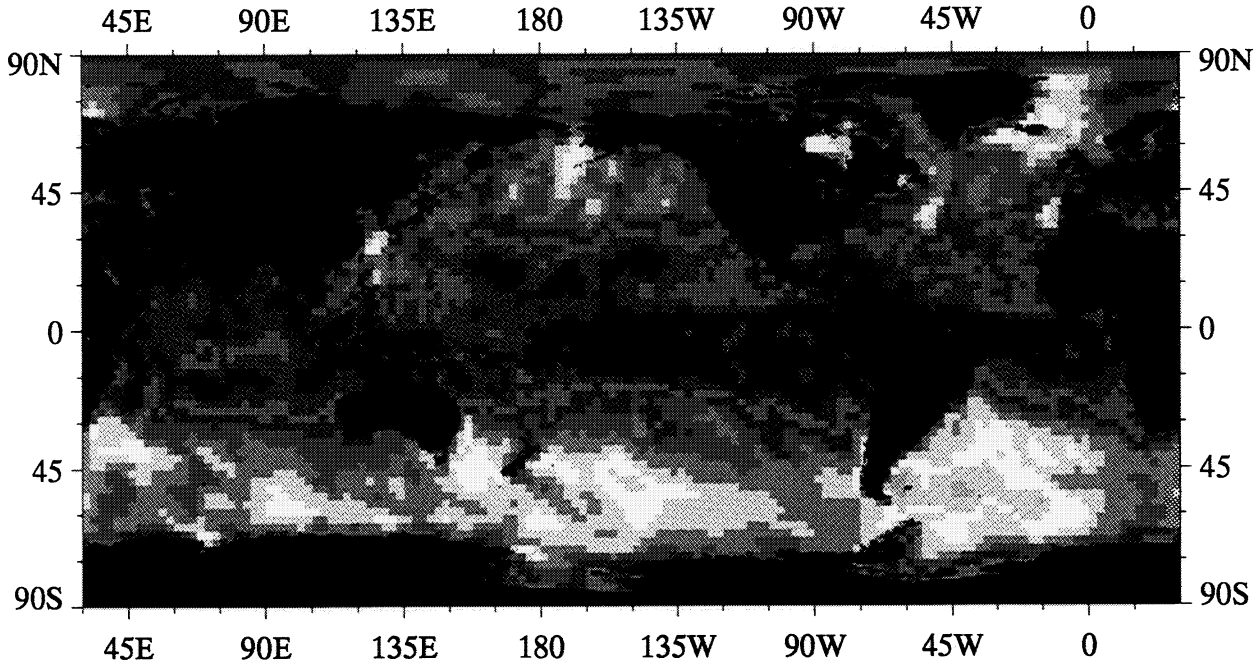


Meridional Wind Speed, September 1990


Standard Deviation of ECMWF 10 m Wind Speed, m $s^{-1}$

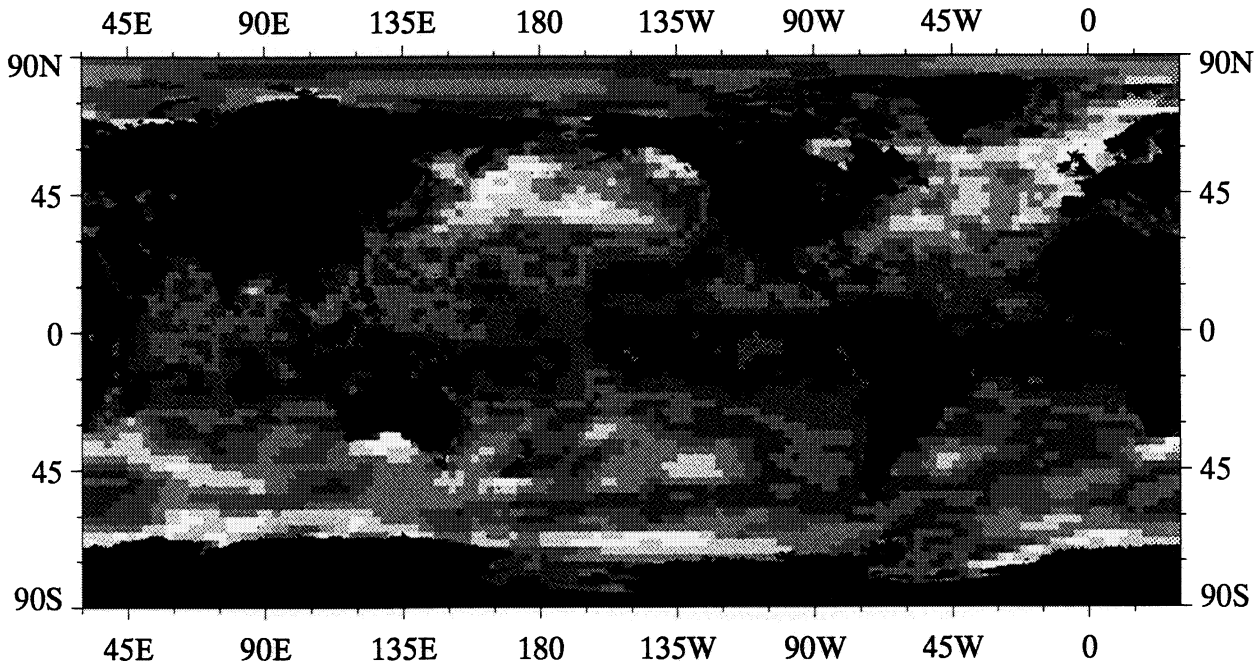


Zonal Wind Speed, October 1990

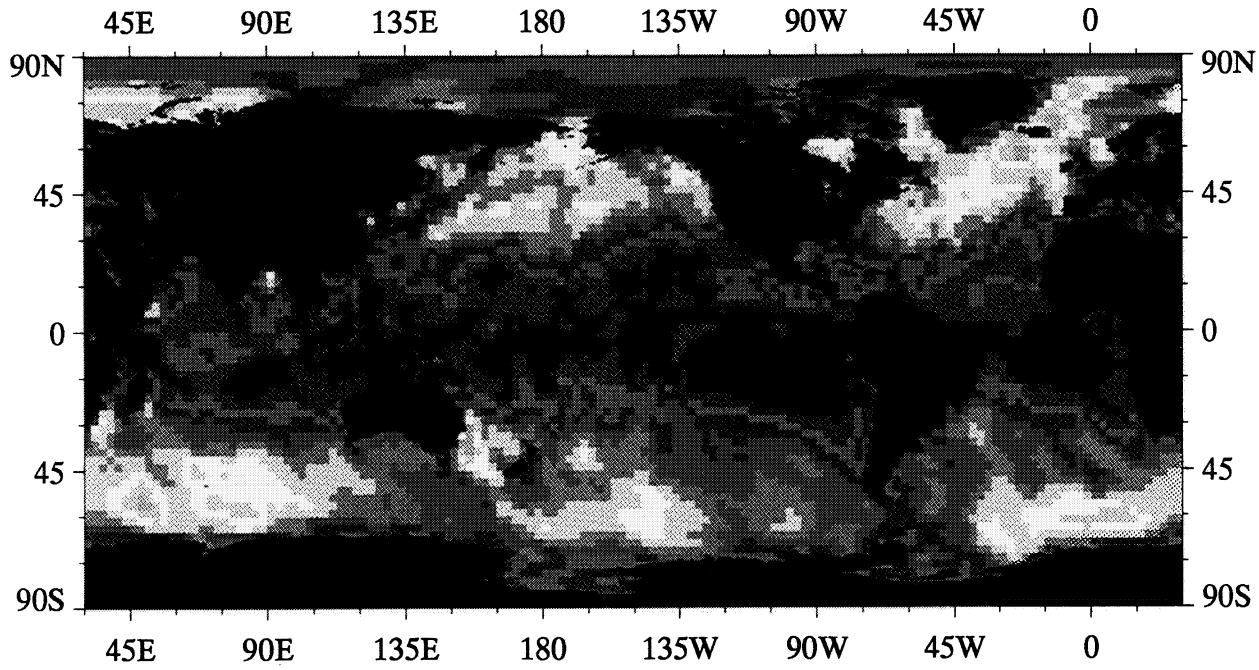


Meridional Wind Speed, October 1990

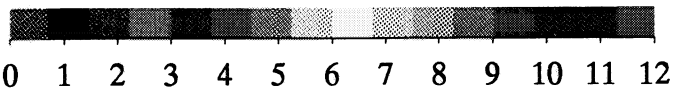


Standard Deviation of ECMWF 10 m Wind Speed, m $s^{-1}$

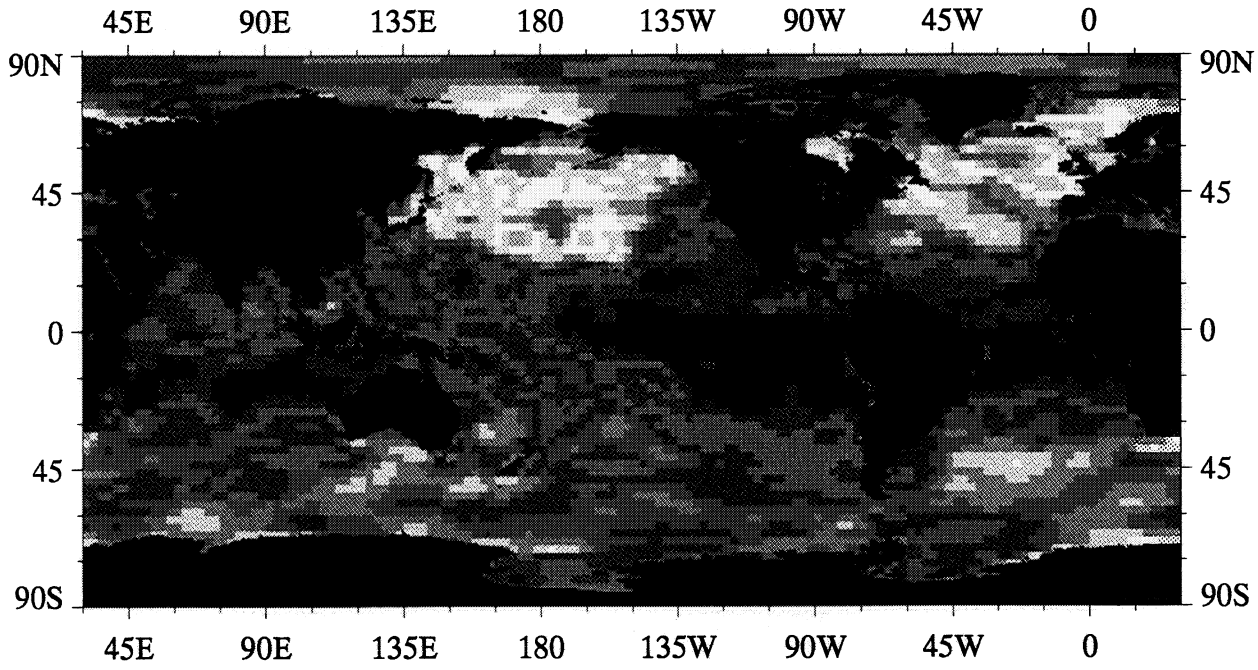


Zonal Wind Speed, November 1990

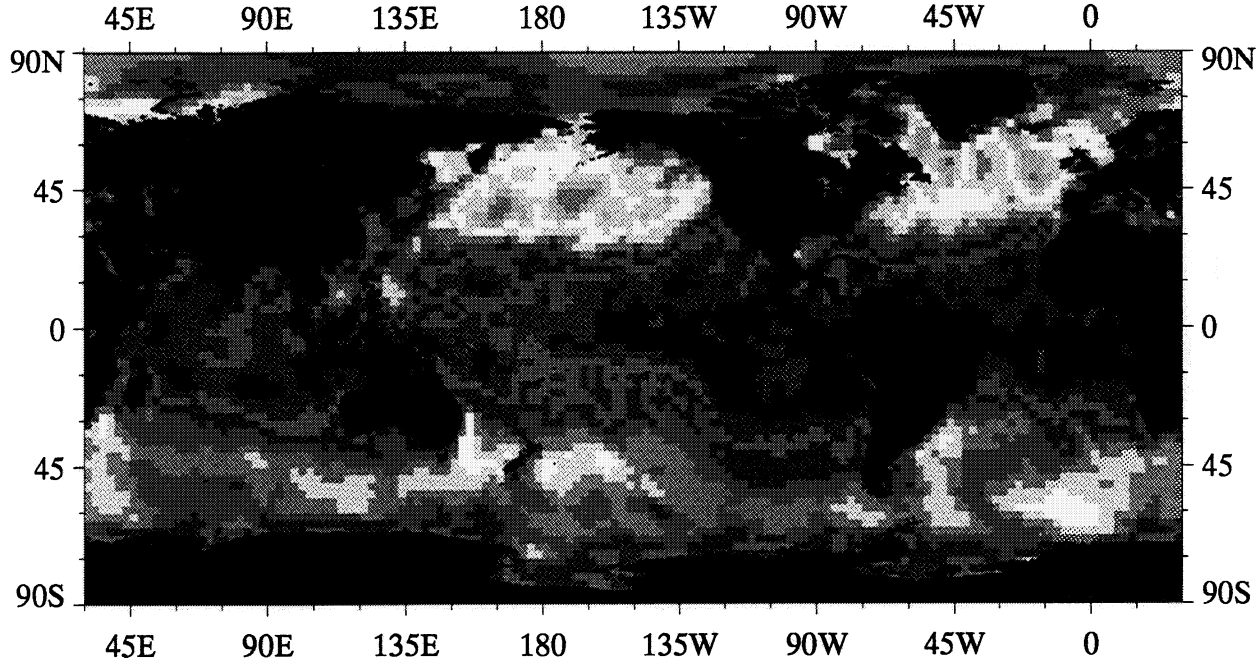


Meridional Wind Speed, November 1990

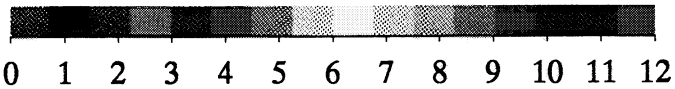


Standard Deviation of ECMWF 10 m Wind Speed, m $s^{-1}$

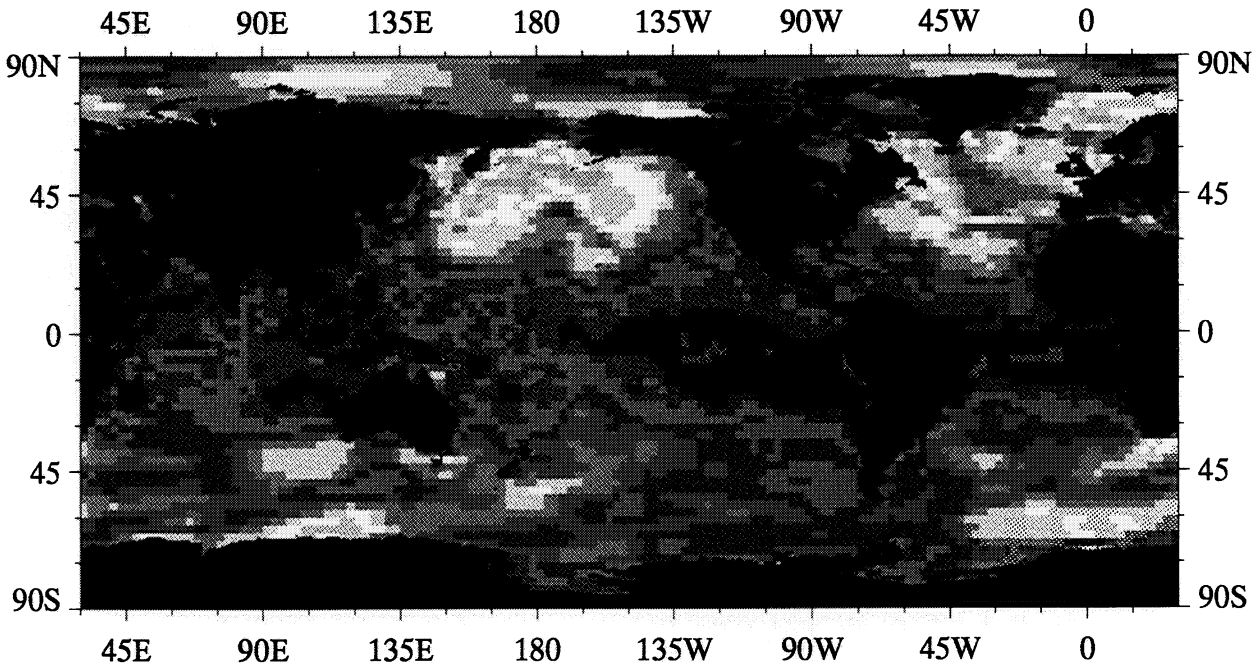


Zonal Wind Speed, December 1990

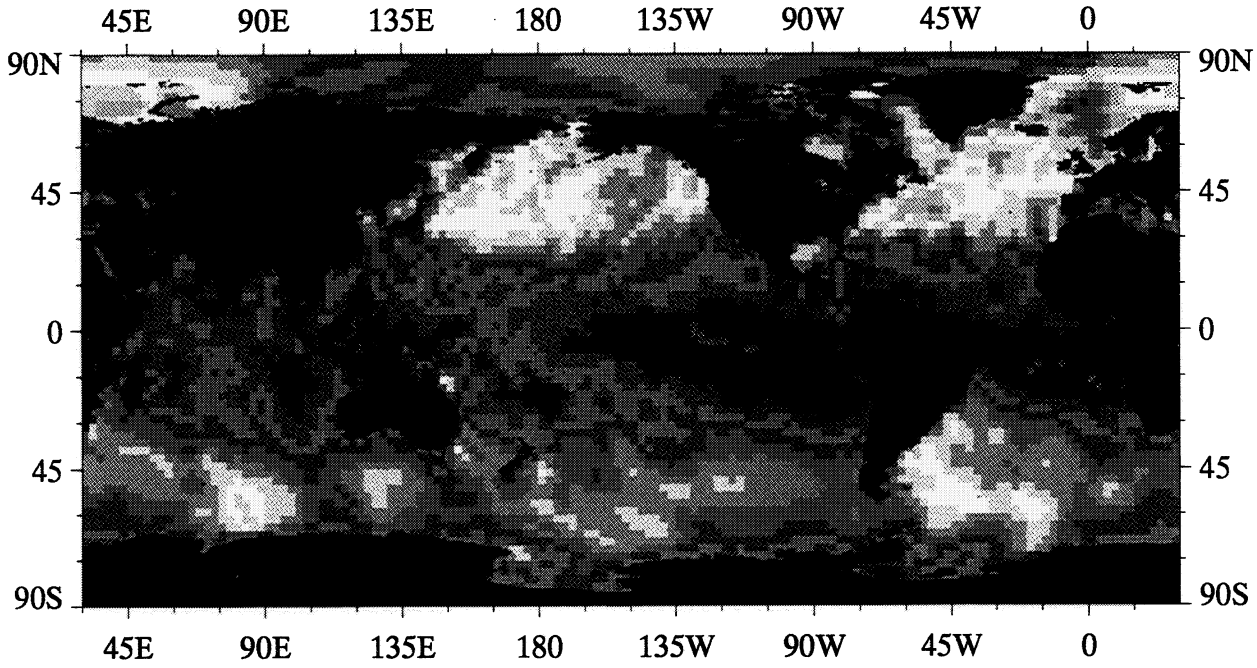


Meridional Wind Speed, December 1990

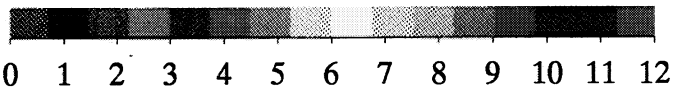


Standard Deviation of ECMWF 10 m Wind Speed, m $s^{-1}$

A12

Annual Mean ECMWF Surface Wind Speed

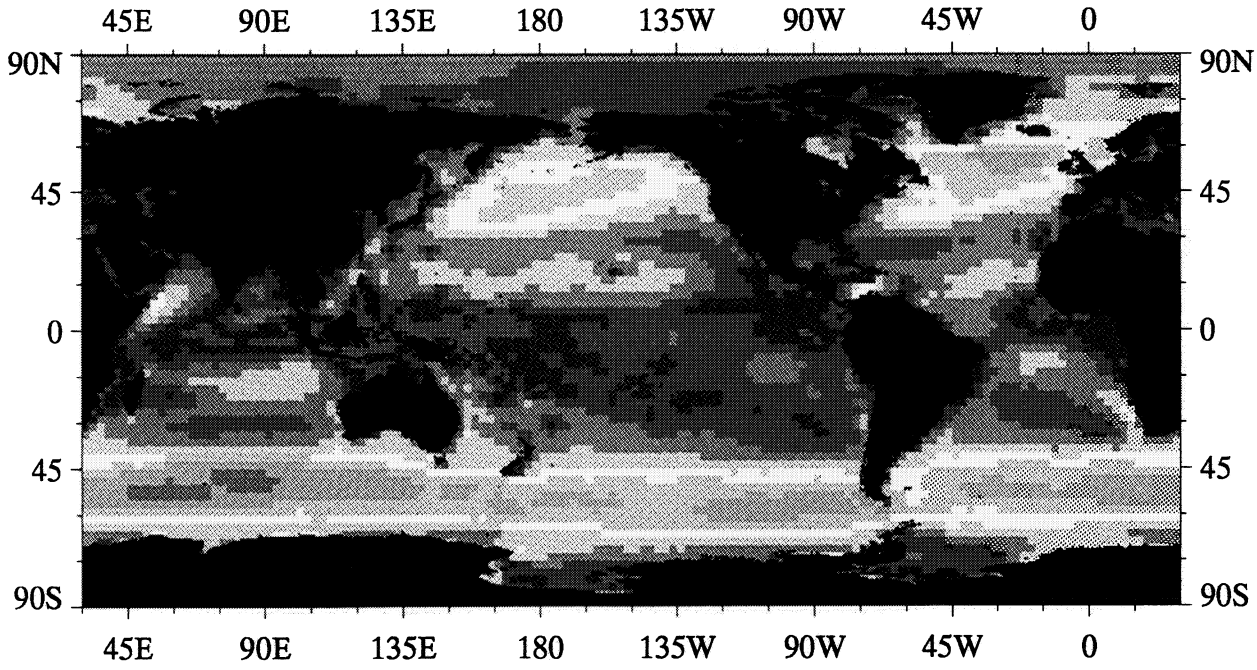


Annual Mean 1990

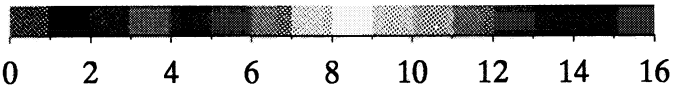


ECMWF 10 m Wind Speed, m $s^{-1}$

A13

Monthly Mean ECMWF Surface Wind Speed

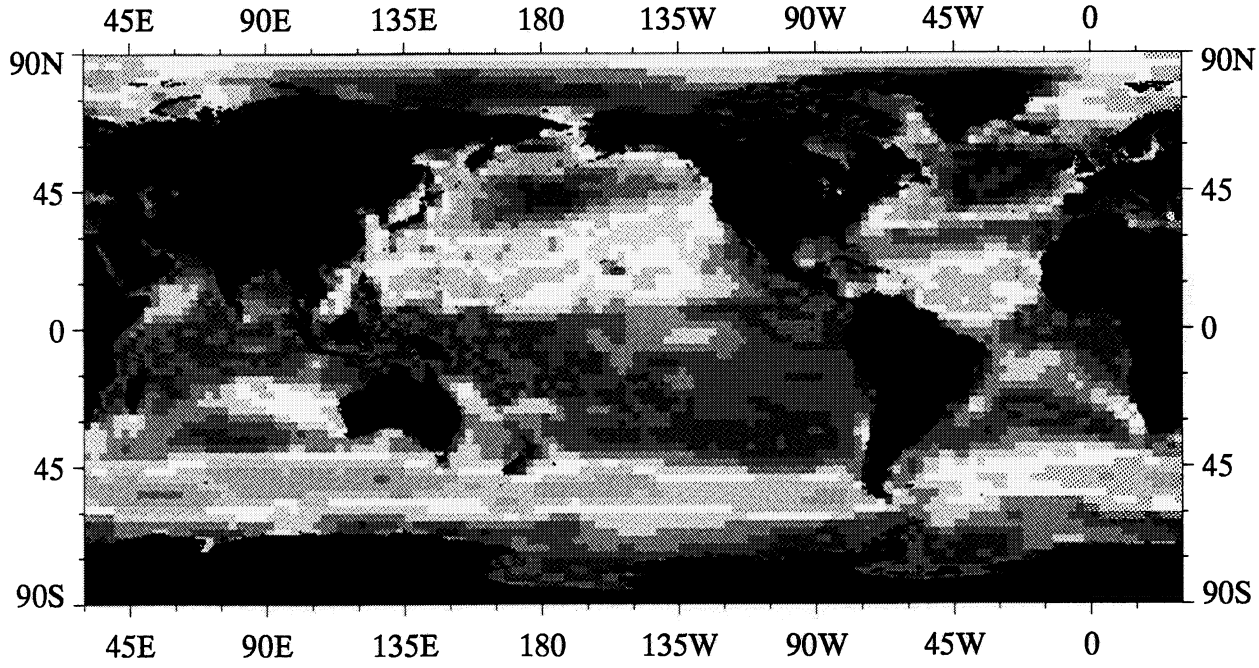


January 1990

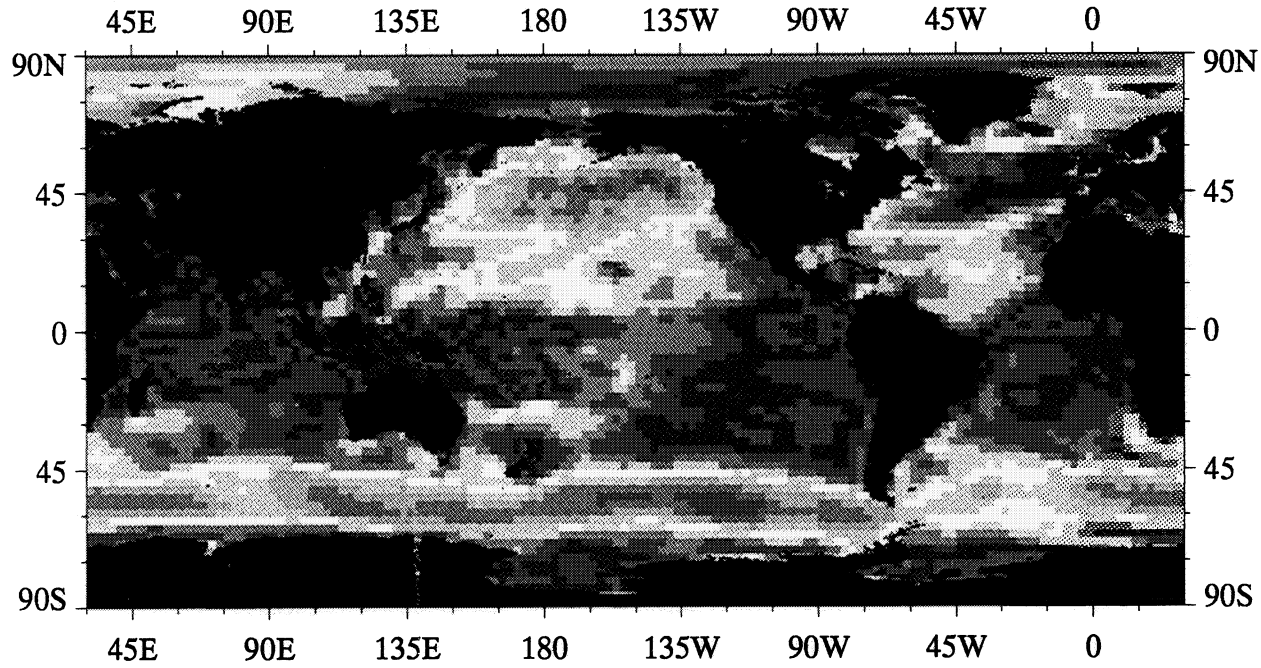


February 1990

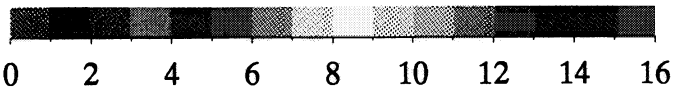


ECMWF 10 m Wind Speed, m $s^{-1}$

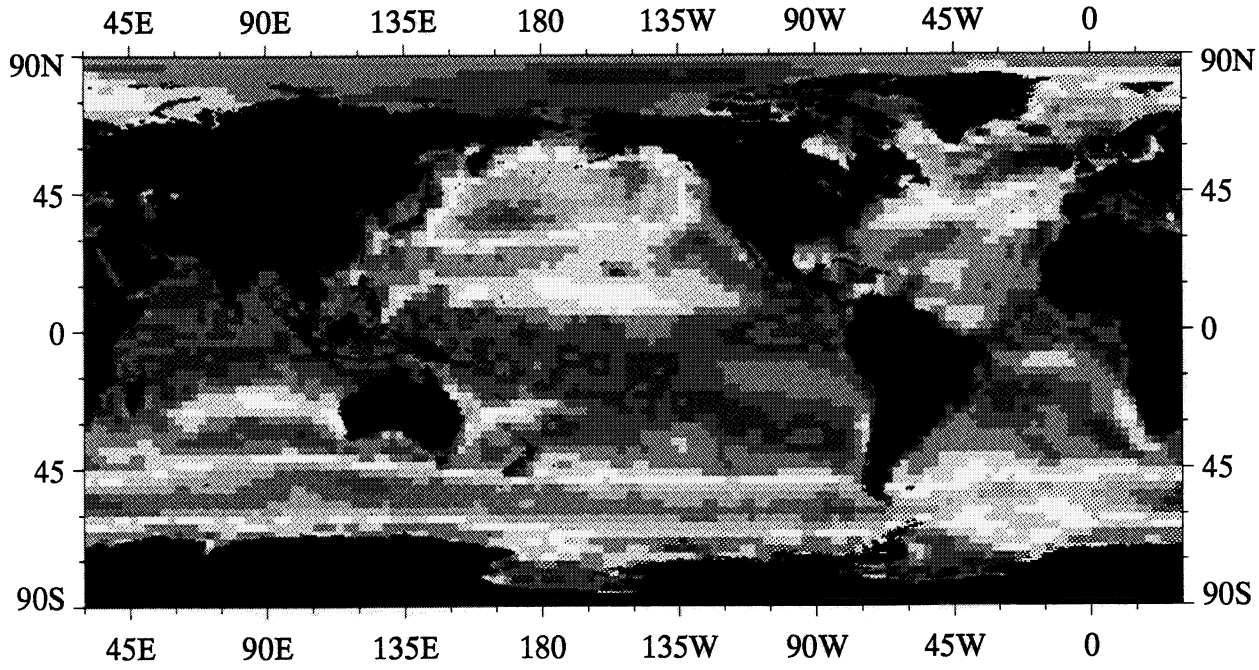


March 1990

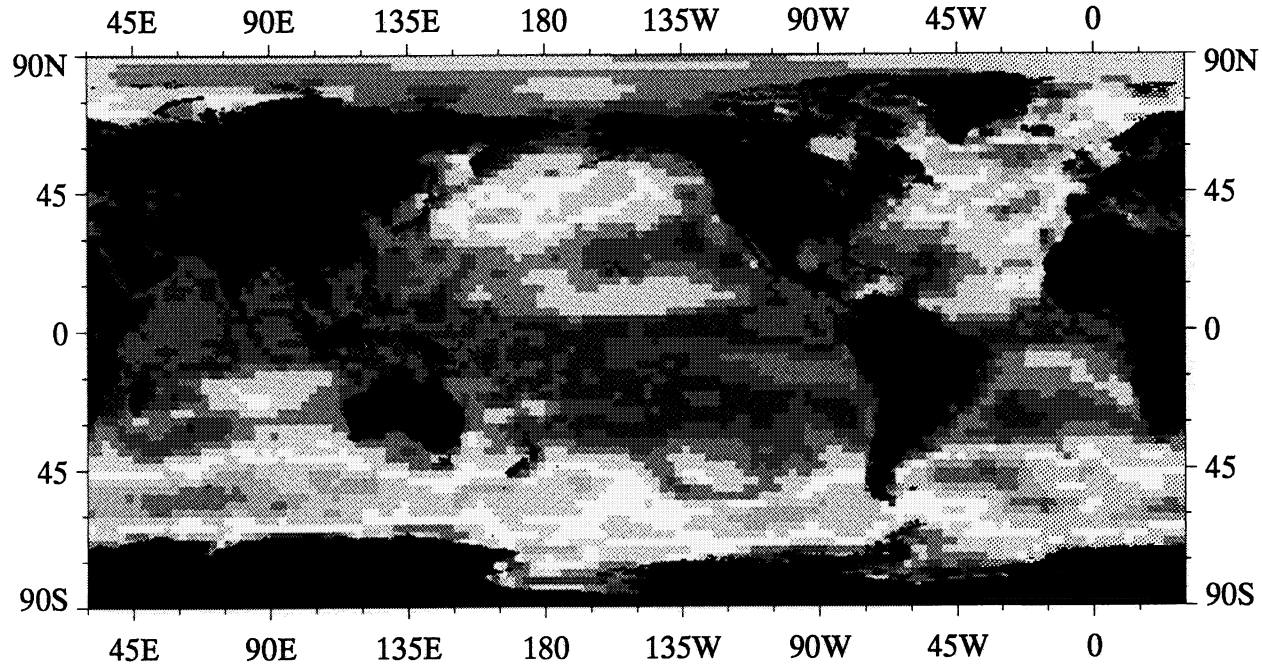


April 1990

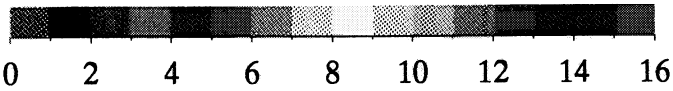


ECMWF 10 m Wind Speed, m $s^{-1}$

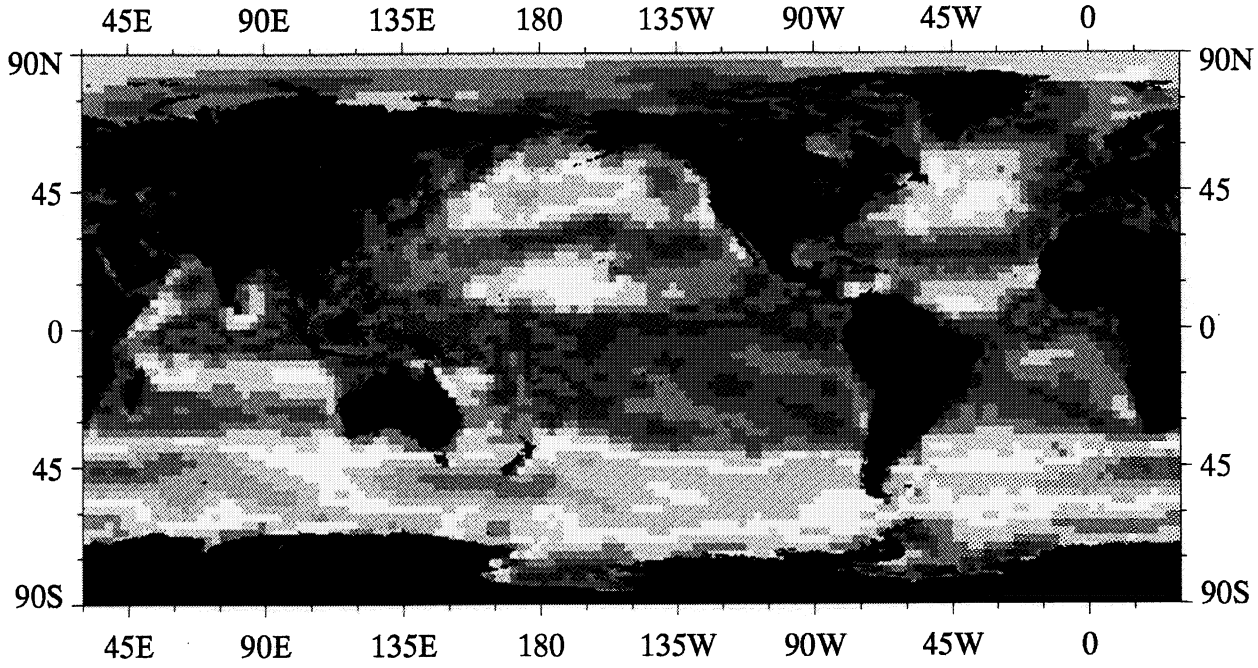


May 1990

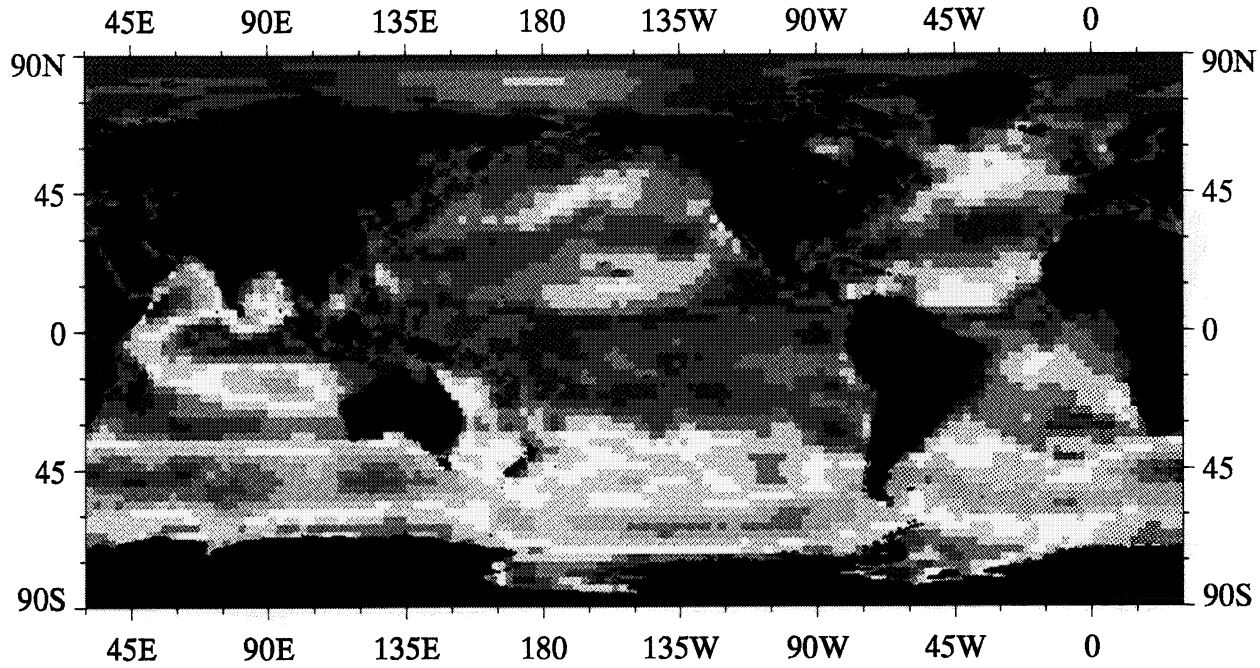


June 1990


ECMWF 10 m Wind Speed, m $s^{-1}$

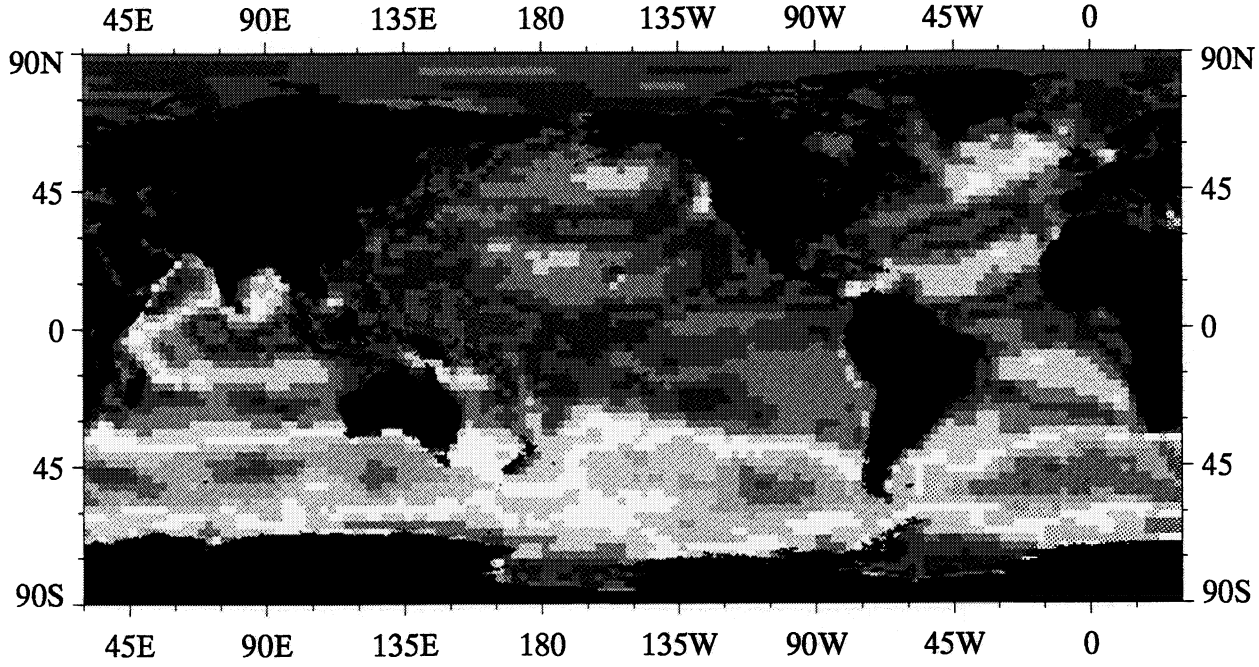


July 1990

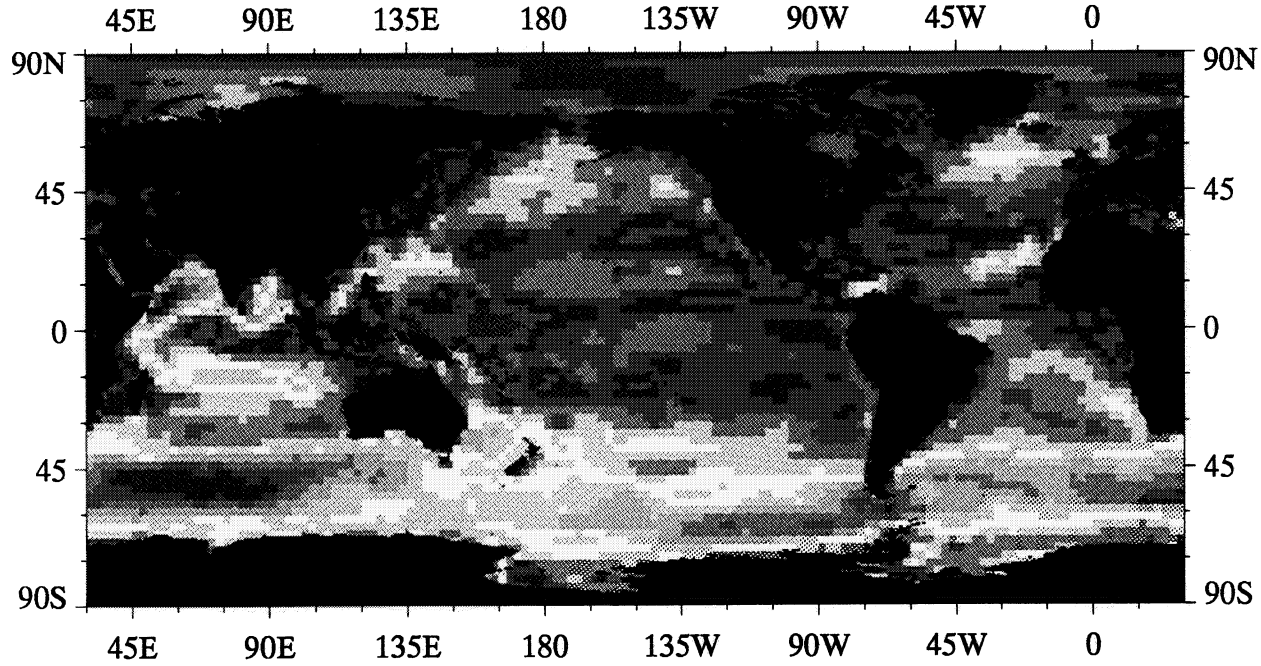


August 1990

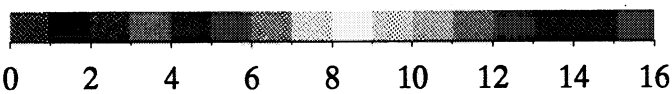


ECMWF 10 m Wind Speed, m $s^{-1}$

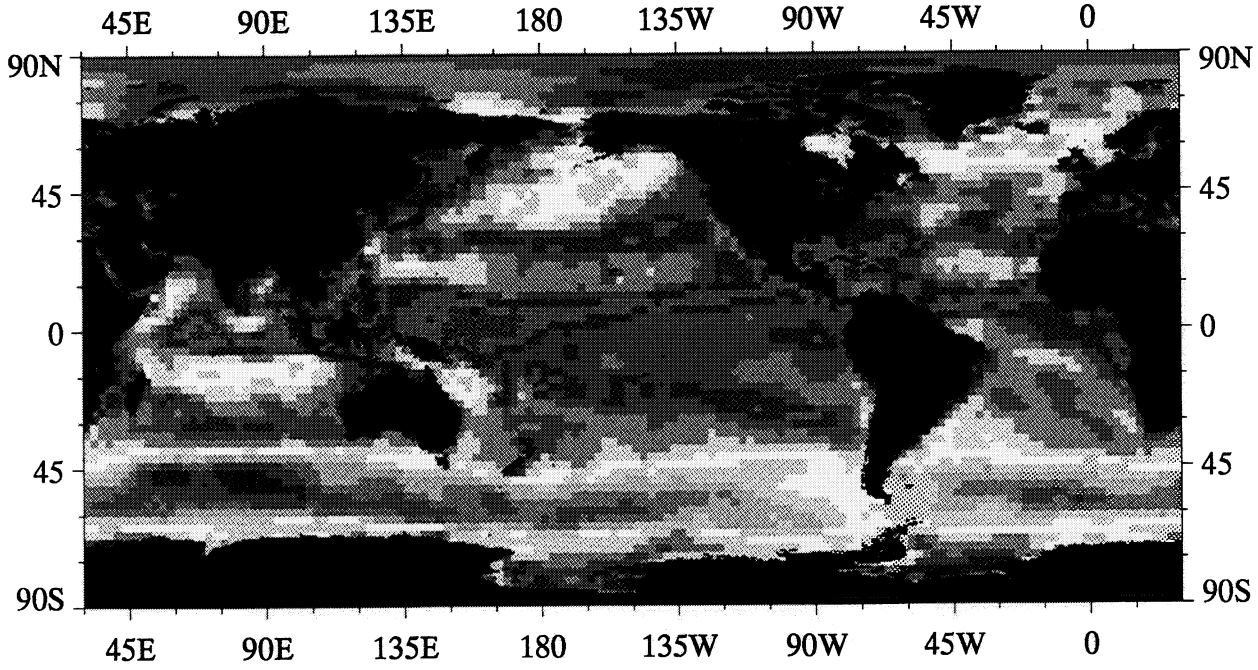


September 1990

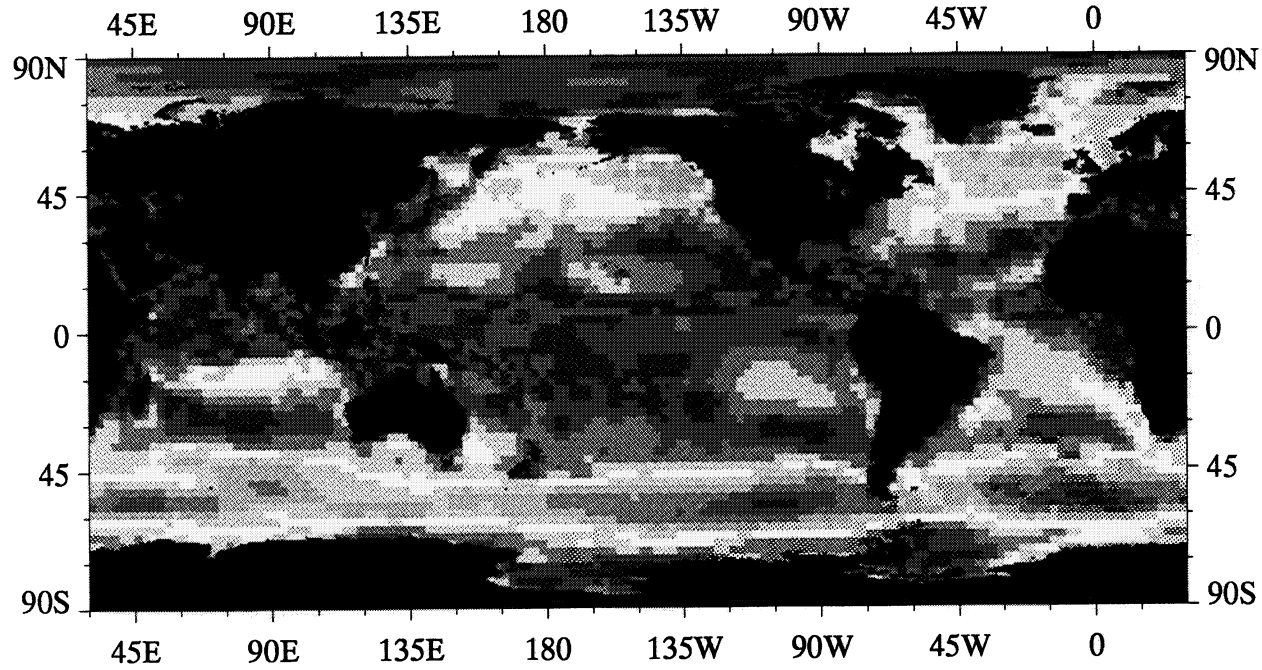


October 1990

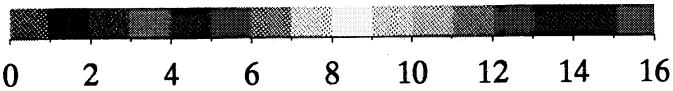


ECMWF 10 m Wind Speed, m $s^{-1}$

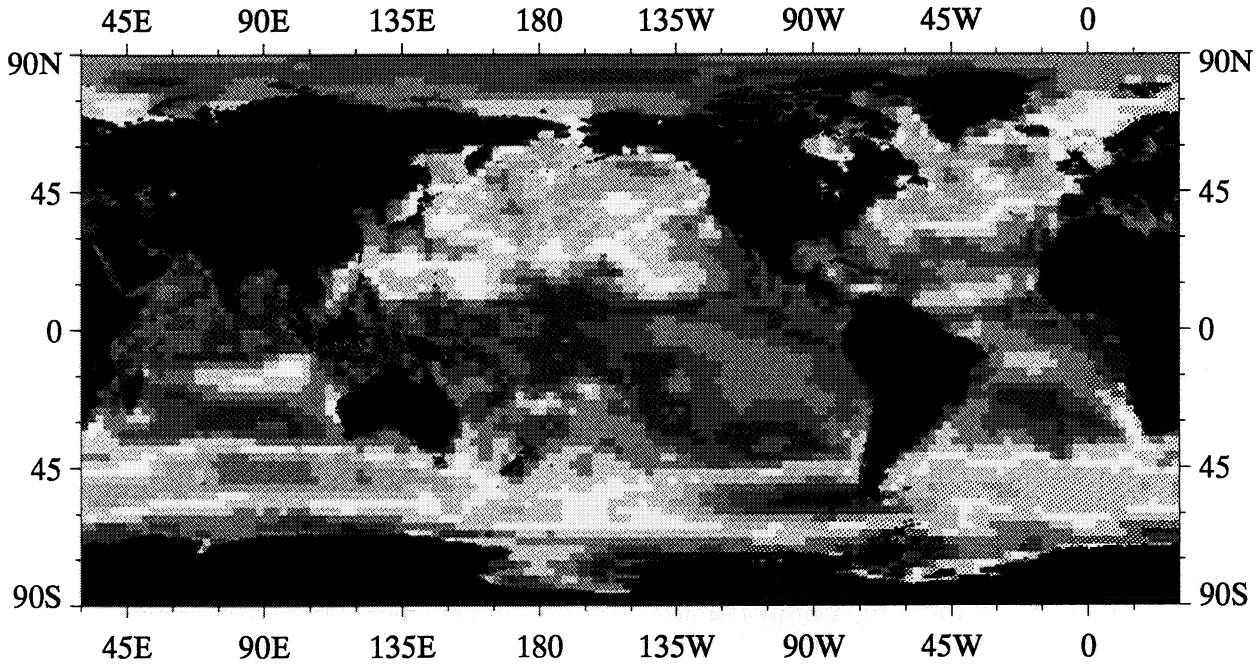


November 1990

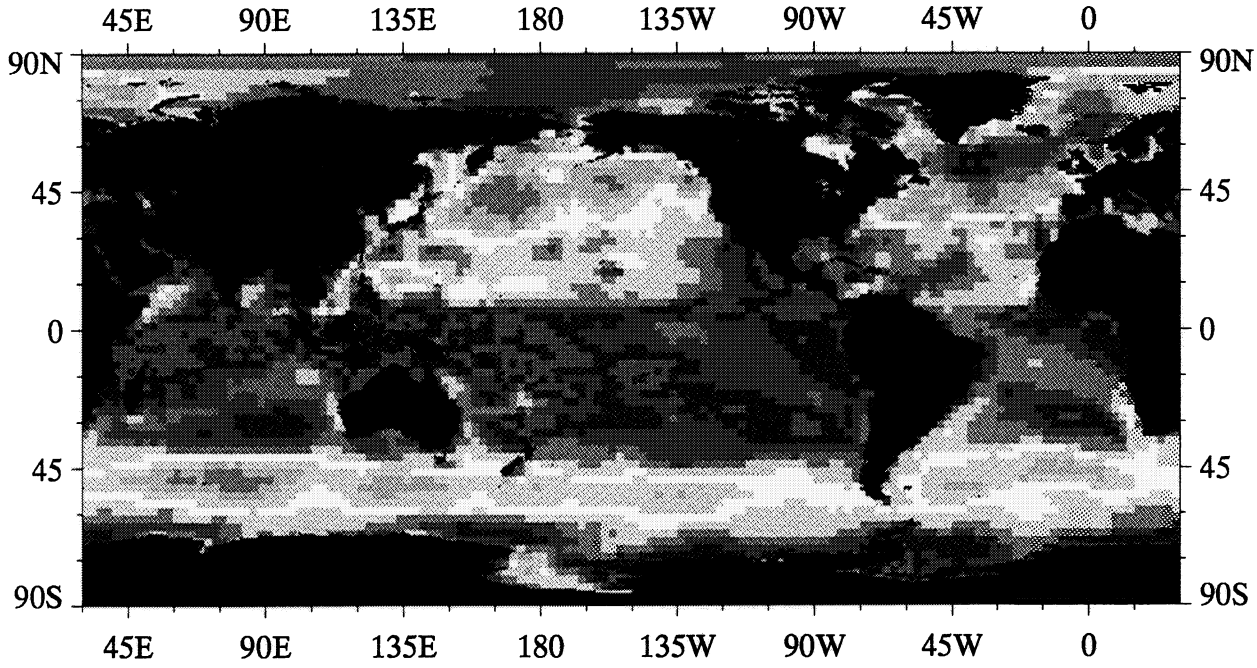


December 1990


ECMWF 10 m Wind Speed, m $s^{-1}$

A14

Monthly Standard Deviation of ECMWF Surface Wind Speed

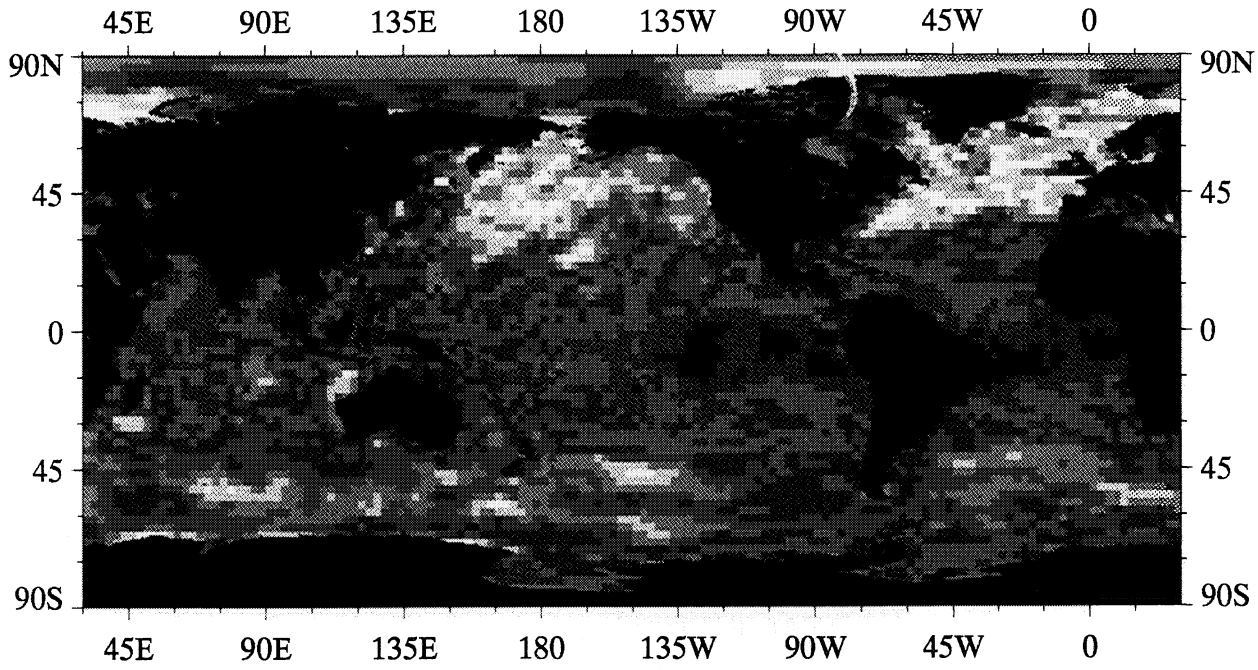


January 1990

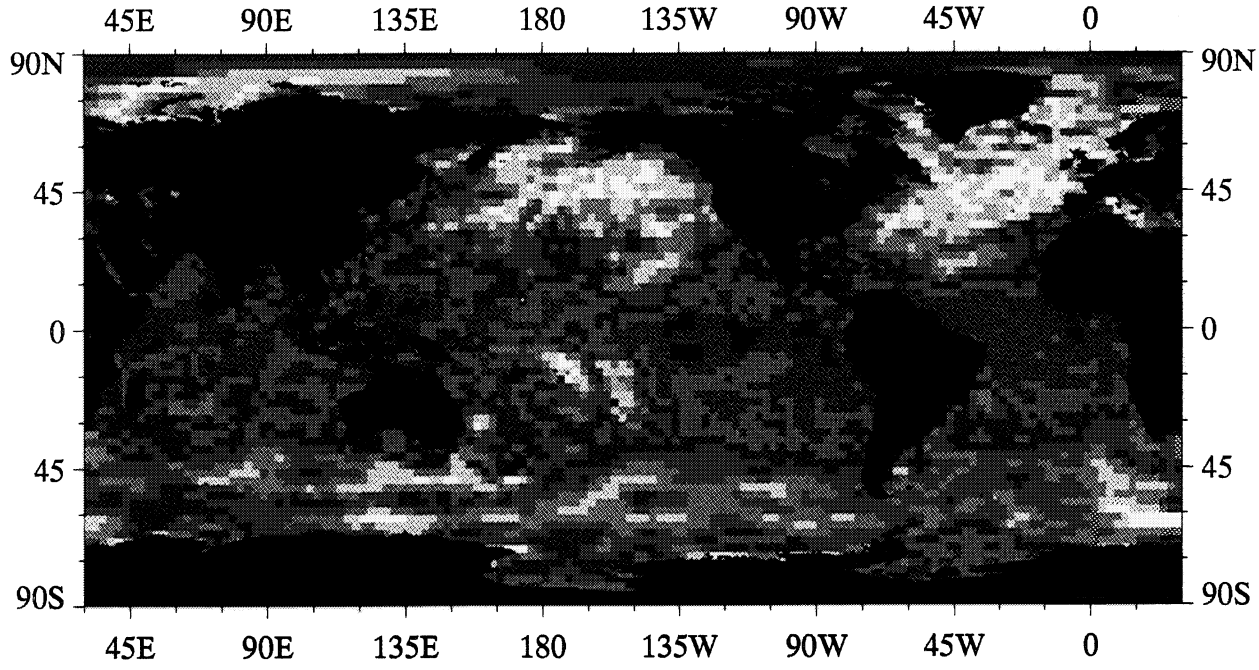


February 1990

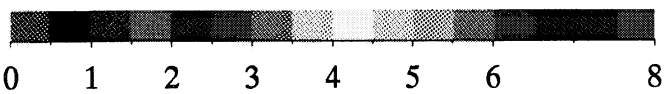


Standard Deviation of ECMWF 10 m Wind Speed, m $s^{-1}$

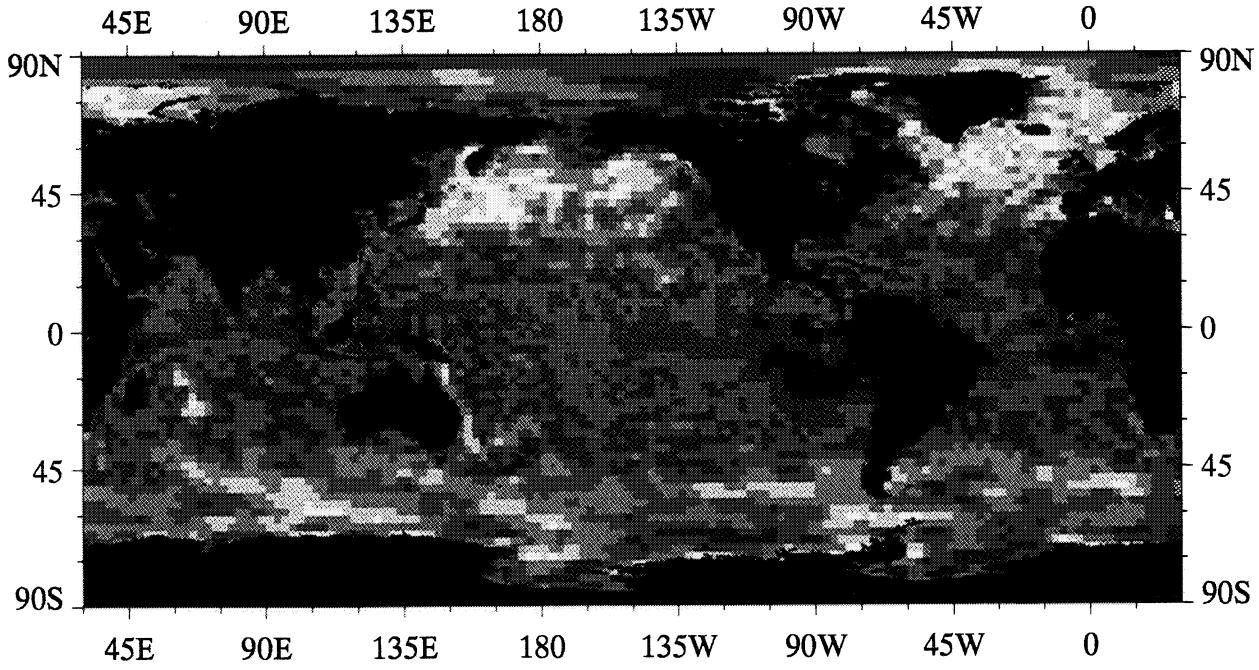


March 1990

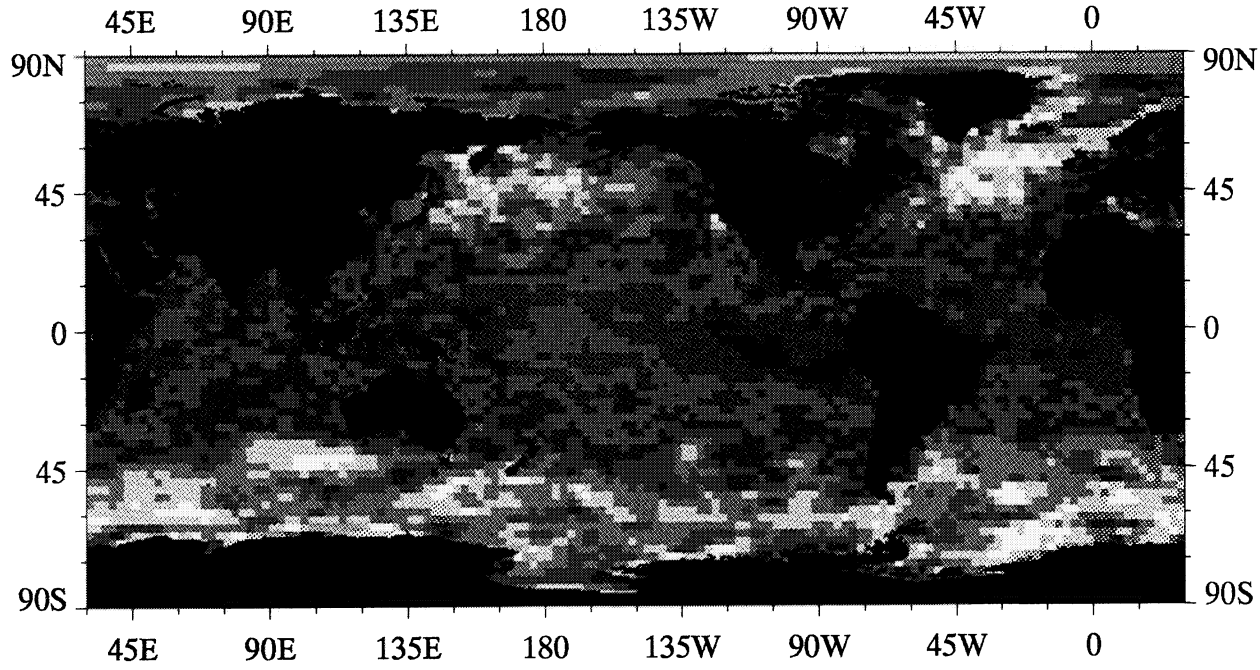


April 1990

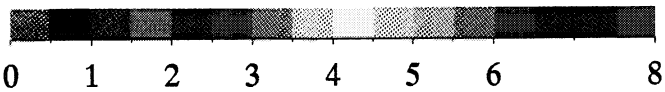


Standard Deviation of ECMWF 10 m Wind Speed, m $s^{-1}$

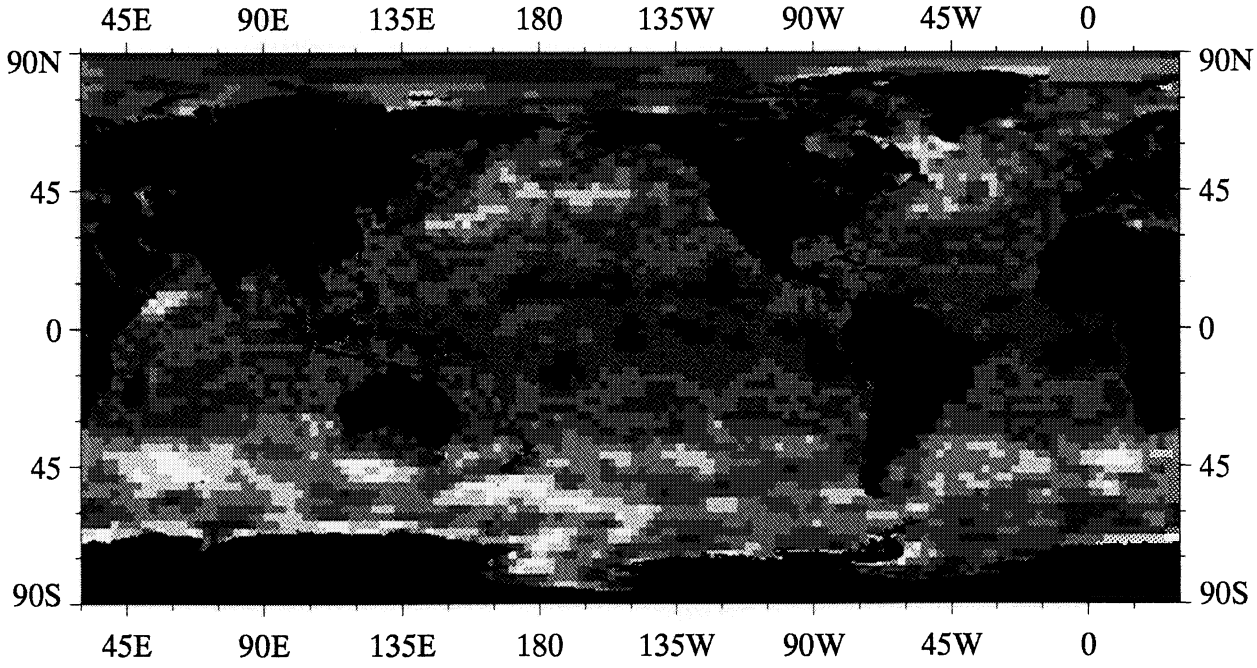


May 1990

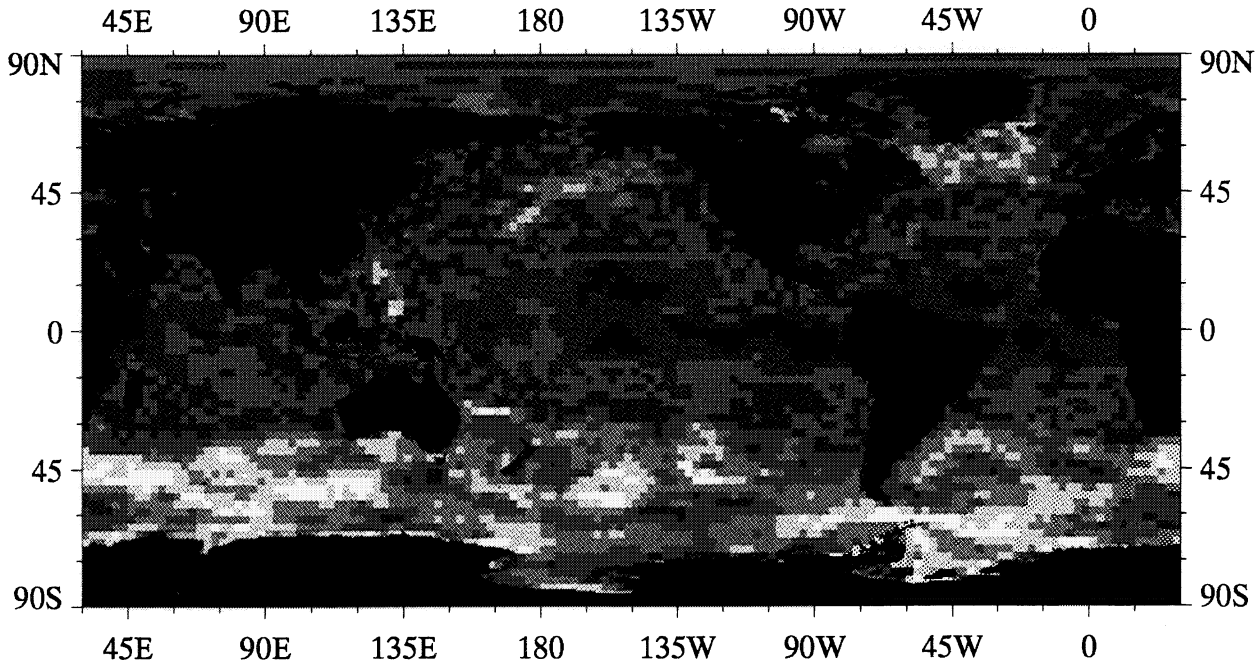


June 1990

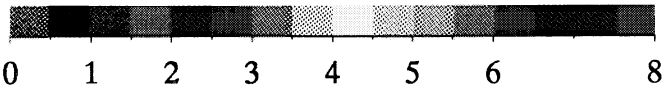


Standard Deviation of ECMWF 10 m Wind Speed, m $s^{-1}$

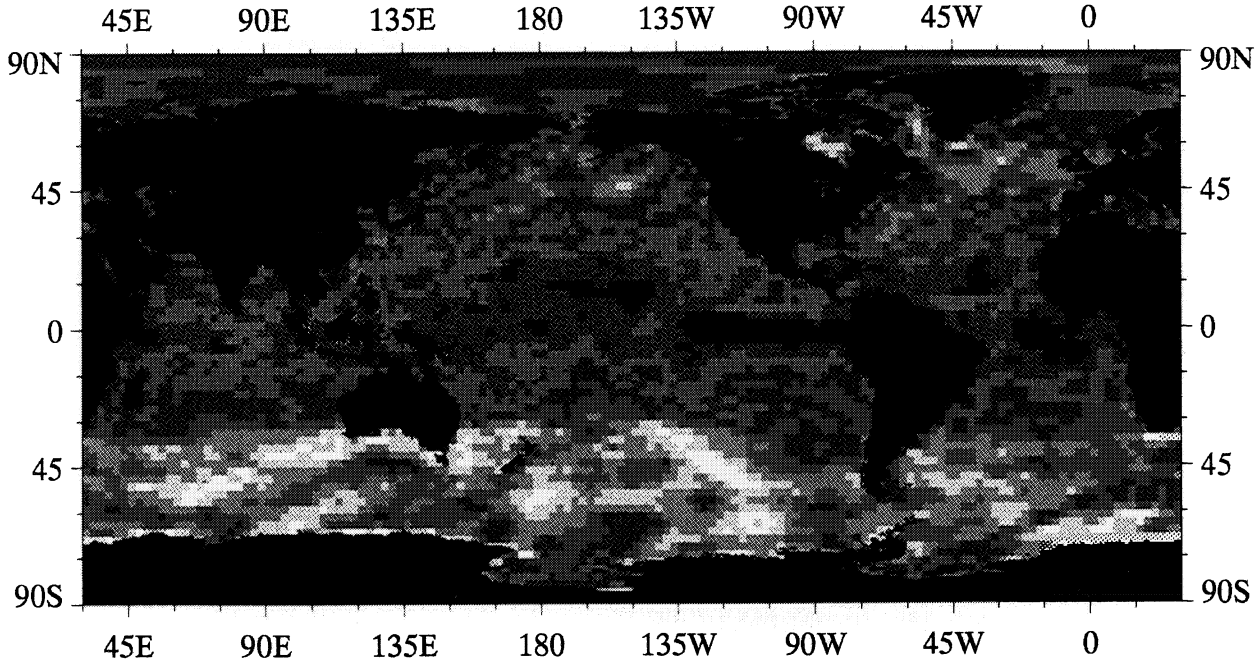


July 1990

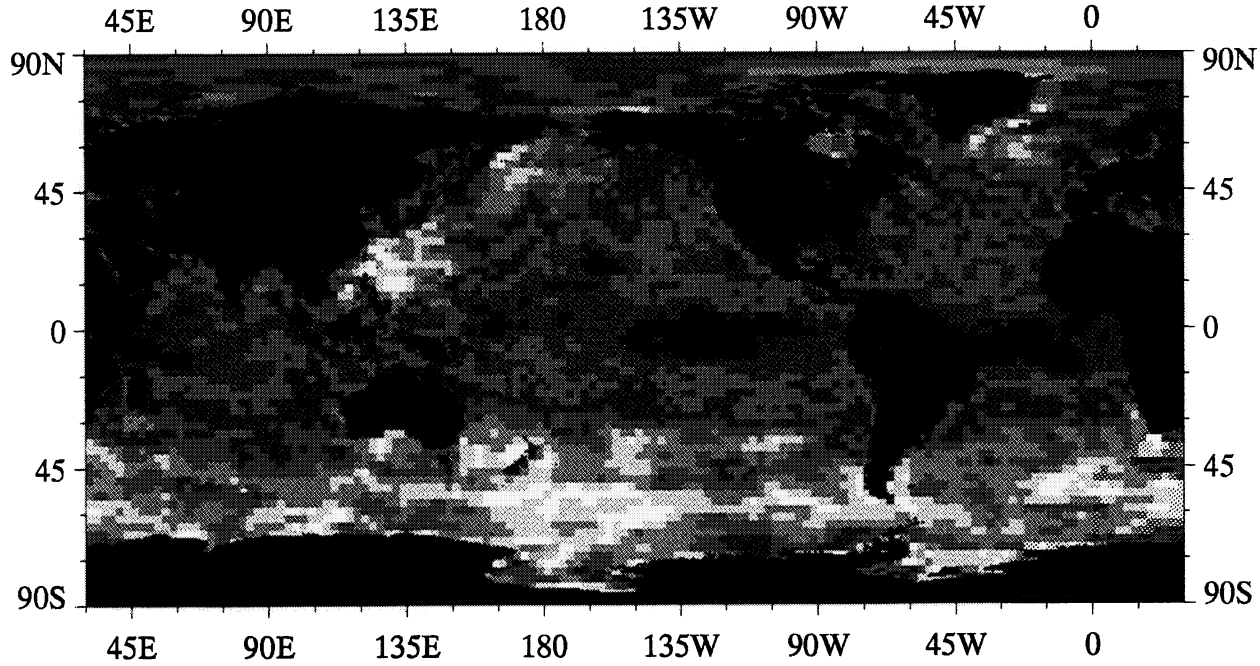


August 1990

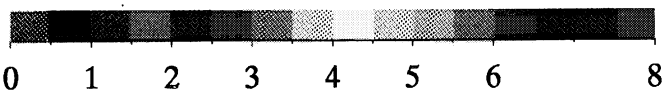


Standard Deviation of ECMWF 10 m Wind Speed, m $s^{-1}$

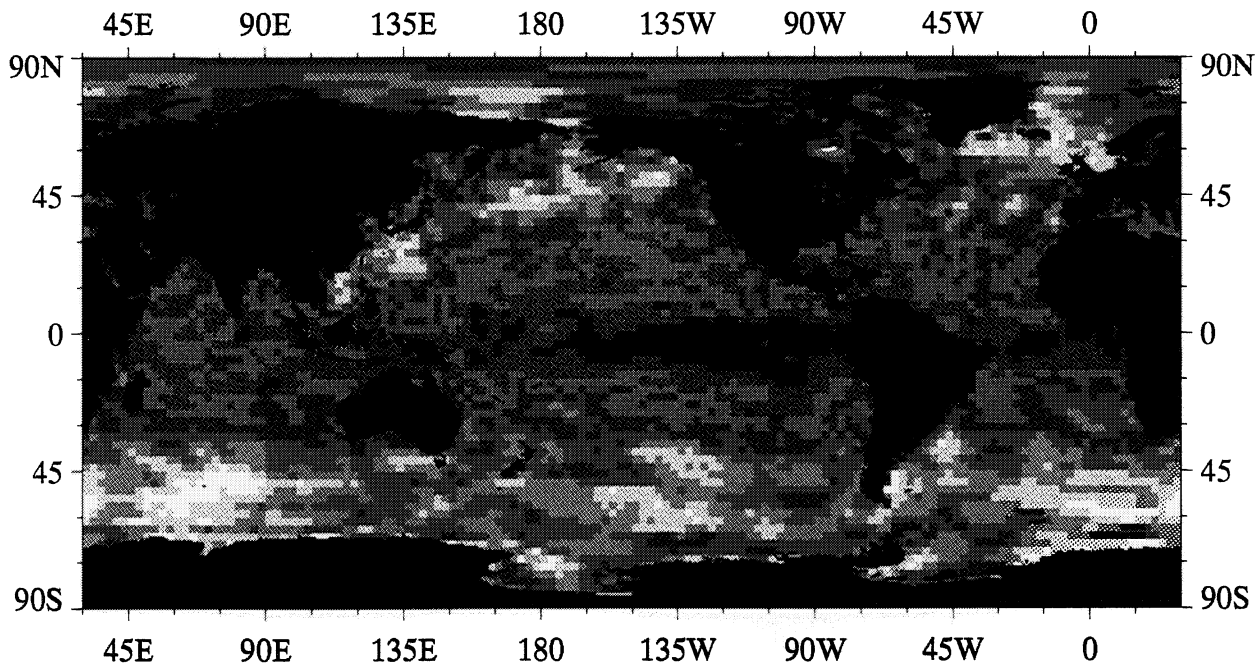


September 1990

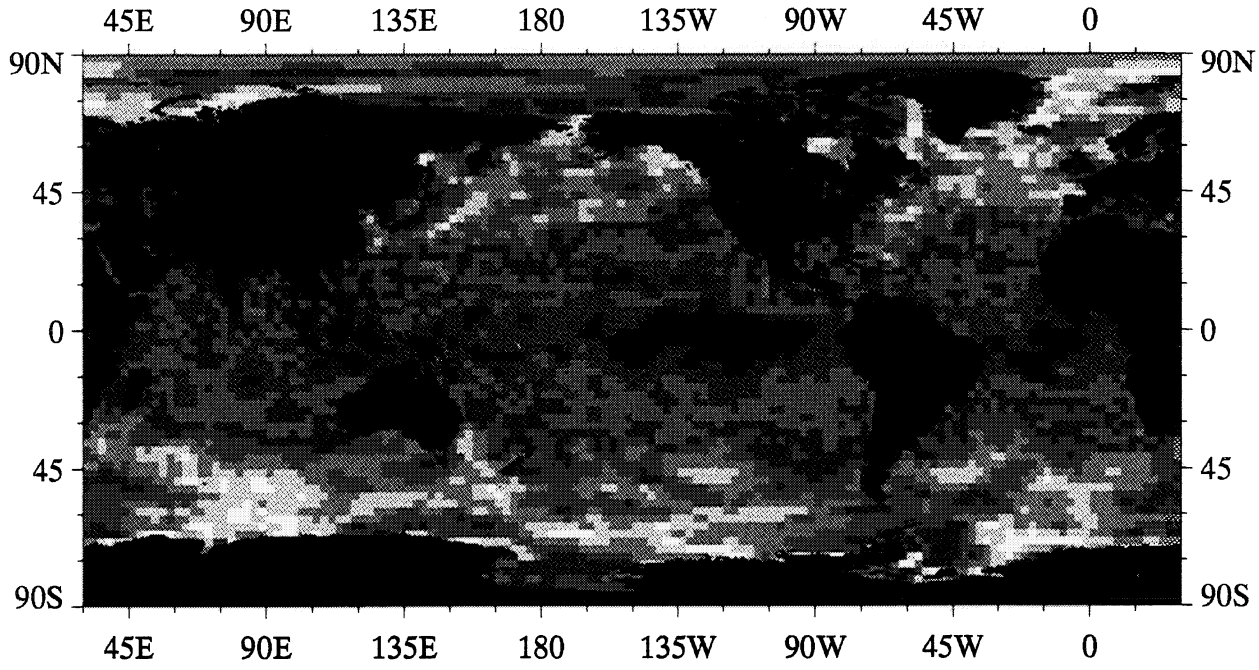


October 1990

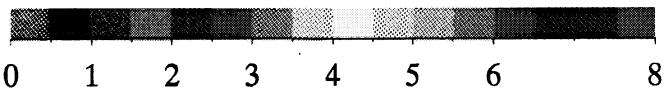


Standard Deviation of ECMWF 10 m Wind Speed, m $s^{-1}$

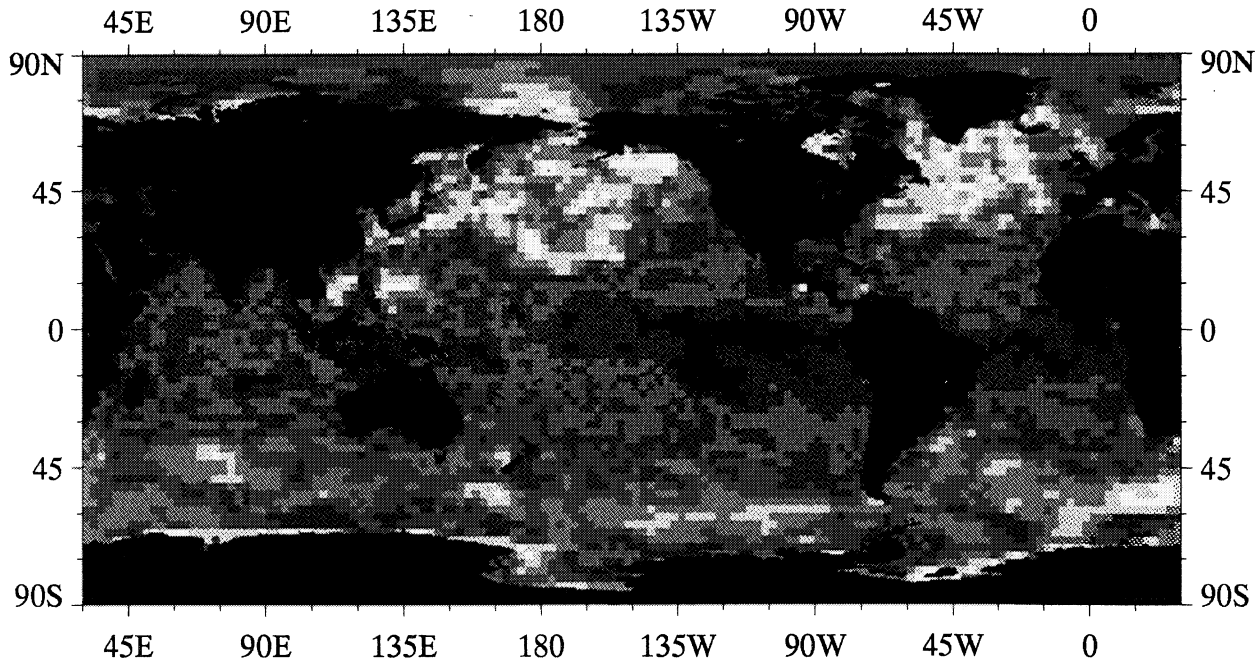


November 1990

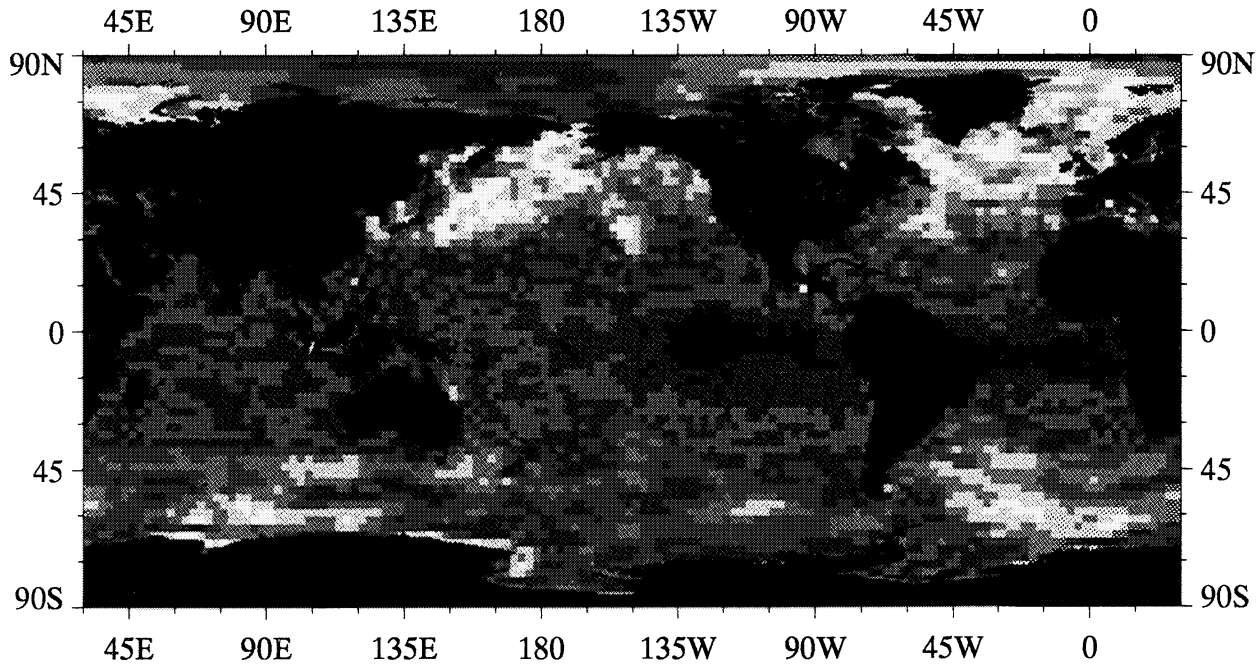


December 1990

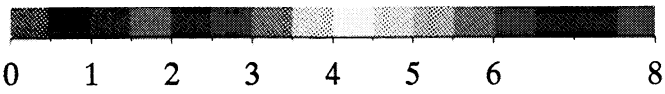


Standard Deviation of ECMWF 10 m Wind Speed, m $s^{-1}$